Éléments finis de plaque à cinématique variable pour les structures sandwich

Girolamo Di Cara

Université Paris Nanterre
200 av. de la République
92001 Nanterre Cedex
www.parisnanterre.fr

Membre de l'université Paris Lumières

Ecole doctorale 139 :
Connaissance, langage, modélisation
Laboratoire Energétique Mécanique Electromagnétisme

Girolamo Di Cara

Variable Kinematics Finite Plate Elements for Sandwich Structures Applications

Thèse présentée et soutenue publiquement le 19/12/2022
en vue de l'obtention du doctorat de Mécanique, Génie Mécanique et Génie Civile
de l'Université Paris Nanterre
sous la direction de M. Olivier Polit
et de M. Michele D'Ottavio

Jury :

Président :	Pascal Casari	Université de Nantes
Rapporteur :	Bruno Castanié	INSA Toulouse
Rapporteur :	Marco Petrolo	Politecnico di Torino
Examinateur :	Aurélio Lima Araújo	Instituto Superior Técnico
Examinateur :	Jean-François Deü	Conservatoire National des Arts et Métiers
Directeur de thèse :	Olivier Polit	Université Paris Nanterre
Co-directeur :	Michele D'Ottavio	Université Paris Nanterre

Abstract

The variable kinematics approach allows to choose different plate models according to the desired level of accuracy. Furthermore, the mixed ESL/LW approach of SGUF makes the model particularly convenient for sandwich structures analysis. The Sublaminate Generalized Unified Formulation (SGUF) is extended for the first time to the framework of Finite Element Method (FEM) for both displacement-based and mixed (RMVT) formulation. A substitute interpolation for the transverse shear strain field, referred to as QC4/CL8 interpolation, makes the developed FEs locking free and insensitive to mesh distortion. The complete expression of finite element matrices for the PVD-based and RMVT-based elements is provided. The possibility of exactly satisfying transverse stress boundary conditions for RMVT-based elements is also investigated for the first time. The flexibility and accuracy of the computational approach is demonstrated on linear static problems of sandwich plates and beams ranging from global bending response to local indentation problems. The challenging phenomenon experienced by laminated composite plates at free edges, known as free-edge effect, is also addressed.

Free and forced vibration of sandwich beams and plates hosting viscoelastic material (VEM) layers are also investigated. A brief survey on viscoelastic models in both time- and frequency-domain is presented along with the solution strategies. In particular, the frequency-dependent behaviour of VEM is modelled according to the fractional derivatives Zener-type model or conventional series development based on the Generalised Maxwell model. The damped properties, i.e. modal loss factors and damped eigenfrequencies, are obtained within the complex modulus approach and compared to those available in the literature for conventional and unconventional sandwich configurations. The frequency response of sandwich panels is computed by a direct approach, i.e. by solving the linear system of equations as many times as the number of frequencies set in the frequency bandwidth of interest.

Finally, stability considerations are addressed within the framework of the classical linearised stability analysis considering a symmetric cross-ply laminate subjected to

a uniaxial uniform strain. The role of geometric and elastic properties on buckling loads and buckled shapes is emphasised by referring to a sandwich panel uniformly strained along the longitudinal direction. The onset of local instabilities in the face sheet of a sandwich panel under three-point flexion solicitation are also addressed. Convergence studies are performed to establish the minimum number of elements for the local instabilities to be grasped.

It is demonstrated that the proposed approach is capable of recovering full three-dimensional response with a 2D FE mesh and with less degrees of freedom than the conventional models available in commercial FE packages. All the findings presented in this dissertation relied on an in-house Finite Element code developed throughout the doctoral project. The proposed Finite Plate Elements are implemented via Fortran subroutines. A dedicated Python GUI (Graphical User Interface) drives the model in the range of admissible analyses. The solution of the linear systems relies on a direct sparse solver, namely the PARDISO Solver Project, whilst generalised eigenvalue problems are solved by resorting the ARnoldi PACKage (ARPACK).

Résumé

L'approche à cinématique variable permet de choisir différents modèles de plaques selon le niveau de précision souhaité. De plus, l'approche mixte ESL/LW de SGUF rend le modèle particulièrement pratique pour l'analyse des structures sandwich. La Sublaminate Generalized Unified Formulation (SGUF) est étendue pour la première fois au cadre de la Méthode des Éléments Finis (MEF) pour la formulation classique aux déplacements et mixte (RMVT). Une interpolation de substitution pour le champ de déformation de cisaillement transverse, appelée interpolation QC4/CL8, rend les EFs développé libres du verrouillage et insensibles à la distorsion du maillage. L'expression complète des matrices pour les éléments basés sur PVD et RMVT est fournie. La possibilité de satisfaire exactement les conditions aux limites des contraintes transverses pour les éléments basés sur la formulation mixte RMVT est également étudiée pour la première fois. La flexibilité et la précision de l'approche de calcul sont démontrées sur des problèmes statiques linéaires de plaques et de poutres sandwich allant de la réponse globale de flexion aux problèmes d'indentation locale.

Les vibrations libres et forcées des poutres et plaques sandwich abritant des couches de matériaux viscoélastique (VEM) sont également étudiées. Une brève étude sur les modèles viscoélastiques dans les domaines temporel et fréquentiel est présentée avec les stratégies de solution. En particulier, le comportement en fonction de la fréquence du VEM est modélisé selon le modèle aux dérivés fractionnaires de type Zener ou modèle de Maxwell généralisé par une expansion en série. Les propriétés amorties, c.-à-d. les facteurs de perte modaux et les fréquences propres amorties, sont obtenues dans le cadre de l'approche par module complexe et comparées à celles disponibles dans la littérature pour des configurations sandwich conventionnelles et non conventionnelles. La réponse en fréquence des panneaux sandwich est calculée par une approche directe, c.-à-d. en résolvant le système linéaire d'équations autant de fois que le nombre de fréquences définies dans la bande passante d'intérêt.

Enfin, la stabilité des structures composites est abordée dans le cadre de l'analyse classique de stabilité linaire en considérant un stratifié croisé symétrique soumis à

une déformation uniforme uniaxiale. Le rôle des propriétés géométriques et élastiques sur les charges de flambement et les déformées modales est mis en évidence en se référant à un panneau sandwich uniformément tendu dans la direction longitudinale. Le début des instabilités locales dans la peau en compression d'un panneau sandwich sous la sollicitation de flexion en trois points est également abordé. Des études de convergence sont réalisées pour établir le nombre minimum d'éléments à saisir pour que les instabilités locales soient saisies.

Il est démontré que l'approche proposée est capable de récupérer une réponse tridimensionnelle avec un maillage 2D EF et avec moins de degrés de liberté que les modèles classiques disponibles dans les logiciels aux éléments finis commerciaux. Tous les résultats présentés dans cette thèse s'appuient sur un code interne aux éléments finis développé tout au long du projet doctoral. Les éléments finis proposés sont implémentés via des routines Fortran. Une interface graphique Python dédiée pilote le modèle dans la gamme des analyses admissibles. La solution des systèmes linéaires repose sur un solveur direct, le PARDISO Solver Project, tandis que le problème aux valeurs propres généralisé est résolu en utilisant le ARnoldi PACKage (ARPACK).

Contents

List of Figures

List of Tables

Nomenclature

Abbreviations

1D, 2D, 3D	One-, Two-, Three-dimensional
AAM	Axiomatic/Asymptotic Method
ADF	Anelastic Displacement Field
CLT	Classical Lamination Theory
CMA	Complex Modulus Approach
CUF	Carrera Unified Formulation
DOF	Degree of Freedom
EHSAPT	Enhanced High-order Sandwich Panel Theory
ESL	Equivalent Single Layer
EVE	Elastic-Viscoelastic-Elastic
FD	Fractional Derivatives
FDZ	Fractional Derivatives Zener-type
FE	Finite Element
FEM	Finite Element Method
FSDT	First-order Shear Defomation Theory
GFEM	Global Finite Element Method
GHM	Golla-Hughes-McTavis
GUF	Generalized Unified Formulation
GUI	Graphical User Interface
HSDT	High-order Shear Defomation Theory
LW	Layer-Wise
MZZF	Murakami's ZigZag Function
PVD	Principle of Virtual Displacements
RMVT	Reissner's Mixed Variational Theorem
SGUF	Sublaminate Generalized Unified Formulation
VEM	Viscoelastic Material

Greek symbols

λ	eigenvalue
ω	frequency [rad/s]
$\epsilon_{ij}, \boldsymbol{\epsilon}$	geometric strain tensor
Ω	in-plane domain (surface)
ξ	natural x coordinate
η	natural y coordinate, loss factor
ζ	non-dimensional thickness coordinate
$\partial a/\partial x$	partial derivative along x of argument a
μ	Poisson's ratio
θ	rotation angle
$\sigma_{ij}, \boldsymbol{\sigma}$	stress tensor
$\alpha, \beta, \mu, \tau, \gamma$	summation indices
ε	tolerance
δ	virtual variation

Latin symbols

V	3D domain (volume)
$\mathbf{R}$	external load vector
$\bar{t}$	external tractions
f	frequency [Hz]
$\mathbf{U}$	generalized displacement vector
$\mathbf{S}$	generalized transverse stress vector
$\mathcal{U}$	generic unknown variable
$\mathbf{K}_\sigma$	initial stress matrix
N_i	isoparametric shape function of node i
P_n	Legendre polynomial of order n
$\mathbf{M}$	mass matrix
$\tilde{\mathbf{C}}$	matrix of elastic coefficients for RMVT formulation (structural reference frame)
$\mathbf{B}$	matrix of geometrical differential operators
$\bar{\mathbf{C}}$	matrix of stiffness coefficients (material reference frame)
$\tilde{\mathbf{C}}$	matrix of stiffness coefficients (structural reference frame)
$\mathbf{F}$	matrix of thickness functions

$\mathcal{N}$	modified field-compatible shape functions
$\hat{\mathcal{U}}$	nodal unknows of the generic variable $\mathcal{U}$
N_p	number of plies
N_l	number of sublaminates
N	order of polynomials expansion
S	panel's aspect ratio
a, b	panel's in-plane dimensions
H	panel's total thickness
p	ply index
x, y	rectilinear in-plane coordinates
z	rectilinear thickness coordinates
G	shear modulus
$\mathbf{K}$	stiffness matrix
k	sublaminate index
F_r	thickness function of order r
h	thickness
$\mathbf{e}$	transverse strains vector obtained from constitutive relations
$\mathbf{u}$	vector of displacements
W	virtual work
E	Young's modulus

Introduction

Sandwich structures are widely employed in applications requiring high weight-specific bending stiffness, for instance aeronautics [1] or naval engineering [2]. Furthermore, the materials constituting the skins and the core can be specifically tailored to furnish, e.g., high energy absorption, acoustic damping, electro-mechanical wave absorption, thermal insulation and fire resistance, which make sandwich panels very suitable candidates for an extremely wide range of engineering applications [3, 4]. A discussion about sandwich panels' applications with respect to their eco-efficiency in view of an environmental footprint reduction of structures has been recently provided by Resende Oliveira *et al.* [5]. The inherent heterogeneity of composite sandwich structures leads to the definition of three *scales*. The distinction relies on the characteristic length of the heterogeneity (see Figure 1) and can be summarized as follows: (i) the *microscale* identifies the fibre-matrix heterogeneity within the individual plies, microstructure of the cellular structure of the honeycomb core, (ii) the *mesoscale* identify the heterogeneity at bi-material interface across the composite stack, (iii) the *macroscale* interests the global behaviour of the whole structure.

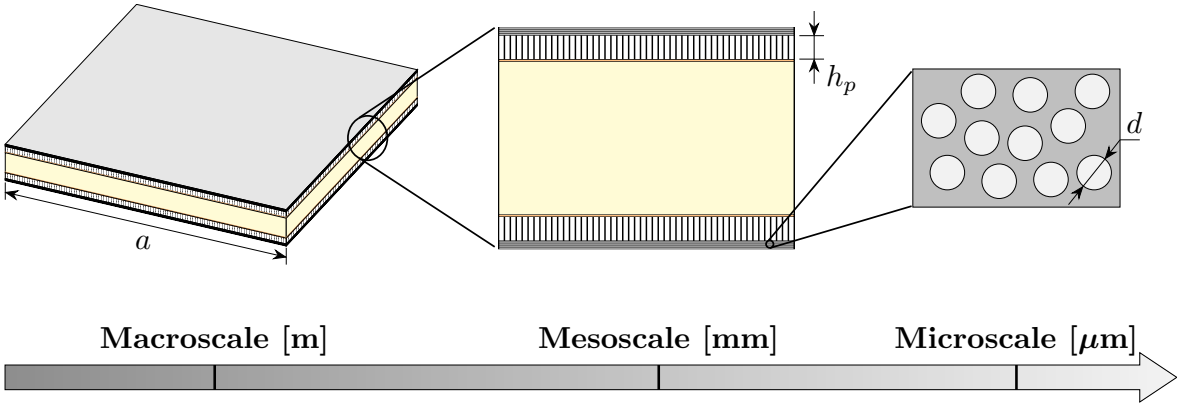

Figure 1: Characteristic lenght scales of a composite sandwich structure.

The development of mathematical theories and numerical models able to ensure an accurate description of both global (macroscale) and local (mesoscale) response of

composite sandwich structures is therefore crucial in the design process. But besides the reliability aspect, numerical models must be effective, i.e. an accurate prediction must be delivered with minimal computational effort. In this context, due to geometric considerations, classical two-dimensional (2D) models such as the Classical Laminate Theory (CLT) or First-order Shear Deformation Theory (FSDT) have been widely used throughout the years. Nevertheless, classical 2D models turn out to be inadequate in describing composite sandwich structures at the mesoscale level due to their heterogeneous cross-sections. Advanced 2D models may hence be addressed by referring for example to the partially mixed variational statement formulated by Reissner [6, 7], and therefore referred to as Reissner's Mixed Variational Theorem (RMVT), to cope with heterogeneity at bi-material interfaces. In particular, partially mixed models allows for the continuity requirement of the transverse stress field at plies' interfaces to be fulfilled.

This work aims at developing a reliable and effective numerical tool able to predict both global and local responses of composite sandwich beams and plates according to different analyses as outlined in the following section.

Structure of the thesis

This dissertation consists of 6 chapters according to the following outline. Chapter 1 provides a brief literature survey about the main topics addressed in the present work, namely sandwich panels modelling, variable kinematics approaches, viscoelastically damped sandwich structures and buckling of sandwich panels. In Chapter 2, displacement-based (PVD) and mixed (RMVT) variational principles are used to derive the semi-discrete governing equations within the framework of Sublaminate Generalized Unified Formulation (SGUF). The through-the-thickness behaviour of the field variables is axiomatically postulated at sublaminate level by choosing the order of expansion as well as the description (ESL or LW) along the thickness direction independently for each of the variables involved in the formulation. The 2D governing equations are solved in a weak form using the Finite Element Method (FEM). Numerical tests are performed to prove the robustness of the proposed FEs concerning the shear locking pathology and mesh distortion.

Chapter 3 presents an assessment and validation of the proposed model when applied to the mechanical analysis of composite structures. Particular emphasis is addressed on problems characterized by steep stress gradients, such as free-edge effects or indentation problems. The dynamic behaviour of sandwich panels with viscoelastic

cores is investigated in Chapter 4. The complex modulus approach is employed to compute the dynamic response in the frequency domain. The predicted damped properties obtained within the proposed FE approach are compared to several benchmark problems found in literature. Chapter 5 deals with the linearised stability analysis of composite laminates and sandwich panels. The initial stress matrix is derived within the SGUF variable kinematics approach by referring to von Kármán nonlinearities. The proposed FEs are applied to global and local buckling analyses and compared against solutions available in the literature or obtained by commercial FE packages. Finally, Chapter 6 draws the conclusions of the thesis and provides an outlook towards future developments.

Chapter 1

Literature Review

Modelling of sandwich panels. A sandwich panel is a structure made up of thin stiff skins, possibly composite, that are separated by a thick and relatively weak core. The analysis and design of composite sandwich panels requires refined models to cope with the strong mismatch between facings and core in terms of mechanical stiffness and geometric thickness. In fact, the strong face-core heterogeneity renders classical models for composite structures, such as *Classical Lamination Theory* (CLT) or *First order Shear Deformation Theory* (FSDT), inappropriate for evaluating bending deflections or vibration characteristics [8]. The need for detailed models is even more stringent if the attention is to be given to local stress response, which is a necessary step for a reliable prediction of the complex failure modes that characterise sandwich panels [9, 10]. As pointed out by Birman and Kardomateas [11], refined models are mandatory also in view of resolving multifield interactions and/or cross-scaling effects, which constitute relevant axis of development towards advanced sandwich applications. For instance, in order to improve the fidelity of the macro/meso-scale models that are customarily employed for the sizing of built-up panel structures, homogenization schemes have been recently proposed that take into account the cellular structure of commonly employed core micro-structures [12–14].

A large number of refined, high-order two-dimensional (2D) models have been thus proposed with the aim of attaining sufficient accuracy without resorting to computationally expensive full three-dimensional (3D) models. Early developments have been exhaustively summarised and assessed by Noor and Burton [15, 16], for more recent overviews we refer to [17–21]. Over the last years, it is worth mentioning the extension from 1D (beams or wide plates) to 2D plate models of the Enhanced High-order Sandwich Panel Theory (EHSAPT) [22] and its extension towards geometrically nonlinear analysis [23].

Since they rely on *ad hoc* assumptions, the accuracy of such axiomatically derived structural models is problem-dependent, for it depends on the physics of the considered problem (materials, geometry, loading ...) as well as on the output quantity of interest in the analysis. The variational-asymptotic approach is a mathematically very elegant manner to cope with this fundamental issue of reduced-order models [24], and it has conducted to relevant applications in the field of the mechanical response of sandwich structures [25, 26]. However, its generalization to complex problems, e.g., involving multifield couplings, still requires a heavy mathematical effort.

A very flexible and general framework for implementing virtually any kind of structural 1D beam and 2D plate/shell models has been proposed by Carrera with his Unified Formulation (CUF) [27–29] and subsequently generalized by Demasi (GUF) [30–32]. The dimensional reduction is carried out within the framework of two variational statements: the classical displacement-based approach expressed by the Principle of Virtual Displacements (PVD), and the mixed approach proposed by Reissner and referred to as Reissner Mixed Variational Theorem (RMVT) [6, 7]. RMVT allows to introduce independent assumptions for the field variables requiring to be interlaminar continuous, i.e., the displacements and the transverse stresses, thus permitting the model to *a priori* fulfil the so-called "C_z^0-Requirements" [33]. Axiomatic *variable kinematics* models are then constructed that can adopt *Equivalent Single Layer* (ESL) as well as *Layer-Wise* (LW) descriptions for the field variables. By virtue of the Unified Formulation, these models are expressed in a compact index notation that enables their implementation in terms of *kernel arrays* or *fundamental nuclei*. As a result, the user can select the model to be employed in the analysis at runtime, thus depending on the desired accuracy and intended output. Since the most refined models of CUF and GUF are capable of representing 3D stress states and singularities through the laminate thickness, see, e.g., [34, 35], the error introduced by a given model with respect to a certain output quantity can be quantitatively assessed, hence allowing to resolve the problem-dependent accuracy issue by resorting to an Axiomatic/Asymptotic Method (AAM) [36–42].

D'Ottavio formally extended GUF upon enabling the possibility of selecting different models for individual sublaminates, which consist of an arbitrary number of contiguous plies within the composite stack [43]. The resulting Sublaminate GUF (SGUF) affords thus a mixed ESL/LW description, illustrated in Figure 1.1, which is particularly meaningful for sandwich panels: in fact, different models can be adopted for the thin and stiff skins and the thick and compliant core layers [44]. Therefore, this feature allows to further optimise the number of unknown functions of the structural

model without affecting the accuracy.

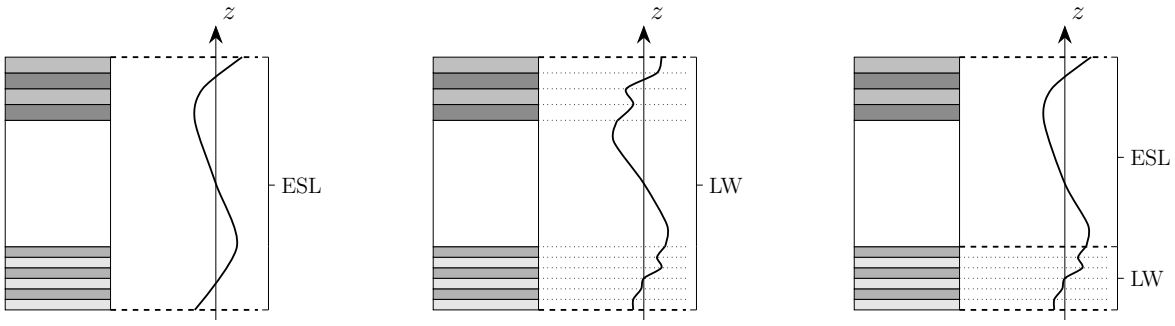

Figure 1.1: Example of different through-thickness models of a multilayered plate.

SGUF has been successfully employed in the framework of a Ritz solution method to the analysis of bending, vibration and buckling of sandwich plates and shells, which could comprise also multiple cores and piezoelectric patches [45–49].

Viscoelastic sandwich structures. Nowadays, especially in automotive and aeronautic industries, structures embedding a layer made up of viscoelastic material (VEM) are of great concern thanks to its capability of suppressing mechanical vibrations and of reducing noise [50, 51]. This kind of structures are naturally assimilated to sandwich panels featured with a viscoelastic core interconnecting two structural skins. It is remarkable that the viscoelastic layer sandwiched between two stiff skins does not need to be thick for attaining satisfying damping properties [52]. However, the benefits offered by embedding a damping layer in the structure come along with some modelling issues, ranging from the physical mechanisms of the viscoelastic layer up to the structural response. In the following, the modelling techniques that have been used through the years to describe the behaviour of VEM are briefly discussed. The focus is given to models inscribed within the Complex Modulus Approach (CMA) in view of their FE implementation [53].

Complex viscoelastic rheological models based on generalised Maxwell model or the generalised Kelvin chain are widely employed to describe the frequency-dependent behaviour of VEM. Among them, it is worth citing the Golla-Hughes-McTavish (GHM) [54] and the Anelastic Displacement Field (ADF) [55]. As a general rule, models based upon series developments can require a large number of parameters for accurately describing the response of VEM, especially if weakly frequency-dependent materials are considered. As an alternative, constitutive laws described by fractional derivatives (FD) [56–58] have been proposed which require a relatively low number of material

parameters, typically four or five [59, 60]. Moreover, the system causality is ensured contrary to viscoelastic models based upon conventional series development such as the GHM or the ADF.

Since the shear-related deformation of the weak viscoelastic core due to the outer stiff layers can not be neglected, refined models need to be considered. Many structural models based on the Finite Element Method (FEM) have been developed through the years to describe the dynamic response of composite sandwich panels hosting a VEM core layer . Early applications consider three-dimensional (3D) FEs to model the viscoelastic core layer. [61–65]. Two-dimensional (2D) plate or shell FEs are used for the thin face sheets and nodal linkage ensure bonding at face-core interfaces. Although the 3D FEs modelling provides accurate predictions, it requires time-intensive simulations. To alleviate the computational burden of 3D modelling techniques, refined 2D models shall be addressed. As already mentioned, LW or ZigZag are required to cope with the strong material mismatch between core and skins [17, 66, 67]. The CLT, when applied to the face sheets, allows to account for the bending stiffness, whilst the axial and shear stresses in the core are included by assuming at least FSDT. LW theories employed to model sandwich structures hosting a VEM layer are discussed in the following. Daya *et al.* [68] investigated the nonlinear vibrations of viscoelastic sandwich beams by assuming the Euler-Bernoulli theory for the thin face sheets whilst the displacement field in the viscoelastic core is modelled according to the first-order shear deformation theory. Moreira *et al.* [67] developed a layerwise FSDT model for the dynamic analysis of sandwich plate hosting a thin viscoelastic core layer. An enhanced description of the transverse shear strain can be achieved by assuming an HSDT for the viscoelastic core layer [69–71]. Plagianakos and Savaranos [72] includes quadratic and cubic polynomial distributions of the in-plane displacements along with linear layerwise theories. In addition, interlaminar shear stress compatibility conditions are imposed to meet the C^1 requirement of transverse shear stresses at plies interfaces. Araujo *et al.* [69] proposed a mixed layerwise FEM-based model which considers both active and passive damping. Passive damping is entrusted with the strong shear deformation of the viscoelastic core layer, whilst active damping is introduced by piezoelectric patches. The displacement field in the viscoelastic core is modelled according to HSDT, whilst FSDT is used for the anisotropic face plies and the piezoelectric plies. The limitations of these models are mainly related to their *ad-hoc* assumptions of the field variables in the face sheets and core layers. Indeed, even though the FSDT is seen to be adequate to model the mechanical behaviour of the thin face sheets, the theory that must be used in the viscoelastic core layer for the prediction to be accurate is problem-dependent.

In particular, Douglas and Yang [73] provided a comprehensive investigation about the role of the *transverse compressional damping* in the vibratory response of three-layer elastic-viscoelastic-elastic (EVE) beams. The outcomes of the investigation suggest the use of full 3D constitutive law to account for the transverse normal strain which affects the dynamic response in a narrow frequency bandwidth centred at the compressional frequency value. In this context, Ren *et al.* [74] proposed a layerwise model in which the face sheets satisfy the CLT assumptions whilst the moderately thick viscoelastic core layer meets a general high-order deformation theory allowing for different polynomials expansion for the in-plane and transverse displacement. It has been proven that compressive and extensional deformations in the viscoelastic core have to be included if an accurate prediction of the energy dissipation of the structure due to the damping layer is sought. This need is even more stringent if structures with multiple cores are to be studied [49]. It thus becomes clear how axiomatic approaches allowing for the kinematics assumptions in the viscoelastic layer to be tuned according to the specific problem represent a turning point in sandwich structure modelling. Ferreira *et al.* [66] proposed a layerwise finite element models for viscoelastic sandwich plate based upon the CUF assuming a linear piecewise distribution of the displacement variables across each individual plies. A comprehensive model assessment is given by Filippi and Carrera in [75] where the modelling advantages offered by the unified formulation are emphasised in the scope of harmonic analysis of passively damped structures.

Buckling of sandwich structures. By virtue of their high bending rigidity, sandwich panels show an improved resistance to buckling as well [4, 10]. However, the thin skins supported by a lightweight core are prone local instabilities referred to as wrinkling, in which the face sheets buckle in a short-wavelength of the order of the core thickness [76]. An outstanding contribution to the understanding of the wrinkling phenomenon has been given by Fagerberg [77–80], ranging from the effects of anisotropy in the face sheets up to the transition from wrinkling to the pure compression failure. It is worth emphasising that this instability does not only arise in compressed struts, but it is likely to occur also in the skin under compression under a global bending deformation [81]. Since this failure mechanism is often catastrophic, it is important to accurately calculate the critical wrinkling loads for a reliable sizing of sandwich panels.

The short-wavelength of the wrinkling has called for a representation of this mechanism as a material failure: given the geometric and constitutive properties of skins and core, analytical formulas for the critical loads have been proposed irrespective of the actual loading and boundary conditions of the panel. This approach proves effec-

tive inasmuch as it can be employed within large scale models of built-up structures, such as the Global FE Model of an aircraft [82]. An extensive literature review over the analytical wrinkling formulae can be found in [83] and in the more recent critical assessment by Ginot *et al.* [84]. It turns out that the validity of such analytical expressions is confined to specific classes of problems and that they prove rather inaccurate when applied on configurations that do not meet the assumptions upon which they are based.

Solid FE models have been also developed for investigating the wrinkling failure [85–87], which are, however, too computationally intensive to be used in a preliminary design phase. So-called "unified" approaches based on high-order structural models have been also proposed that are capable of predicting both global buckling and local wrinkling [88, 89]. These approaches are attractive because they open the possibility of investigating the interaction between global and local instabilities [90, 91].

CUF models, accounting for geometrical nonlinearities, have been developed by Pagani and Carrera for buckling and post-buckling analyses of laminated composites beams and isotropic plates [92–94]. CUF and SGUF models have been also applied successfully to sandwich buckling and wrinkling problems by referring to Navier-type [95] and to Ritz solutions [46]. The Ritz method does in particular allow to broaden the studies towards anisotropic panels with arbitrary boundary conditions. Thanks to the adopted high-order in-plane functions, it has been proven that very refined SGUF models are capable of grasping the short wavelength response even in configurations involving anisotropic face sheets and multi-axial loads. These findings are the encouraging starting points for the finite element developments proposed in Chapter 5 of this dissertation.

Chapter 2

Sublaminate-GUF FEM

Contents

2.1 Geometry description

Let us consider a multilayered rectangular plate of total thickness h, composed of N_p orthotropic, elastic and perfectly bonded plies occupying the volume $V = \Omega \times \{-h/2 \leq x_3 \leq h/2\}$ in the Cartesian frame $(x_1, x_2, x_3 \equiv z)$, see Figure 2.1 (left). The reference surface Ω is thus chosen to lie in the plate midplane ($z = 0$). The boundary ∂V is split in the portion ∂V_u with an imposed displacement field $\bar{u}$ and ∂V_t with

imposed tractions $\bar{t}$ such that $\partial V_u \cup \partial V_t = \partial V$ and $\partial V_u \cap \partial V_t = \emptyset$. Unless differently stated, the Einstein summation convention is employed with Latin indices varying in $\{1,2,3\}$ and Greek indices in $\{1,2\}$. The laminate cross-section is shown in Figure 2.1 (right), where $p = 1,2 \dots N_p$ is the index for the physical plies and $k = 1,2 \dots N_l$ is the index for the numerical layers in which the laminate is subdivided into. The number of physical plies composing the k^{th} numerical layer is indicated as N_p^k. Non-dimensional coordinates $\zeta_k \in \{-1,1\}$ and $\zeta_p \in \{-1,1\}$ are introduced in order to define the interpolations across the thickness of the k^{th} layer and the p^{th} ply, respectively:

$$\zeta_\square = \frac{2}{h_\square} z - \frac{z_t^\square + z_b^\square}{z_t^\square - z_b^\square} \qquad \text{with} \quad \square = p, k \tag{2.1}$$

where $h_k = z_t^k - z_b^k$ and $h_p = z_t^p - z_b^p$ denotes the layer and ply thickness, respectively. The relation between the non-dimensional ply-specific and layer-specific coordinates is obtained as:

$$\zeta_p = \frac{h_k}{h_p}\zeta_k + \frac{2}{h_p}\left(z_{0_k} - z_{0_p}\right) = \frac{2}{\zeta_k^{p,t} - \zeta_k^{p,b}}\left(\zeta_k - \frac{\zeta_k^{p,t} + \zeta_k^{p,b}}{2}\right) \tag{2.2}$$

where $z_{0_\square} = (z_t^\square + z_b^\square)/2$ are the mid-plane coordinates of the k^{th} layer ($\square = k$) and the p^{th} ply ($\square = p$), respectively. Finally, $\zeta_k^{p,t}$ and $\zeta_k^{p,b}$ are the values of the non-dimensional coordinate ζ_k at the top and bottom interfaces, respectively, of the physical ply p inside the k^{th} sublaminate, i.e., $\zeta_p\left(\zeta_k = \zeta_k^{p,t}\right) = 1$ and $\zeta_p\left(\zeta_k = \zeta_k^{p,b}\right) = -1$.

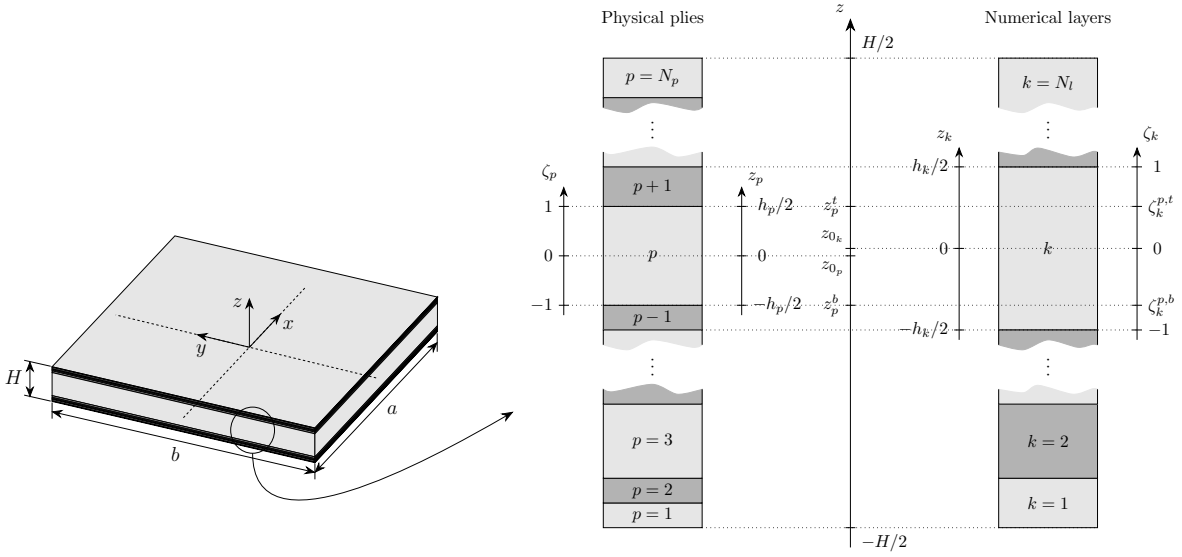

Figure 2.1: Multilayered plate as an assembly of N_p physical plies (left) and N_l numerical layers (right). Global z, layer-specific z_k and ply-specific z_p coordinates are used for the description of the model along with the non-dimensional layer- and ply-specific coordinates ζ_k and ζ_p[43].

2.2 Variational statements

Variational formulations are used to introduce the axiomatic modeling along the thickness coordinate. The conventional displacement-based approach (PVD) as well as the mixed approach by Reissner (RMVT) will be employed for deriving the governing equations of the composite plate. In either case, the governing equations are expressed by equating the internal virtual work with the virtual work done by the external tractions $\bar{t}$:

$$\delta W_i = \delta W_e \qquad \text{with} \quad \delta W_e = \int_{\partial V_t} \delta u \, \bar{t} \, \mathrm{d}\Gamma \tag{2.3}$$

where δ is the usual variational operator and u the displacement vector field. Invoking the assumption of small perturbations, the setting is provided by the classical linear elasticity with small displacements and strains:

$$\epsilon_{ij} = \frac{1}{2}\left(u_{i,j} + u_{j,i}\right) \tag{2.4}$$

2.2.1 Principle of Virtual Displacements

The Principle of Virtual Displacements (PVD) yields the weak form of the equilibrium equations under the assumption of a compatible kinematic field and the verification of the constitutive law. The strain and stress fields are split into their in-plane (subscript b), transverse normal (subscript n) and transverse shear (subscript s) components as

$$\begin{aligned} \boldsymbol{\epsilon}_b &= \begin{bmatrix} \epsilon_{11} & \epsilon_{22} & 2\epsilon_{12} \end{bmatrix}^T; \quad \epsilon_n = \epsilon_{33}; \quad \boldsymbol{\epsilon}_s = \begin{bmatrix} 2\epsilon_{23} & 2\epsilon_{13} \end{bmatrix}^T \\ \boldsymbol{\sigma}_b &= \begin{bmatrix} \sigma_{11} & \sigma_{22} & \sigma_{12} \end{bmatrix}^T; \quad \sigma_n = \sigma_{33}; \quad \boldsymbol{\sigma}_s = \begin{bmatrix} \sigma_{13} & \sigma_{23} \end{bmatrix}^T \end{aligned} \tag{2.5}$$

where T is the transposition operator. Referring to the contracted (Voigt) notation, the constitutive link for each physical ply p is expressed in matrix form in the Cartesian frame (x, y, z) of the plate as

$$\begin{bmatrix} \boldsymbol{\sigma}_b \\ \sigma_n \\ \boldsymbol{\sigma}_s \end{bmatrix}^{(p)} = \begin{bmatrix} \tilde{\mathbf{C}}_{bb} & \tilde{\mathbf{C}}_{bn} & 0 \\ \tilde{\mathbf{C}}_{bn}^T & \tilde{C}_{nn} & 0 \\ 0 & 0 & \tilde{\mathbf{C}}_{ss} \end{bmatrix}^{(p)} \begin{bmatrix} \boldsymbol{\epsilon}_b \\ \epsilon_n \\ \boldsymbol{\epsilon}_s \end{bmatrix}^{(p)} \tag{2.6}$$

in which the stiffness coefficients $\tilde{\mathbf{C}}$ of the orthotropic ply are expressed in the plate's Cartesian frame through a rotation angle θ_p about the $z-$axis [96] (more details are given in Appendix A). The virtual internal work for the PVD is thus expressed by the

following integral equation

$$\begin{aligned}\delta W_{int} &= \int_V \delta\boldsymbol{\epsilon}_b^T\boldsymbol{\sigma}_b + \delta\boldsymbol{\epsilon}_n^T\boldsymbol{\sigma}_n + \delta\boldsymbol{\epsilon}_s^T\boldsymbol{\sigma}_s \,\mathrm{d}V = \\ &= \int_\Omega \sum_{p=1}^{N_p} \int_{h_p} \Big\{\delta\boldsymbol{\epsilon}_b^{(p)T}\tilde{\mathbf{C}}_{bb}^{(p)}\boldsymbol{\epsilon}_b^{(p)} + \delta\boldsymbol{\epsilon}_b^{(p)T}\tilde{\mathbf{C}}_{bn}^{(p)}\epsilon_n^{(p)} + \delta\epsilon_n^{(p)T}\tilde{\mathbf{C}}_{bn}^{(p)T}\boldsymbol{\epsilon}_b^{(p)} + \delta\epsilon_n^{(p)T}\tilde{C}_{nn}^{(p)}\epsilon_n^{(p)} \\ &\qquad + \delta\boldsymbol{\epsilon}_s^{(p)T}\tilde{\mathbf{C}}_{ss}^{(p)}\boldsymbol{\epsilon}_s^{(p)} \,\mathrm{d}z\Big\} \,\mathrm{d}x\,\mathrm{d}y\end{aligned} \tag{2.7}$$

2.2.2 Reissner's Mixed Variational Theorem

The RMVT allows to introduce independent approximations for the transverse stress field in view of an *a priori* fulfilment of the interlaminar equilibrium [6, 7]. The virtual internal work for the RMVT can be written as

$$\begin{aligned}\delta W_{int} &= \int_V \delta\boldsymbol{\epsilon}_b^T\boldsymbol{\sigma}_b + \delta\epsilon_n\sigma_n + \delta\boldsymbol{\epsilon}_s^T\boldsymbol{\sigma}_s + \delta\sigma_n^T(\epsilon_n - e_n) + \delta\boldsymbol{\sigma}_s^T(\boldsymbol{\epsilon}_s - \boldsymbol{e}_s) \,\mathrm{d}V \\ &= \int_\Omega \sum_{p=1}^{N_p} \int_{h_p} \Big\{\delta\boldsymbol{\epsilon}_b^{(p)T}\mathbf{C}_{bb}^{(p)}\boldsymbol{\epsilon}_b^{(p)} + \delta\boldsymbol{\epsilon}_b^{(p)T}\mathbf{C}_{bn}^{(p)}\sigma_n^{(p)} + \delta\epsilon_n^{(p)T}\sigma_n^{(p)} + \delta\boldsymbol{\epsilon}_s^{(p)T}\boldsymbol{\sigma}_s^{(p)} + \delta\sigma_n^{(p)T}\epsilon_n^{(p)} \\ &\qquad + \delta\sigma_n^{(p)T}\mathbf{C}_{bn}^{(p)T}\boldsymbol{\epsilon}_b^{(p)} - \delta\sigma_n^{(p)T}C_{nn}\sigma_n^{(p)} + \delta\boldsymbol{\sigma}_s^{(p)T}\boldsymbol{\epsilon}_s^{(p)} - \delta\boldsymbol{\sigma}_s^{(p)T}\mathbf{C}_{ss}^{(p)}\boldsymbol{\sigma}_s^{(p)} \,\mathrm{d}z\Big\} \\ &\qquad \mathrm{d}x\,\mathrm{d}y\end{aligned} \tag{2.8}$$

in which the following definitions have been used for the in-plane stresses $\boldsymbol{\sigma}_b$ and the transverse strains $\boldsymbol{e} = [e_n\, \boldsymbol{e}_s]^T$ in each ply p:

$$\begin{bmatrix}\boldsymbol{\sigma}_b \\ e_n \\ \boldsymbol{e}_s\end{bmatrix} = \begin{bmatrix}\mathbf{C}_{bb} & \mathbf{C}_{bn} & 0 \\ -\mathbf{C}_{bn}^T & C_{nn} & 0 \\ 0 & 0 & \mathbf{C}_{ss}\end{bmatrix}\begin{bmatrix}\boldsymbol{\epsilon}_b \\ \sigma_n \\ \boldsymbol{\sigma}_s\end{bmatrix} \tag{2.9}$$

where the coefficients of this *mixed form* of Hooke's law are related to those of Eq. (A.9) by

$$\mathbf{C}_{bb} = \tilde{\mathbf{C}}_{bb} + \tilde{\mathbf{C}}_{bn}\tilde{C}_{nn}^{-1}\tilde{\mathbf{C}}_{bn}^T; \quad \mathbf{C}_{bn} = \tilde{\mathbf{C}}_{bn}\tilde{C}_{nn}^{-1}; \quad C_{nn} = \tilde{C}_{nn}^{-1}; \quad \mathbf{C}_{ss} = \tilde{\mathbf{C}}_{ss}^{-1} \tag{2.10}$$

2.2.3 Variable-kinematics plate model in SGUF

The plate model is defined upon introducing *ad hoc* assumptions for the distribution across the thickness of the generic dependent variable $\mathcal{U}$ of the variational framework to be used, i.e., $\mathcal{U} \in \{u_i\}$ for a PVD model and $\mathcal{U} \in \{u_i, \sigma_{i3}\}$ for an RMVT model. The assumptions are expressed in each sublaminate k and *independently for each variable*

$\mathcal{U}^k$ according to the GUF notation [43] as follows

$$\mathcal{U}^k\left(x,y,z_k\right)=\sum_{\mu_\mathcal{U}=0}^{N_\mathcal{U}^k}F_{\mu_\mathcal{U}}\left(\zeta\right)\hat{\mathcal{U}}_{\mu_\mathcal{U}}^k\left(x,y\right) \tag{2.11}$$

In each sublaminate, the generic variable $\mathcal{U}^k$ can be described either in an ESL sense by setting $\zeta=\zeta_k$, or in a LW sense by setting $\zeta=\zeta_p$. In this latter case, the approximation is defined as the assembly all N_p^k ply-specific contributions:

$$\mathcal{U}^k\left(x,y,z_k\right)=\sum_{p=1}^{N_p^k}\mathcal{U}^{(p)}\left(x,y,z_p\right)=\sum_{p=1}^{N_p^k}\sum_{\mu_\mathcal{U}=0}^{N_\mathcal{U}^k}F_{\mu_\mathcal{U}}\left(\zeta_p\right)\hat{\mathcal{U}}_{\mu_\mathcal{U}}^{(p)}\left(x,y\right) \tag{2.12}$$

where the symbol "$\sum$" is employed with abuse of notation to express the assembly of plies' contributions. Note that Eq. (2.12) implies that the expansion order $N_\mathcal{U}^k$ is the same for all the N_p^k plies within the sublaminate. The model for the whole multilayer is eventually constructed upon assembling in a LW sense all sublaminate-specific contributions. The adopted thickness functions are defined in terms of the orthogonal Legendre polynomials $P_n(\zeta)$:

$$P_0=1;\quad P_1=\zeta;\quad P_{n+1}=\frac{(2n+1)\zeta\,P_n\,-\,nP_{n-1}}{n+1} \tag{2.13}$$

The thickness functions are defined as:

$$\begin{gathered}N_\mathcal{U}^k=0:F_0=1;\quad N_\mathcal{U}^k\geq 1:F_0(\zeta)=\frac{P_0(\zeta)-P_1(\zeta)}{2};\ F_1(\zeta)=\frac{P_0(\zeta)+P_1(\zeta)}{2};\\ F_r(\zeta)=P_r(\zeta)-P_{r-2}(\zeta)\text{ for }r\geq 2\end{gathered} \tag{2.14}$$

It is noted that this approximation is used for both ESL and LW descriptions. A slope discontinuity at plies' interfaces can be introduced within an ESL description by referring to Murakami's zig-zag function (MZZF). The MZZF allows the displacement field to emulate the zig-zag effect when superposed to Eq. (2.11). According to [97], the Murakami's zig-zag function $M\left(z\right)$ is defined as

$$M\left(z\right)=\left(-1\right)^p\zeta_p \tag{2.15}$$

A detailed review about the use of MZZF in modelling multilayered structures is given in [98]. The assembly procedures of LW contributions is carried out by imposing the continuity of the variable $\mathcal{U}$, i.e., by stating the perfect bond condition of adjacent plies and sublaminates. By virtue of the property $F_0(-1)=F_1(1)=1, F_r(\pm 1)=0$, it is straight-forward to enforce the continuity within a classical assembly procedure, see [43] for more details.

2.2.4 The semi-discrete governing equations of the plate

The approximations across the thickness coordinate that define the plate model are introduced following the compact notation Eq. (2.12) into the virtual work expressions Eq. (2.7) (PVD) or Eq. (2.8) (RMVT). As a result, the virtual internal work defined by the generic unknown variable $\mathcal{U}_s$ and the virtual variation $\delta\mathcal{U}_q$ can be expressed as

$$\delta W_{int}\left(\delta\hat{\mathcal{U}}_q(x,y),\hat{\mathcal{U}}_s(x,y)\right)=\sum_{k=1}^{N_l}\sum_{p=1}^{N_p^k}\delta W_{int}^{(p)}\left(\delta\hat{\mathcal{U}}_q^{(p)}(x,y),\hat{\mathcal{U}}_s^{(p)}(x,y)\right) \tag{2.16}$$

where the contribution of the p^{th} ply of the k^{th} sublaminate can be written as follows:

$$\delta W_{int}^{(p)}\left(\delta\hat{\mathcal{U}}_q^{(p)},\hat{\mathcal{U}}_s^{(p)}\right)=\int_\Omega\left(\partial_\mu^q\left[\delta\hat{\mathcal{U}}_{q_{\mu_q}}^{(p)}(x,y)\right]\right)\,Z^{p\,\mu_{\mathcal{U}_q}\,\tau_{\mathcal{U}_s}}_{\partial_z^q\mathcal{U}_q\,\partial_z^s\mathcal{U}_s\,QS}\left(\partial_\tau^s\left[\hat{\mathcal{U}}_{s_{\tau_s}}^{(p)}(x,y)\right]\right)\,\mathrm{d}x\,\mathrm{d}y \tag{2.17}$$

The operator $\partial_\mu^q[\cdot]$ (resp. $\partial_\tau^s[\cdot]$) indicates that the variable $\hat{\mathcal{U}}_s$ $\left(\text{resp. }\delta\hat{\mathcal{U}}_q\right)$ may be partially derived with respect to the in-plane coordinates, depending on the strain component involved in the specific virtual work contribution being considered. Furthermore, the thickness integral Z has been introduced as

$$Z^{p\,\mu_{\mathcal{U}_q}\,\tau_{\mathcal{U}_s}}_{\partial_z^q\mathcal{U}_q\,\partial_z^s\mathcal{U}_s\,QS}=\int_{h_p}\left(\partial_z^q\left[F_{\mu_{\mathcal{U}_q}}(\zeta_p)\right]\right)\,c^p_{QS}\,\left(\partial_z^s\left[F_{\tau_{\mathcal{U}_s}}(\zeta_p)\right]\right)\,\mathrm{d}z \tag{2.18}$$

where the notation $\partial_z[\cdot]$ indicates that a derivation with respect to the thickness coordinate z may be required for defining the strain component pertaining to the specific contribution to the virtual work. The coefficient c^p_{QS} can represent a material parameter (with $Q,S\in\{1,6\}$), or a unitary coefficient, because in RMVT the compatible transverse strains are directly work-conjugated to the transverse stress variables. Note also that transverse stress variables are never derived with respect to any coordinate when the RMVT in Eq. (2.17) is used.

Eq. (2.17) is the generic expression of the model-invariant *kernel* of the semi-discrete stiffness matrix, which is computed upon cycling over all indices q,μ_q,s,τ_s and subsequently assembled over all plies p and sublaminates k. Specific instances of the *kernels* are formed by expressing all individual virtual work contributions pertaining to the model. PVD-based models rely on 6 *kernels*, whereas RMVT-based models require 17 *kernels* (if the locking-free interpolation scheme is addressed, see Section 2.3.2).

The thickness integrals are explicitly carried out and assembled across the whole multilayer section, which yields the dimensionally reduced 2D model. The strong form of the 2D governing equations, obtained upon integration by parts of those terms subjected to the derivative ∂_μ^q, have been given in [43] and solved the framework of the Navier solution. Weak-form solutions have been addressed in [45] by referring to the

Ritz method. In this thesis, reference is made to the weak-form solution defined within FEM, as discussed in the following.

2.2.5 Employed models and acronyms

Unless stated otherwise, SGUF models for the sandwich plates are specified by the GUF-type model employed for the facesheets and the core separated by a slash, see also [43]. The meaning of the models' acronyms is recalled in Figure 2.2. The plane stress assumption $\sigma_{33} = 0$ is represented in RMVT-models by dropping off the σ_{33} variable, which is indicated in the acronym by replacing the expansion order N_{s_3} by a dot $(\cdot)$. Simplified CUF-type acronyms are used if the same description (ESL or LW) and expansion order N is used for *all* variables, e.g., $\mathrm{D}_{\mathrm{Z2\,Z2}} = \mathrm{EDZ2}$, $\mathrm{M}^{\mathrm{L7\,L7}}_{\mathrm{L7\,L7}} = \mathrm{LM7}$, $\mathrm{M}^{\mathrm{E4\,E4}}_{\mathrm{Z4\,Z4}} = \mathrm{EMZ4}$ etc. FSDT is obtained as ED_{10}, CLT is obtained from FSDT upon penalyzing the transverse shear stiffness.

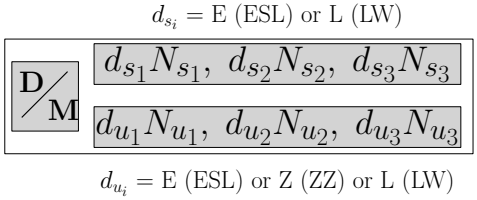

Figure 2.2: Model acronym in the framework of GUF.

2.2.6 Transverse stress boundary conditions

It is worthwhile noticing that some additional features are here introduced for the first time concerning the approximations of the transverse stresses in mixed RMVT-based models. In particular, prescribed zero values can be enforced as homogeneous boundary conditions for the transverse shear stresses, across the thickness at the top and/or bottom surfaces $z = \pm\frac{H}{2}$ and for the nodal DOF of the FE in the $(x, y)-$plane. In order to indicate the exact satisfaction of the homogeneous boundary conditions for the transverse shear stress at the plates' top and bottom surfaces, the symbol ⁝ is appended after the expansion order, e.g., $\mathrm{EM}^{2\vdots\cdot}_{10}$ is a refined FSDT that retains a quadratic transverse shear stress satisfying the homogeneous conditions $\sigma_{\alpha 3}(x, y, \pm\frac{H}{2}) = 0$. Due to symmetry considerations, sometimes only the upper half of the laminate is to be considered (e.g. symmetric lamination schemes), in this situation the homogenous condition on transverse stress field must be enforced only at top surface and it will be referred to as ⁞.

2.3 FE Approximations for SGUF plate models

Four-node from the Lagrangian family and eight-node serendipity quadrilateral elements are used to discretize the laminate in-plane behaviour (see Figure 2.3 and Figure 2.4).

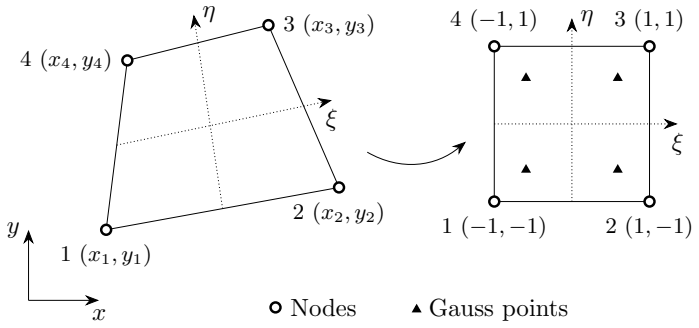

Figure 2.3: Four-node Lagrangian quadrangular element in the physical Cartesian frame (x, y) and in the natural frame (ξ, η).

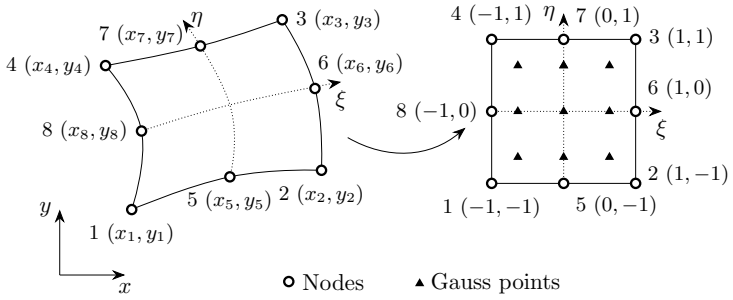

Figure 2.4: Eight-node serendipity quadrangular element in the physical Cartesian frame (x, y) and in the natural frame (ξ, η).

The isoparametric interpolation is employed for the displacement variables as well as the stress variables for the RMVT-based formulation except for the z-constant term of the transverse shear strains $\gamma_{\mu 3}$. Knowing this term to be responsible of the so-called shear locking pathology for thin plates, the field-compatible approximations QC4 (4-node) and CL8 (8-node) have been used to interpolate it over the element [99, 100]. The QC4 and CL8 interpolations were first proposed by Polit [101] for FSDT and were recently extended to variable-kinematics CUF-type models by Le [99, 100]. It is worthwhile noticing that QC4 interpolation is equivalent to MITC4 proposed by Dvorkin and Bathe in [102] and applied to CUF-based FEs by Cinefra *et al.* [103].

2.3.1 Strain-displacement relations

The development of FEs for the QC4/CL8 interpolations requires a new definition of the strain field. As already discussed, this interpolation has been introduced as a countermeasure to the shear locking pathology that affects thin structures and that results in a spuriously stiff bending response. In particular, only the $z-$constant part of the transverse shear strain field is responsible of this pathology, hence this will be the term the new field-compatible interpolation is addressed to. By introducing the compact matrix notation, the geometrical relation between the strain field and the assumed displacement field reads:

$$\begin{aligned}
\boldsymbol{\epsilon}_b^{(p)}(x,y,z_p) &= \mathbf{F}_{b\mu_\mathcal{U}}(z_p)\,\mathbf{B}_{bi}(x,y)\,\mathbf{U}_{\mu_\mathcal{U}i}^{(p)} \\
\epsilon_n^{(p)}(x,y,z_p) &= \mathbf{F}_{n\mu_\mathcal{U}}(z_p)\,\mathbf{B}_{ni}(x,y)\,\mathbf{U}_{\mu_\mathcal{U}i}^{(p)} \\
\boldsymbol{\epsilon}_s^{(p)}(x,y,z_p) &= \boldsymbol{\gamma}^0(x,y) + \boldsymbol{\gamma}^h(x,y,z_p) = \\
&= \mathbf{J}^{-1}\mathbf{F}^0_{s\mu_\mathcal{U}}\bar{\mathbf{B}}_{si}(x,y)\,\mathbf{U}_{\mu_\mathcal{U}i}^{(p)} + \mathbf{F}^h_{s\mu_\mathcal{U}}(z_p)\,\mathbf{B}_{si}(x,y)\,\mathbf{U}_{\mu_\mathcal{U}i}^{(p)}
\end{aligned} \tag{2.19}$$

with $\boldsymbol{U}_{\mu_\mathcal{U}i}^{(p)}$ the displacement DOF vector of the i-th node related to the ply p and the expansion order index $\mu_\mathcal{U}$:

$$\mathbf{U}_{\mu_\mathcal{U}i}^{(p)} = \left[U_{x_{\mu_{u_x}}}\; U_{y_{\mu_{u_y}}}\; U_{z_{\mu_{u_z}}}\right]_i^{(p)\,T} \tag{2.20}$$

The index i goes to 1 up to the number of nodes in the element. The explicit expressions for the matrices containing the through-thickness functions ($\mathbf{F}_{b\mu_\mathcal{U}}$, $\mathbf{F}_{n\mu_\mathcal{U}}$, $\mathbf{F}^0_{s\mu_\mathcal{U}}$ and $\mathbf{F}^h_{s\mu_\mathcal{U}}$) as well as the ones containing the in-plane derivatives of the shape functions ($\mathbf{B}_{bi}$, $\mathbf{B}_{ni}$, $\bar{\mathbf{B}}_{si}$ and $\mathbf{B}_{si}$) are given in Appendix B.2. It should be noticed that the matrix $\mathbf{F}_{s\mu_\mathcal{U}}$ has been split in the $z-$constant part $\mathbf{F}^0_{s\mu_\mathcal{U}}$ and the higher-order, $z-$dependent part $\mathbf{F}^h_{s\mu_\mathcal{U}}$ in order to introduce the correction in $\bar{\mathbf{B}}_{si}$ for the shear locking pathology. Furthermore, the $z-$ constant part of the transverse shear field is defined in the natural coordinates (ξ,η) in order to enhance the plate response to distorted element geometries, through the introduction of the Jacobian matrix $\mathbf{J}$ evaluated at Gauss points in the definition of $\boldsymbol{\gamma}^0$. The $z-$dependent part of transverse shear strains are interpolated as usual by means of isoparametric shape functions. The 4- and 8-node isoparametric interpolation has been widely used and argued in literature and for this reason is here omitted for brevity. The interpolation scheme involved in the definition of the $z-$constant component $\boldsymbol{\gamma}^0$ of the transverse shear strain field is detailed in Appendix B.1.

2.3.2 FE matrices

The governing equations for both PVD-based and RMVT-based formulations are finally derived by substituting the strain-displacement relations (Eq. (2.19)) in the weak form of the equilibrium equations (Eq. (2.7), Eq. (2.8)) along with the constitutive law (Eq. (A.9), Eq. (2.9)). They lead to the following algebraic systems in which the unknowns are the through-thickness parameters defining the displacement field and, for the RMVT approach, the transverse stress field:

$$\text{PVD:} \quad \begin{bmatrix} \mathbf{K}_{u_x u_x} & \mathbf{K}_{u_x u_y} & \mathbf{K}_{u_x u_z} \\ & \mathbf{K}_{u_y u_y} & \mathbf{K}_{u_y u_z} \\ \text{sym} & & \mathbf{K}_{u_z u_z} \end{bmatrix} \begin{bmatrix} \mathbf{U}_x \\ \mathbf{U}_y \\ \mathbf{U}_z \end{bmatrix} = \begin{bmatrix} \mathbf{R}_x \\ \mathbf{R}_y \\ \mathbf{R}_z \end{bmatrix} \tag{2.21}$$

$$\text{RMVT:} \quad \begin{bmatrix} \mathbf{K}_{u_x u_x} & \mathbf{K}_{u_x u_y} & \mathbf{0}_{u_x u_z} & \mathbf{K}_{u_x s_x} & \mathbf{K}_{u_x s_y} & \mathbf{K}_{u_x s_z} \\ & \mathbf{K}_{u_y u_y} & \mathbf{0}_{u_y u_z} & \mathbf{K}_{u_y s_x} & \mathbf{K}_{u_y s_y} & \mathbf{K}_{u_y s_z} \\ & & \mathbf{0}_{u_z u_z} & \mathbf{K}_{u_z s_x} & \mathbf{K}_{u_z s_y} & \mathbf{K}_{u_z s_z} \\ & & & \mathbf{K}_{s_x s_x} & \mathbf{K}_{s_x s_y} & \mathbf{0}_{s_x s_z} \\ & \text{sym} & & & \mathbf{K}_{s_y s_y} & \mathbf{0}_{s_y s_z} \\ & & & & & \mathbf{K}_{s_z s_z} \end{bmatrix} \begin{bmatrix} \mathbf{U}_x \\ \mathbf{U}_y \\ \mathbf{U}_z \\ \mathbf{S}_x \\ \mathbf{S}_y \\ \mathbf{S}_z \end{bmatrix} = \begin{bmatrix} \mathbf{R}_x \\ \mathbf{R}_y \\ \mathbf{R}_z \\ \mathbf{0} \\ \mathbf{0} \\ \mathbf{0} \end{bmatrix} \tag{2.22}$$

It is worth emphasising that, in contrast to the algebraic systems of the RMVT formulation obtained in the framework of Navier's strong form solution or Ritz' weak form solutions, the coupling terms $\mathbf{K}_{u_x s_y}$ and $\mathbf{K}_{u_y s_x}$ are non-zero due to the QC4 interpolation scheme. All kernels from which the contributions of the stiffness matrices are obtained through opportune cycling over the various indices are explicitly expressed in Appendix C.

2.4 Numerical transverse shear locking test

In this section, the robustness of the present finite plate element with respect to transverse shear locking pathology is demonstrated considering the example illustrated in Figure 2.5. The exact 3D elasticity solution proposed by Pagano in [104] has been extended by Kardomateas towards more realistic core materials, in particular transversely isotropic cores that are stiffer in the transverse direction than in the in-plane directions, e.g., honeycomb cores [105].

This exact solution is here used to evaluate the convergence properties of the developed FEs. The Kardomateas-TestCase (K-TC) considers a simply-supported square

three-layered sandwich panel subjected to a bi-sinusoidal pressure load, see Figure 2.5, with Graphite/Epoxy unidirectional faces and a glass-phenolic honeycomb core. The geometry and material data are listed in Table 2.1.

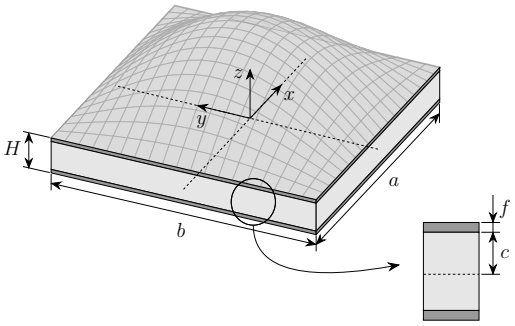

Figure 2.5: K-TC: Three-layered, simply supported square plate under a bi-sinusoidal pressure load.

Table 2.1: K-TC: Sandwich plate geometry and material data.

$a = b = \{10, 10^2, 10^3\}\, H$; $f = \{2, 0.2, 0.02\}$ mm; $2c = \{16, 1.6, 0.16\}$ mm		
	T300/5208 Graphite/Epoxy	Glass-phenolic honeycomb
E_{11} [GPa]	181	0.032
E_{22} [GPa]	10.3	0.032
E_{33} [GPa]	10.3	0.3
ν_{12}	0.277	0.25
ν_{13}	0.277	0.027
ν_{23}	0.4	0.027
G_{12} [GPa]	7.17	13
G_{13} [GPa]	7.17	48
G_{23} [GPa]	5.96	48

The results are evaluated in terms of the following non-dimensional local response parameters:

$$\begin{aligned}
&\bar{U}(z) = u_x(-a/2, 0, z)\,\frac{E_{11}^f}{q_0 H S^3}; && \bar{V}(z) = u_y(0, -b/2, z)\,\frac{E_{11}^f}{q_0 H S^3};\\
&\bar{W}(z) = u_z(0, 0, z)\,\frac{E_{11}^f}{100 q_0 H}; && \bar{S}_{\alpha\alpha}(z) = \sigma_{\alpha\alpha}(0, 0, z)\,\frac{1}{q_0 S^2};\\
&\bar{S}_{xy}(z) = \sigma_{xy}(-a/2, -b/2, z)\,\frac{1}{q_0 S^2}; && \bar{S}_{xz}(z) = \sigma_{xz}(-a/2, 0, z)\,\frac{1}{q_0 S};\\
&\bar{S}_{yz}(z) = \sigma_{yz}(0, -b/2, z)\,\frac{1}{q_0 S}; && \bar{S}_{zz}(z) = \sigma_{zz}(0, 0, z)\,\frac{1}{q_0}
\end{aligned} \tag{2.23}$$

where $S = a/H$ is the plate's length-to-thickness ratio, E_{11}^f is the Young's modulus of the face material and q_0 the amplitude of the pressure load. A regular mesh is considered with $N = 1, 2, 4, 8, 16, 32$ elements along the edges of the quarter plate (see Figure 2.6), whose length-to-thickness ratio ranges from thick $S = 10$ up to thin $S = 10^3$ plate. The convergence analysis is carried out for two representative models, namely the displacement-based FSDT/FSDT and the RMVT-based $\mathrm{EM}_{10}^{2\vdots\cdot}/\mathrm{EM}_{32}^{21}$. FE results are reported in terms of relative error with respect to the Navier-type closed-form solution for the corresponding model. These analytical solutions are given in Table 2.2, whose values are labelled by the superscript ^{a}. The non-dimensional in-plane

displacement $\bar{U}$ is evaluated at the bottom of the plate, the transverse displacement $\bar{W}$ and bending stress $\bar{S}_{xx}$ at the top surface and the transverse stress $\bar{S}_{xz}$ at facesheet-core interface. Note that throughout the thesis, transverse stresses for PVD-based models are evaluated through the constitutive law.

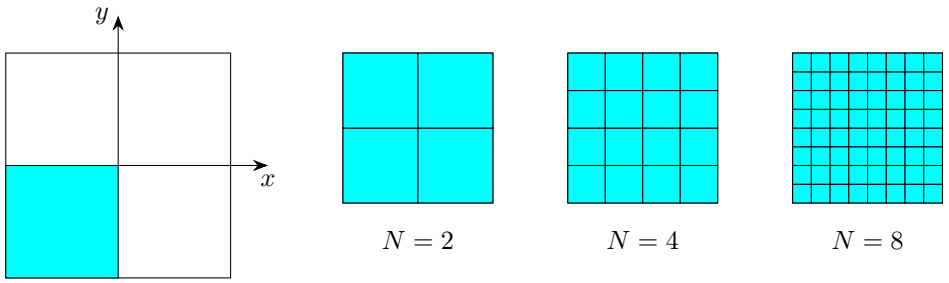

Figure 2.6: Regular meshes for the quarter plate.

Table 2.2: K-TC: Reference values obtained by the Navier-type closed-form solution.

Model	$S = a/H$	$\bar{U}^a\,(-H/2)$	$\bar{W}^a\,(H/2)$	$\bar{S}^a_{xx}\,(H/2)$	$\bar{S}^a_{xz}\,(0.4H^-)$
FSDT/FSDT	10	0.4918643294	230.2174542	1.6339367620	0.2068595369
	10^2	0.3162183647	230729.4323	1.01546741	0.3061014777
	10^3	0.3166019035	2018522809	1.014763335	0.3092905016
$\mathrm{EM}^{2\vdots\cdot}_{10}/\mathrm{EM}^{21}_{32}$	10	0.4903456822	231.7002615	1.640280194	0.2065009079
	10^2	0.3162178627	230733.5721	1.0154599550	0.3059699424
	10^3	0.3166018998	2018523087	1.0147632530	0.3091640006

Figure 2.7 and Figure 2.8 report, in log-log scale, the relative error of non-dimensional local response parameters for the four-node element (left) and eight-node element (right) with respect to the number of nodes, for three different length-to-thickness ratios ($S = 10,\ 10^2\ 10^3$). Both displacement-based and mixed model are investigated.

For the displacement-based model, the strong locking pathology affecting the fully-integrated isoparametric (ISO4) element when the plate becomes thin ($S \geq 10^2$) is eliminated by resorting to the QC4 interpolation, which thus recovers the asymptotic linear convergence rate. The quadratic eight-node element is less sensitive to shear locking phenomenon with respect to the linear four-node element. Nevertheless, for the very thin plate $S = 10^3$, the element locks when the isoparametric interpolation scheme is employed. Furthermore, as the plate becomes thinner, the eight-node isoparametric element loses the monotone convergence rate as can be inferred from Figure 2.7 and Figure 2.8 (right). On the other hand the asymptotic quadratic convergence rate of the displacement field is perfectly recovered by the CL8 interpolation.

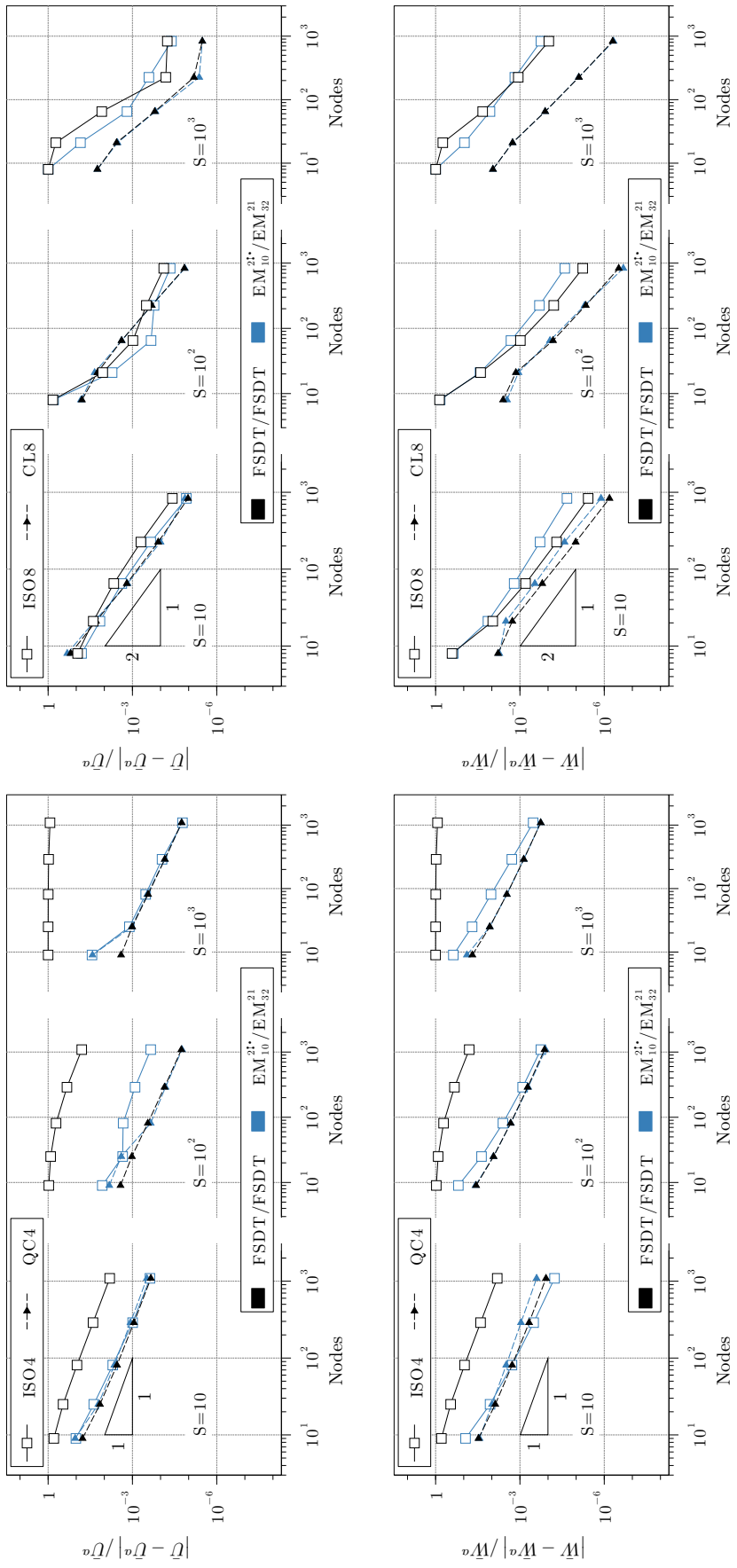

Figure 2.7: K-TC. Convergence to the Navier-type solution of displacements for different length-to-thickness ratios of a simply-supported sandwich plate under bi-sinusoidal pressure load.

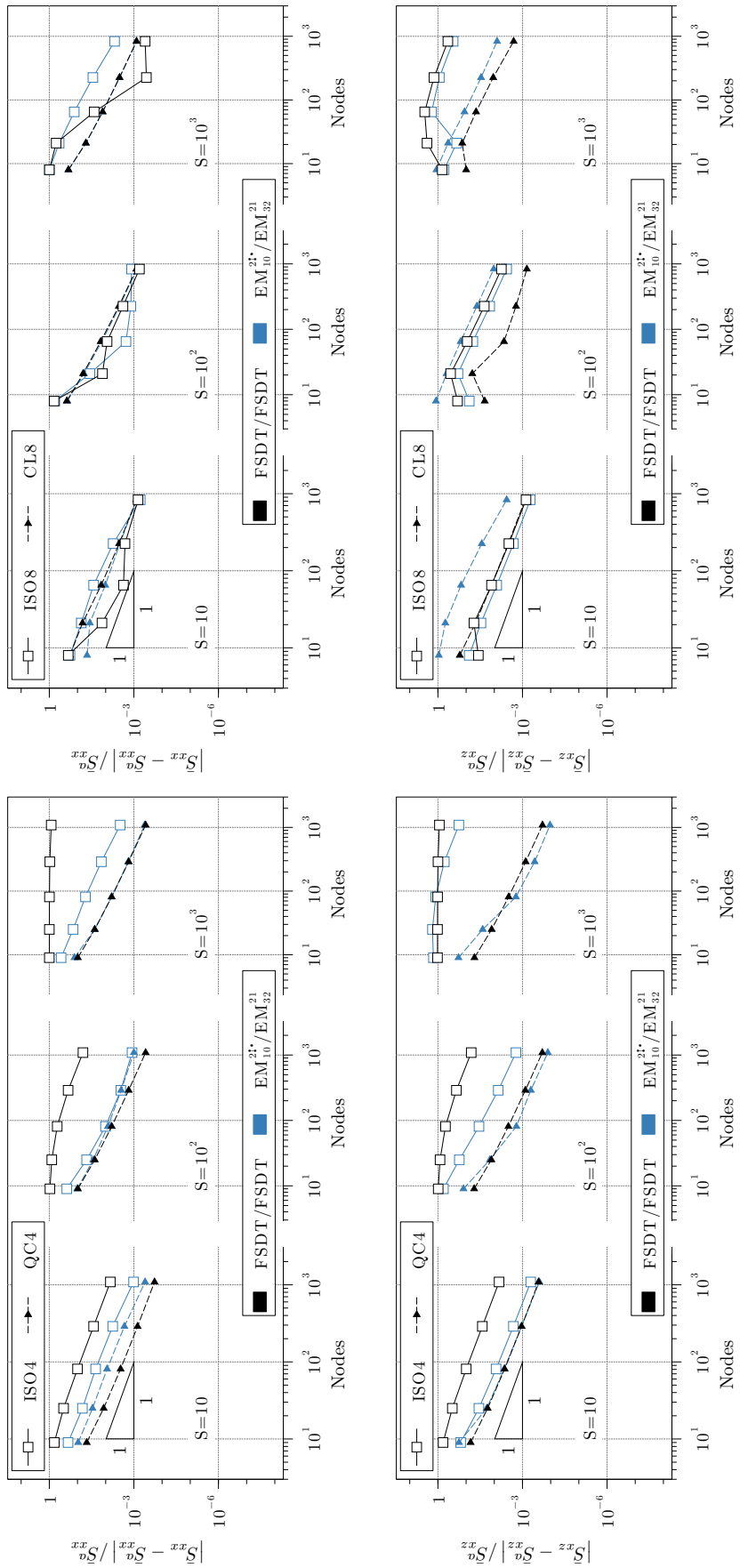

Figure 2.8: K-TC. Convergence to the Navier-type solution of stresses for different length-to-thickness ratios of a simply-supported sandwich plate under bi-sinusoidal pressure load.

As far as the mixed RMVT based model is concerned, the isoparametric four-node mixed element is much less sensitive to shear locking [106], which thus yields very similar results compared to the mixed element whose transverse shear strain is interpolated following the QC4 scheme. Indeed, several plate FE have been developed based on mixed formulations for alleviating the locking issues [107–110]. Nevertheless, the locking-free QC4/CL8 interpolation schemes provides more accurate results as well as a better convergence rate (especially for thin plates) than the corresponding isoparametric element also in the case of full-mixed model.

Transverse stress symmetry conditions. Figure 2.9 compares the convergence of the RMVT-model for the whole plate to that obtained for the quarter plate for a fixed value of length-to-thickness ratio ($S = 10$), in which the symmetry conditions are imposed on both displacement *and transverse stresses*. A perfect match can be appreciated which proves that it is possible to enforce boundary conditions on transverse stress variables on the FE nodes. Whenever symmetry considerations can be exploited in the 2D domain to reduce the size of the FE mesh, results obtained by RMVT models will henceforth verify *a priori* the homogeneity of the transverse shear stresses at the symmetry edges.

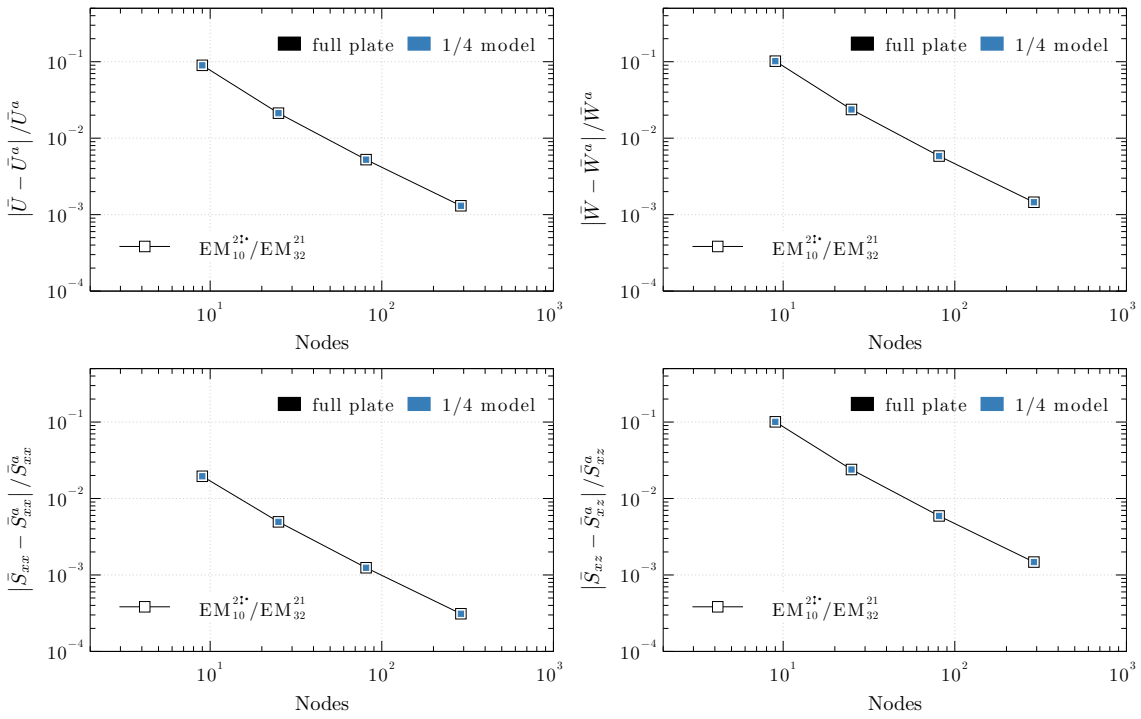

Figure 2.9: K-TC. Comparison between the convergence for the whole plate case and the quarter plate with displacement and stress symmetry boundary conditions.

2.5 Mesh distortion test

The same test-case investigated in Section 2.4 is addressed to asses the performance of the present finite plate element with respect to distorted meshes. A length-to-thickness ratio of 10 is considered along with a total thickness $H = 20$ mm, resulting in a plate dimension $a = 200$ mm. A 2×2 mesh is considered for the quarter plate. The degree of mesh distortion is represented by the dimension s, defining the coordinates of the mid-node, ranging from the undistorted case ($s = 0$) up to the most distorted mesh with $s = \pm 24$ (see Figure 2.10). Considering the dimensions of the plate, the mid-node is hence located at $(-a/4 + s, -a/4 + s)$. The results are given in terms of normalized

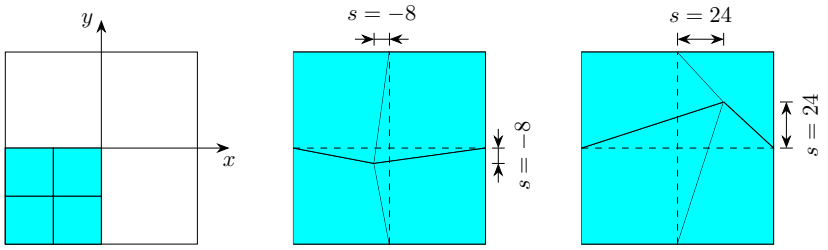

Figure 2.10: Mesh distorsion defined by the parameter s for the quarter plate.

non-dimensional local parameter $\bar{W}$ in Eq. (2.23) with respect to the undistorted mesh value $\bar{W}^{(0)}$.

The sensitivity analysis is carried out for the displacement-based and the mixed models already discussed in Section 2.4. Figure 2.11 shows the results obtained for both linear four-node (top) and quadratic eight-node elements (bottom). As far as the four-node element is concerned, the QC4 interpolation scheme turns out to be less sensitive to mesh distortion compared to the isoparametric element, regardless the variational formulation. As pointed out in Section 2.4, the eight-node element proves to be very robust not only regarding locking pathology but also mesh distortion. It can be noticed that the sensitivity to mesh distortion completely vanish for the displacement-based model when the CL8 interpolation scheme is considered.

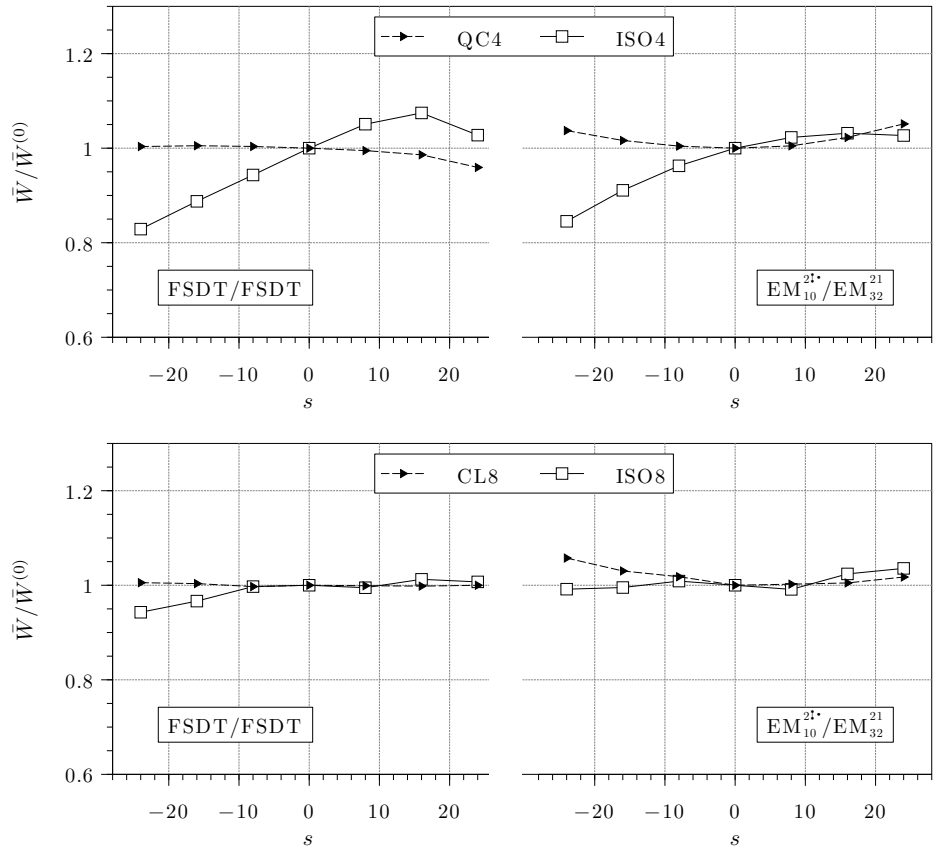

Figure 2.11: Variation of the normalized non-dimensional local parameter $\bar{W}$ with respect to the mesh distortion factor s for both four-node (top) and eight-node (bottom) elements.

Chapter 3

Linear Static Analysis of Composite Panels

Contents

The mixed ESL/LW approach turns out to be particularly suitable for describing the behaviour of bi-dimensional structures such as sandwich composite plates. In this chapter several numerical tests will be performed in order to highlight the capability of the presented FEM-based tool to deal with challenging, fully three-dimensional problems, starting with the free edge effect in laminated plates [111–113]. Then, a model assessment is provided by referring to the three-dimensional elasticity solution for sandwich plates proposed in [114]. ESL models fail to accurately recover the full 3D response of sandwich plates especially when a high facesheet-to-core stiffness ratio occurs. On the other hand a full LW model lead to a number of DOFs comparable to those required by a 3D finite element. Moreover, a sandwich plate is made up of thin and stiff facesheets and one or multiple thick and compliant cores, in which the three-dimensional stress state is normally confined. The SGUF approach is hence exploited

in order to enrich the kinematics model in the sandwich core as well as to regroup the plies constituting the composite face sheets. The FE formulation allows to explore a wide range of practical problems thanks to its flexibility to easily deal with any kind of boundary and loading conditions. In this context a numerical investigation has been carried out on the indentation benchmarks proposed in [115–118] with the purpose of assessing the mixed ESL/LW FEM tool as a reliable software for recovering sandwich plates behaviour while reducing the computational cost.

3.1 Free-edge effect in symmetric composite laminates

Delamination is known to be one of the major failure mechanisms in multilayered composites structures. The causes lie in the significant interlaminar stresses which arise in particular at the free edges, due to mismatch in geometric and elastic properties between plies [119]. This phenomenon, referred as *free-edge effect*, leads to a fully three-dimensional stress state, therefore computationally efficient two-dimensional theories, such as CLT, fail to grasp the steep stress gradient occurring in the proximity of the free edge [120]. This section points out the capability of the proposed finite plate element within the framework of the mixed ESL/LW approach to accurately capture the three-dimensional response of composite laminates. The case study is illustrated in Figure 3.1 and the material properties of the orthotropic plies are reported in Table 3.1.

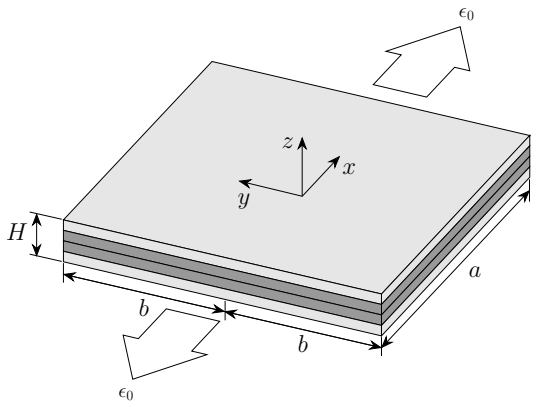

Figure 3.1: Rectangular panel subjected to uniform axial strain ϵ_0.

Table 3.1: Geometric and material data for the free-edge testcase.

$a = 20b;\ b = 8h_p;\ H = 4h_p$	
h_p [mm]	1
E_{11} [GPa]	137.9
E_{22} [GPa]	14.48
E_{33} [GPa]	14.48
G_{i3} [GPa]	5.86
ν_{i3}	0.21

It considers a symmetric laminate made up of four layers loaded by a uniform axial strain ϵ_0 acting along the $x-$direction. The plies are assumed to be of equal thickness $h_p = 1$ mm, so that the total thickness of the panel is $H = 4h_p$. The plate width is

taken to be $2b$ with $b = 8h_p$. The plate length-to-width ratio needs to be sufficiently large to entail a stress state independent of the $x-$coordinate by virtue of *Saint Venant principle*. A unitary axial strain ϵ_0 is applied via a prescribed longitudinal displacement $\bar{u} = a/2$ at $x = \pm a/2$ (see Figure 3.1). Under these assumptions, the equilibrium equations without body forces read

$$\frac{\partial \sigma_{yx}}{\partial y} + \frac{\partial \sigma_{zx}}{\partial z} = 0, \quad \frac{\partial \sigma_{yy}}{\partial y} + \frac{\partial \sigma_{zy}}{\partial z} = 0, \quad \frac{\partial \sigma_{yz}}{\partial y} + \frac{\partial \sigma_{zz}}{\partial z} = 0 \tag{3.1}$$

with $\sigma_{zy} = \sigma_{yz}$ due to rotational equilibrium. Assuming a traction-free condition along the edges of the panel, the following boundary conditions are to be met

$$\sigma_{yy} = \sigma_{yz} = \sigma_{yx} = 0 \qquad \text{at} \quad y = \pm b \tag{3.2}$$

in addition to the static condition at plate's top and bottom faces $\sigma_{iz}\,(x, y, z = \pm H/2) = 0$. Two lamination schemes are investigated, the cross-ply $[0°/90°]_s$ and $[90°/0°]_s$ laminates. Special emphasis will be given to the appropriate through-thickness approximations. Indeed, stability of mixed formulations has been investigated by Boffi *et al.* in [121]. It is well known that the axiomatic transverse stress field must be wisely chosen to prevent spurious oscillations in the solution, see also Demasi [122].

3.1.1 Cross-ply laminates

The cross-ply lamination schemes $[0°/90°]_s$ and $[90°/0°]_s$ are studied in this section. Due to problem symmetry, only the quarter plate is considered. Furthermore, the symmetric stacking sequence allows to further reduce the computational model by considering only the upper half of the laminate relative to the mid-surface. The in-plane discretization involves 35 elements along the $y-$direction with a non-unit spacing ratio in order to obtain the smallest elements drew near to the free-edge (Figure 3.2). Due to the constant strain state along the $x-$direction entailed by the large length-to-

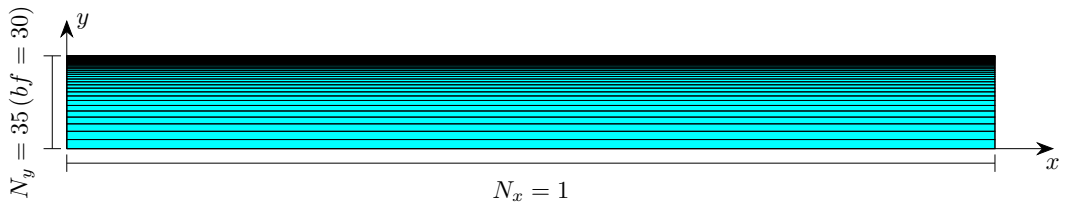

Figure 3.2: FE in-plane discretization employed for the free-edge benchmark. The refinement along the $y-$direction is necessary to grasp the steep gradients in proximity of the free edge.

width ratio of the plate, only one finite element is considered along the longitudinal

axis. The results obtained with different advanced models are compared to those given by Wang and Crossman [111] and Tahani and Nosier [112]. It should be noted that the transverse stress values provided by Wang and Crossman [111] at the free edge ($y = b$) are actually located at $y = 0.9985b$ and that Tahani and Nosier [112] refers to the most expensive model, in terms of computational effort, obtained by employing 15 mathematical layers for each physical ply of the laminate. Since no normal-shear coupling is present for cross-ply laminates, the symmetry conditions are defined as:

$$\begin{gathered} u_x\left(x=0,y,z\right)=0; u_y\left(x,y=0,z\right)=0; u_z\left(x,y,z=0\right)=0 \\ \sigma_{xz}\left(x=0,y,z\right)=0; \sigma_{yz}\left(x,y=0,z\right)=0 \end{gathered} \tag{3.3}$$

Because of the symmetry along the z-direction, only the traction-free condition at the top face of the reduced model is enforced by constraining the transverse stresses DOF at $z = \frac{H}{2}$ to be nil. The symbol $\overset{\bullet}{0}$ is hence appended to transverse stress variable expansion order to complete the model acronym (see Section 2.2.5). In accordance with [122], RMVT-based models require particular attention in choosing the number of transverse stress parameters. This choice is not entirely free and the number of parameters employed to model the displacement field must be taken into account to avoid spurious oscillations in the solution. Due to homogeneous boundary conditions on transverse stress field, the following relation stands as a general rule [123]:

$$N_{s_i} = N_{u_i} + 1 \qquad \text{with} \quad i = x, y, z \tag{3.4}$$

Figure 3.3 and Figure 3.4 report the transverse shear stress σ_{yz} and transverse normal stress σ_{zz} evolution along the normalized $y-$coordinate at bi-material interface $z = h_p$ and at laminate mid-surface $z = 0$ (only for the normal component of the transverse stress field). The y-coordinate is normalized with respect to the half-width b of the panel. The RMVT-based model $\mathrm{LM}_{44}^{5\overset{\bullet}{0}5\overset{\bullet}{0}}$, meeting the condition expressed in Eq. (3.4), is considered.

The transverse normal stress along the half-width at laminate mid-surface is shown in Figure 3.3. A good agreement can be found between the present solution and the reference curves for both $[0°/90°]_s$ and $[90°/0°]_s$ lamination schemes. As the free-edge is approached, the interlaminar normal stress rises or the $[0°/90°]_s$ laminate (or drops for the $[90°/0°]_s$) although a finite value seems to be attained at $y = b$. A slightly different converged value at free-edge is obtained compared to the one given by Wang and Crossman. A different behaviour can be observed at bi-material interface for the $[0°/90°]_s$ lamination scheme (Figure 3.4a) where the steep stress gradient suggests the presence of a singularity at free edge As far as the transverse shear stress at bi-material interface is concerned (Figure 3.4b), no singular behaviour occurs at $y = b$, the

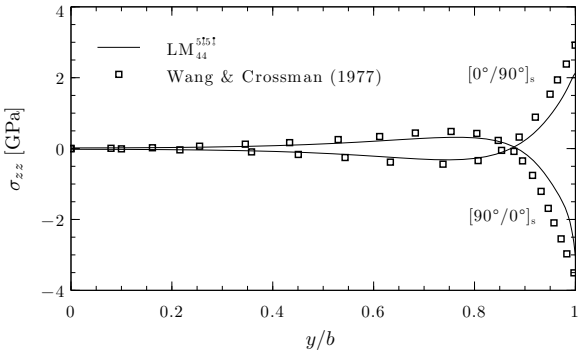

Figure 3.3: Transverse normal stress along the mid-plane $z = 0$ for the cross-ply lamination scheme $[0°/90°]_s$ under a uniform extension ϵ_0 along the $x-$direction.

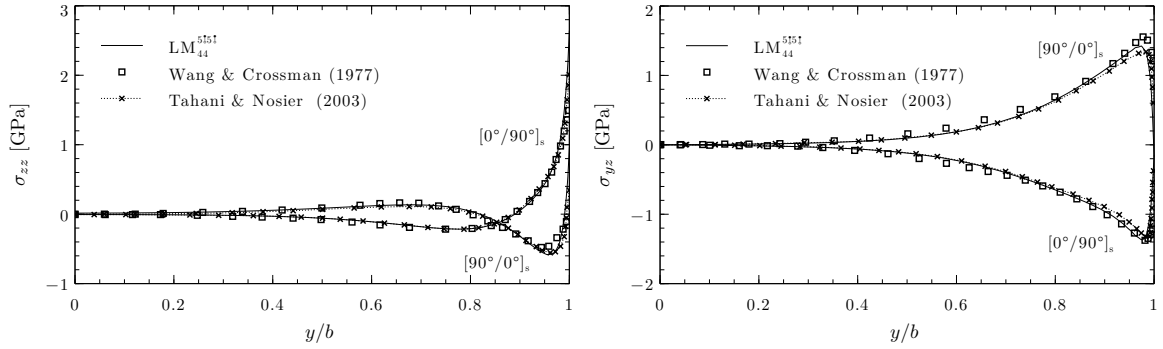

(a) Transverse normal stress. **(b)** Transverse shear stress.

Figure 3.4: Interlaminar stresses along the bi-material interface $z = h_p$ for the cross-ply lamination scheme $[0°/90°]_s$ under a uniform extension ϵ_0 along the $x-$direction.

transverse shear stress increases towards the free edge to finally meet the traction-free condition at free edge in a natural manner within the partially mixed formulation. It is to be noted that the magnitude of transverse shear stress at free edge is almost the same for both configuration despite the change in sign.

In Figure 3.5 the interlaminar normal stress along the free-edge is plotted for both $[0°/90°]_s$ and $[90°, 0°]_s$ lamination schemes. The hybrid-stress-based FE formulation proposed by Spilker and Chou [124] has been also referred for the $[90°, 0°]_s$ case. The partially mixed CUF-based LM4 model is also included. It is observed that the interlaminar normal stress between the plies with different orientation is smaller for the $[90°, 0°]_s$ when compared to $[0°/90°]_s$. The partially mixed formulations exhibit an oscillatory behaviour around solutions found in literature. Moreover, the CUF-based model is found to violate the homogenous condition at plate's top surface. Within the GUF, the variable expansion orders are tuned independently, allowing to increase the order so to impose stress boundary conditions without undermining the stability

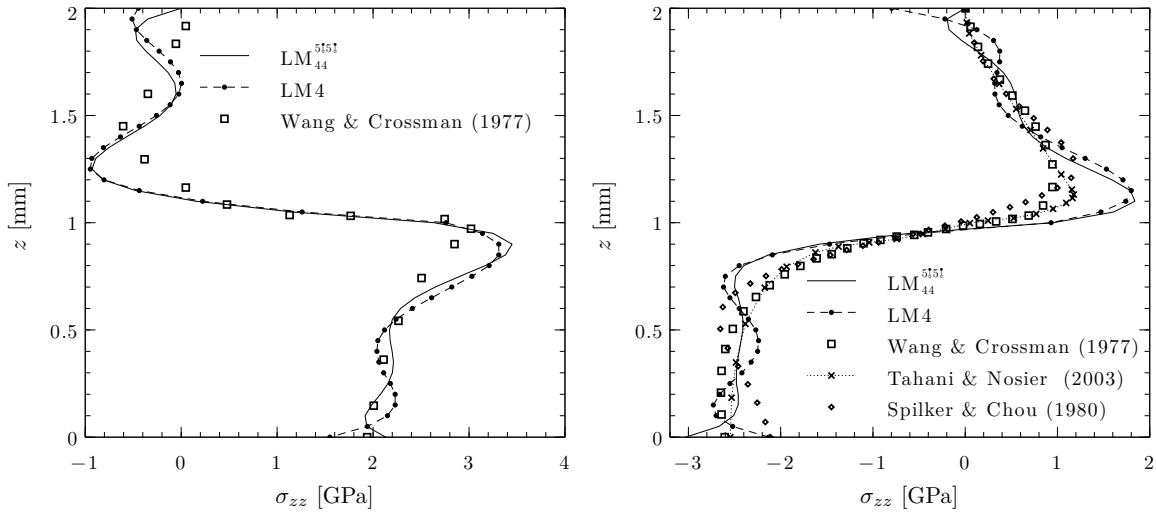

(a) $[0°/90°]_s$ **(b)** $[90°/0°]_s$

Figure 3.5: Through-thickness distribution of transverse normal stress at free-edge ($y = b$) for the cross-ply lamination schemes $[0°/90°]_s$ and $[90°, 0°]_s$ under a uniform extension ϵ_0 along the $x-$direction.

considerations of [122, 123]. However, the nil derivative condition of transverse normal stress at laminate top surface is still violated. To overcome these issues and provide a proper representation of the transverse normal stress at free edge a refinement of the through-thickness assumption is to be considered. In Figure 3.6 (left) this refinement is

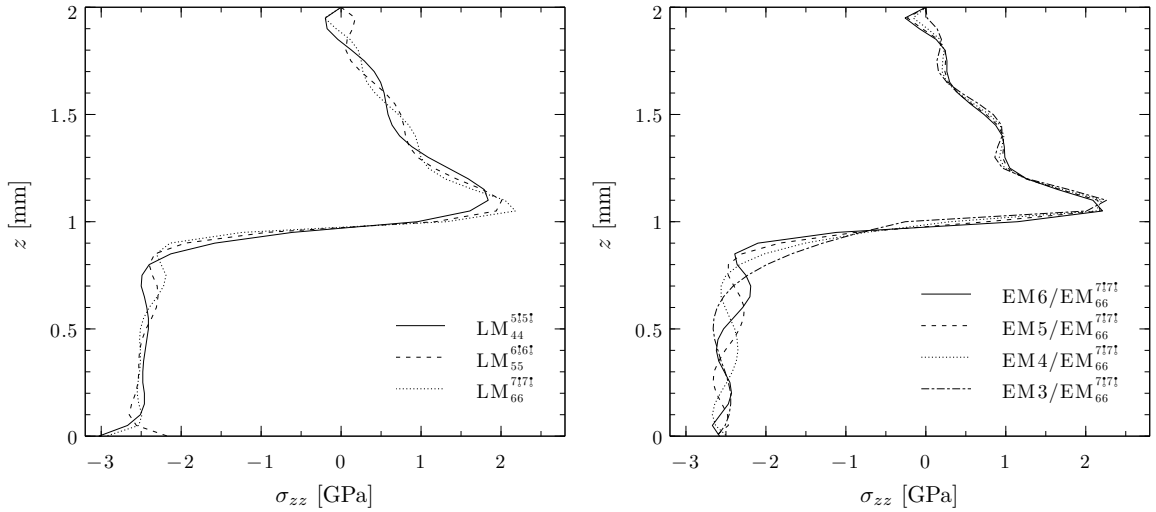

Figure 3.6: Influence of assumed transverse stress field on through-thickness distribution of σ_{zz} at plate free-edge for the $[90°/0°]_s$ cross-ply laminate under a uniform extension ϵ_0 along the $x-$direction.

firstly obtained by increasing the expansion orders for the transverse stress field. The magnitude of interlaminar normal stress at bi-material interface is shown to increase with increased N_{s_z}. However, the pattern of the response still remains oscillatory. The

influence of through-thickness assumptions for the plies with different orientation is also studied upon using different models for the outer ply (90°) and the inner ply (0°). This is done by introducing 2 sublaminates (see Figure 3.6 right). The top layer is always modelled according to $\mathrm{EM}_{66}^{7\mathfrak{k}7\mathfrak{k}}$ in order to allow to impose the stress BC at the top surface. Since no homogenous conditions are to be imposed on inner layer, a classical CUF model with $N \in \{3, ..., 6\}$ is employed. It is observed that the transverse normal stress distribution in the ply oriented at 90° is slightly affected by the expansion order chosen for the 0° layer. Nevertheless, no substantial improvement can be appreciated and a further model refinement is therefore presented next.

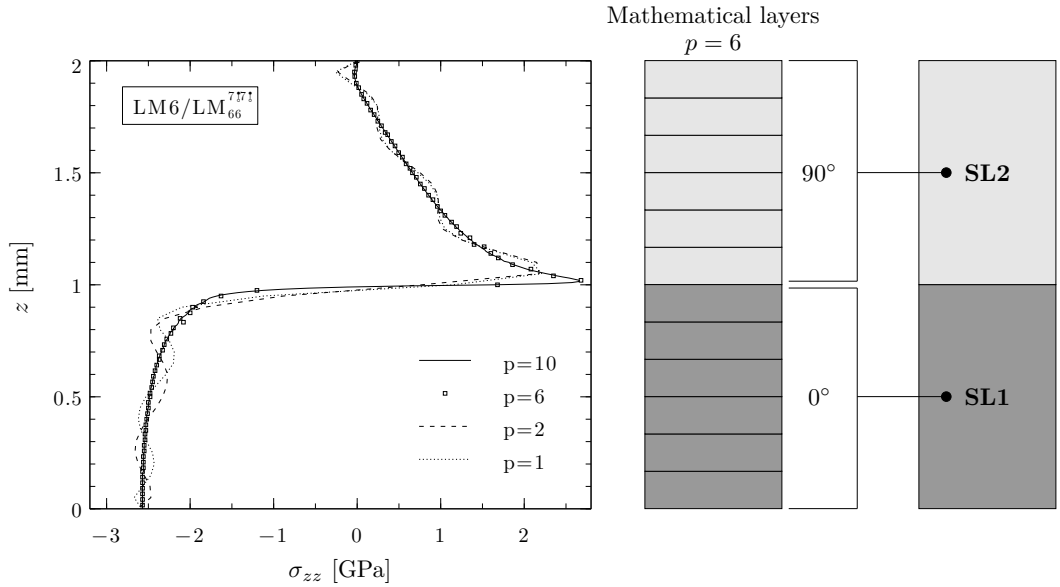

Figure 3.7: Convergence of interlaminar normal stress in $[90°/0°]_s$ laminate under a uniform extension ϵ_0 along the $x-$direction.

In Figure 3.7 the SGUF model LM6/$\mathrm{LM}_{66}^{7\mathfrak{k}7\mathfrak{k}}$ is considered for further refinement by splitting each physical ply into p (with $p \in \{2, 6, 10\}$) mathematical layers. The convergence analysis shows that increasing the number of mathematical layers alleviates the oscillatory nature of response along with ensuring the zero derivative condition expressed by Eq. (3.1). No significant improvement is experienced refining the model with more than six mathematical layers. The peak stress at bi-material interface steadily increases as the number of mathematical layers is increased until the converged value of $p = 6$ is attained. As far as the the maximum value of interlaminar normal stress at laminate mid-plane ($z = 0$) is concerned, the partially mixed LM6/$\mathrm{LM}_{66}^{7\mathfrak{k}7\mathfrak{k}}$ model is sufficient to accurately grasp the normal stress value, regardless any further refinement by means of mathematical layers. A comparison with the results reported in Figure 3.5b shows that the present model is capable of resolving the very steep gradient

at bi-material interface to a higher extent with respect to previously published results.

3.2 Models assessment for sandwich panels

Numerical studies are conducted in this section to assess the accuracy of both displacement-based and partially mixed models in retrieving the global/local response of a sandwich panel under static loading conditions. Particular emphasis shall be addressed to SGUF idealisation of the composite stack as a tool able to provide as accurate predictions as most refined models but significantly reducing the global size of the problem.

3.2.1 Kardomateas sandwich panel

The Kardomateas-TestCase (K-TC) described in Section 2.4 is here considered to assess several plate theories. Different displacement-based as well as mixed models have been investigated by evaluating the through-thickness distributions of the parameters in Eq. (2.23) and by comparing them to the exact 3D solution proposed in [114]. Based on the previous convergence analysis, a mesh of 16×16 elements is used for a quarter plate and the QC4 interpolation is adopted for the PVD models in order to remove the shear locking pathology. In their comprehensive assessment of PVD models for sandwich applications Carrera and Brischetto [8] have shown that an Equivalent Single Layer (ESL) description for the displacement field leads to significant error for very high skin-to-core stiffness ratios. The results in Table 3.2 extend this result to the partially mixed formulation, which is shown to exhibit the same issue for low order CUF models (i.e., EM2). The results also confirm that the use of Murakami's Zig-Zag function (MZZF) improves the accuracy of ESL description for the displacement-based as well as the mixed formulations leading to the conclusion that it is more important to resolve the slope discontinuity of the displacement field across the facesheet-core interface rather than to enhance the polynomial order of the approximation. The beneficial effect of MZZF is also visible in the distributions displayed in Figure 3.8.

On the other hand, high order Layer-Wise (LW) models are able to accurately recover the 3D response of the sandwich plate. As it can be appreciated in Figure 3.9, the interlaminar discontinuity of the transverse stress field of displacement-based models, can be reduced upon increasing the expansion order of the approximation, up to match the *a priori* continuous transverse stress field of RMVT-based models.

Table 3.2 reports results also for several SGUF models, in which one sublaminate is used for each of the facesheets and the core. Thanks to the SGUF approach, the

Table 3.2: K-TC: Assessment of classical and mixed models. Values in parentheses are the absolute percentage errors with respect to the exact 3D solution.

Model (nDOF)	$\bar{U}\,(-H/2)$	$\bar{W}\,(H/2)$	$\bar{S}_{xx}\,(H/2)$	$\bar{S}_{xz}\,(0.4H^{-})$
Ref [114]	**0.4903**	**231.37**	**1.6421**	**0.2064**
Displacement-based models				
ED2 (9)	0.3005 (*38.71%*)	29.812 (*87.12%*)	0.9719 (*40.81%*)	0.0089 (*95.71%*)
ED4 (15)	0.3892 (*20.63%*)	130.31 (*43.68%*)	1.2759 (*22.30%*)	0.0341 (*83.48%*)
EDZ4 (18)	0.4901 (*0.05%*)	231.26 (*0.05%*)	1.6292 (*0.78%*)	0.2052 (*0.55%*)
LD4 (39)	0.4908 (*0.09%*)	231.48 (*0.05%*)	1.6407 (*0.08%*)	0.2061 (*0.11%*)
CLT/FSDT (9)	0.4941 (*0.78%*)	230.14 (*0.53%*)	1.6386 (*0.21%*)	0.2066 (*0.11%*)
FSDT/FSDT (9)	0.4923 (*0.40%*)	230.33 (*0.45%*)	1.6327 (*0.57%*)	0.2066 (*0.13%*)
FSDT/ED_{12} (11)	0.4909 (*0.12%*)	231.78 (*0.18%*)	1.6394 (*0.16%*)	0.2079 (*0.73%*)
FSDT/ED_{32} (15)	0.4909 (*0.12%*)	231.78 (*0.18%*)	1.6394 (*0.16%*)	0.2063 (*0.05%*)
Mixed models w/o homogeneous stress BC				
EM2 (18)	0.1809 (*63.11%*)	158.55 (*31.47%*)	0.6436 (*60.81%*)	0.3601 (*74.47%*)
EM4 (30)	0.4747 (*3.19%*)	223.95 (*3.21%*)	1.5893 (*3.21%*)	0.1522 (*26.23%*)
EMZ4 (33)	0.4940 (*0.74%*)	231.96 (*0.25%*)	1.6512 (*0.56%*)	0.1858 (*9.96%*)
LM4 (78)	0.4910 (*0.13%*)	231.71 (*0.15%*)	1.6416 (*0.03%*)	0.2067 (*0.15%*)
$EM^{2\cdot}_{10}/EM^{0\cdot}_{10}$ (19)	0.4926 (*0.46%*)	230.55 (*0.35%*)	1.6336 (*0.51%*)	0.2072 (*0.38%*)
$EM^{2\cdot}_{10}/EM^{2\cdot}_{10}$ (23)	0.4926 (*0.46%*)	230.55 (*0.35%*)	1.6336 (*0.51%*)	0.2071 (*0.36%*)
$EM^{2\cdot}_{10}/EM^{01}_{12}$ (23)	0.4912 (*0.17%*)	232.01 (*0.27%*)	1.6403 (*0.11%*)	0.2071 (*0.37%*)
$EM^{2\cdot}_{10}/EM^{21}_{32}$ (31)	0.4912 (*0.17%*)	232.01 (*0.28%*)	1.6404 (*0.10%*)	0.2068 (*0.21%*)
Mixed models w/ homogeneous stress BC on $\sigma_{\alpha z}$				
$EM^{2\updownarrow\cdot}_{10}/EM^{0\cdot}_{10}$ (15)	0.4924 (*0.42%*)	230.58 (*0.34%*)	1.6331 (*0.55%*)	0.2072 (*0.38%*)
$EM^{2\updownarrow\cdot}_{10}/EM^{2\cdot}_{10}$ (19)	0.4924 (*0.42%*)	230.58 (*0.34%*)	1.6331 (*0.55%*)	0.2071 (*0.34%*)
$EM^{2\updownarrow\cdot}_{10}/EM^{01}_{12}$ (19)	0.4910 (*0.14%*)	232.03 (*0.29%*)	1.6397 (*0.14%*)	0.2071 (*0.37%*)
$EM^{2\updownarrow\cdot}_{10}/EM^{21}_{32}$ (27)	0.4910 (*0.13%*)	232.04 (*0.29%*)	1.6398 (*0.14%*)	0.2068 (*0.21%*)

facesheet-core interface can be described in a LW sense and dedicated expansion orders can be used in individual sublaminates: it is hence possible to locally enrich the model for the relatively soft and thick core while keeping simple models for the relatively stiff and thin facesheets, which eventually allows to reduce the number of DOF without affecting the accuracy.

Figure 3.10 compares the local response evaluated in the PVD framework against the 3D solution [114]. The facesheets are modelled according to CLT or FSDT and different kinematics for the core have been investigated, ranging from kinematics invoking the plane-stress constitutive law (FSDT) up to fully 3D models (ED_{12} and ED_{32}). The

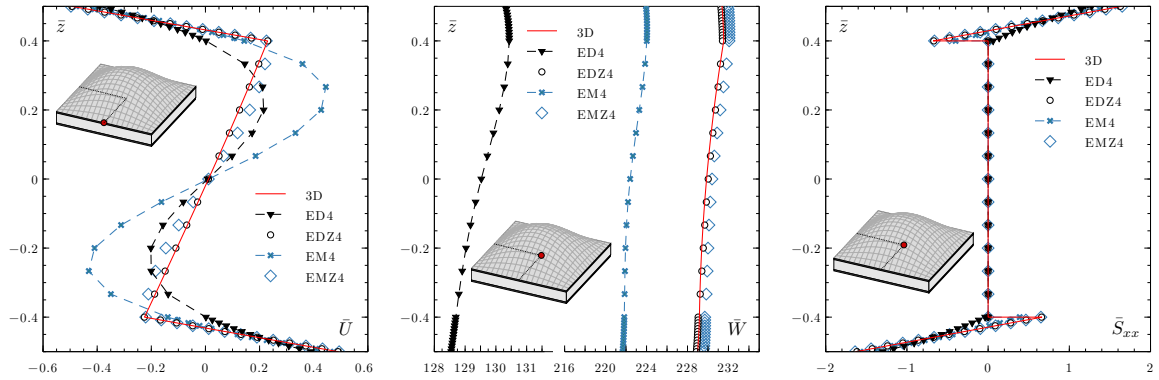

(a) $\bar{U}(z)$ **(b)** $\bar{W}(z)$ **(c)** $\bar{S}_{xx}(z)$

Figure 3.8: K-TC: Influence of MZZF on Equivalent Single Layer plate theories.

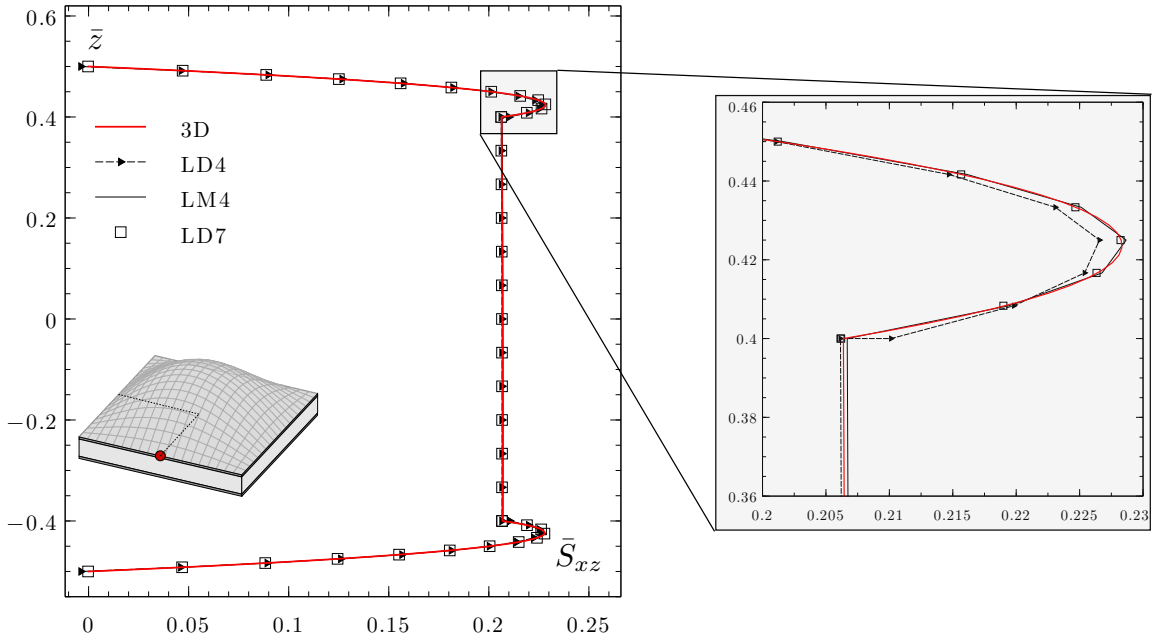

Figure 3.9: K-TC: Transverse stress $\bar{S}_{xz}$ discontinuity at layer interfaces for displacement-based models.

benefits of an explicit representation of the facesheet-core interfaces are clearly visible: all SGUF models yield errors well below 1%. The advantage is also obvious of enhancing the transverse normal response by locally increasing the expansion order inside the core layer only. Since the transverse normal deformation is mostly confined within the thick core layer, all RMVT models reported in Table 3.2 adopt simple plane-stress models for the facesheets without any substantial accuracy loss.

The discontinuity of the derivative at layer interfaces, imposed by the fact that the sublaminates are always assembled in layerwise-sense, provides a very good agreement between the in-plane response of the sandwich plate and the reference solution.

Moreover, a linear approximation across the thickness appears to be sufficient for the present example. The transverse displacement is quite good as long as a kinematics is chosen that involves a 3D constitutive law for the core is chosen. Low order displacement-based models can only provide a rough estimate of the transverse stress field. In order to obtain an accurate estimate of transverse stresses through the thickness direction of the plate several RMVT models have been investigated in Table 3.2. All facesheet models involve a constant deflection so the postulated transverse stress field neglects the transverse stretch. For the core, kinematics up to a quadratic out-of-plane displacement are considered and for them the transverse stretch is no longer neglected.

Finally, Figure 3.11 compares the through-thickness distribution of the transverse shear stresses $\bar{S}_{xz}$ and $\bar{S}_{yz}$ for the mixed SGUF-based model $\mathrm{EM}^{2}_{10}/\mathrm{EM}^{21}_{32}$ against the equivalent PVD-based model. The accuracy improvement is actually modest unless the homogeneous boundary conditions at the plate's top and bottom surfaces are exactly prescribed: the model $\mathrm{EM}^{2\vdots\cdot}_{10}/\mathrm{EM}^{21}_{32}$ is clearly capable of recovering the exact 3D solution with 15 displacement DOF and 12 stress DOF per node.

3.2.2 Cho-Averill sandwich panel

The sandwich panels studied by Cho and Averill [125] (S1-TC) is addressed to highlight the versatility of the sublaminate version of GUF compared to classical CUF and fully three-dimensional approaches. It considers a simply-supported thick square plate (length-to-thickness ration $a/H = 4$) with a symmetric sandwich section made up of a weak core constrained by two laminated facesheets. Each facesheet consists of five plies and has a thickness h_f equal to 10% of the total thickness H. The remaining 80% is occupied by the weak core material. A bi-sinusoidal pressure load of magnitude q is applied at top surface. The geometric and material properties are summarized in Table 3.3. The lamination scheme is reported in Table 3.4 where the relative thickness as well as the material is assigned to each ply. Since loading and boundary conditions exhibit a symmetric behaviour along both x and y directions, only the quarter plate is modelled. Symmetry boundary conditions are thus exploited for both displacement and transverse stress fields.

The elasticity solution given by Burton and Noor [15] and the 3D finite element solution obtained by means of the commercial software Abaqus are used for comparison. A converged solution is obtained by discretizing the sandwich structure with 8×8 quadratic brick elements C3D20R in the $(xy)-$plane directions. The through-thickness

discretization involves 2 elements for each ply constituting the facesheet and 3 elements for the thick core. A total number of 28539 DOFs is associated to this 3D Abaqus model. The same in-plane discretization of the 3D Abaqus model will be used for all the presented bi-dimensional models. Hence, the mesh will be characterised by 8×8 eight-node serendipity elements.

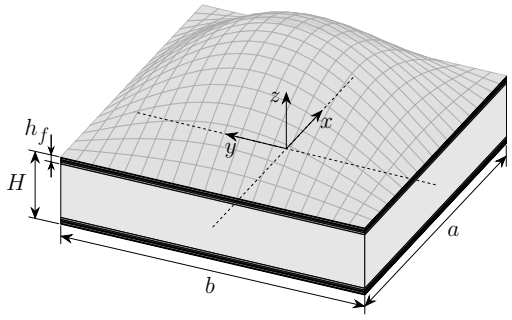

Figure 3.12: S1-TC: Square sandwich panel subjected to bi-sinusoidal pressure load.

Table 3.3: S1-TC: Geometric and material data.

$a = 4;\ b = a;\ S = a/H = 4;\ h_f/H = 0.1$				
	M1	M2	M3	C1
E_{11} [GPa]	6.9	224.8	172.4	0.345
E_{22} [GPa]	172.4	69	69	1.034
E_{33} [GPa]	6.9	69	69	0.345
G_{12} [GPa]	3.45	56.6	3.45	0.15
G_{13} [GPa]	1.38	56	3.45	0.15
G_{23} [GPa]	3.45	3.45	1.38	0.290
ν_{12}	0.01	0.10	0.25	0.01
ν_{13}	0.25	0.10	0.25	0.15
ν_{23}	0.25	0.25	0.25	0.15

Table 3.4: S1-TC: Lamination scheme.

Ply n.	1	2	3	4	5	6	7	8	9	10	11
h_p/H	0.01	0.025	0.015	0.02	0.03	0.8	0.03	0.02	0.015	0.025	0.01
Material	M1	M2	M3	M1	M3	C1	M3	M1	M3	M2	M1

CUF-type model LM2. The first analysis aims at comparing the 3D approach against the hierarchical bi-dimensional refined models in the framework of CUF. The comparison is carried out via a direct correlation between the number of degrees of freedom (DOFs) required by the models. The most refined model within the CUF formulation, involving a comparable number of DOFs, is the partially mixed layerwise model with an assumed quadratic expansion along the thickness direction. All results are provided in terms of nondimensional stresses with respect to the magnitude of the bi-sinusoidal pressure load q, versus the nondimensional thickness coordinate z/H. The through-thickness distributions of in-plane stress components σ_{xx} and σ_{xy} is plotted in Figure 3.13. The facesheet region is enlarged and shaded in light gray. A perfect correlation between the 3D and 2D CUF model is found for both direct and shear

stress components, both accurately recover the elasticity solution. By contrast, as far as the transverse stress field is concerned, the classical CUF model fails to properly predict the distributions along the thickness direction, see Figure 3.14. In particular, an oscillatory behaviour of solution is visible in facesheets intralaminar regions. These oscillations may be explained by the difficulty of low order CUF models to naturally satisfy the traction-free conditions for the transverse stresses at plate' top and bottom faces. As it can be seen in the magnified region next to the top and bottom surfaces of Figure 3.14, an oscillation is introduced in these plies by the quadratic LM2 model. This oscillation is then propagated in the other plies of the facesheet.

The second analysis aims to show how this issue can be easily overcome by the SGUF approach, i.e., regrouping the plies constituting the facesheet into one sublaminate and selecting different orders of expansion for displacement and transverse stress fields. The two models depicted in Figure 3.15 are considered to prove the full potential of the modelling through sublaminates.

SGUF model 1 & 2: 3 sublaminates. Due to the mismatch, in terms of elastic properties, between the facesheets and the core, the most intuitive idealization consists in splitting the sandwich panels into three sublaminates, see Figure 3.15 (left). The weak core is modelled according to EM^{22}_{33} theory. Two distinct GUF models for the facesheets are investigated:

- in the former the equivalent FSDT plate theory within the partially mixed formulation is used for the facesheet. The model acronym is thus $\mathrm{EM}^{2\overset{1}{\bullet}\cdot}_{10}/\mathrm{EM}^{22}_{33}/\mathrm{EM}^{2\overset{\bullet}{1}\cdot}_{10}$.
- the second model is $\mathrm{EM}^{2\overset{1}{\bullet}3}_{14}/\mathrm{EM}^{22}_{33}/\mathrm{EM}^{2\overset{\bullet}{1}3}_{14}$ and it assumes a cubic expansion of the transverse normal stress along the facesheet thickness. It is to be noted that a fourth order transversal displacement is needed in this case to prevent spurious oscillations to occur [122].

For both models the traction-free condition at plate's top and bottom surfaces for the transverse shear field is enforced by constraining the corresponding DOF to be nil.

Figure 3.16 and Figure 3.17 report the through-thickness distributions of the in-plane stress components σ_{xx} and σ_{xy}, and transverse stress components σ_{xz} and σ_{zz} respectively. As far as the in-plane behaviour is concerned, both the low order and refined GUF model for the facesheet provide an accurate representation of the mechanics across the facesheet and a good agreement is found when comparing the models with the elasticity solution given by Burton and Noor. The parabolic distribution of the transverse shear stress as well as the maximum value are well recovered despite the

use of an Equivalent Single Layer theory. Although the $\mathrm{EM}_{10}^{2\mathring{\bullet}\cdot}/\mathrm{EM}_{33}^{22}/\mathrm{EM}_{10}^{2\mathring{\bullet}\cdot}$ theory neglects the transverse normal stress in the facesheets, an accurate prediction across the core is still achieved. Moreover, the interlaminar value at facesheet-core interface seems not to suffer the lack of stress parameters in the adjoining regions, as long as a rich enough expansion in the core region is set. The $\mathrm{EM}_{14}^{2\mathring{\bullet}3}/\mathrm{EM}_{33}^{22}/\mathrm{EM}_{14}^{2\mathring{\bullet}3}$ model, retaining a cubic expansion of the transverse normal stress across the facesheets, is in good agreement with the reference solution not only but also the static conditions at plate's top bottom surface are met in a completely natural manner.

SGUF model 3: 2 sublaminates. As already discussed in Section 3.1, interlaminar stresses are the cause of the onset and progression of delamination in the laminated composites. Therefore, determining the stress state at layer interfaces accurately is crucial for design purposes. However, in order to obtain an accurate prediction in those regions, layerwise theories are to be considered with a consequent increase in global size of the problem with increased number of layers. In addition, in most scenarios the region where the maximum stress value is supposed to be reached is known, depending on laminate stacking sequence. In this case, in view of minimizing the number of DOF, refined models could be used only in those areas of the laminated composite where an accurate prediction is required while low order models may be employed to describe the regions devoid of interest. The mixed ESL/LW approach allows to explore unconventional configurations precisely for addressing this need. In this context, a second idealization including only two sublaminates is depicted in Figure 3.15 (right). The first sublaminate regroups the bottom skin and the core layer while the top facesheet layers form the second sublaminate. The most computationally efficient partially mixed theory is used for the first sublaminate, in particular the $\mathrm{EM}_{10}^{0\cdot}$. It still retains a FSDT theory for the displacement field, but in this case the transverse shear field is assumed to be constant along the thickness direction and the transverse normal stress is neglected. This assumption does not lead to any spurious oscillation since no-homogeneous boundary condition is enforced at plate's bottom surface. The sublaminate regrouping the upper facesheet layers is modelled once again according to $\mathrm{EM}_{14}^{2\mathring{\bullet}3}$. The through-thickness distributions of the transverse stress field for the two-sublaminates idealization model are shown in Figure 3.18.

The transverse shear stress at core-upper facesheet interface is accurately predicted even if a constant distribution is assumed across the first sublaminate, see Figure 3.18a. On the other hand, the maximum value attained in the facesheet is slightly underestimated. The transverse normal stress distribution across the upper facesheet is in

perfect agreement with the elasticity solution as it can be seen in Figure 3.18b. Finally, the total number of DOFs related to each model is resumed in Table 3.5. The full layerwise CUF model stand as the most expansive model when compared with 3D model obtained in Abaqus and the presented 2D theories based on SGUF. On the other hand, SGUF models leads to a significant reduction of the computational cost being still able to provide a quasi-3D level of accuracy. It has been proved that the number of unknown functions can be shrunk even more if an accurate representation is required only in a narrow region of the laminated composite, assessing the modelling through sublaminates as an effective global-local technique for multilayered structures analysis.

Table 3.5: S1-TC: DOFs comparison between commercial software 3D FEM and 2D models.

	Model	DOFs
	Abaqus 3D	28539
CUF model	LM2	31050
SGUF model 1	$EM_{14}^{2\updownarrow 3}/EM_{33}^{22}/EM_{14}^{2\updownarrow 3}$	11700
SGUF model 2	$EM_{10}^{2\updownarrow\cdot}/EM_{33}^{22}/EM_{10}^{2\updownarrow\cdot}$	8100
SGUF model 3	$EM_{10}^{0\cdot}/EM_{14}^{2\updownarrow 3}$	5850

3.3 Local bending and indentation problems

A class of problems involving a three-dimensional deformation state is addressed in this section. Classical bi-dimensional models fail to grasp the local effects due to particular loading conditions. For example, localised pressures or concentrated forces call for a refinement of the through-thickness approximation to describe the steep gradients in the proximity of the loaded area. An assessment and validation of the present FE approach in dealing with challenging, three-dimensional problems is given in the following by addressing the Meyer-Piening case study [126] and the Navarro indentation problem [116].

3.3.1 Meyer-Piening benchmark

The analytical solution provided by Meyer-Piening [126] for three-dimensional class of problems involving sandwich plates is used here in order to assess the proposed numerical tool. The Meyer-Piening TestCase (M-TC) considers a simply supported rectangular unsymmetric sandwich plate subjected to a localised transverse pressure.

The sandwich plate geometry, as well as the elastic properties for the thin facesheets and the core are summarized in Table 3.6. A uniform pressure load $p_0 = 1$ MPa is applied at top surface on a rectangular area delimited by $x \in [47.5, 52.5]$ mm and by $y \in [90, 110]$ mm, as illustrated in Figure 3.19.

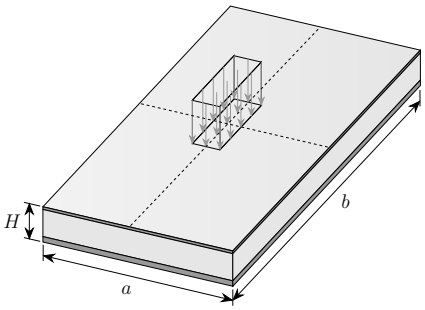

Figure 3.19: M-TC: Sandwich plate with localised uniform pressure.

Table 3.6: M-TC: Geometric and material data

$a = 100$ mm; $b = 200$ mm; $H = 12$ mm			
	Lower face	Core	Upper face
h [mm]	0.5	11.4	0.1
θ	0	0	0
E_{11} [GPa]	70	3	70
E_{22} [GPa]	71	3	71
E_{33} [GPa]	69	2.8	69
G [GPa]	26	1	26
ν	0.3	0.25	0.3

A strong form solution can be obtained by means of a quasi-analytical Navier-type solution with a Fourier series expansion for representing the localised pressure load. The in-plane distributions for this benchmark are characterized by significant gradients in proximity of the localised pressure load. For this reason, a regular mesh is refined towards the plate center as illustrated in Figure 3.20. Exploiting symmetry, only one-quarter of the plate needs to be modeled and it has been discretized with 8×12 elements.

Present FE results are compared in Table 3.7 against the results obtained with the Navier solution by considering the mixed model LM7 in order to establish the error induced by the FE approach. To emphasize the role played by the presence of the sublaminates, the values are evaluated at the top and bottom of the sandwich plate as well as at facesheet-core interfaces located at $z = 5.9$ and $z = -5.5$. The results provided by the FEM model are seen to closely match the reference ones, with an absolute percentage of errors less than 5%.

An assessment is next carried out to highlight the capability of SGUF models to accurately reproduce the sandwich plate response with a reduced number of DOFs when compared to the high-order full LW model LM7. The results of this analysis are summarized in Table 3.8. The variables u_z, σ_{xx} and σ_{zz} are evaluated at the center of the plate $(x = 0, y = 0)$ and the transverse shear stress σ_{xz} at the boundary of the load application area, where its maximum value is reached $(x = -2.5, y = 0)$. Table 3.8

Table 3.7: M-TC: Comparison between Navier-type solution and FEM solution for the LM7 model

Model	z	u_z [mm]	σ_{xx} [MPa]	σ_{xz} [MPa]	σ_{zz} [MPa]
LM7[a]	6	-3.78	-624	0	-1.04
	5.9^+	-3.78	580	-0.17	-0.85
	-5.5^-	-2.14	-138	-0.04	-0.18
	-6	-2.14	146	0	0
LM7	6	-3.73 (*1.16%*)	-625 (*0.27%*)	0 (*0.00%*)	-1 (*4.00%*)
	5.9^+	-3.73 (*1.16%*)	582 (*0.34%*)	-0.17 (*0.00%*)	-0.83 (*2.4%*)
	-5.5^-	-2.13 (*0.47%*)	-138 (*0.00%*)	-0.04 (*0.00%*)	-0.17 (*5.55%*)
	-6	-2.13 (*0.47%*)	146 (*0.00%*)	0 (*0.00%*)	0 (*0.00%*)

reports also the active parameters at node of the hierarchical model, referred to as nDOF.

Figure 3.21 shows the transverse displacement u_z and the bending stress σ_{xx} distributions along two sections cut at $x = 0$ and $y = 0$, where $\bar{x} = 2x/a$ and $\bar{y} = 2y/b$ are the non-dimensional coordinates spanning the x and y directions respectively. The results show that the use of FSDT for modeling the core is not suitable for grasping the local indentation: the core kinematics must include the transverse normal stretch if the effect of the local pressure load is to be resolved. As long as the in-plane gradients of the response are concerned, no difference is appreciated between the mixed $\mathrm{EM}^{2\cdot}_{10}/\mathrm{EM}^{21}_{32}$ model and the displacement-based $\mathrm{FSDT}/\mathrm{ED}_{32}$ model.

In order to appreciate the difference between the RMVT-based and PVD-based models, Figure 3.22 reports the through-thickness distributions of the transverse displacement u_z, the bending stress σ_{xx} and transverse stresses σ_{xz} and σ_{zz}. The improved transverse stress response of mixed models is obvious. Furthermore, it is possible to enhance the transverse stress approximation locally in the core and the facesheets so to very accurately retrieve the reference solution, see Figure 3.22c and Figure 3.22d. The effect is particularly emphasized of exactly satisfying the homogeneous stress conditions at the plate's top and bottom surfaces. As already mentioned in Section 3.1, the expansion orders for the transverse stress variables in RMVT models can not be freely chosen without considering the displacement field. In particular, a number of displacement parameters greater than the stress parameters ($N_u > N_s$) produces spurious kinematic modes resulting in an oscillatory behaviour of the displacement field. On the opposite, if a number of stress parameters greater than the displacement parameters is set ($N_s > N_u$), spurious stress modes occur and the oscillations migrate to the transverse stress variables. So, $N_s = N_u$ should be preferred. Moreover, if stress

Table 3.8: M-TC: Assessment of classical and mixed SGUF models for the Meyer-Piening sandwich plate under a localised pressure load. The absolute percentage error is calculated w.r.t. LM7 solution.

Model (nDOF)	z	u_z [mm]	σ_{xx} [MPa]
LM7 (132)	6	-3.73 (-)	-625 (-)
	5.9^{+}	-3.73 (-)	582 (-)
	-5.5^{-}	-2.13 (-)	-138 (-)
	-6	-2.13 (-)	146 (-)
FSDT/FSDT (9)	6	-2.65 (*28.95%*)	-73 (*88.32%*)
	5.9^{+}	-2.65 (*28.95%*)	39 (*93.30%*)
	-5.5^{-}	-2.65 (*24.41%*)	-276 (*100.00%*)
	-6	-2.65 (*24.41%*)	283 (*93.84%*)
FSDT/ED_{32} (15)	6	-3.72 (*0.27%*)	-610 (*2.4%*)
	5.9^{+}	-3.72 (*0.27%*)	567 (*2.58%*)
	-5.5^{-}	-2.12 (*0.47%*)	-138 (*0.00%*)
	-6	-2.12 (*0.47%*)	146 (*0.00%*)
$\mathrm{EM}^{2\cdot}_{10}/\mathrm{EM}^{21}_{32}$ (31)	6	-3.73 (*0.00%*)	-613 (*1.92%*)
	5.9^{+}	-3.73 (*0.00%*)	569 (*2.23%*)
	-5.5^{-}	-2.13 (*0.00%*)	-139 (*0.72%*)
	-6	-2.13 (*0.00%*)	147 (*0.68%*)
$\mathrm{EM}^{2\boldsymbol{\cdot}}_{10}/\mathrm{EM}^{21}_{32}$ (27)	6	-3.73 (*0.00%*)	-613 (*1.92%*)
	5.9^{+}	-3.73 (*0.00%*)	580 (*0.34%*)
	-5.5^{-}	-2.13 (*0.00%*)	-139 (*0.72%*)
	-6	-2.13 (*0.00%*)	147 (*0.68%*)

BCs are imposed, N_s must be augmented by the number of suppressed stress DOF.

3.3.2 Indentation of a sandwich beam

The indentation of a sandwich beam is finally investigated by referring to the problem considered by Navarro *et al.* [116] and, therefore, referred to as Navarro-TestCase (N-TC). In contrast to previous TC, here a beam problem is considered. The problem is defined in the $(x, z)-$plane as displayed in Figure 3.23, with a concentrated load $P = 1000$ N acting at the centre of the beam at the top surface and the bottom of the beam fully clamped ($u_x = u_z = 0$). The data for geometry and material properties is given in Table 3.9. Symmetry is exploited to reduce the computational model to one-half of the beam.

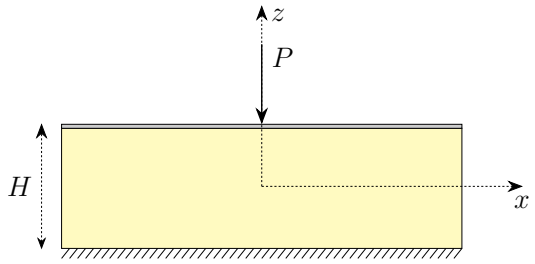

Figure 3.23: N-TC: Sandwich beam with indentation load.

Table 3.9: N-TC: Geometric and material data.

$a = 100$ mm; $b = 1$ mm; $H = 31$ mm		
	Core	Upper face
h [mm]	30	1
θ	0	0
E_{11} [GPa]	0.2	100
E_{22} [GPa]	0.2	100
E_{33} [GPa]	0.2	100
G [GPa]	0.087	38.46
ν	0.15	0.3

Navarro *et al.* developed a very effective model for core crushing, which is based on a semi-analytical continuum-based model proposed by Vlasov [116]: considering a homogenous and isotropic core, its elastic response is given in terms of a simple two-parameters "elastic foundation" model, which relies upon the assumption of zero in-plane displacement in the core and on a decay function of the core deformation that annihilates the perturbation at the bottom of the core [127, 128].

In the following, present SGUF FEM results are compared against the semi-analytical Vlasov's model as well as a reference elasticity solution obtained by the commercial FE package Abaqus. It will be shown that the present approach, which is more general than Vlasov's "elastic foundation" model, is capable of providing very accurate results with only a 2D mesh in the $(xy)-$plane and reduced number of DOF when compared to the commercial FE packages. Following [116], the Abaqus model for one-half of the beam consists of 200 two-nodes shear-deformable plane beam elements (B21) for

the facesheet and 4200 four-nodes plane stress elements (CPS4R) for the core. This results in a discrete model with 9805 DOF. The axial displacement u_x inside the core is suppressed in order to better reproduce Vlasov's assumption.

The present SGUF models adopt FSDT for the facesheet and high-order models for the core, in which the axial displacement is expanded only linearly along the thickness in order to minimise the axial deformation of the core as per Vlasov's assumption. High-order expansions are adopted for the transverse displacement in the core, ranging from cubic up to sixth-order: the core models are thus expressed as $\mathrm{ED}_{1\,N_{u_z}}$ with $N_{u_z} \in \{3, \dots 6\}$. As far as the 2D mesh is concerned, the beam is modeled with only one 4-node plate element across the width, by imposing $u_y = 0$. 50 elements are used along the beam axis, with a bias factor (the ratio of the largest edge size to the smallest) of 10 to increase the mesh density towards the loading area to accurately grasp the localised stress field (Figure 3.24). The number of total DOF of the considered SGUF models is compared against the Abaqus model in Table 3.10. Figure 3.25 shows the distributions along the beam axis ($x-$direction) of the transverse displacement u_z and bending stiffness σ_{xx} at the top of the skin ($z = H/2 = 15.5$ mm), as well as the transverse shear stress σ_{xz} and the transverse normal stress σ_{zz} in the core just below the interface with the facesheet ($z = 14.5$ mm). A very satisfying agreement of the SGUF model $\mathrm{FSDT/ED}_{14}$ with the reference Abaqus solution is obtained. The discrepancy in the maximum transverse shear stress (Figure 3.25c) is attributed to the particular kinematics that has been adopted inside the core. Concerning Vlasov's model, it is capable of very precisely reproducing the local indentation of the facesheet (transverse displacement and bending stress, see Figure 3.25a and Figure 3.25b), but the transverse stresses inside the core appear to be less accurate. In particular, the maximum value of the transverse normal stress predicted by Vlasov's model in correspondence of the concentrated load is quite unsatisfactory (Figure 3.25d).

Figure 3.26 shows the convergence of transverse normal stress at the facesheet-core interface upon increasing the expansion order N_{u_z}, with emphasis on the region of the applied concentrated load. It can be seen that the maximum compressive stress appears to converge towards a finite value of approximately -95 MPa. Therefore, the present SGUF modeling approach allows to recover full three-dimensional results with a simple 2D mesh and, hence, a reduced number of DOF compared to the standard FEM available in commercial packages (see Table 3.10).

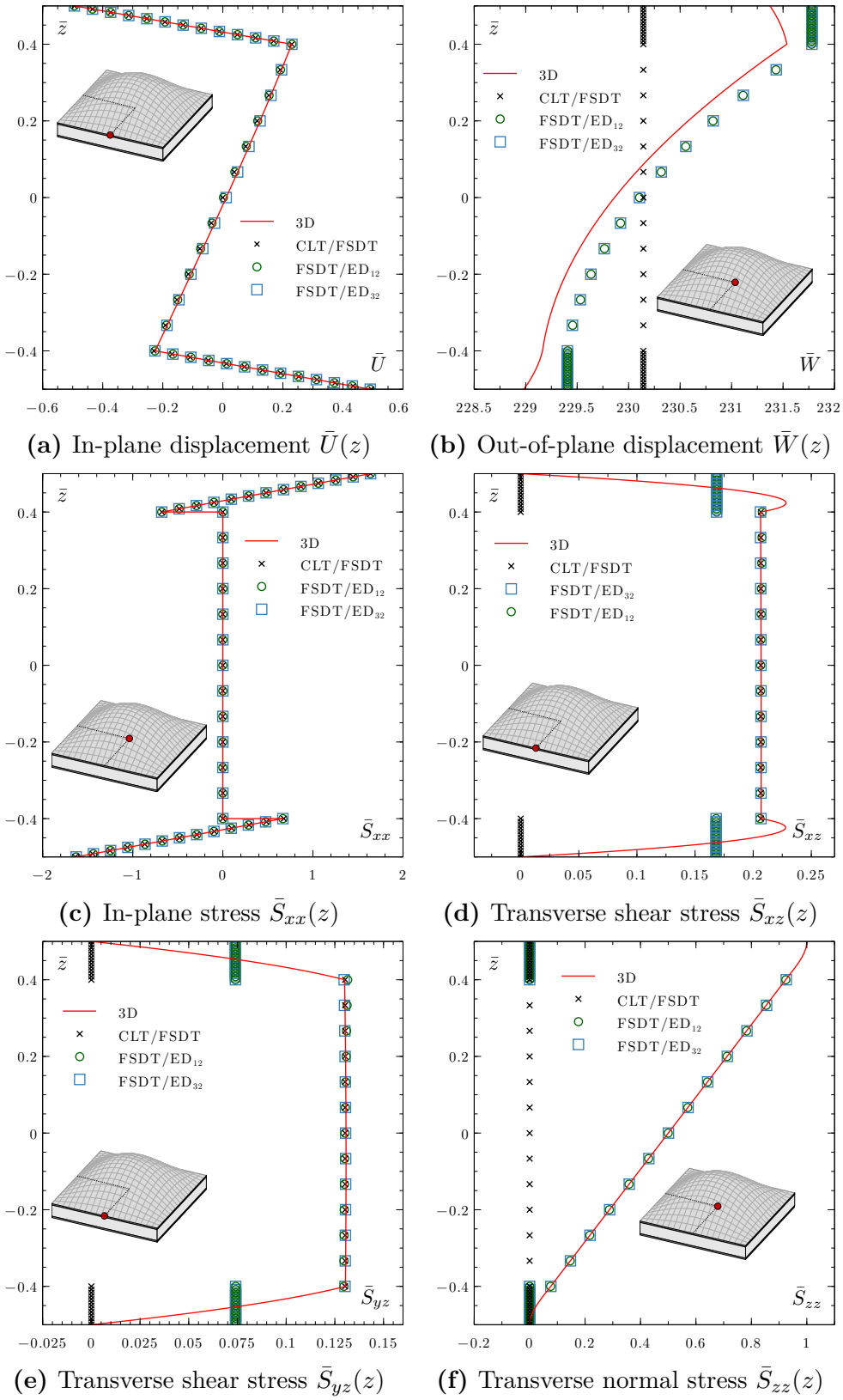

(a) In-plane displacement $\bar{U}(z)$ **(b)** Out-of-plane displacement $\bar{W}(z)$

(c) In-plane stress $\bar{S}_{xx}(z)$ **(d)** Transverse shear stress $\bar{S}_{xz}(z)$

(e) Transverse shear stress $\bar{S}_{yz}(z)$ **(f)** Transverse normal stress $\bar{S}_{zz}(z)$

Figure 3.10: K-TC: Through-thickness distributions of local response parameters for displacement-based SGUF models.

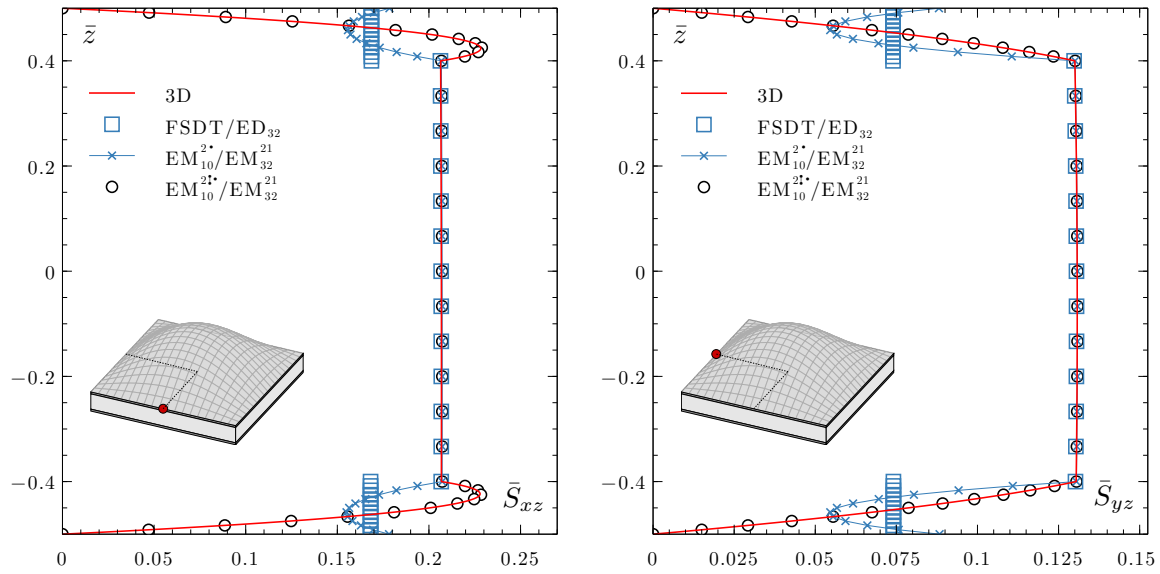

(a) Transverse shear stress $\bar{S}_{xz}(z)$ **(b)** Transverse shear stress $\bar{S}_{yz}(z)$

Figure 3.11: K-TC: Influence of homogenous stress boundary conditions on transverse shear stresses through-thickness distributions.

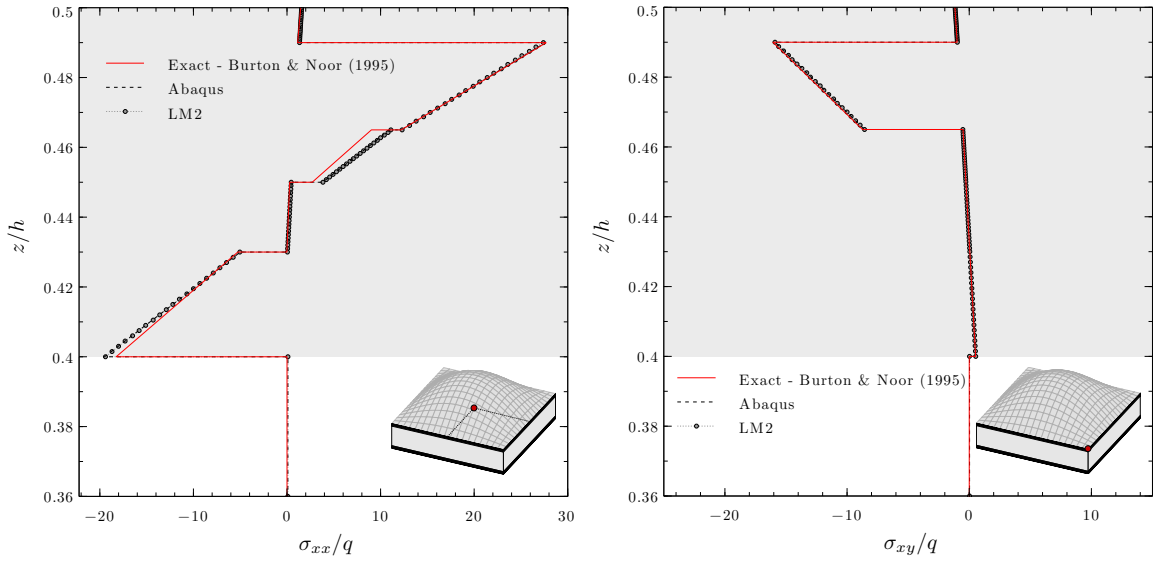

(a) Bending stress **(b)** Shear stress

Figure 3.13: S1-TC: Through-thickness distribution of nondimensional in-plane stress components σ_{xx}/q at $(x = 0, y = 0)$ (a) and σ_{xy}/q at $(x = -a/2, y = -b/2)$ (b). Comparison between Abaqus 3D elements and 2D CUF model.

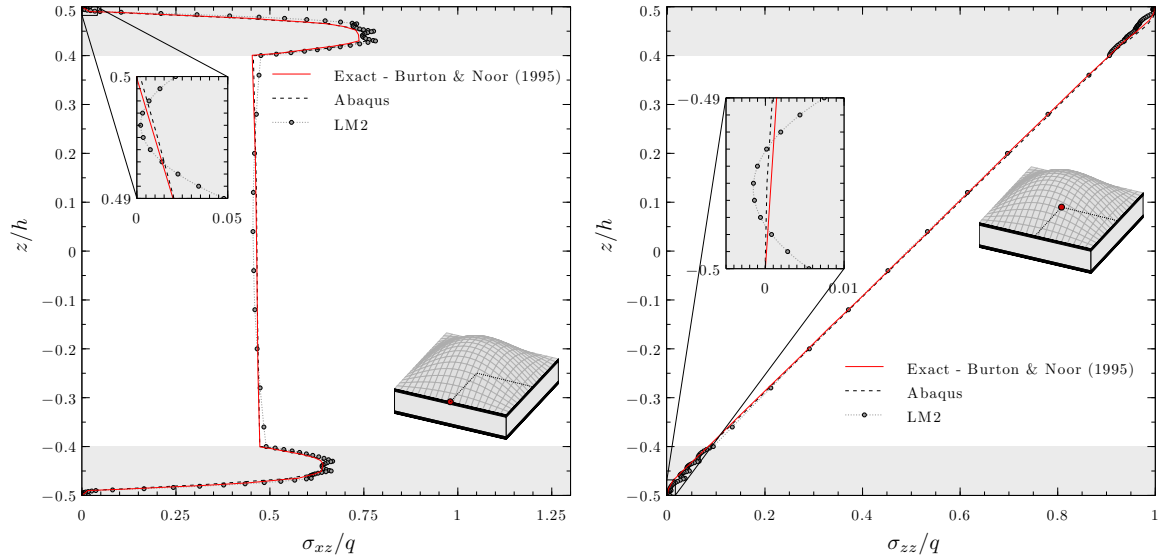

(a) Transverse shear stress **(b)** Transverse normal stress

Figure 3.14: S1-TC: Through-thickness distribution of nondimensional transverse stress components σ_{xz}/q at $(x = -a/2, y = 0)$ (a) and σ_{zz}/q at $(x = 0, y = 0)$ (b). Comparison between Abaqus 3D elements and 2D CUF model.

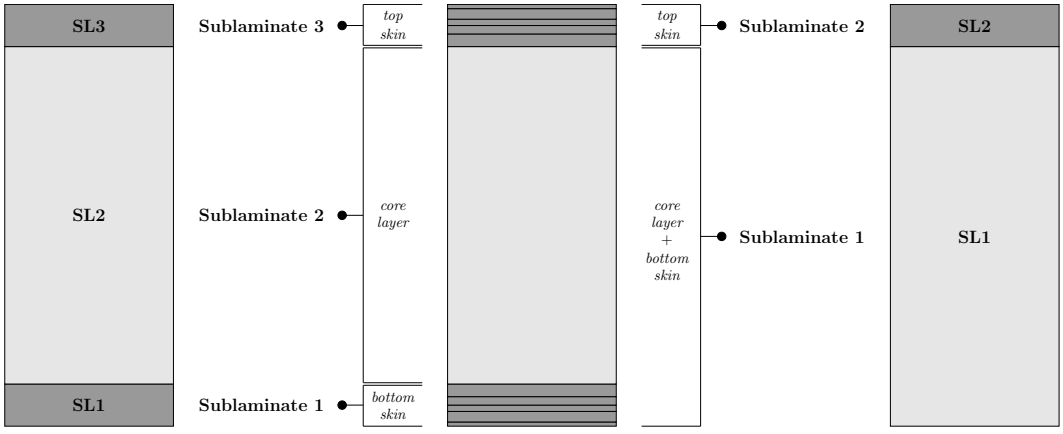

Figure 3.15: S1-TC: Sandwich structure idealization into three sublaminates (left) and two sublaminates (right).

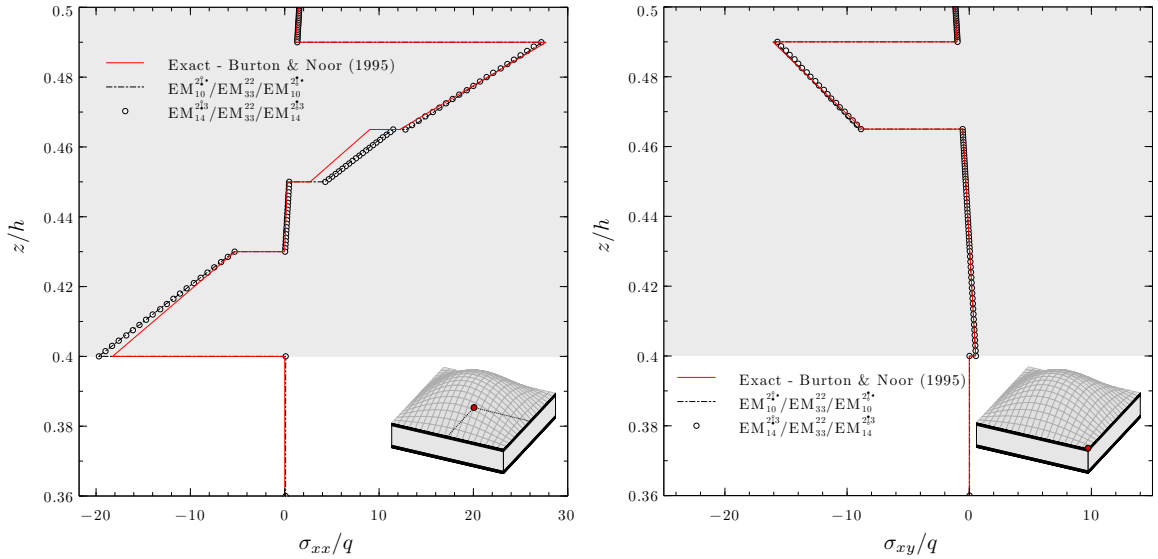

(a) Bending stress **(b)** Shear stress

Figure 3.16: S1-TC: Through-thickness distribution of nondimensional in-plane stress components σ_{xx}/q at $(x = 0, y = 0)$ (a) and σ_{xy}/q at $(x = -a/2, y = -b/2)$ (b). Comparison between different theories obtained in the framework of SGUF.

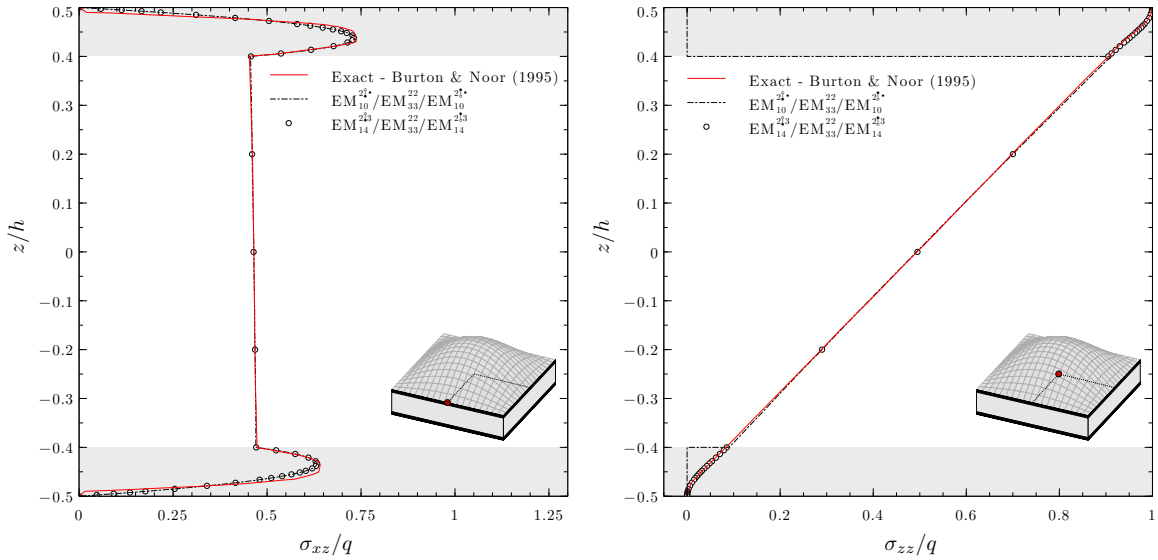

(a) Transverse shear stress **(b)** Transverse normal stress

Figure 3.17: S1-TC: Through-thickness distribution of nondimensional transverse stress components σ_{xz}/q at $(x = -a/2, y = 0)$ (a) and σ_{zz}/q at $(x = 0, y = 0)$ (b). Comparison between different theories obtained in the framework of SGUF.

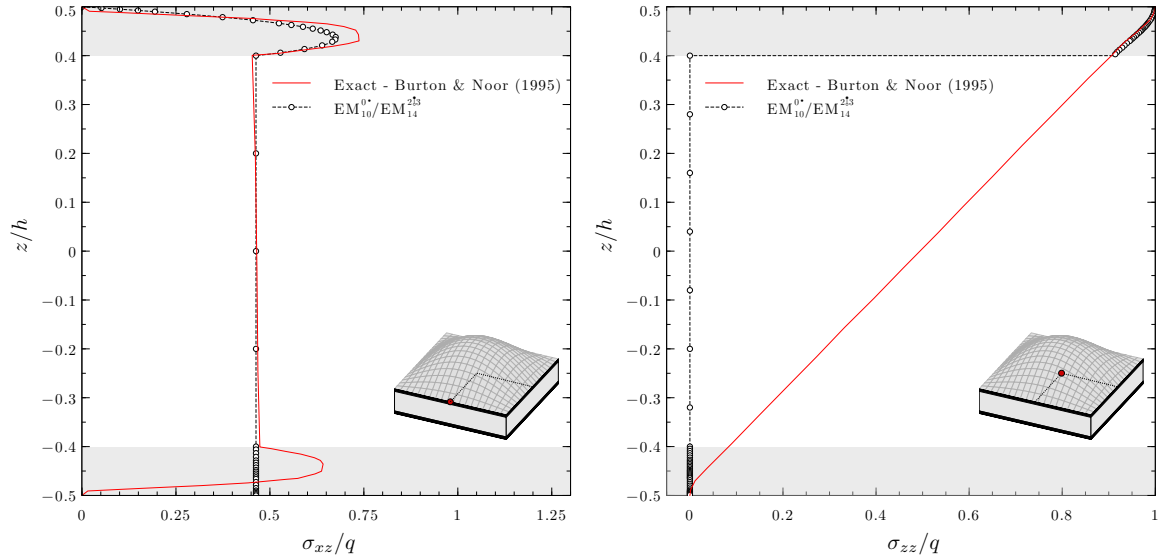

(a) Transverse shear stress **(b)** Transverse normal stress

Figure 3.18: S1-TC: Through-thickness distribution of nondimensional transverse stress components σ_{xz}/q at $(x = -a/2, y = 0)$ (a) and σ_{zz}/q at $(x = 0, y = 0)$ (b). Effectiveness of localised theory based on SGUF.

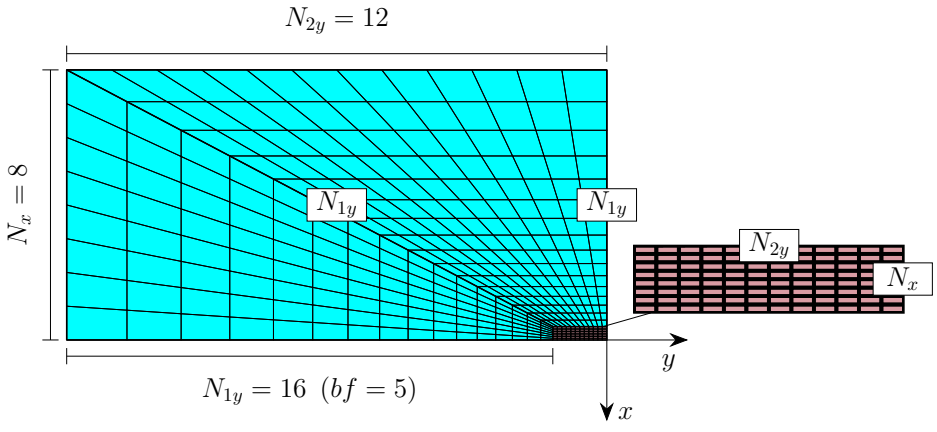

Figure 3.20: M-TC: Refined mesh in proximity of the localised pressure load.

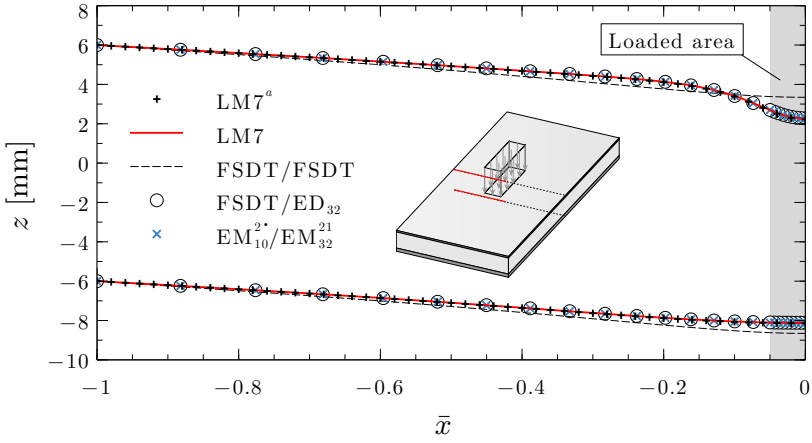

(a) Cut plane at $y = 0$.

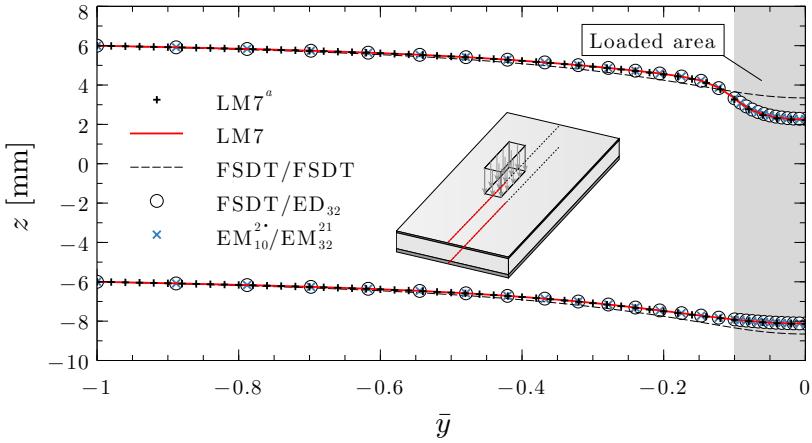

(b) Cut plane at $x = 0$.

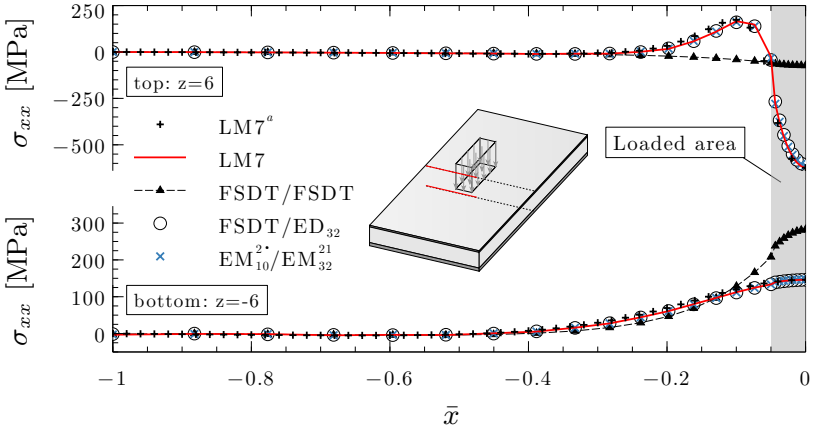

(c) Bending stress σ_{xx}.

Figure 3.21: M-TC: In-plane distribution of coordinate z and bending stress σ_{xx} at top and bottom surfaces.

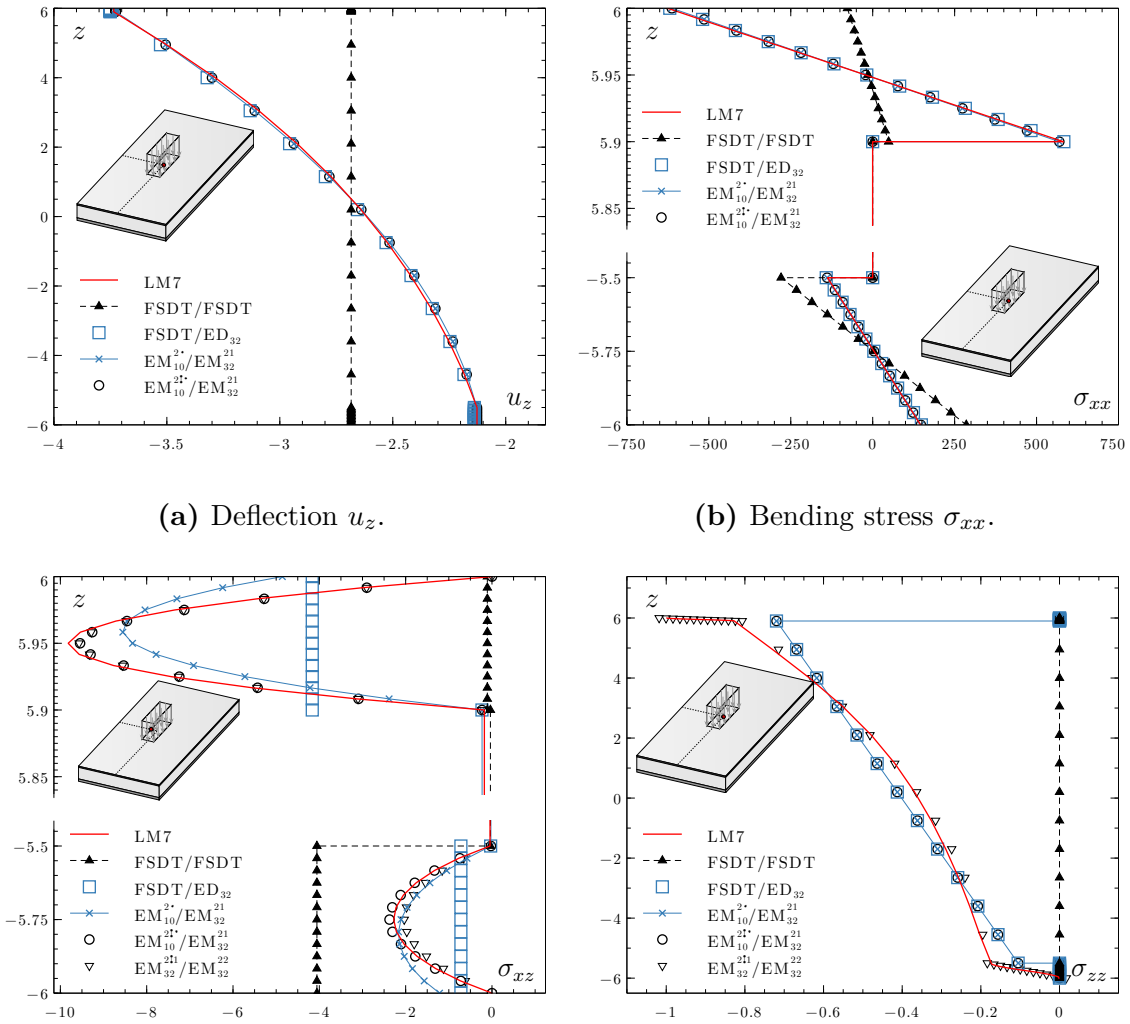

(a) Deflection u_z. **(b)** Bending stress σ_{xx}.

(c) Transverse shear stress σ_{xz}. **(d)** Transverse normal stress σ_{zz}.

Figure 3.22: M-TC: Through-thickness distributions of deflection u_z, bending stress σ_{xx} and transverse stresses σ_{xz} and σ_{zz}.

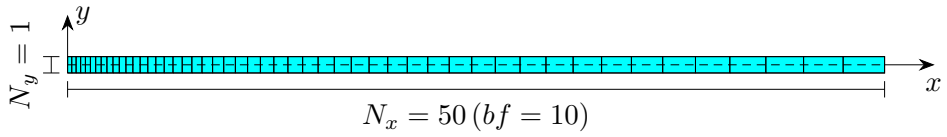

Figure 3.24: N-TC: Refined mesh in the proximity of the concentrated point load.

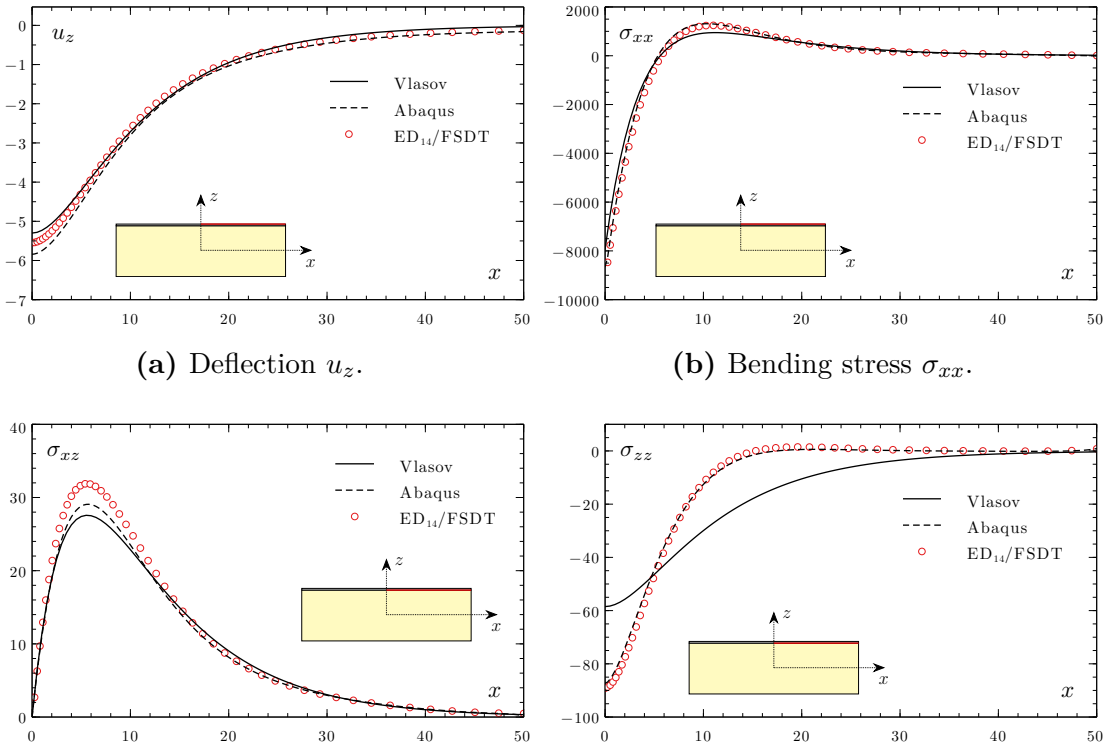

(a) Deflection u_z. **(b)** Bending stress σ_{xx}.

(c) Transverse shear stress σ_{xz}. **(d)** Transverse normal stress σ_{zz}.

Figure 3.25: N-TC: In-plane distributions of deflection u_z, bending stress σ_{xx} in the skin and transverse stresses σ_{xz} and σ_{zz} in the foam.

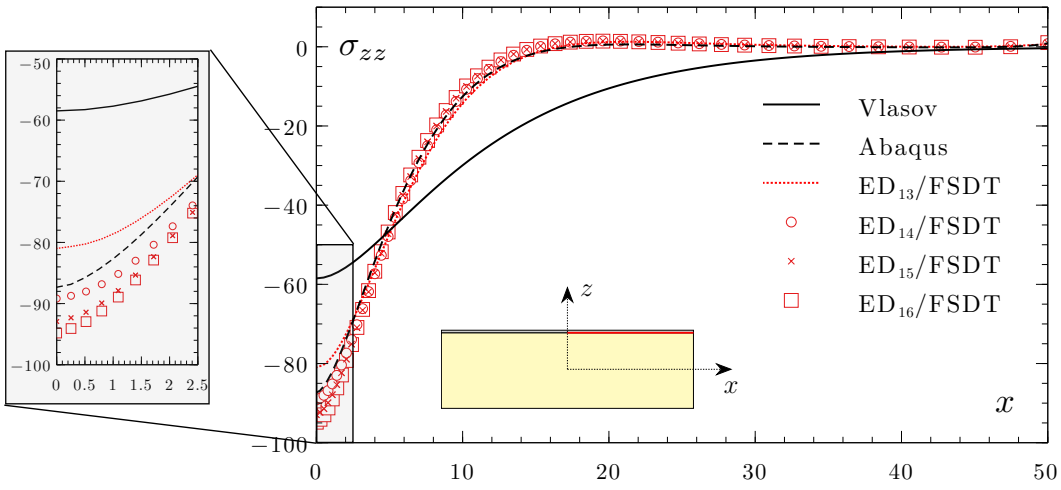

Figure 3.26: N-TC: Influence of out-of-plane displacement approximation order on transverse normal stress σ_{zz}.

Table 3.10: N-TC: DOFs comparison between commercial software FEM and 2D SGUF model.

Model	DOFs
ED_{13}/FSDT	1020
ED_{14}/FSDT	1122
ED_{15}/FSDT	1224
ED_{16}/FSDT	1326
Abaqus	9805

Chapter 4

Viscoelastic Dynamic Analysis of Sandwich Panels

Contents

In this chapter, free and forced vibrations of sandwich beams and panels with embedded viscoelastic layer are studied. Governing equations of motion are derived

for classical displacement-based models as well as for advanced models based on partially mixed formulation, and then solved via FE method. The *Complex Modulus Approach* (CMA) is used to model the constant or frequency-dependent viscoelastic material (VEM) behaviour. In this context, the *Anelastic Displacement Field* (ADF) and *Fractional Derivatives Zener* (FDZ) constitutive models are used for representing the frequency-dependence of VEM. Modal loss factors and damped eigenfrequencies can be obtained by employing a complex eigensolver or by resorting the modal strain energy (MSE) approach [63, 129]. These resolution methods will be assessed referring to the viscoelastic sandwich beam studied by Bilasse *et al.* in [130]. A frequency-dependent viscoelastic law leads to a nonlinear eigenvalue problem, hence an iterative algorithm based on fixed-point iteration method has been implemented and successfully validated against the sandwich plate hosting a 3M-ISD polymer core. Further studies have been conducted on a triple-core sandwich construction designed by the Garteur consortium [131] in order to emphasise the role of transverse normal deformation of the weak viscoelastic layer. The forced harmonic response of viscoelastic sandwich plate is also discussed and the results are compared to Ritz solution given by D'Ottavio *et al.* in [49].

4.1 Viscoelastic models in time- and frequency-domain

Starting from the assumption of linear viscoelasticity, the one-dimensional constitutive law in the time-domain for an isotropic viscoelastic material (VEM), taking into account the previous history of deformation $\epsilon(t)$, is given by the Riemann convolution integral [132]

$$\sigma(t) = \int_{-\infty}^{t} E(t-\tau) \frac{\mathrm{d}\epsilon(\tau)}{\mathrm{d}\tau} \, \mathrm{d}\tau \tag{4.1}$$

where $E(t)$ is the *relaxation modulus*. Upon introducing the scalar function describing the material memory $h(t)$, the relaxation modulus can be written as [133]

$$E(t) = E_0 - h(t) \tag{4.2}$$

where $E_0 = E(t \to 0)$ is the instantaneous modulus. Note that the following relation for the memory function $h(t)$ holds

$$h(t) = 0 \quad \text{for} \quad t < 0 \tag{4.3}$$

which implies the $h(t)$ being a causal function, i.e. the response is influenced only by the history of deformation. If the instantaneous strain does not have any viscous

effects, the stress-strain relation in Eq. (4.1) becomes [133]

$$\sigma(t) = E_0 \epsilon(t) - \int_{-\infty}^{t} h(t-\tau) \frac{\mathrm{d}\epsilon(\tau)}{\mathrm{d}\tau} \, \mathrm{d}\tau \tag{4.4}$$

In FE applications the damping behaviour is typically modelled in the frequency-domain due to difficulties in experimentally measuring the relaxation modulus in the time-domain [134]. The constitutive damping model in the frequency-domain shall meet the condition expressed in Eq. (4.3). In other words, the corresponding time-domain model need to be causal. A frequency-domain model, fulfilling the causality condition, can be obtained by applying the Fourier transform to the time-domain model in Eq. (4.4), yielding the following definition of the complex modulus E^*:

$$E^*(\omega) = E'(\omega) + \mathrm{i}\, E''(\omega) = E'(\omega)\left[1 + \mathrm{i}\, \eta(\omega)\right] \tag{4.5}$$

where $\mathrm{i} = \sqrt{-1}$ is the imaginary unit. The real part of the complex modulus, denoted by $E' = E^*(\omega \to 0)$, is called storage modulus, the imaginary part is a measure of the dissipated energy and for this reason E'' is referred as loss modulus. Consequently, the prime and double-prime notations do not imply any derivatives. The loss factor $\eta(\omega)$ is defined as the ratio between the loss and storage modulus

$$\eta(\omega) = \frac{E''(\omega)}{E'(\omega)} \tag{4.6}$$

For a linear, homogeneous and isotropic viscoelastic material the following relationship between the extensional and shear modulus holds

$$G^*(\omega) = \frac{E^*(\omega)}{2(1+\nu)} \tag{4.7}$$

where, for simplicity, the Poisson's ratio ν is assumed to be independent from frequency. In the next paragraphs, the viscoelastic models in the frequency domain used throughout the thesis are presented.

4.1.1 Structural damping model

The structural damping model, also referred as to hysteretic damping, is widely employed to describe the viscoelastic behaviour of those materials whose dynamic properties are not significantly affected by the working frequency. The loss factor and dynamic modulus are assumed to be constant and Eq. (4.5) becomes:

$$E^* = E'(1 + \mathrm{i}\,\eta) \tag{4.8}$$

Despite the simplicity of the model, the constant assumption for the loss factor leads to the violation of memory function causality as extensively discussed in [135, 136].

4.1.2 Anelastic Displacement Fields model

Lesieutre and Bianchini [55] provided a linear viscoelasticity model based on the decomposition of displacement field in an elastic part and an anelastic one, which describes that part of strain which is not instantaneously proportional to stress. The frequency dependence of stiffness and damping for a viscoelastic material, modelled via the ADF approach has the form

$$G^{*}(\omega) = G_0 \left(1 + \sum_{j=1}^{n} \frac{\Delta_j \omega}{\omega - \mathrm{i}\,\Omega_j}\right) \tag{4.9}$$

where G^* is the complex modulus, ω is the angular frequency in radians per second and G_0 takes on the same physical meaning of E' in Eq. (4.5). The parameter n is the number of anelastic displacement fields used in the model, each characterized by a *relaxation time* $Z_j = 1/\Omega_j$ and a *relaxation strength* Δ_j $(j = 1, 2, \ldots, n)$. The accuracy of the ADF model in describing the frequency-dependent behaviour of a viscoelastic material depends on the number of anelastic displacement fields used in the series. It is to be noted that the values defining the series are identified in a specific frequency range, the model reliability is guaranteed insofar solely inside such identification frequency range.

4.1.3 Fractional Derivatives Zener model

Through the years, fractional derivatives models has been proved to be a very suitable way to describe the frequency-dependent behaviour of the dynamic properties of viscoelastic materials [137–140]. The basic assumption is to leave behind the viscous dashpot element in the classic spring-dashpot model on behalf of a more physical representation of the dynamic behaviour. Note that the viscous dashpot assumes the solid to behave like a fluid regarding the internal friction nature of the solid itself. In the fractional derivatives model the stress is assumed to be directly proportional to the strain through the differential operator $\mathrm{d}^{\alpha}/\mathrm{d}t^{\alpha}$ with $0 < \alpha < 1$. The main advantage of fractional derivatives models is to be sought in using relatively few parameters compared to ADF model. In the following, reference will be made to the four-parameter Zener type model firstly introduced by Caputo *et al.* [141, 142]. The stress-strain relationship in the time domain, for the four-parameter model, can be hence defined by the linear differential equation [59]

$$\sigma(\omega) + \tau^{\alpha} \frac{\mathrm{d}^{\alpha}\sigma(t)}{\mathrm{d}t^{\alpha}} = G_0 \epsilon(t) + G_{\infty} \tau^{\alpha} \frac{\mathrm{d}^{\alpha}\epsilon(t)}{\mathrm{d}t^{\alpha}} \tag{4.10}$$

where G_0 has the same meaning given in Eq. (4.9), $G_\infty = G^*(\omega \to \infty)$ is the *unrelaxed* or *asymptotic* modulus and τ is the relaxation time. Note that for the model to be physically meaningful and comply with the second law of thermodynamics [143], the following conditions must hold

$$G_\infty > G_0 \geq 0\,, \quad \tau > 0 \tag{4.11}$$

which add to the condition on fractional derivative order α already introduced. Upon using the Fourier transform on Eq. (4.10), the stress-strain relationship in the frequency domain reads

$$\sigma^*(\omega) = \left[\frac{G_0 + G_\infty (\mathrm{i}\,\omega\tau)^\alpha}{1 + (\mathrm{i}\,\omega\tau)^\alpha}\right] \epsilon^*(\omega) = G^*(\omega)\,\epsilon^*(\omega) \tag{4.12}$$

The complex modulus associated to the four parameters fractional derivatives model is thus

$$G^*(\omega) = \left[\frac{G_0 + G_\infty (\mathrm{i}\,\omega\tau)^\alpha}{1 + (\mathrm{i}\,\omega\tau)^\alpha}\right] \tag{4.13}$$

4.2 Free-vibration analysis

The nonlinear generalized eigenvalue problem for the sandwich panel hosting a frequency-dependent viscoelastic layer reads

$$\left[\mathbf{K}^*(\omega) - \lambda^2(\omega)\,\mathbf{M}\right]\mathbf{U}^* = 0 \tag{4.14}$$

in which $\mathbf{K}^*$ and $\mathbf{M}$ are the global complex stiffness and mass matrices of the structure respectively, obtained in FEM analysis upon assembling the element matrices, and λ^2 and $\mathbf{U}^*$ are the complex eigenvalues and complex modal shapes of the system. The complex stiffness matrix $\mathbf{K}^*$ can be written as:

$$\mathbf{K}^*(\omega) = \mathbf{K}_R(\omega) + \mathrm{i}\,\mathbf{K}_I(\omega) \tag{4.15}$$

where $\mathbf{K}_R$ and $\mathbf{K}_I$ are the real and the imaginary part giving the stiffness and the damping of the structure, respectively. If a frequency-independent VEM material is considered, e.g. a material whose dynamic properties are described by the structural damping model, Eq. (4.14) reduces to the following linear form

$$\left[\mathbf{K}^* - \lambda^2\mathbf{M}\right]\mathbf{U}^* = 0 \tag{4.16}$$

The resolution methods of problem Eq. (4.14) (or Eq. (4.16)), as well as the iteration algorithms for the nonlinear counterpart of the generalized eigenvalue problem, are described hereafter.

4.2.1 Complex Eigensolution (CE) approach

The Arnoldi algorithm [144] is being exploited to solve the generalized eigenvalue problem for all the numerical applications treated throughout the thesis. The CE method consists in solving the generalized eigenvalue problem of Eq. (4.16) by considering the complex stiffness matrix $\mathbf{K}^*$ within the Arnoldi algorithm. As a result, the eigenvalues and eigenvector are complex. The complex eigenvalue λ of the $i-$th mode is given by:

$$\lambda_i^2 = \omega_i^2 \left(1 + \mathrm{i}\, \eta_i\right) \tag{4.17}$$

where ω_i is the natural frequency and η_i the modal loss factor. Natural frequencies are defined as the real part of the corresponding eigenvalue:

$$\omega_i = \sqrt{Re\left(\lambda_i^2\right)} \tag{4.18}$$

As far as the modal loss factor is concerned, within the CE method it is simply defined as the ratio between the imaginary part and the real part of the eigenvalue:

$$\eta_i = \frac{Im\left(\lambda_i^2\right)}{Re\left(\lambda_i^2\right)} \tag{4.19}$$

Notwithstanding the complex approach provides an accurate solution, complex eigensolvers require a relevant computational effort.

4.2.2 Iterative Complex Eigensolution (ICE) approach

An iterative CE scheme (ICE) is to be considered for solving Eq. (4.14), i.e. for VEM exhibiting a frequency-dependent behaviour. In this case an even higher computational effort is required since the solver has to seek for complex eigensolutions, for each mode, as many times as requested by the convergence to be achieved. The Iterative Complex Eigensolution (ICE) approach is referred in this thesis [145]. It is based on the fixed-point iteration method and the initial guess of the natural frequencies is obtained by solving the real eigenvalue problem. A detailed representation of the ICE algorithm is given in Algorithm 1. The number of iterations requested for achieving convergence is further discussed.

Algorithm 1 The ICE algorithm for N modes [49].

1: solve Eq. (4.14) with $\omega = 0$: compute $\lambda(0)$ ▷ Initial guess: N real eigenvalues
2: **for** $i = 1 : N$ **do**
3: Initialize the error $\varepsilon = 1$ and the eigenfrequency $\tilde{\omega} = \lambda_i(0)$
4: **while** $\varepsilon > \varepsilon_{tol}$ **do** ▷ used tolerance: $\varepsilon_{tol} = 10^{-6}$
5: solve $[\mathbf{K}^*(\tilde{\omega}) - \lambda^2(\tilde{\omega})\,\mathbf{M}]\mathbf{U}^* = 0$
6: compute the error: $\varepsilon = \dfrac{|\tilde{\omega} - \sqrt{Re(\lambda_i^2(\tilde{\omega}))}|}{\sqrt{Re(\lambda_i^2(\tilde{\omega}))}}$
7: update the eigenfrequency: $\tilde{\omega} = \sqrt{Re(\lambda_i^2(\tilde{\omega}))}$
8: **end while**
9: $\omega_i = \tilde{\omega}$; $\eta_i = \dfrac{Im(\lambda_i^2)}{Re(\lambda_i^2)}$ ▷ converged solution: damped eigenfrequency & modal loss factor
10: **end for**

4.2.3 Modal Strain Energy (MSE) approach

The modal strain energy (MSE) method was introduced as an efficient approach to estimate the modal loss factors of structures hosting viscoelastic damping layers. [146, 147]. Based on the assumption that the undamped modes are representative of the damped system, Johnson and Kienholz [63] proposed a direct method which consist in providing an estimation of the modal damping ratio as the ratio between the storage energy, evaluated from the modal strain energy of the entire structure, and the dissipation energy, calculated from the undamped modal shapes. The storage energy is obtained from Eq. (4.16) upon considering the real part only of the complex stiffness matrix $\mathbf{K}^*$. Thus, the complex eigenvalue problem in Eq. (4.16) reduces to the following real counterpart

$$\left[\mathbf{K}_R - \lambda^2 \mathbf{M}\right] \mathbf{U} = 0 \tag{4.20}$$

where the eigenvalues λ^2 and the eigenvectors $\mathbf{U}$ are real quantities. The modal loss factor, within the MSE approach, is expressed as

$$\eta_i = \frac{\mathbf{u}_i^T \mathbf{K}_I \mathbf{u}_i}{\mathbf{u}_i^T \mathbf{K}_R \mathbf{u}_i} \tag{4.21}$$

where η_i and $\mathbf{u}_i$ are the loss factor and the undamped modal shape of the $i-$th mode. Since the influence of the imaginary modal shapes is neglected, the accuracy of the estimated modal loss factor is strongly affected by the damping properties of VEM and its usage is hence restricted to lightly damped structures.

4.2.4 Iterative Modal Strain Energy (IMSE) approach

An iterative version of the MSE, referred as to IMSE, has been proposed to estimate the damping properties of a structure embedding frequency-dependent viscoelastic layers. The variation of storage and dissipation energy with changed frequency is to be considered in order to obtain an accurate estimation of the modal loss factor. Thus, the initial guess, obtained just like the ICE procedure by considering a nil initial circular frequency, is subsequently updated taking into account the change in stiffness induced by the frequency-dependent VEM. The iterative procedure stops when the requested level of accuracy, set by the chosen tolerance value, is achieved. A representation of the IMSE procedure is given in Algorithm 2.

Algorithm 2 The IMSE algorithm for N modes [49].

1: solve Eq. (4.14) with $\omega = 0$: compute $\lambda(0)$ ▷ Initial guess: N real eigenvalues
2: **for** $i = 1 : N$ **do**
3: Initialize the error $\varepsilon = 1$ and the eigenfrequency $\tilde{\omega} = \lambda_i(0)$
4: **while** $\varepsilon > \varepsilon_{tol}$ **do** ▷ used tolerance: $\varepsilon_{tol} = 10^{-6}$
5: solve $[Re(\mathbf{K}^*(\tilde{\omega})) - \lambda^2(\tilde{\omega})\mathbf{M}]\mathbf{U} = 0$
6: compute the error: $\varepsilon = \dfrac{|\tilde{\omega} - \lambda_i(\tilde{\omega})|}{\lambda_i(\tilde{\omega})}$
7: update the eigenfrequency and modal shape: $\tilde{\omega} = \lambda_i(\tilde{\omega})$; $\mathbf{u}_i = \mathbf{u}_i(\tilde{\omega})$
8: **end while**
9: $\omega_i = \tilde{\omega}$; $\eta_i = \dfrac{\mathbf{u}_i^T Im(\mathbf{K}(\omega_i))\mathbf{u}_i}{\mathbf{u}_i^T Re(\mathbf{K}(\omega_i))\mathbf{u}_i}$ ▷ converged solution: damped eigenfrequency & modal loss factor
10: **end for**

4.2.5 Sandwich beam-plate with polymer core

The viscoelastic sandwich beam-plate (B1-TC) studied in [129, 130, 148] is addressed in order to validate the proposed finite plate element against the dynamic behaviour of slightly to very damped structures. It considers a beam-plate made up of a thin polymer layer (core) constrained by two elastic facesheets. The material and structural data are summarised in Table 4.1. The viscoelastic behaviour of the core is described within the structural damping approach (see Section 4.1.1) and is, therefore, frequency-independent: constant loss factor is taken as $\eta_c \in \{0.1, 0.6, 1, 1.5\}$. Three sublaminates have been employed to discretize the through-thickness behaviour of the sandwich structure, each of them modelled according to FSDT with a unitary shear correction factor. It is worth noting that the three sublaminates approach is, in this case, equivalent to the LW displacement-based GUF model that goes by the acronym LD_{10}. As far as the in-plane discretization is concerned, due to the high length-to-

thickness ratio ($S = 56$) 14 CL8 elements are used along the longitudinal direction ($x-$axis). Only one finite element is used cross the width, so as to allow a direct comparison between the present 2D FE and the 1D models used in the references.

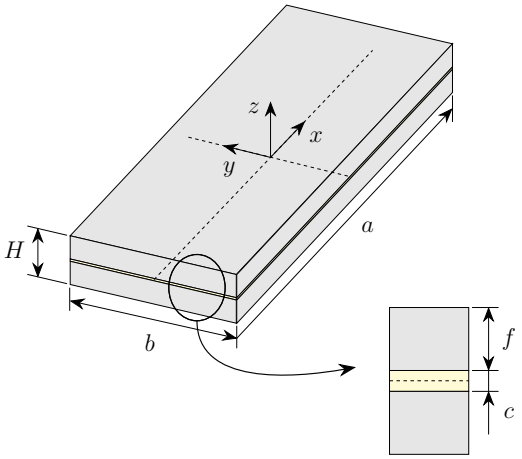

Figure 4.1: B1-TC: Sandwich beam-plate geometry.

Table 4.1: B1-TC: Geometric and material data.

$a = 177.8$ mm; $b = 12.7$ mm
$f = 1.524$; $c = 0.127$ mm; $H = 3.175$ mm

	Core	Facesheet
$\theta\,[^\circ]$	0	0
E_0 [MPa]	1.794	-
E [MPa]	-	69000
ν	0.3	0.3
G_0 [MPa]	0.69	-
G [MPa]	-	26538.5
$\rho\left[\mathrm{kg/m^3}\right]$	968.1	2766

Both CE and MSE resolution methods are investigated. In particular, an attempt to comprehensively establish the application domain of the MSE approach regarding the damped properties of VEM as well as the degree of hyperstaticity is given. Table 4.2 compares the damped eigenfrequencies f and the normalized modal loss factors η/η_c corresponding to the first four vibration modes obtained by the present 2D FE approach against two 1D beam models: the exact analytical formula given by Rao [149], if the simply supported configuration (SFSF) is considered, and the FE solution proposed by Bilasse *et al* in [150] for the cantilever configuration (CFFF). In addition, 2D FE results given by Bilasse in [130] and obtained by resorting to the asymptotic numerical method (ANM), are also listed. A perfect agreement is observed when comparing the results obtained with the present CE approach to those pertaining to one dimensional beam reference models. Furthermore, an accuracy improvement with respect to the FE solution given in [130] may be noted for the vibration modes aside from the fundamental flexural mode. Indeed, the solution provided by Bilasse is shown to slightly overestimate the value of damped eigenfrequencies when compared to present results regardless of boundary conditions set or loss factor of VEM. Concerning the modal loss factor, an opposite behaviour is observed with an underestimation of the modal damping, even though the difference is less noticeable.

Table 4.2: B1-TC: Damped eigenfrequencies and normalized loss factors for the first four vibration modes. Comparison between CE and MSE approaches against the FEM models by Bilasse [130, 150] and the analytical formula given in [149].

	SFSF beam-plate						SS beam		CFFF beam-plate						CF beam	
	Present CE		Present MSE		FEM [130]		Analytical [149]		Present CE		Present MSE		FEM [130]		FEM [150]	
η_c	f [Hz]	η/η_c	Δf [%]	$\Delta\eta$ [%]	f [Hz]	η/η_c	f [Hz]	η/η_c	f [Hz]	η/η_c	Δf [%]	$\Delta\eta$ [%]	f [Hz]	η/η_c	f [Hz]	η/η_c
0.1	148.52	0.3500	0.05	-0.15	148.56	0.3500	148.51	0.3502	64.3	0.281	0.06	-0.43	64.3	0.281	64.1	0.281
	488.70	0.1955	0.01	-0.02	489.28	0.1954	488.47	0.1958	297.4	0.242	0.03	-0.13	298.1	0.242	296.7	0.242
	1035.95	0.1068	0.00	0.00	1038.74	0.1066	1034.69	0.1071	746.4	0.153	0.01	-0.03	749.0	0.153	744.5	0.154
	1799.16	0.0649	0.00	0.03	1807.57	0.0647	1795.13	0.0653	1399.7	0.088	0.00	-0.01	1406.9	0.088	1395.7	0.089
0.6	150.71	0.3327	1.50	-5.37	150.75	0.3327	150.71	0.3329	65.7	0.246	2.22	-14.90	65.7	0.245	65.5	0.246
	489.98	0.1941	0.27	-0.75	490.56	0.1940	489.75	0.1944	299.9	0.232	0.86	-4.49	300.6	0.232	299.2	0.232
	1036.64	0.1066	0.07	-0.18	1039.43	0.1064	1035.38	0.1069	748.2	0.152	0.25	-0.96	750.7	0.152	746.3	0.153
	1799.57	0.0649	0.02	-0.05	1807.99	0.0646	1795.54	0.0652	1400.7	0.088	0.07	-0.36	1407.8	0.088	1396.6	0.089
1	154.43	0.3050	3.87	-14.92	154.47	0.3051	154.42	0.3052	67.6	0.202	5.00	-39.79	67.7	0.202	67.5	0.202
	492.30	0.1915	0.74	-2.09	492.87	0.1914	492.06	0.1918	303.8	0.217	2.13	-11.50	304.5	0.217	303.1	0.218
	1037.90	0.1062	0.19	-0.51	1040.69	0.1060	1036.63	0.1065	751.3	0.150	0.66	-2.60	753.9	0.149	749.4	0.150
	1800.34	0.0648	0.07	-0.16	1808.75	0.0646	1796.30	0.0651	1402.4	0.087	0.19	-0.92	1409.5	0.087	1398.3	0.088
1.5	160.73	0.2625	7.64	-33.57	160.77	0.2625	160.72	0.2626	70.1	0.153	8.36	-84.64	70.2	0.153	69.9	0.153
	496.74	0.1868	1.62	-4.70	497.30	0.1867	496.49	0.1871	309.9	0.197	4.04	-22.89	310.6	0.197	309.1	0.198
	1040.36	0.1055	0.43	-1.15	1043.13	0.1054	1039.07	0.1059	757.2	0.145	1.43	-5.62	759.7	0.145	755.2	0.146
	1801.83	0.0646	0.15	-0.38	1810.23	0.0644	1797.78	0.0650	1405.5	0.087	0.41	-1.85	1412.6	0.086	1401.4	0.087

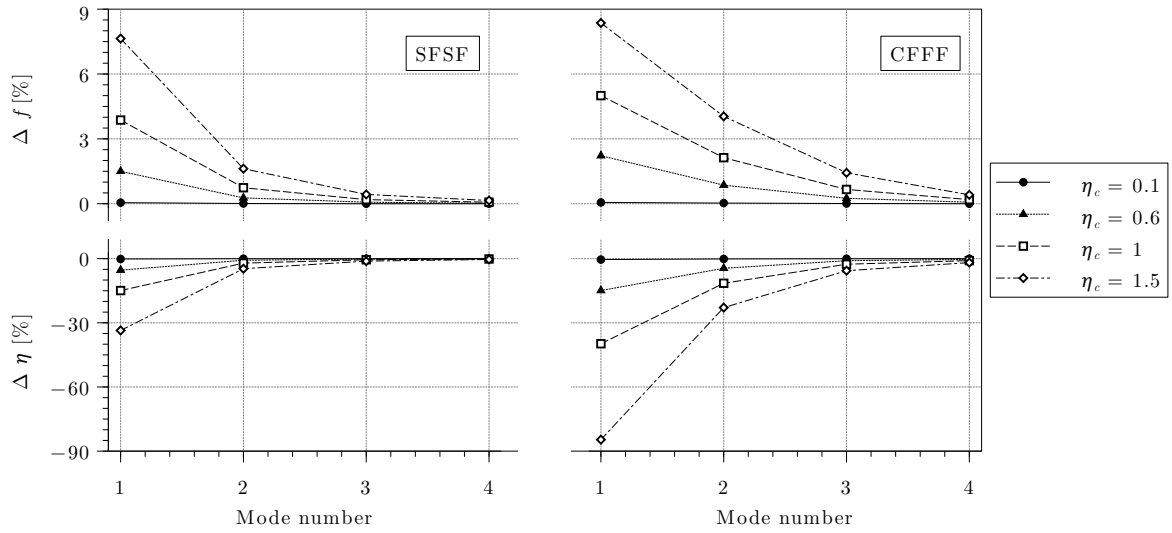

Figure 4.2: B1-TC: Eigenfrequency and modal loss factor percentage errors of the MSE approach compared to the Complex Eigensolution (CE) of the SFSF (left) and CFFF (right).

Table 4.2 reports also the comparison between CE and MSE methods in terms of percentage error related to modal frequencies and loss factor, calculated as

$$\Delta f = \frac{f_{\text{CE}} - f_{\text{MSE}}}{f_{\text{CE}}} \times 100 \qquad \text{and} \qquad \Delta\eta = \frac{\eta_{\text{CE}} - \eta_{\text{MSE}}}{\eta_{\text{CE}}} \times 100 \tag{4.22}$$

The error distributions versus the mode number for four different values of VEM loss factor η_c are plotted in Figure 4.2. Both simply supported and cantilever configurations are investigated. For $\eta_c = 0.1$ the MSE method exactly recovers the eigenfrequencies and modal loss factors obtained with the complex approach. As the material loss factor increases, the use of MSE method leads to non-negligible errors, especially if the firsts eigenmodes are considered. Indeed, the influence of imaginary modal shapes is noteworthy in the low frequency range and becomes less relevant as the frequencies increases. Concerning the two sets of boundary conditions, it is observed that the MSE appears to be more inaccurate in predicting the damped properties in the CFFF configuration rather than the SFSF. Since the damping is essentially due to the shear deformation of the constrained VEM, this increased inaccuracy is attributed to the different relevance of transverse shear strain energy in the two configurations. This phenomenon mostly affects the modal loss factor with an increase of roughly 60% of error between the two SFSF and CFFF configurations. This analysis leads to the conclusion that, as computationally efficient as the MSE method is, a CE approach is to be considered for highly damped structures especially if an accurate prediction of the modal loss factor is sought. The MSE method remains a viable option for slightly damped structure, providing an accurate solution while drastically reducing

the computational cost of the analysis when compared to the complex eigensolvers [49].

4.2.6 Triple-core Sandwich Panel

The present FE is next applied to a triple-core sandwich structure designed by the *Garteur* consortium, and therefore referred to as Garteur-TestCase (G-TC), and addressed to noise reduction essentially in helicopter cabins. Benchmark studies have been carried out by Simon *et al* with a view to assessing mathematical and numerical approaches to describe the vibro-acoustic behaviour of helicopter trim-panels [131]. In particular, the SGUF within the weak-form solution obtained by the Ritz method has been proved to be a reliable tool for acoustic transmission loss estimation. In addition, D'Ottavio *et al* has broadened the investigation conducted in [131] to refined kinematics models. As a result, high-order theories turn out to be necessary if a proper and comprehensive characterization of the dynamic behaviour is sought [49]. In the following, results obtained with the present FE will be compared with those given in [49], providing a validation of the proposed plate element in handling unconventional panel configurations. Some additional consideration will be also made about the influence of FE discretization on the dynamic response.

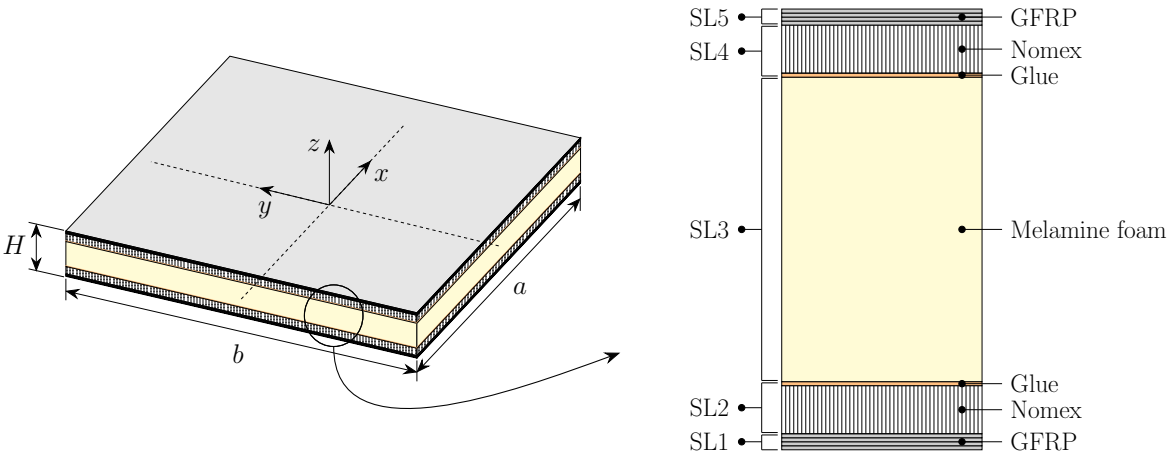

Figure 4.3: G-TC: Geometry and composite stack of the triple-core sandwich panel. Idealization of the whole stack into five sublaminates.

The G-TC considers a fully clamped (CCCC) square panel made up of 13 plies forming a triple-core sandwich. The composite stack arrangement is illustrated in Figure 4.3 and summarized in Table 3.3 along with the geometric and viscoelastic material data. The stiffness of the panel is mainly given by the outer facesheets made up of a set of 4 glass fabric (GFRP) plies, whereas the damping properties are obtained

Table 4.3: G-TC: Geometric/material data and stacking sequence of the triple-core sandwich panel.

$a = b = 840$ mm; $H = 21.68$ mm									
Material (ply no.)	h_p	$E_{11} = E_{22}$ [MPa]	E_{33} [MPa]	ν	G_{11} [MPa]	G_{22} [MPa]	G_{33} [MPa]	η	$\rho\left[\mathrm{kg/m^3}\right]$
GFRP $(1-4;\ 10-13)$	0.275	21000	21000	0.13	3000	3000	3000	0.01	1600
Nomex (5; 9)	3	1	330	0	1	85	38	0.05	96
Glue (6; 8)	0.240	1.950	1.950	0.4	700	700	700	0.01	1050
Melamine foam (7)	13	0.5	0.23	0	0.065	0.065	0.065	0.1	11.7

by embedding a melamine foam core glued between two nomex honeycomb cores. The elastic properties are given in the laminate reference frame so each layer is assumed to be oriented at 0°. It is worth noticing that no Poisson coupling is assumed in the nomex plies nor in the melamine foam. Frequency-independent loss factors are considered for all the materials. The considerations outlined in [48] have driven the idealization of the stack into five sublaminates, as shown in Figure 4.3: the outer glass fabric layers are regrouped into one sublaminate modelled according to FSDT with reduced stiffness coefficients; a single sublaminate with a LD_{10} theory is used for the nomex and glue layers; the melamine foam core forms the 3^{th} sublaminate for which 3 different plate theories will be used: FSDT, ED_{12} and ED_{32}.

Following the notation used in [49], the 3 different kinematic models for the melamine foam core are hereinafter referred to as $\mathrm{MF}\{1,0\}$, $\mathrm{MF}\{1,2\}$ and $\mathrm{MF}\{3,2\}$. FSDT and ED_{12} plate theories involve a shear correction factor of $\kappa^2 = 5/6$ to enhance the

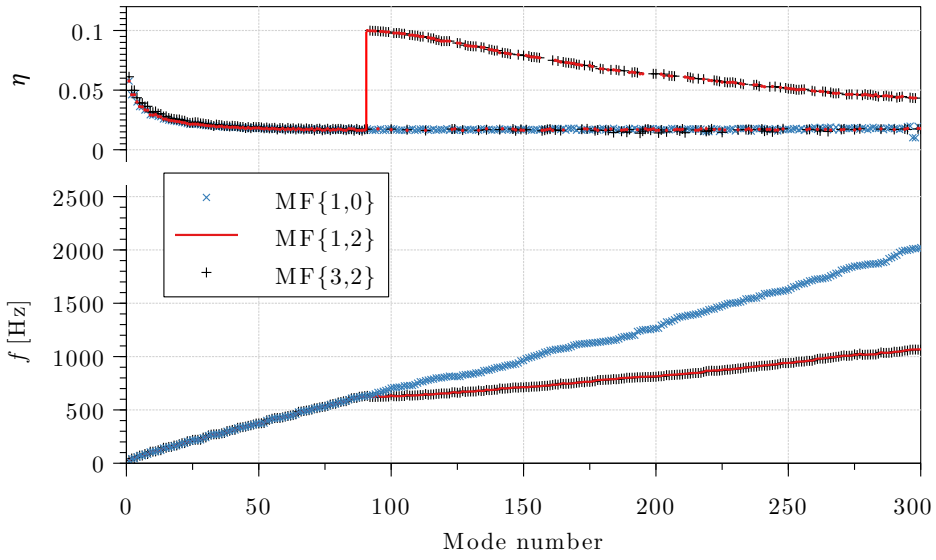

Figure 4.4: G-TC: Frequency and modal loss factor distributions corresponding to the first 300 vibration modes of the CCCC triple-core panel for three different kinematic models used for the melamine foam core.

numerical predictions especially in the low frequency range. As far as the in-plane discretization is concerned, a mesh of 16 CL8 elements for the four edges of the panel is employed.

Figure 4.4 reports the first 300 eigenfrequencies for the 3 plate theories adopted for the melamine foam. Starting from a frequency value of approximately 620 Hz, a change of slope is observed for the models retaining a three-dimensional constitutive law. This results in increased loss factor due to the presence of thickness modes associated to the melamine foam stretch. From this point onwards, both short-wave in-plane modes and long-wave thickness modes coexist increasing the so-called *modal-density*. Obviously, a mode involving thickness-wise effects can not be grasped by the bi-dimensional model MF$\{1, 0\}$, whose modal density remains constant over the whole frequency range.

Furthermore, the use of a higher-order approximation for the in-plane displacement

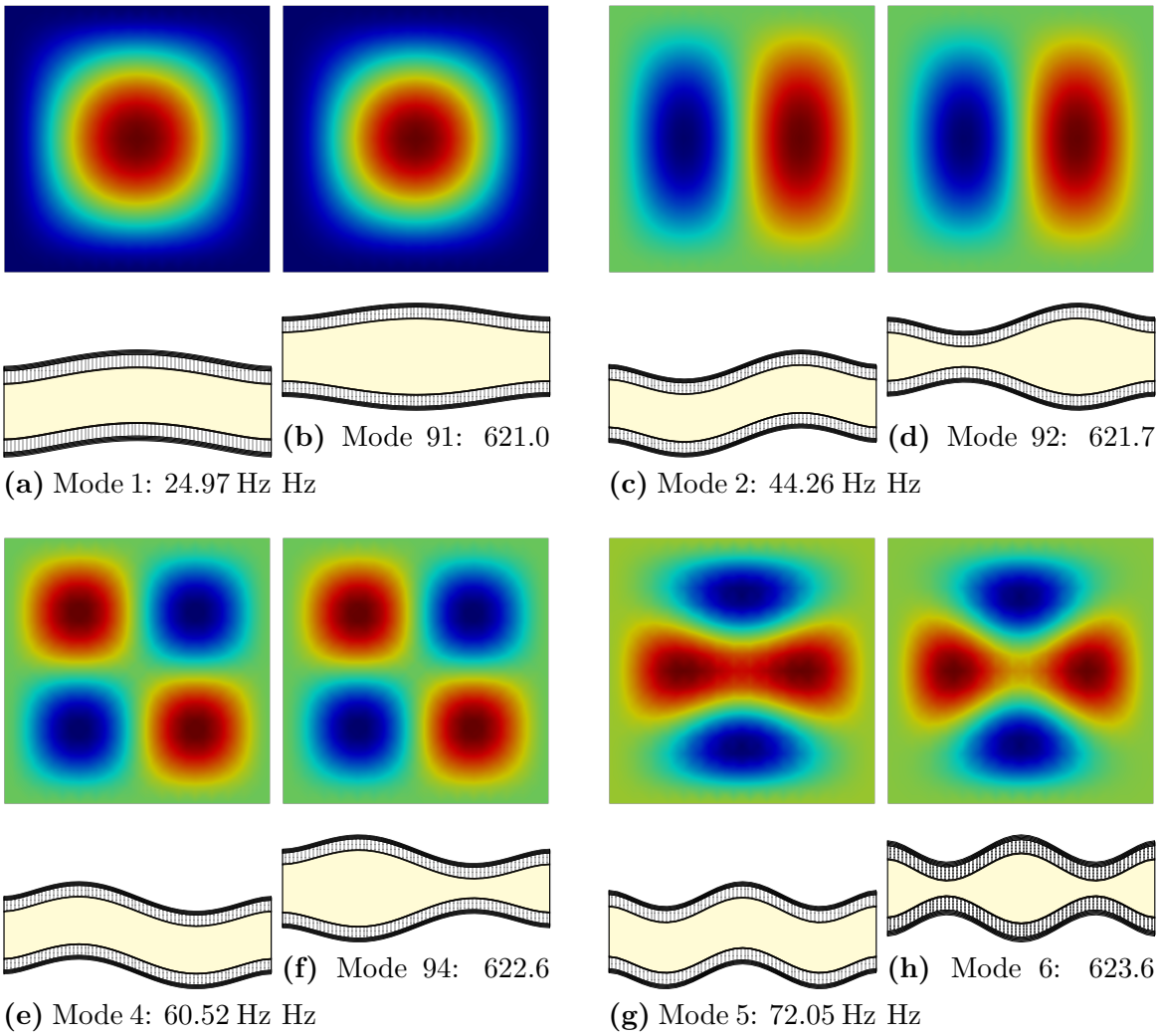

(a) Mode 1: 24.97 Hz Hz **(b)** Mode 91: 621.0 **(c)** Mode 2: 44.26 Hz Hz **(d)** Mode 92: 621.7 **(e)** Mode 4: 60.52 Hz Hz **(f)** Mode 94: 622.6 **(g)** Mode 5: 72.05 Hz Hz **(h)** Mode 6: 623.6

Figure 4.5: G-TC: Modal shapes comparison between couples of modes exhibiting the same in-plane pattern but a different behaviour along the thickness direction.

does not result in any significant benefit since the MF$\{1,2\}$ and MF$\{3,2\}$ overlap perfectly. As far as the modal loss factor is concerned, it is worth emphasising that starting from the transition frequency value, the modes involving a change of the melamine foam thickness become predominant, thus a jump in the modal loss factor distribution in Figure 4.4 (top) is experienced to get to the material loss factor of the melamine foam.

Figure 4.5 shows the in-plane pattern and cross-sectional view for 4 couples of modes sharing the same number of half-waves along the in-plane directions. Despite each couple has a similar in-plane pattern, a completely different behaviour is observed along the thickness direction. As already discussed, from a frequency of 621 Hz the modes start involving a significant transverse deformation of the melamine foam core as clearly shown by modal shape cross-sections (where the melamine foam core is shaded in yellow for the sake of clarity).

Finally, Figure 4.6 shows the modal distribution of both frequency and modal loss factor for four different meshes compared to the converged Ritz solution obtained with an expansion order of 26 in both directions [49]. The convergence analysis has been carried out for the MF$\{1,2\}$ model. As expected, a coarse FE discretization skips several vibration modes, resulting in a steeper modal distribution. As the number of elements increases, a flatter curve is obtained until a near-perfect overlapping of FE and Ritz solutions when convergence is achieved. It is worth noting that, notwithstanding the chosen in-plane discretization, the frequency value corresponding to the transition is

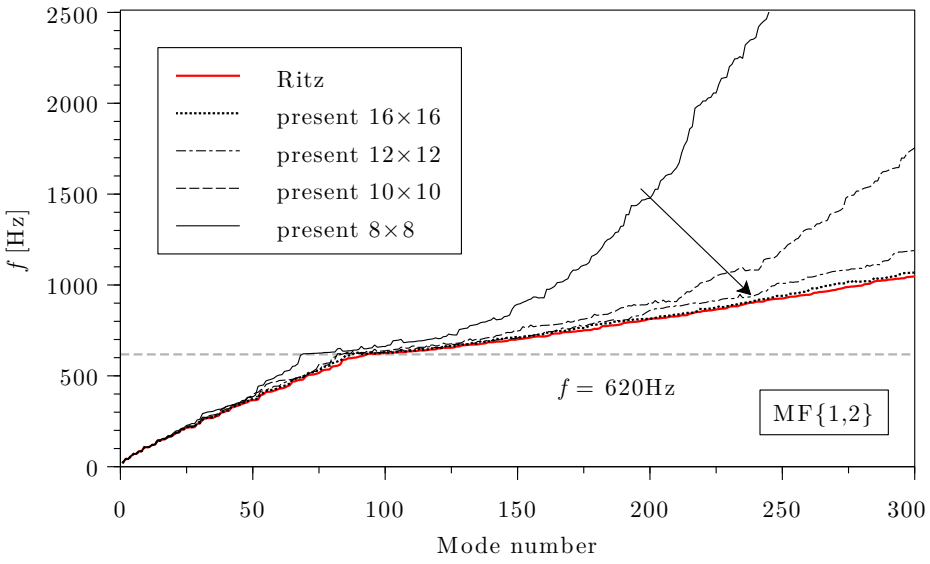

Figure 4.6: G-TC: Convergence analysis of the present FE with respect to Ritz solution with $R = S = 26$.

accurately recovered. This represents a valuable information at the preliminary design stage to establish the frequency range where long-wave thickness modes are expected to appear.

4.2.7 Sandwich plate with frequency-dependent core

The capability of the present FE of dealing with frequency-dependent VEM are evaluated by referring to the sandwich plate investigated by Bilasse *et al.* in [49, 130] and referred to as B2-TC. It considers a very thin rectangular plate ($a/H \approx 196$) made up of two stiff elastic skins which constrain a thin layer of isotropic and frequency-dependent 3M-ISD112 VEM. The geometric and elastic material data are summarized in Table 4.4. The ADF approach (see Section 4.1.2) is used to model the frequency-dependent elastic moduli of the 3M-ISD112 material. In particular, the 6-parameters model (3 anelastic fields, each requiring 2 parameters), referred to hereinafter as ADF-3 and defined in Table 4.5, provides an accurate representation of the VEM damped properties in the frequency range of interest[151] and therefore it will be addressed for the present analysis. It is worth noting that, since the viscoelastic properties are strongly affected by the working temperature, the parameters defining the frequency-dependent behaviour of VEM must be identified in a specific temperature range. For the present analysis a temperature of 27°C is considered.

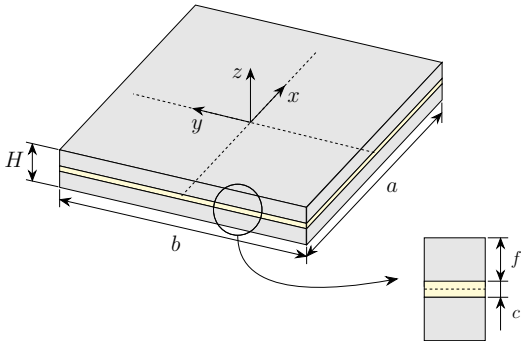

Figure 4.7: B2-TC: Sandwich plate geometry.

Table 4.4: B2-TC: Geometric and material data.

$a = 348$ mm; $b = 304.8$ mm $f = 0.762$ mm; $c = 0.254$ mm; $H = 1.778$ mm		
	3M-ISD122 (27°C)	Facesheet
E_0 [MPa]	1.794	-
E [MPa]	-	68900
ν	0.5	0.3
G_0 [MPa]	0.5	-
G [MPa]	-	26500
$\rho \left[\text{kg/m}^3\right]$	1600	2740

In the first place, a convergence analysis with respect to the FE discretization is performed for both CCCC and CFCF sets of boundary conditions where the iterative CE (ICE) procedure detailed in Section 4.2.2 has been used to solve the nonlinear eigenvalue problem. A three-sublaminates idealization of the composite stack is assumed.

Table 4.5: B2-TC: Maxwell series terms at 27°C of the 3M-ISD112 viscoelastic material [55].

j	Δ_j	Ω_j
1	0.746	468.7
2	3.265	4742.4
3	43.284	71532.5

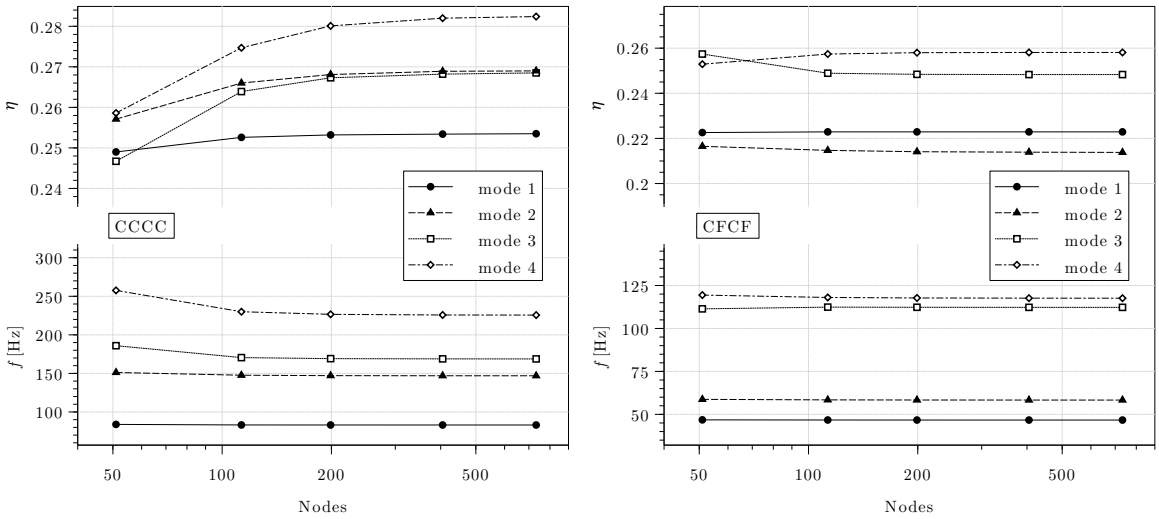

Figure 4.8: B2-TC: FE Convergence rate of the viscoelastic response (f, η) for the first 4 vibration modes of the CCCC (left) and CFCF (right) sandwich panel.

Each sublaminate is modelled according to FSDT kinematics with reduced stiffness coefficients. Indeed, no significant thickness-wise effects are experienced due to the slenderness of the sandwich panel. On the other hand, the high length-to-thickness ratio calls for the CL8 quadratic element to avoid locking pathology. Figure 4.8 shows the convergence rate of the damped eigenfrequency and modal loss factor versus the number of nodes, in semi-logarithmic scale, for the first 4 vibration modes of the CCCC (left) and CFCF (right) sandwich panel. Plate boundary conditions and modal number notwithstanding, the damped frequency converges very quickly and a value of 113 nodes turns out to be sufficient, corresponding to a 6×5 mesh (in x and y directions, respectively). However, a finer mesh is required for the modal loss factor to converge. Moreover, the convergence rate strongly depends on mode number and considered boundary condition. Indeed, the 4^{th} mode of the CCCC configuration needs a 16×14 quadratic elements for the modal loss factor of to converge. This accuracy comes along a significant increase in computational cost which must be taken into account especially if an iterative solver is involved.

Table 4.6 compares the undamped f_0 and damped f eigenfrequencies and modal

Table 4.6: B2-TC: Undamped and damped eigenfrequencies and modal loss factors for the first four vibration modes of the CFCF and CCCC sandwich plate with a frequency-dependent core's modulus. Comparison between the iterative procedures ICE and MSE against the Ritz solution given in [49].

	Present ICE			Present IMSE				Ritz ADF-3 [49]		
BC	f_0 [Hz]	f [Hz]	η	f [Hz]	η	Δf [%]	$\Delta\eta$ [%]	f_0 [Hz]	f [Hz]	η
CFCF	44.26	46.69	0.223	46.00	0.231	1.48	-3.81	44.26	46.69	0.223
	54.86	58.32	0.214	57.37	0.225	1.63	-5.38	54.87	58.33	0.214
	100.43	112.28	0.248	108.86	0.279	3.05	-12.28	100.43	112.28	0.248
	107.46	117.61	0.258	115.68	0.270	1.64	-4.49	107.46	117.61	0.258
CCCC	76.57	83.10	0.253	81.69	0.265	1.70	-4.46	76.57	83.10	0.253
	133.50	146.92	0.269	144.44	0.281	1.69	-4.31	133.49	146.91	0.269
	153.54	168.78	0.268	166.05	0.279	1.62	-4.06	153.52	168.76	0.269
	204.40	225.63	0.282	221.81	0.294	1.69	-4.00	204.34	225.59	0.283

loss factors η obtained by the present FE approach with both ICE and IMSE procedures to those given by D'Ottavio with the Ritz approach in [49] for the two sets of boundary conditions previously investigated. The undamped eigenfrequency f_0 is obtained by solving the eigenvalue problem of Eq. (4.14) under the assumption $\omega = 0$. The converged value of the eigenfrequency at the end of the iterative process is labelled as f. For the sake of comparison, the reference Ritz solution listed in Table 4.6 refers to the same ADF-3 model and the ICE procedure and involves an expansion order of 10 in both x and y directions ($R = S = 10$). Relying on the previous convergence analysis, a 16×14 mesh has been employed to ensure a FE converged solution. A perfect agreement is found between the present FE approach and the Ritz solution. The percentage differences between the damped properties obtained with the IMSE and those calculated by exploiting the ICE procedure are also reported in Table 4.6. A quite acceptable approximation is obtained for both damped eigenfrequency and modal loss factor at the end of the iterative procedure, with a percent error which sticks around 1.5% and 4%, respectively. The 3^{th} mode is seen to deviate from this trend, leading to a non-negligible increase in the percent error when adopting the IMSE method. This phenomenon may be explained by the strong coupling experienced for this mode for which the contribution of the imaginary modal shape can not be neglected. It is worth underlying the number of iterations required by the two implemented iterative procedures: assuming a tolerance value of $\varepsilon_{tol} = 1e^{-6}$, the ICE needs 6 iterations to converge, whereas only 5 iterations appears to be sufficient for the IMSE procedure. As mentioned in [49], Ritz method required 7 iterations, if the ICE procedure is considered and 6 for the IMSE. The gap of one iteration between the two procedures is retained,

but the Ritz method appears to converge more slowly with respect to the present FE approach.

4.3 Frequency Response Function (FRF) of Viscoelastic Sandwich Panels

The semi-discrete dynamic equilibrium equations of a system hosting viscoelastic damping plies within the framework of finite element method reads

$$\mathbf{M}\ddot{\mathbf{u}}(t) + [\mathbf{K}_R(\omega) + \mathrm{i}\,\mathbf{K}_I(\omega)]\,\mathbf{u}(t) = \mathbf{f}(t) \tag{4.23}$$

It is worth mentioning that in Eq. (4.23) the only source of damping is given by the imaginary part of stiffness matrix, i.e. no damping proportional to the velocity is considered. Assuming an harmonic load in the form

$$\mathbf{f}(t) = \mathbf{F}e^{\mathrm{i}\,\omega t} \tag{4.24}$$

where $\mathbf{F}$ is the constant amplitude vector, the steady state harmonic response can be written as

$$\mathbf{u}(t) = \mathbf{U}^*(\omega)\,e^{\mathrm{i}\,\omega t} \tag{4.25}$$

where $\mathbf{U}^*(\omega)$ is the complex generalized displacement vector. Substituting Eq. (4.25) and Eq. (4.24) into Eq. (4.23) yields

$$\left[\mathbf{K}_R(\omega) + \mathrm{i}\,\mathbf{K}_I(\omega) - \omega^2\mathbf{M}\right]\mathbf{U}^*(\omega) = \mathbf{F} \tag{4.26}$$

The Direct Frequency Response (DFR) consist in solving the algebraic system in Eq. (4.26) for each value of frequency the frequency range of interest is discretised into, providing the entire response of the system in the frequency domain. This criterion is employed to build the Frequency Response Function (FRF), particularly useful to quantify the response of the system to a specific excitation. The FRF is obtained from Eq. (4.26) considering a single input (external excitation) F_i applied at $i-$th DOF, and a single output (a displacement) U_o^* corresponding to the $o-$th DOF and solving the algebraic system of equations for all the values of frequency in the bandwidth of interest

$$\left[\mathbf{K}_R(\omega_l) + \mathrm{i}\,\mathbf{K}_I(\omega_l) - \omega_l^2\mathbf{M}\right]\mathbf{U}^*(\omega_l) = \mathbf{F}_i \tag{4.27}$$

Based on the specific application, the receptance FRF is evaluated as

$$H_{oi}(\omega_l) = \frac{U_o^*(\omega_l)}{F_i} \tag{4.28}$$

or in decibel

$$H_{oi}(\omega_l) = 20\log_{10}\left|\frac{U_o^*(\omega_l)}{F_i}\right| \tag{4.29}$$

where F_i is the only non-zero component of the amplitude vector and $U_o^*(\omega_l)$ is the displacement measured at $o-$th DOF of the vector $\mathbf{U}^*(\omega_l)$. Figure 4.9 illustrates the flow diagram, which is merely a representation of the implemented algorithm, allowing to generate the frequency response function of the system.

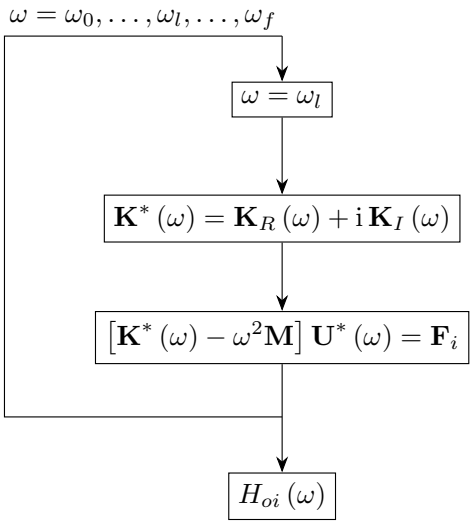

Figure 4.9: Frequency Response Function evaluation algorithm [145].

4.3.1 Harmonic analysis of sandwich plate with frequency-dependent core

The same case study of Section 4.2.7 involving the frequency-dependent 3M-ISD112 VEM is addressed to provide further insights about the capability of the developed FE numerical tool. This time the sandwich panel, whose geometric and material data are given in Table 4.4, is simply supported on the four edges (SSSS) and subjected to a harmonic point load excitation of amplitude $F = -2$ kN acting at the top surface at point $P(-a/4, -b/4, H/2)$ as shown in Figure 4.10. A converged mesh involving 8 CL8 elements in both x and y directions is employed. Figure 4.11 shows the damped dynamic response of the sandwich panel in the frequency band $f \in [0, 300]$ Hz. The receptance FRF, expressed in decibel, is evaluated in terms of transverse displacement u_z, measured at the bottom surface of the plate and at the same in-plane coordinates of the applied harmonic excitation. The present FE solution is compared to converged Ritz solution given by D'Ottavio *et al.* [49] and to results obtained by Bilasse et Oguamanam [152]. In particular, only the resonance and anti-resonance frequency values are extrapolated from the curves given in [152]. The solution of Ref.[152] is obtained by assuming the face sheets to be modelled according to the

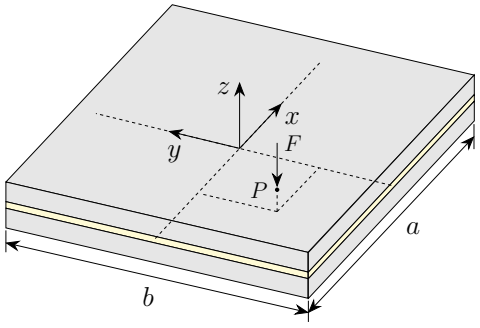

Figure 4.10: B2-TC: Simply supported sandwich plate with 3M ISD112 frequency-dependent core subjected to a harmonic point load excitation.

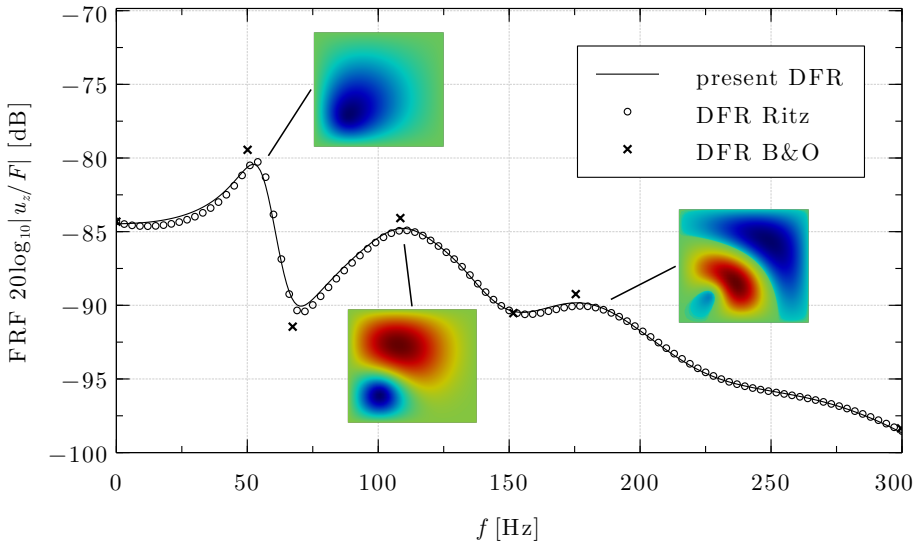

Figure 4.11: B2-TC: Frequency Response Function (FRF) of the simply supported sandwich panel with 3M ISD112 frequency-dependent core for a bandwidth of 300 Hz.

classical Kirchhoff-Love plate theory, whilst the FSDT is used for the core. A refined FE mesh resulting in a number of DOF equal to 5887 is employed in Ref.[152]. It is worth noticing that Bilasse and Oguamanam's solution is based on the assumption that the damped eigenfrequency may be approximated by the undamped value obtained by solving the corresponding real generalized eigenvalue problem. All results are obtained with the DFR detailed in Section 4.2 by assuming the frequency dependence of VEM properties to be described according to the ADF-3 model. Figure 4.11 comes along with further information about the modal shape corresponding to each resonant peak. The position of the harmonic excitation triggers a specific set of modes characterized by a non-nil vertical deflection of the point right where the load is applied. Over the frequency band, a sort of pattern which involves an increasing number of half-waves along the in-plane directions with increased peak number can be recognised. A very

good agreement is found between the present FE approach and both Ritz and Bilasse and Oguamanam' solutions, providing a validation of the numerical tool in dealing with the forced vibrations of damped sandwich structures.

4.3.2 FRF of viscoelastic sandwich beam with SVDT core

The harmonic response of a three-layered sandwich beam is investigated in this section by referring to the problem studied by Cortés *et al.* [153] and, therefore referred to as Cortés-TestCase (C-TC). The sandwich beam consists of two constraining metallic layers enclosing an isotropic and frequency-dependent viscoelastic core made up of *Soundown Vibration Damping Tile* (SVDT) material. The dimensions and material properties of the beam are presented in Table 4.7 and illustrated in Figure 4.12.

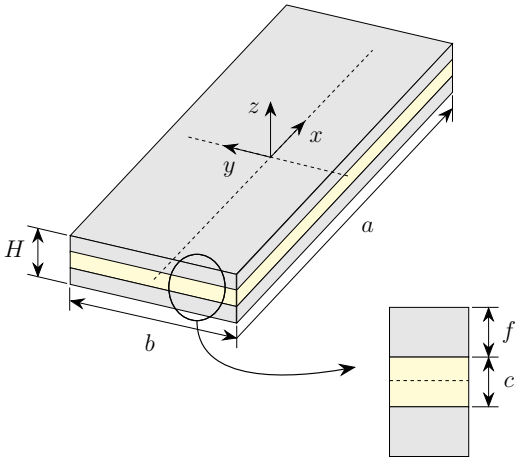

Figure 4.12: C-TC: Sandwich beam-plate geometry.

Table 4.7: C-TC: Geometric and material data.

$a = 200$ mm; $b = 20$ mm		
$f = 1$; $c = \{1, 5, 10\}$ mm		
$H = \{3, 7, 12\}$ mm		
	Core (SVDT)	Facesheet
E_0 [MPa]	353	-
E [MPa]	-	176200
ν	0.45	0.3
G_0 [MPa]	121.7	-
G [MPa]	-	67769
$\rho \left[\text{kg/m}^3\right]$	1423	7782

The frequency-dependence of VEM elastic properties is represented by the four parameters fractional derivative Zener (FDZ) model described in Section 4.1.3. The complex Young's modulus is hence written as:

$$E^* = \frac{E_0 + E_\infty \left(\mathrm{i}\,\omega\tau\right)^\alpha}{1 + \left(\mathrm{i}\,\omega\tau\right)^\alpha} \tag{4.30}$$

The parameters $E_0, E_{inf}, \tau, \alpha$ are obtained by fitting the experimental data of the storage modulus and loss factor identified by Cortés and Elejabarrieta [153, 154]. Their values are summarised in Table 4.8. Cortés *et al.* employ a plane beam model, for which 3D solutions are obtained by discretizing the sandwich cross-section (the $(xz)-$plane) with plane stress elements. A converged mesh involving 60 four-node bilinear elements

Table 4.8: C-TC: Parameters of the FDZ model employed for the frequency-dependent viscoelastic core.

E_0 [MPa]	E_∞ [MPa]	τ [μs]	α
353	3462	314.9	0.873

along the longitudinal direction of the beam is considered. An accurate description of the through-thickness displacement and stress field is ensured by using 4 elements along the thickness direction for each layer. Based on that, 793 nodes and 1586 DOF are associated to the FE model. On the other hand, a beam-plate approach is proposed within the present FE framework where only one finite plate element is used to discretize the beam width ($y-$direction). Concerning the longitudinal direction of the beam, 20 CL8 elements have shown to provide the desired level of accuracy for the mesh to be considered converged. Consequently, 103 nodes are associated to the mesh. The validation of the present FE approach is carried out by assuming a layerwise FSDT description (LD_{10}) of the multilayered structure. The theory-related number of DOFs associated to this model is 9, resulting in a total number of DOFs of 927.

The first analysis is about the dynamic response of the cantilever sandwich beam subjected to a harmonic unitary point load excitation acting oat the bottom surface at point $P\,(-a/2, 0, -H/2)$, as shown in Figure 4.13. The response is evaluated in terms

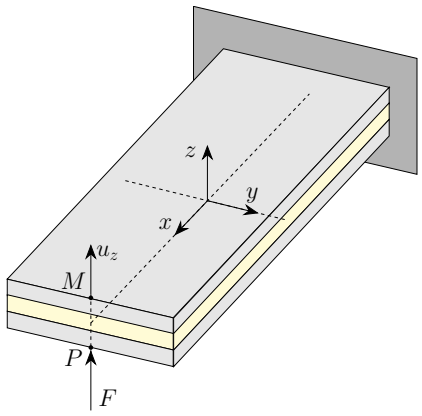

Figure 4.13: C-TC: Cantilever three-layered sandwich beam with SVDT core layer subjected to a harmonic unitary point load excitation.

of the transverse displacement u_z measured at the same in-plane coordinates of the point P but at the top surface (point M in Figure 4.13). Since a unitary amplitude is considered for the harmonic excitation, the transverse displacement and the unique non-nil element of the FRF receptance matrix have the same value. The influence of the VEM layer on the dynamic behaviour of the three-layered sandwich beam is

studied regarding the thickness of the viscoelastic core layer. Three thicknesses for the SVDT material layer are therefore considered, spanning from thin $c = 1$ mm to very thick $c = 10$ mm with an intermediate value of $c = 5$ mm.

Figure 4.14 plots the transverse displacement in logarithmic scale observed at point M (see Figure 4.13) for the three different thicknesses of the core layer in the frequency band $[0 - 4]$ kHz. The present FE results are seen to be in perfect agreement with the

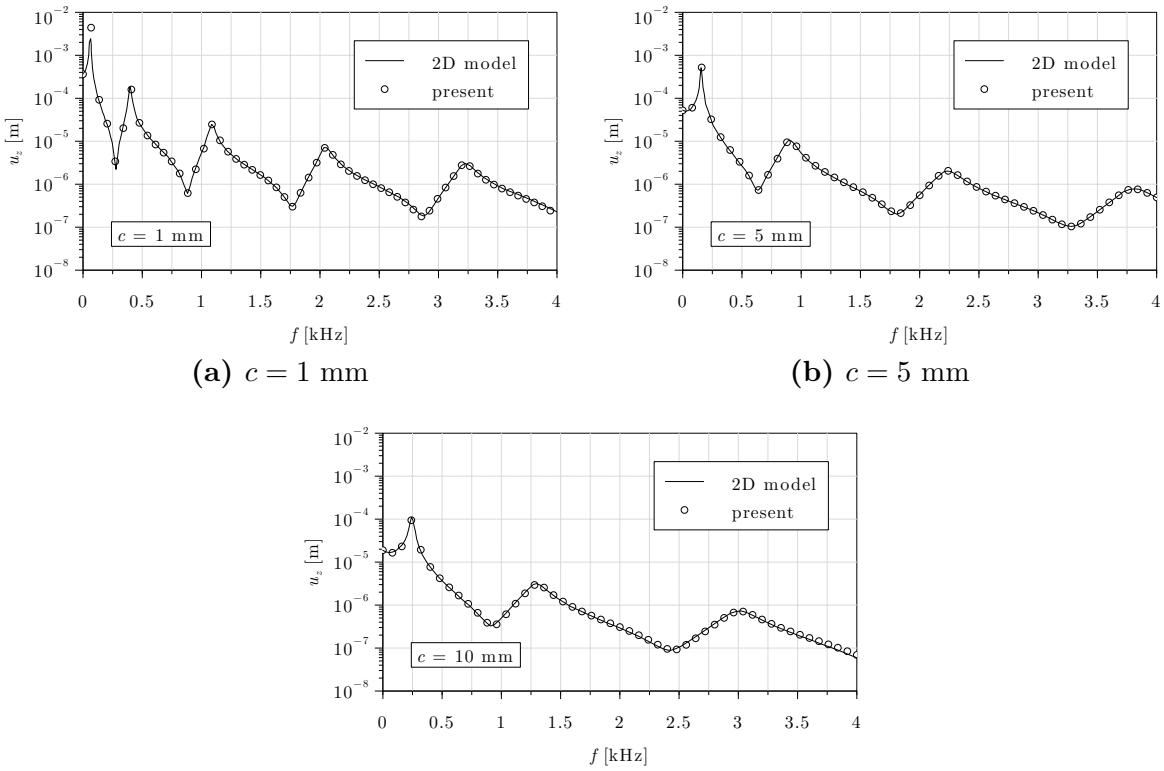

(a) $c = 1$ mm **(b)** $c = 5$ mm

(c) $c = 10$ mm

Figure 4.14: C-TC: Frequency response function for the cantilever sandwich beam and three different thicknesses of the SVDT core: (a) $c = 1$ mm, (b) $c = 5$ mm, (c) $c = 10$ mm.

2D model given by Cortés *et al.* in [153], providing a validation of the present beam-plate approach. As expected, increasing the thickness of the core results in decreasing the amplitude of the response as well as the number of resonance frequencies due to the additional stiffness of the sandwich structure.

The second analysis sets the focus on establishing the nature and extent of elastic properties of the viscoelastic core in affecting the dynamic response of the three-layered sandwich beam. For this purpose, three different facesheet-to-core stiffness ratios are investigated. In particular, the complex modulus of the viscoelastic core layer is obtained from Eq. (4.30) upon multiplying by a factor of 10^0, 10^{-2} and 10^{-4} and referred to as *hard*, *moderately hard* and *soft* core, respectively. As far as the plate theory is

concerned, a sublaminate idealization of the multilayered structure is considered in addition to the LD_{10} theory previously used. The bottom and top skins are still modelled according to FSDT, but this time the transverse displacement in the core layer is assumed to be quadratic along the thickness direction in order to retain the 3D constitutive law without introducing the Poisson locking. The acronym associated to this model is hence FSDT/ED_{12}. Figure 4.15 compares the transverse displacement measured at point M for the three elastic properties and thicknesses values used for the core layer in the frequency band $[0-4]$ kHz. The thickness of the viscoelastic layer notwithstanding, no differences are noticed between LD_{10} and FSDT/ED_{12} throughout the whole frequency band of interest when the structure hosts the hard core. Indeed, as long as the facesheet-to-core stiffness ratio is low, the thickness-wise deformation of the core is negligible, yielding an equivalence of LD_{10} and FSDT/ED_{12} theories. As the stiffness of the viscoelastic layer decreases, the curve pertaining to the plane-stress model of the core starts deviating from the FSDT/ED_{12} one. This effect is more pronounced as the thickness of the core increase. Concerning the soft core, it is worth noticing that the response is merely affected by the choice of the plate theory when the thin core case is considered (Figure 4.15a). On the other hand, if a quadratic transverse displacement is considered, the additional damping introduced by the increased thickness results in a much more flat FRF where the peaks appear to be rounded-off. In addition, at high frequencies both in-plane and long-wave thickness modes coexist leading to a higher modal density, as it can be observed in Figure 4.15c. The LD_{10} theory being unable to grasp the thickness modes associated to the stretch of the core is seen to have a lower number of peaks than the FSDT/ED_{12}.

To sum up, pure three-dimensional effects arise with increased thickness and facesheet-to-core stiffness ratio especially in the higher frequency band. As a result, the plane stress assumption underlying the FSDT turns out to be inadequate to accurately describe these thickness-wise effects. Refined theories, retaining a fully three-dimensional constitutive law, are therefore required to correctly grasp the damped behaviour of sandwich structures hosting a very soft and thick viscoelastic layer. The variable kinematics approach allows hence to adapt the computational model to the problem considered.

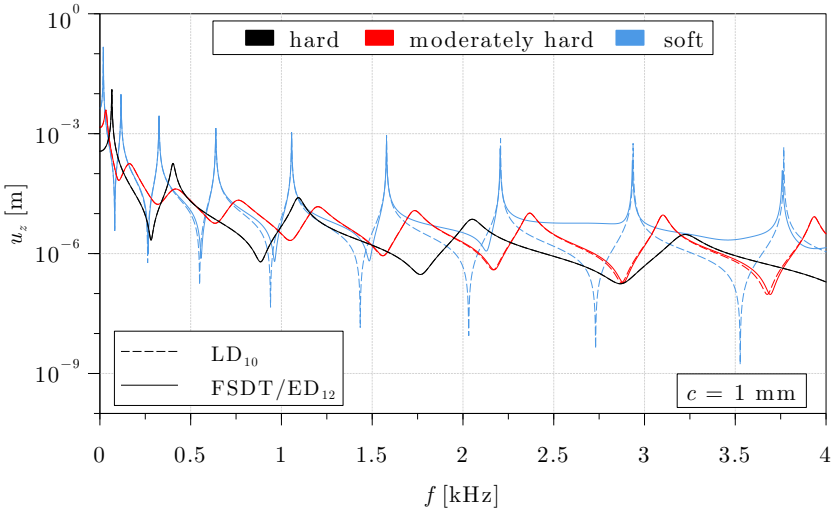

(a) $c = 1$ mm

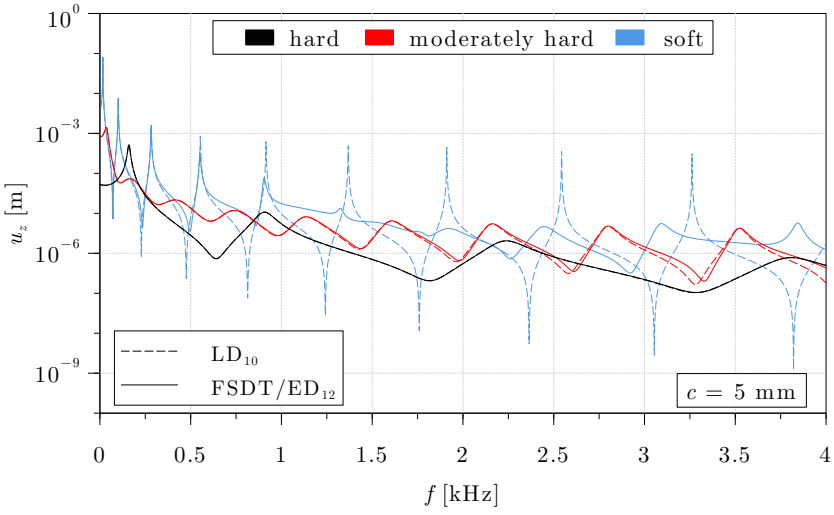

(b) $c = 5$ mm

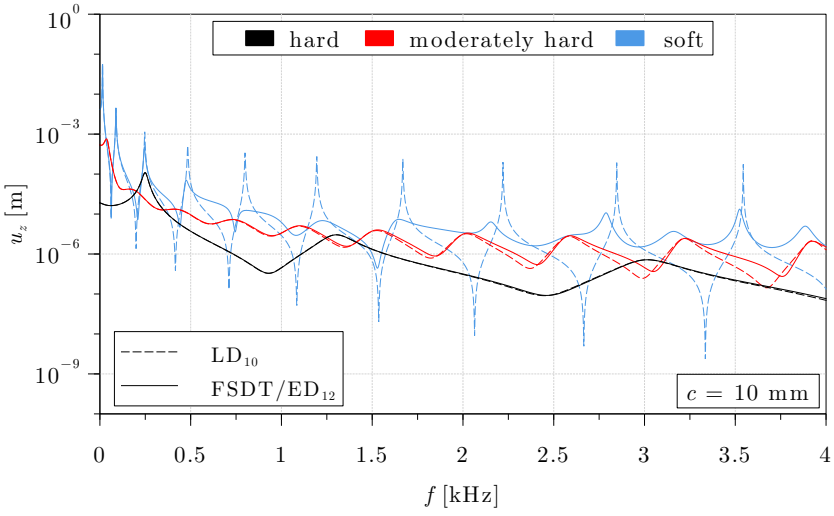

(c) $c = 10$ mm

Figure 4.15: C-TC: Frequency response function of the cantilever sandwich beam plate with soft-moderately hard-hard core. Three different thicknesses of the SVDT material core are studied: (a) $c = 1$ mm, (b) $c = 5$ mm, (c) $c = 10$ mm

Chapter 5

Linearised Stability Analysis

Contents

The global and local instability phenomena of multilayered structures under different loading conditions are discussed in this chapter. Particular emphasis is placed on the failure mechanisms of sandwich panels due to compressive stress. The variational framework of the classical linearised stability analysis for the present variable kinematics approach is derived in the first section. A first validation is given by addressing the overall buckling of a symmetric cross-ply laminate under a uniaxial compression [155]. This case study is also used to assess the influence of von Kàrmàn's assumptions on buckling loads prediction. Local instabilities (wrinkles) are addressed in the last section. This failure mechanism concerns the face sheets of sandwich panels and it is characterized by a half-wavelength of the order of the panel thickness or smaller. Therefore, a very fine FE mesh is in general required.

5.1 Extension of SGUF to geometrical nonlinearities

The general framework for a geometrically nonlinear analysis is first presented, which will be subsequently simplified to derive the initial "geometrical" stress matrix required for conducting the classical linearized buckling analysis.

A Total Lagrangean approach is adopted, in which the deformation of the body is described in terms of Cartesian coordinates x_i used to define the geometry in the initial (undeformed) configuration, Displacements and their gradients are defined with respect to the Cartesian axis x_i. Strains and stresses are thus referred to the initial configuration and the integrals are accordingly evaluated with respect to the initial volume V^0 and bounding surfaces $S^0 = \partial V^0$. Neglecting body forces, the PVW in the finite displacement settings reads [156, Eq. (3.49)]

$$\int_{V^0} \sigma_{ij} \delta E_{ij} \, \mathrm{d}V - \int_{S^0_\sigma} \bar{F}_i \delta u_i \, \mathrm{d}S = 0 \tag{5.1}$$

where $\bar{F}_i$ is the external force vector per unit (undeformed) surface that is prescribed on the portion S^0_σ of S. Displacements $\bar{u}_i$ are prescribed at the remaining portion of the boundary S^0_u, with $S^0_u \cup S^0_\sigma = S$ and $S^0_u \cap S^0_\sigma = \emptyset$. The virtual internal work is expressed in terms of Green-Lagrange (GL) strains E_{ij} and the work-conjugate second Piola-Kirchkoff (PK2) stresses σ_{ij}. The general definition of the GL strain field is [156, Eq. (3.19)]

$$E_{ij} = \frac{1}{2}\left(u_{i,_j} + u_{j,_i}\right) + \frac{1}{2}\left(u_{k,_i} u_{k,_j}\right) = \epsilon_{ij} + \eta_{ij} \tag{5.2}$$

The incremental formulation of the PVW Eq. (5.1) represents the final configuration Ω as an initial (equilibrium) state Ω_I that is perturbed by the configuration Ω':

$$\int_{V^0} \left(\sigma_{ij(I)} + \sigma'_{ij}\right) \delta \left(E_{ij(I)} + E'_{ij}\right) \, \mathrm{d}V - \int_{S^0_\sigma} \left(\bar{F}_{i(I)} + \bar{F}'_i\right) \delta u'_i \, \mathrm{d}S = 0 \tag{5.3}$$

The stress state has been decomposed into that pertaining to the initially stressed state $\sigma_{ij(I)}$ and that related to the perturbation σ'_{ij}. The analysis will be limited to geometrical nonlinearities with finite displacements, a linear elastic constitutive law is therefore employed as

$$\sigma_{ij} = C_{ijkl} \left(E_{kl\,(I)} + E'_{kl}\right) \tag{5.4}$$

The GL strains related to the perturbation are obtained as

$$\begin{aligned} 2E'_{ij} &= 2\left(E_{ij(I)} + E'_{ij}\right) - 2E_{ij(I)} = \\ &= \left[\left(u_i + u'_i\right)_{,j} + \left(u_j + u'_j\right)_{,i}\right] + \left[\left(u_k + u'_k\right)_{,i}\left(u_k + u'_k\right)_{,j}\right] \\ &- \left(u_{i,j} + u_{j,i}\right) - \left(u_{k,i}u_{k,j}\right) = \\ &= \left(\delta_{kj} + u_{k,j}\right)u'_{k,i} + \left(\delta_{ki} + u_{k,i}\right)u'_{k,j} + u'_{k,i}u'_{k,j} \end{aligned} \tag{5.5}$$

where δ_{ij} denotes the Kronecker symbol. These incremental GL strains are conveniently decomposed into the contributions that depends *linearly* and *quadratically* on the perturbation displacements:

$$E'_{ij} = e_{ij}\left(u'_l\right) + \eta_{ij}\left(u'_l u'_m\right) \tag{5.6}$$

The virtual variation of the incremental PVW Eq. (5.3) are taken only for the perturbation displacements u'_i because the initial state Ω_I is a given (fixed) equilibrium state for which

$$\int_{V^0} \sigma_{ij(I)}\delta e'_{ij}\ \mathrm{d}V - \int_{S^0_\sigma} \bar{F}_{i(I)}\delta u'_i\ \mathrm{d}S = 0 \tag{5.7}$$

Finally, "small perturbation" are assumed, which allows to linearise the incremental PVW upon retaining only contributions at most quadratic in u'_i:

$$\cancel{\delta e_{ij}C_{ijkl}\eta_{kl}}\,(u'_i)^3 \qquad \cancel{\delta\eta_{ij}C_{ijkl}e_{kl}}\,(u'_i)^3 \qquad \cancel{\delta\eta_{ij}C_{ijkl}\eta_{kl}}\,(u'_i)^4 \tag{5.8}$$

The incremental form of the PVW eventually reads:

$$\int_{V^0} \delta\eta'_{ij}\sigma_{ij(I)} + \delta e'_{ij}C_{ijkl}e'_{kl}\ \mathrm{d}V - \int_{S^0_\sigma} \bar{F}'_i\delta u'_i\ \mathrm{d}S = 0 \tag{5.9}$$

This variational form can be conveniently used for solving static deformation problems involving large displacements by means of incremental-iterative solution algorithms. In the following, further assumptions are introduced that limit the scope to a bifurcation buckling problem.

5.1.1 Linear bifurcation buckling (Euler method)

Within the classical Euler's method, the geometrical nonlinearity is introduced to provide the possibility of a system to have multiple equilibrium solutions under a given load, i.e., to characterise a "bifurcation point". In this framework, the already introduced "small perturbation" represents the possible equilibrium configuration adjacent to the "initial" one under the same external actions. Therefore, the external load is

not incremented ($\bar{F}'_i \equiv 0$), and the incremental PVW furnishes an eigenvalue problem whose eigenvalue corresponds to the initial stress state at which a (non-zero) perturbation exists:

$$\int_{V^0} \delta\eta'_{ij}\sigma_{ij(I)} + \delta e'_{ij} C_{ijkl} e'_{kl} \, \mathrm{d}V = 0 \tag{5.10}$$

The following additional simplifying assumptions are conveniently introduced to focus on the bifurcation buckling of panels under initial in-plane stresses.

- von Kármán approximation: since the principal buckling mode of in-plane stressed panels concerns the out-of-plane deflection, it is convenient to retain only the nonlinear contribution of the transverse displacement u_3 to the in-plane strains $E'_{\alpha\beta}$. Therefore, the general GL perturbation strains Eq. (5.6) are reduced to

$$E'_{\alpha\beta} = e'_{\alpha\beta}(u'_i) + \eta'_{\alpha\beta}({u'_3}^2); \quad \text{and} \quad E'_{i3} = \epsilon'_{i3} = \frac{1}{2}\left(u'_{i,3} + u'_{3,i}\right) \tag{5.11a}$$

  where

$$e'_{\alpha\beta} = \frac{1}{2}\left(u'_{\alpha,\beta} + u'_{\beta,\alpha}\right) + u_{3,\alpha}u'_{3,\beta} = \epsilon'_{\alpha\beta} + u_{3,\alpha}u'_{3,\beta}; \qquad \eta'_{\alpha\beta} = \frac{1}{2}u'_{3,\alpha}u'_{3,\beta} \tag{5.11b}$$

- Undeformed pre-stressed configuration: the approximation is next introduced that neglects the changes of geometrical configuration that may be induced by the initial stress state, i.e. only the initial stress is retained. This amounts to consider Ω_I as the stress-free reference configuration Ω_0 with, in particular, $u'_3 \approx 0$ in Eq. (5.11). Therefore the nonlinear perturbation strains are further reduced to

$$E'_{\alpha\beta} = \frac{1}{2}\left(u'_{\alpha,\beta} + u'_{\beta,\alpha}\right) + \frac{1}{2}u'_{3,\alpha}u'_{3,\beta} = \epsilon'_{\alpha\beta} + \eta'_{\alpha\beta} \tag{5.12}$$

- Nonlinear strains are discarded from the definition of the initial in-plane stresses:

$$\sigma_{\alpha\beta\,(I)} \;=\; C_{\alpha\beta kl}E_{kl\,(I)} \;\approx\; C_{\alpha\beta kl}\epsilon_{kl\,(I)} \tag{5.13}$$

  This assumptions allows to obtain a *linear* eigenvalue problem since the initial stress (the eigenvalue) results to be independent of the perturbation.

Finally, the variational framework for the linear bifurcation buckling problem of a body under an initial in-plane stress has the following expression

$$\int_{V^0} \delta\eta'_{\alpha\beta}\,\sigma_{\alpha\beta\,(I)} + \delta\epsilon'_{ij}\,C_{ijkl}\,\epsilon'_{kl}\,\mathrm{d}V \;=\; 0 \tag{5.14}$$

The initial stress is as usual defined as a reference stress state $\sigma^0_{\alpha\beta\,(I)}$ that is scaled by a load factor λ. The reference stress state can be defined in different manners as detailed below.

1. Prescribed uniform stress: σ^0 constant in the whole body

2. Prescribed uniform strain: a uniform strain ϵ_0 is prescribed over the whole domain, and the corresponding initial stress is defined from Eq. (5.13). It is customary to refer to a plane stress setting, i.e., $\sigma_{i3\,(I)} \equiv 0$, in order to properly account for a pure in-plane stress state. Thus the initial in-plane stresses are related to the initial (infinitesimal) in-plane strains through the reduced stiffness:

$$\sigma_{\alpha\beta\,(I)} \;=\; Q_{PQ}\,\epsilon_{Q\,(I)} \tag{5.15}$$

with $P, Q \in \{1, 2, 6\}$ are the indices of the compact notation corresponding to the in-plane quantities and $Q_{PQ} = C_{PQ} - C_{P3}C_{3Q}/C_{33}$.

3. In-plane stresses obtained from a previous FE computation: a linear static computation is at first carried out to obtain the initial stresses from Eq. (5.15), in which the strains are computed as usual from the nodal solution. It is worth emphasising that, depending on the nodal solution, the approximation of Eq. (5.12) can generate some inaccuracies.

5.1.2 Definition of the initial stress matrix

After introducing suitable approximation for the displacement unknowns within a discretization scheme, we look for the value λ such that a non-trivial perturbed configuration $\{\mathbf{U}'\}^T \neq \{0\}$ exists (adjacent equilibrium state) that verifies:

$$\{\delta\mathbf{U}'\}^T \left[\mathbf{K} + \lambda\mathbf{K}_\sigma\right] \{\mathbf{U}'\} = \{\mathbf{0}\} \tag{5.16}$$

In this context, the matrix $\mathbf{K}_\sigma$ is known as "initial stress" matrix. Following Eq. (5.9), it is defined as

$$\{\mathbf{U}'\}^T \left[\mathbf{K}_\sigma\right] \{\mathbf{U}'\} = \int_{V^0} \delta\eta'_{\mu\tau}\sigma_{\mu\tau(I)}\,\mathrm{d}V = \int_{V^0} \delta\eta'_P \tilde{Q}_{PQ}\epsilon_{Q(I)}\,\mathrm{d}V \tag{5.17}$$

Substituting the definition of the initial membrane stress

$$\begin{aligned}\int_{V^0} \delta\eta'_P \tilde{Q}_{PQ}\epsilon_{Q(I)}\,\mathrm{d}V = \int_{V^0} &\delta\eta'_1 \left(\tilde{Q}_{11}\epsilon_{1(I)} + \tilde{Q}_{12}\epsilon_{2(I)} + \tilde{Q}_{16}\epsilon_{6(I)}\right) + \\ &+\delta\eta'_2 \left(\tilde{Q}_{12}\epsilon_{1(I)} + \tilde{Q}_{22}\epsilon_{2(I)} + \tilde{Q}_{26}\epsilon_{6(I)}\right) + \\ &+\delta\eta'_6 \left(\tilde{Q}_{16}\epsilon_{1(I)} + \tilde{Q}_{26}\epsilon_{2(I)} + \tilde{Q}_{66}\epsilon_{6(I)}\right)\,\mathrm{d}V\end{aligned} \tag{5.18}$$

The virtual variations of the incremental strain that is quadratic in the perturbation displacements U' read

$$\delta\eta'_1 = \delta u'_{3,1} u'_{3,1}; \quad \delta\eta'_2 = \delta u'_{3,2} u'_{3,2}; \quad \delta\eta'_6 = \delta u'_{3,1} u'_{3,2} + \delta u'_{3,2} u'_{3,1} \tag{5.19}$$

The linear strain of the initial pre-buckling configuration (I) are

$$\epsilon_{1(I)} = u_{1(I),1}; \quad \epsilon_{2(I)} = u_{2(I),2}; \quad \epsilon_{6(I)} = u_{1(I),2} + u_{2(I),1} \tag{5.20}$$

Thus, dropping out the subscript (I)

$$\begin{aligned}
\left\{\delta\mathbf{U}'\right\}^T \left[\mathbf{K}_\sigma\right] \left\{\mathbf{U}\right\} = \int_{V^0} & \delta u'_{3,1} \left(\tilde{Q}_{11}\epsilon_1 + \tilde{Q}_{12}\epsilon_2 + \tilde{Q}_{16}\epsilon_6\right) u'_{3,1} + \\
& + \delta u'_{3,2} \left(\tilde{Q}_{12}\epsilon_1 + \tilde{Q}_{22}\epsilon_2 + \tilde{Q}_{26}\epsilon_6\right) u'_{3,2} + \\
& + \delta u'_{3,1} \left(\tilde{Q}_{16}\epsilon_1 + \tilde{Q}_{26}\epsilon_2 + \tilde{Q}_{66}\epsilon_6\right) u'_{3,2} + \\
& + \delta u'_{3,2} \left(\tilde{Q}_{16}\epsilon_1 + \tilde{Q}_{26}\epsilon_2 + \tilde{Q}_{66}\epsilon_6\right) u'_{3,1} \, \mathrm{d}V = \\
= \int_{V^0} & \delta u'_{3,1} \left\{\tilde{Q}_{11}u_{1,1} + \tilde{Q}_{12}u_{2,2} + \tilde{Q}_{16}u_{1,2} + \tilde{Q}_{16}u_{2,1}\right\} u'_{3,1} + \\
& + \delta u'_{3,2} \left\{\tilde{Q}_{12}u_{1,1} + \tilde{Q}_{22}u_{2,2} + \tilde{Q}_{26}u_{1,2} + \tilde{Q}_{26}u_{2,1}\right\} u'_{3,2} + \\
& + \delta u'_{3,1} \left\{\tilde{Q}_{16}u_{1,1} + \tilde{Q}_{26}u_{2,2} + \tilde{Q}_{66}u_{1,2} + \tilde{Q}_{66}u_{2,1}\right\} u'_{3,2} + \\
& + \delta u'_{3,2} \left\{\tilde{Q}_{16}u_{1,1} + \tilde{Q}_{26}u_{2,2} + \tilde{Q}_{66}u_{1,2} + \tilde{Q}_{66}u_{2,1}\right\} u'_{3,1} \, \mathrm{d}V
\end{aligned} \tag{5.21}$$

The same through-thickness plate approximation introduced in Section 2.2.3 according to SGUF notation, is used for the virtual variations of the displacement increments. The summation index for the virtual variation is μ, that for the unknown is τ. Similar expressions are hence introduced for the displacements at the initial configuration (I), for which the summation index γ is used:

$$\begin{aligned}
u_{x(I)}(x,y,z) &= \sum_{\gamma_{u_x}=0}^{N_{u_x}} F_{\gamma_{u_x}}(z)\, \hat{u}_{\gamma_{u_x}}(x,y) \\
u_{y(I)}(x,y,z) &= \sum_{\gamma_{u_y}=0}^{N_{u_y}} F_{\gamma_{u_y}}(z)\, \hat{u}_{\gamma_{u_y}}(x,y) \\
u_{z(I)}(x,y,z) &= \sum_{\gamma_{u_z}=0}^{N_{u_z}} F_{\gamma_{u_z}}(z)\, \hat{u}_{\gamma_{u_z}}(x,y)
\end{aligned} \tag{5.22}$$

where the subscript (I) has been dropped out from the in-plane functions $\hat{u}_\gamma$ without loss of clarity. These expressions are substituted into the variational statements and derivatives as well as integrations with respect to the through-thickness coordinate $x_3 = z$ are carried out explicitly. The through-thickness integrals for the initial stress matrix $[K_\sigma]$ have to include the actual displacements $u_{\alpha(I)}$, with $\alpha = 1, 2$ due to von Kármán approximation. Note that only in-plane derivatives occur in the initial stress matrix. Following the notation proposed in Eq. (2.18), the through-thickness integrals are

$$Z^{\mu_{u_r}\tau_{u_s}\gamma_{u_\alpha}}_{u_r u_s u_t} = \int_{z_p^{bot}}^{z_p^{top}} F_{\mu_{u_r}} F_{\tau_{u_s}} F_{\gamma_{u_\alpha}} \, \mathrm{d}z \tag{5.23}$$

Note that the integration is intended to be carried out over the thickness $h_p = \left[z_p^{bot}, z_p^{top}\right]$ of each ply separately. The initial stress matrix thus reads

$$\begin{aligned}
\left\{\delta\hat{u}'_{\mu}\right\}^T \left[K^{\sigma}_{\mu\tau}\right] \left\{\hat{u}'_{\tau}\right\} = \int_{V^0} \frac{\partial\, \delta\hat{u}'_{z_{\mu u_z}}}{\partial y} \Bigg\{ & \\
& \left[\tilde{Q}_{12} Z^{\mu_{u_z}\tau_{u_z}\gamma_{u_x}}_{u_z u_z u_x} \frac{\partial \hat{u}_{x_{\gamma u_x}}}{\partial x} + \tilde{Q}_{22} Z^{\mu_{u_z}\tau_{u_z}\gamma_{u_y}}_{u_z u_z u_y} \frac{\partial \hat{u}_{y_{\gamma u_y}}}{\partial y} + \right. \\
& \left. + \tilde{Q}_{26} Z^{\mu_{u_z}\tau_{u_z}\gamma_{u_x}}_{u_z u_z u_x} \frac{\partial \hat{u}_{x_{\gamma u_x}}}{\partial y} + \tilde{Q}_{26} Z^{\mu_{u_z}\tau_{u_z}\gamma_{u_y}}_{u_z u_z u_y} \frac{\partial \hat{u}_{y_{\gamma u_y}}}{\partial x} \right] \frac{\partial \hat{u}'_{z_{\tau u_z}}}{\partial y} + \\
& + \left[\tilde{Q}_{16} Z^{\mu_{u_z}\tau_{u_z}\gamma_{u_x}}_{u_z u_z u_x} \frac{\partial \hat{u}_{x_{\gamma u_x}}}{\partial x} + \tilde{Q}_{26} Z^{\mu_{u_z}\tau_{u_z}\gamma_{u_y}}_{u_z u_z u_y} \frac{\partial \hat{u}_{y_{\gamma u_y}}}{\partial y} + \right. \\
& \left. + \tilde{Q}_{66} Z^{\mu_{u_z}\tau_{u_z}\gamma_{u_x}}_{u_z u_z u_x} \frac{\partial \hat{u}_{x_{\gamma u_x}}}{\partial y} + \tilde{Q}_{66} Z^{\mu_{u_z}\tau_{u_z}\gamma_{u_y}}_{u_z u_z u_y} \frac{\partial \hat{u}_{y_{\gamma u_y}}}{\partial x} \right] \frac{\partial \hat{u}'_{z_{\tau u_z}}}{\partial x} \Bigg\} + \\
& + \frac{\partial\, \delta\hat{u}'_{z_{\mu u_z}}}{\partial x} \Bigg\{ \left[\tilde{Q}_{16} Z^{\mu_{u_z}\tau_{u_z}\gamma_{u_x}}_{u_z u_z u_x} \frac{\partial \hat{u}_{x_{\gamma u_x}}}{\partial x} + \tilde{Q}_{26} Z^{\mu_{u_z}\tau_{u_z}\gamma_{u_y}}_{u_z u_z u_y} \frac{\partial \hat{u}_{y_{\gamma u_y}}}{\partial y} + \right. \\
& \left. + \tilde{Q}_{66} Z^{\mu_{u_z}\tau_{u_z}\gamma_{u_x}}_{u_z u_z u_x} \frac{\partial \hat{u}_{x_{\gamma u_x}}}{\partial y} + \tilde{Q}_{66} Z^{\mu_{u_z}\tau_{u_z}\gamma_{u_y}}_{u_z u_z u_y} \frac{\partial \hat{u}_{y_{\gamma u_y}}}{\partial x} \right] \frac{\partial \hat{u}'_{z_{\tau u_z}}}{\partial y} + \\
& + \left[\tilde{Q}_{11} Z^{\mu_{u_z}\tau_{u_z}\gamma_{u_x}}_{u_z u_z u_x} \frac{\partial \hat{u}_{x_{\gamma u_x}}}{\partial x} + \tilde{Q}_{12} Z^{\mu_{u_z}\tau_{u_z}\gamma_{u_y}}_{u_z u_z u_y} \frac{\partial \hat{u}_{y_{\gamma u_y}}}{\partial y} + \right. \\
& \left. + \tilde{Q}_{16} Z^{\mu_{u_z}\tau_{u_z}\gamma_{u_x}}_{u_z u_z u_x} \frac{\partial \hat{u}_{x_{\gamma u_x}}}{\partial y} + \tilde{Q}_{16} Z^{\mu_{u_z}\tau_{u_z}\gamma_{u_y}}_{u_z u_z u_y} \frac{\partial \hat{u}_{y_{\gamma u_y}}}{\partial x} \right] \frac{\partial \hat{u}'_{z_{\tau u_z}}}{\partial x} \Bigg\} \, \mathrm{d}x \, \mathrm{d}y
\end{aligned} \tag{5.24}$$

The in-plane incremental solution in the FEM framework is expressed as follow:

$$\begin{aligned}
\delta\hat{u}'_{\mu_{u_x}}(x,y) &= \sum_{i=1}^{n} N_i(x,y)\, \delta U_{x_{\mu u_x} i}; \quad \hat{u}'_{\tau u_x}(x,y) = \sum_{j=1}^{n} N_j(x,y)\, U_{x_{\tau u_x} j} \\
\delta\hat{u}'_{\mu_{u_y}}(x,y) &= \sum_{i=1}^{n} N_i(x,y)\, \delta U_{y_{\mu u_y} i}; \quad \hat{u}'_{\tau u_y}(x,y) = \sum_{j=1}^{n} N_j(x,y)\, U_{y_{\tau u_y} j} \\
\delta\hat{u}'_{\mu_{u_z}}(x,y) &= \sum_{i=1}^{n} N_i(x,y)\, \delta U_{z_{\mu u_z} i}; \quad \hat{u}'_{\tau u_z}(x,y) = \sum_{j=1}^{n} N_j(x,y)\, \delta U_{z_{\tau u_z} j}
\end{aligned} \tag{5.25}$$

where n is the number of FE nodes. Expansions of the virtual variation and of the unknown are discriminated through the use of the summation indices i and j respectively. Differentiation and integration with respect to the in-plane coordinates x, y as they occur in the initial stress matrix are carried out according to following notation:

$$\mathcal{I}^{defghn}_{u_r u_s u_\alpha ijl} = \int_{\Omega} \frac{\partial^{d+e} N_{u_r i}}{\partial x^d \partial y^e} \left(\frac{\partial^{h+n} N_{u_\alpha l}}{\partial x^h \partial y^n}\right) \frac{\partial^{f+g} N_{u_s j}}{\partial x^f \partial y^g} \, \mathrm{d}x \, \mathrm{d}y \quad (d,e,f,g,h,n = 0,1) \tag{5.26}$$

where N is the FE interpolation over the 2D elementary domain. The initial stress stiffness matrix has finally the following expression:

$$\begin{aligned}
\left\{\delta U'_{\mu i}\right\}^T \left[K^{\sigma}_{\mu\tau ij}\right] \left\{U'_{\tau j}\right\} = \delta U'_{z_{\mu u_z i}} \Bigg[& \\
& \tilde{Q}_{11} Z^{\mu_{u_z}\tau_{u_z}\gamma_{u_x}}_{u_z u_z u_x} \mathcal{I}^{101010}_{u_z u_z u_x ijl} U_{x_{\gamma_{u_x} l}} + \tilde{Q}_{12} Z^{\mu_{u_z}\tau_{u_z}\gamma_{u_y}}_{u_z u_z u_y} \mathcal{I}^{101001}_{u_z u_z u_y ijl} U_{y_{\gamma_{u_y} l}} + \\
& + \tilde{Q}_{16} Z^{\mu_{u_z}\tau_{u_z}\gamma_{u_x}}_{u_z u_z u_x} \mathcal{I}^{101001}_{u_z u_z u_x ijl} U_{x_{\gamma_{u_x} l}} + \tilde{Q}_{16} Z^{\mu_{u_z}\tau_{u_z}\gamma_{u_y}}_{u_z u_z u_y} \mathcal{I}^{101010}_{u_z u_z u_y ijl} U_{y_{\gamma_{u_y} l}} + \\
& + \tilde{Q}_{12} Z^{\mu_{u_z}\tau_{u_z}\gamma_{u_x}}_{u_z u_z u_x} \mathcal{I}^{010110}_{u_z u_z u_x ijl} U_{x_{\gamma_{u_x} l}} + \tilde{Q}_{22} Z^{\mu_{u_z}\tau_{u_z}\gamma_{u_y}}_{u_z u_z u_y} \mathcal{I}^{010101}_{u_z u_z u_y ijl} U_{y_{\gamma_{u_y} l}} + \\
& + \tilde{Q}_{26} Z^{\mu_{u_z}\tau_{u_z}\gamma_{u_x}}_{u_z u_z u_x} \mathcal{I}^{010101}_{u_z u_z u_x ijl} U_{x_{\gamma_{u_x} l}} + \tilde{Q}_{26} Z^{\mu_{u_z}\tau_{u_z}\gamma_{u_y}}_{u_z u_z u_y} \mathcal{I}^{010110}_{u_z u_z u_y ijl} U_{y_{\gamma_{u_y} l}} + \\
& + \tilde{Q}_{16} Z^{\mu_{u_z}\tau_{u_z}\gamma_{u_x}}_{u_z u_z u_x} \mathcal{I}^{011010}_{u_z u_z u_x ijl} U_{x_{\gamma_{u_x} l}} + \tilde{Q}_{26} Z^{\mu_{u_z}\tau_{u_z}\gamma_{u_y}}_{u_z u_z u_y} \mathcal{I}^{011001}_{u_z u_z u_y ijl} U_{y_{\gamma_{u_y} l}} + \\
& + \tilde{Q}_{66} Z^{\mu_{u_z}\tau_{u_z}\gamma_{u_x}}_{u_z u_z u_x} \mathcal{I}^{011001}_{u_z u_z u_x ijl} U_{x_{\gamma_{u_x} l}} + \tilde{Q}_{66} Z^{\mu_{u_z}\tau_{u_z}\gamma_{u_y}}_{u_z u_z u_y} \mathcal{I}^{011010}_{u_z u_z u_y ijl} U_{y_{\gamma_{u_y} l}} + \\
& + \tilde{Q}_{16} Z^{\mu_{u_z}\tau_{u_z}\gamma_{u_x}}_{u_z u_z u_x} \mathcal{I}^{100110}_{u_z u_z u_x ijl} U_{x_{\gamma_{u_x} l}} + \tilde{Q}_{26} Z^{\mu_{u_z}\tau_{u_z}\gamma_{u_y}}_{u_z u_z u_y} \mathcal{I}^{100101}_{u_z u_z u_y ijl} U_{y_{\gamma_{u_y} l}} + \\
& + \tilde{Q}_{66} Z^{\mu_{u_z}\tau_{u_z}\gamma_{u_x}}_{u_z u_z u_x} \mathcal{I}^{100101}_{u_z u_z u_x ijl} U_{x_{\gamma_{u_x} l}} + \tilde{Q}_{66} Z^{\mu_{u_z}\tau_{u_z}\gamma_{u_y}}_{u_z u_z u_y} \mathcal{I}^{100110}_{u_z u_z u_y ijl} U_{y_{\gamma_{u_y} l}} \\
& \Bigg] U'_{z_{\tau_{u_z} j}}
\end{aligned} \tag{5.27}$$

Note that no transverse shear appears in the initial stress matrix, therefore the classical isoparametric approach can be used for the FE approximations. Furthermore, the summation convention over repeated indices implies that the sum over the expansion indices γ and l used for the definition of the initial stress must be carried out for each couple of indices μ, τ and i, j.

5.2 Global buckling of multilayered panels

The failure mechanism which involves the whole structure and referred to as *overall buckling*, is investigated in this section. The buckling preload is determined by uniformly straining the structure along the longitudinal direction. No explicit pre-buckling analysis is then required because a uniform strain is directly imposed. A model assessment is provided in order to establish the influence of through-the-thickness approximation on the critical buckling load prediction.

5.2.1 Uniaxial compression of symmetric cross-ply laminates

A validation and assessment of the proposed hierarchic approach is given in this section by referring to the buckling problem proposed by Noor [155], and therefore referred to

as Noor-TestCase (No-TC). It considers a symmetric cross-ply laminate $[0°/90°/\dots]$ with an odd number of plies. Two stacking sequences which involve, respectively, three (Figure 5.1(a)) and nine (Figure 5.1(b)) plies are investigated. For both stacking sequences, the outer plies are oriented at 0°. The total thickness of the plies at 0° and 90° is the same. Based on the number of plies N_p and on the total thickness of the plate H, the relative thickness of plies oriented at 0° and 90° is calculated as:

$$\frac{h_{0°}}{H} = \frac{1}{N_p + 1}\,; \quad \frac{h_{90°}}{H} = \frac{1}{N_p - 1} \tag{5.28}$$

The geometric and elastic properties are given in Table 5.1. Two width-to-thickness ratio are investigated, ranging from moderately-thick ($b/H = 10$) to thin ($b/H = 100$) plate.

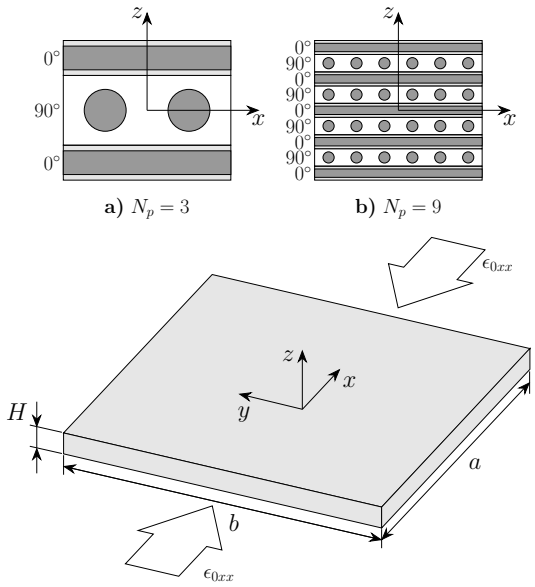

Figure 5.1: No-TC: Cross-ply laminate geometry.

Table 5.1: No-TC: Geometric and material data.

$a = b = 10$ mm $b/H = \{10, 100\} \Rightarrow H = \{1, 0.1\}$ mm	
	Material 1
E_L [MPa]	$\{3, 10, 20, 30, 40\}$
E_T [MPa]	1
ν_{LT}	0.25
ν_{TT}	0.25
G_{LT} [MPa]	0.6
G_{TT} [MPa]	0.5

Pre-buckling. The pre-buckling equilibrium configuration is determined by assuming an imposed uniform strain along the $x-$direction, as shown in Figure 5.1. The resulting layerwise uniform stress σ^p_{0xx} in the initial configuration is calculated according to the stiffness coefficient $\tilde{C}^p_{11}$ as:

$$\sigma^p_{0xx} = \tilde{C}^p_{11}\epsilon_{0xx} \tag{5.29}$$

where the imposed initial strain ϵ_{0xx} is assumed to be unitary in the following for simplicity. All the results presented hereinafter are given in terms of nondimensional buckling load $\bar{N}$, calculated as:

$$\bar{N} = N_{cr}\frac{b^2}{E_T H^3} \tag{5.30}$$

where N_{cr} is the *critical load*, defined as

$$N_{cr} = \lambda_{cr}\epsilon_{0xx} \sum_{p=1}^{N_p} \int_{h_p} \tilde{C}_{11}^{p} \, \mathrm{d}z = \tilde{A}_{11}\lambda_{cr}\epsilon_{0xx} \tag{5.31}$$

In Eq. (5.31), $\tilde{A}_{11}$ is the membrane stiffness coefficient of the multilayered composite plate and λ_{cr} is the lowest eigenvalue of the linearized buckling problem expressed by Eq. (5.16).

Buckling. A preliminary analysis is performed to establish the convergence behaviour of the present FE solution. The three-ply lamination scheme of Figure 5.1(a) is considered. The orthotropic ratio is set to $E_L/E_T = 10$. All edges of the plate are simply-supported. The convergence analysis is carried out for both moderately-thick ($b/H = 10$) and thin ($b/H = 100$) plate. Given the symmetry of the problem, only the quarter plate is modelled and a regular mesh with $N = 1, 2, 4, 6, 8, 10$ quadratic elements along the edges of the quarter plate is considered: For the thick plate case ($b/H = 10$) the isoparametric 8-node FE are used, while the CL8 FE are employed for the thin plate case ($b/H = 100$), in order to avoid transverse shear locking issues.

Table 5.2 compares the nondimensional buckling load obtained with the present FE approach against those obtained with the Navier's method for several hierarchical models. When available, the exact 3D elasticity solution of Noor [155] is also listed for an additional comparison. Percent differences are reported in the parenthesis with respect to the Navier solution. Since both present FE and Navier approaches rely on the same approximations along the thickness direction of the plate, and for this latter the solution in the 2D domain is found in a closed-form, the percent differences allow to provide a direct measure of the quality of the in-plane discretization.

Table 5.2: No-TC: Nondimensional uniaxial buckling load $\bar{N} = N_{cr}b^2/E_T H^3$ of a simply-supported symmetric square plate ($E_L/E_T = 10$) loaded in compression with an imposed uniform strain: convergence of the present FE with respect to the Navier solution.

Model	Navier	Present FE					
		10x10	8x8	6x6	4x4	2x2	1x1
$a/h = 10$ - Exact 3D [155]: $\bar{N} = 9.7621$							
LD4	9.7628	9.7629 (0.001)	9.7630 (0.002)	9.7635 (0.007)	9.7658 (0.031)	9.8069 (0.452)	10.7833 (10.453)
LD3	9.7628	9.7629 (0.001)	9.7630 (0.002)	9.7635 (0.007)	9.7658 (0.031)	9.8069 (0.452)	10.7833 (10.453)
LD2	9.7710	9.7711 (0.001)	9.7712 (0.002)	9.7717 (0.007)	9.7741 (0.032)	9.8156 (0.456)	10.7945 (10.475)
LD1	9.8530	9.8531 (0.001)	9.8532 (0.002)	9.8537 (0.007)	9.8561 (0.031)	9.8985 (0.462)	10.881 (10.433)
EDZ4	9.7695	9.7695 (0.000)	9.7697 (0.002)	9.7701 (0.006)	9.7725 (0.031)	9.8138 (0.453)	10.7921 (10.467)
ED4	9.7705	9.7706 (0.001)	9.7707 (0.002)	9.7712 (0.007)	9.7736 (0.032)	9.8149 (0.454)	10.7935 (10.470)
ED3	9.7720	9.7720 (0.000)	9.7722 (0.002)	9.7726 (0.006)	9.7750 (0.031)	9.8164 (0.454)	10.7953 (10.472)
ED2	9.9945	9.9946 (0.001)	9.9948 (0.003)	9.9952 (0.007)	9.9979 (0.034)	10.0446 (0.501)	11.0461 (10.522)
ED1	10.2037	10.2038 (0.001)	10.2039 (0.002)	10.2044 (0.007)	10.2071 (0.033)	10.2536 (0.489)	11.2507 (10.261)
FSDT ($\kappa = 5/6$)	9.9653	9.9654 (0.001)	9.9655 (0.002)	9.9659 (0.006)	9.9682 (0.029)	10.0084 (0.433)	10.8666 (9.044)
$a/h = 100$							
LD4	11.4711	11.4712 (0.001)	11.4713 (0.002)	11.4719 (0.007)	11.4754 (0.037)	11.5384 (0.587)	12.4645 (8.660)
LD3	11.4711	11.4712 (0.001)	11.4713 (0.002)	11.4719 (0.007)	11.4754 (0.037)	11.5384 (0.587)	12.4645 (8.660)
LD2	11.4712	11.4713 (0.001)	11.4714 (0.002)	11.4720 (0.007)	11.4755 (0.037)	11.5388 (0.589)	12.4651 (8.664)
LD1	11.5171	11.5172 (0.001)	11.5173 (0.002)	11.5179 (0.007)	11.5215 (0.038)	11.5852 (0.591)	12.5151 (8.665)
EDZ4	11.4711	11.4713 (0.002)	11.4714 (0.003)	11.4720 (0.008)	11.4755 (0.038)	11.5389 (0.591)	12.4650 (8.664)
ED4	11.4712	11.4713 (0.001)	11.4714 (0.002)	11.4720 (0.007)	11.4756 (0.038)	11.5389 (0.590)	12.4651 (8.664)
ED3	11.4712	11.4713 (0.001)	11.4714 (0.002)	11.4720 (0.007)	11.4756 (0.038)	11.5389 (0.590)	12.4651 (8.664)
ED2	11.4742	11.4744 (0.002)	11.4745 (0.003)	11.4751 (0.008)	11.4787 (0.039)	11.5422 (0.593)	12.4693 (8.673)
ED1	11.7636	11.7637 (0.001)	11.7639 (0.003)	11.7645 (0.008)	11.7682 (0.039)	11.8332 (0.592)	12.7814 (8.652)
FSDT ($\kappa = 5/6$)	11.4740	11.4741 (0.001)	11.4743 (0.003)	11.4749 (0.008)	11.4784 (0.038)	11.5419 (0.592)	12.4675 (8.659)

The convergence behaviour of several CUF models is also presented in Table 5.2. FSDT model involves a shear correction factor of $\kappa = 5/6$ to enhance the numerical prediction of the buckling load. The results for the most refined mesh from both moderately-thick and thin plates are in perfect agreement with those obtained within the Navier's method, demonstrating that the present FE approach allows an accurate prediction of the buckling behaviour of multilayered composite plate. The quadratic element is found to converge very quickly since a 2×2 mesh leads to a percent difference less than 1%. The same convergence rate can be appreciated for the thin plate case, demonstrating the absence of shear locking pathology. The most refined mesh, involving 10×10 quadratic elements, ensure a perfect convergence with respect to Navier solution and will be therefore used for all results presented hereinafter.

Table 5.3 outlines the influence of the orthotropy ratio E_L/E_T and the number of plies on the buckling loads for symmetric cross-ply laminates with a width-to-thickness ratio equal to 10. The comparison is made in terms of nondimensional buckling load $\bar{N}$ as expressed in Eq. (5.30). The value in parentheses indicates the percent difference between the present FE solution and the exact 3D elasticity given by Noor[155]. A close agreement is found when the most refined plate model (LD4) is considered. It is worth noting that a cubic expansion is sufficient to provide a converged solution within the presented testcase.

The accuracy of low order models is affected by the orthotropy ratio of the plate: as the ratio E_L/E_T increases, a higher value of the percent difference is obtained meaning an overestimation of the buckling load. This trend is somehow reversed once the convergence of the axiomatic model is achieved (LD3 and LD4 models). Furthermore, ESL models appears to be sufficient for laminates with a low orthotropy ratios; a LW description is to be considered for an accurate prediction if the laminate has a high orthotropy ratio.

Increasing the number of plies results in a laminate which behaves like an isotropic material, the net effect of the orthotropy ratio becomes therefore less important. As a results, a quadratic order for the polynomial approximation is found to be adequate to provide an accurate prediction of the buckling loads.

The influence of different boundary conditions on nondimensional uniaxial buckling load $\bar{N} = N_{cr}b^2/E_T H^3$ is investigated in Table 5.4 for both moderately-thick and thin plates and different orthotropy ratios. The plate is considered simply-supported (S) along the edges parallel to the $y-$axis, whereas the edges parallel to the $x-$axis may be simply-supported (S), clamped (C) or free (F). Since only the quarter plate is modelled, symmetry conditions are prescribed at the left and bottom edges, and for this reason

Table 5.3: No-TC: Nondimensional uniaxial buckling load $\bar{N} = N_{cr}b^2/E_T H^3$ of a simply-supported symmetric square plate ($b/H = 10$) loaded in compression with an imposed uniform strain: assessment of classical models for different orthotropy ratios E_L/E_T and number of plies N_p.

Model	E_L/E_T				
	3	10	20	30	40
$N_p = 3$					
Exact 3D [155]	5.3044	9.7621	15.0191	19.3040	22.8807
LD4	5.3052 (0.015)	9.7629 (0.008)	15.0197 (0.004)	19.3046 (0.003)	22.8812 (0.002)
LD3	5.3052 (0.015)	9.7629 (0.008)	15.0197 (0.004)	19.3046 (0.003)	22.8812 (0.002)
LD2	5.3067 (0.043)	9.7711 (0.092)	15.0464 (0.182)	19.3584 (0.282)	22.9690 (0.386)
LD1	5.3583 (1.016)	9.8531 (0.932)	15.2144 (1.300)	19.6300 (1.689)	23.3474 (2.040)
EDZ4	5.3054 (0.019)	9.7695 (0.076)	15.0468 (0.184)	19.3614 (0.297)	22.9740 (0.408)
ED4	5.3058 (0.026)	9.7706 (0.087)	15.0513 (0.214)	19.3718 (0.351)	22.9923 (0.488)
ED3	5.3061 (0.032)	9.7720 (0.101)	15.0552 (0.240)	19.3786 (0.386)	23.0022 (0.531)
ED2	5.3557 (0.967)	9.9946 (2.382)	15.6459 (4.173)	20.4028 (5.692)	24.4817 (6.997)
ED1	5.6321 (6.178)	10.2038 (4.525)	15.8102 (5.267)	20.5359 (6.382)	24.5912 (7.476)
FSDT ($\kappa = 5/6$)	5.3992 (1.787)	9.9654 (2.083)	15.3514 (2.213)	19.7567 (2.345)	23.4529 (2.501)
$N_p = 9$					
Exact 3D [155]	5.3352	10.0417	15.9153	20.9614	25.3436
LD4	5.3355 (0.006)	10.0420 (0.003)	15.9156 (0.002)	20.9617 (0.001)	25.3438 (0.001)
LD3	5.3355 (0.006)	10.0420 (0.003)	15.9156 (0.002)	20.9617 (0.001)	25.3438 (0.001)
LD2	5.3355 (0.006)	10.0420 (0.003)	15.9157 (0.003)	20.9619 (0.002)	25.3442 (0.002)
LD1	5.3417 (0.122)	10.0585 (0.167)	15.9588 (0.273)	21.0401 (0.375)	25.4622 (0.468)
EDZ4	5.3357 (0.009)	10.0461 (0.044)	15.9315 (0.102)	20.9939 (0.155)	25.3950 (0.203)
ED4	5.3385 (0.062)	10.0575 (0.157)	15.9622 (0.295)	21.0487 (0.416)	25.4765 (0.524)
ED3	5.3385 (0.062)	10.0579 (0.161)	15.9630 (0.300)	21.0502 (0.424)	25.4786 (0.533)
ED2	5.3811 (0.860)	10.2302 (1.877)	16.4245 (3.199)	21.8793 (4.379)	26.7208 (5.434)
ED1	5.6645 (6.172)	10.4567 (4.133)	16.6136 (4.388)	22.0409 (5.150)	26.8602 (5.984)
FSDT (k=5/6)	5.4127 (1.453)	10.1896 (1.473)	16.1460 (1.450)	21.2651 (1.449)	25.7153 (1.467)

they are omitted from the notation. Two letters are therefore sufficient to uniquely define the boundary conditions of the plate. For instance, the notation SC will refer to the quarter plate, simply supported along the right edge and clamped along the top edge. Particular attention should be paid on the use of symmetry boundary conditions because only symmetric modal shapes (and corresponding critical loads levels) will be considered. The buckling mode of the investigated configurations is always the fundamental bending mode, which is symmetric.

It is observed that the less the structure is constrained, the more the most refined LD4 solution is quickly recovered. So, for the thin plate case, a quadratic order of the polynomial expansion provides converged solutions for both SF and SS configurations,

Table 5.4: No-TC: Nondimensional uniaxial buckling load $\bar{N} = N_{cr}b^2/E_T H^3$ of a three-ply symmetric square plate loaded in compression with an imposed uniform strain: influence of different boundary conditions for a moderately-thick ($b/H = 10$) and thin ($b/H = 100$) plate and varying the orthotropy ratio E_L/E_T.

Model	E_L/E_T								
	3			20			40		
	Boundary conditions			Boundary conditions			Boundary conditions		
	SF	SS	SC	SF	SS	SC	SF	SS	SC
$a/h = 10$									
LD4	2.1575	5.3052	9.2446	10.9448	15.0197	22.3841	17.6416	22.8812	32.3409
LD3	2.1575	5.3052	9.2447	10.9448	15.0197	22.3845	17.6416	22.8812	32.3417
LD2	2.1577	5.3067	9.2595	10.9464	15.0464	22.6827	17.6460	22.9690	33.0632
LD1	2.1696	5.3583	9.3663	11.0832	15.2144	22.8904	18.0010	23.3474	33.4903
EDZ4	2.1579	5.3054	9.2491	10.9558	15.0468	22.6097	17.6711	22.9740	32.9270
ED4	2.1580	5.3058	9.2505	10.9564	15.0513	22.6664	17.6718	22.9923	33.1022
ED3	2.1582	5.3061	9.2534	10.9592	15.0552	22.6825	17.6782	23.0022	33.1372
ED2	2.1756	5.3557	9.4139	11.4075	15.6459	24.2536	18.8590	24.4817	34.9639
ED1	2.2387	5.6321	9.8844	11.4412	15.8102	24.5099	18.8753	24.5912	37.1383
FSDT ($\kappa = 5/6$)	2.1789	5.3992	9.3751	11.0325	15.3514	23.5703	17.7343	23.4529	35.0266
$a/h = 100$									
LD4	2.2889	5.7489	10.6568	14.4829	19.6494	31.6866	28.7411	35.9422	56.3383
LD3	2.2889	5.7489	10.6568	14.4829	19.6495	31.6866	28.7411	35.9422	56.3383
LD2	2.2889	5.7489	10.6571	14.4830	19.6498	31.6943	28.7413	35.9436	56.3676
LD1	2.2983	5.7994	10.7663	14.4940	19.6964	31.7946	28.7595	35.9967	56.4735
EDZ4	2.2890	5.7489	10.6573	14.4834	19.6499	31.6934	28.7428	35.9440	56.3639
ED4	2.2891	5.7489	10.6575	14.4838	19.6499	31.6955	28.7428	35.9443	56.3721
ED3	2.2892	5.7489	10.6577	14.4839	19.6499	31.6960	28.7430	35.9443	56.3726
ED2	2.2894	5.7495	10.6600	14.4916	19.6600	31.7266	28.7732	35.9804	56.4775
ED1	2.3622	6.0718	11.2957	14.5657	19.9422	32.2725	28.8487	36.2580	57.0139
FSDT ($\kappa = 5/6$)	2.2892	5.7500	10.6377	14.4854	19.6553	31.6994	28.7463	35.9554	56.4184

whereas the more constrained one (SC) requires the polynomial order to be at least cubic. This trend is confirmed for the thick plate case also, and irrespective of the orthotropy ratio. Furthermore, the FSDT model with a shear correction factor $\kappa = 5/6$ provides a nearly perfect estimation of the critical buckling load for the SF configuration and $b/h = 100$.

All these results are presented for the first time and can be used as a benchmark for further investigations.

5.3 Local instabilities of sandwich panels

Local instabilities arising in the composite face sheets of sandwich structures due to mismatch in geometric and elastic properties of the constituent plies are studied in this section. Indeed, the higher stiffness of face sheets compared to the core cause them to carry the whole compressive load the sandwich plate is subjected to. Consequently, an unstable behaviour may be locally detected in the outer skins while the whole structure remains stable [83]. In the following, two different loading conditions are investigated:

Uniaxial compression. An uniaxial unitary compression strain is imposed along the longitudinal direction of the panel. The resulting compression stress is uniform along the ply thickness and proportional to its stiffness coefficient C_{11}^{p}. Both global and local buckling can occur depending on geometry and relative properties between skins and core.

Transverse load. A three-point-bending test is performed. The transverse load triggers a non-uniform stress state across the face sheets. In particular, a transverse load acting downwards causes the top face sheet to be compressed (negative axial stress σ_{xx}) and the bottom one to be in tension (positive axial stress σ_{xx}), in the bent configuration. The compressed face sheet may therefore buckle into the core by forming short-wavelength wrinkles.

5.3.1 Wrinkling of sandwich strut under uniaxial compression

The capability of the present FE to accurately recover both buckling loads and buckled shapes for a variety of skins and core considerations is demonstrated by referring to the case study of Ref.[83]. It considers a sandwich panel subjected to uniaxial compression along the longitudinal direction as shown in Figure 5.2 for which analytical solutions were found by referring to the CUF LM4 model and Navier's solution. The case study will be referred to as D'Ottavio TestCase (DO-TC). Following the work of Ref.[83], the problem is confined in the $(xz)-$plane corresponding to the cross section of the plate by resorting the plane strain assumption.

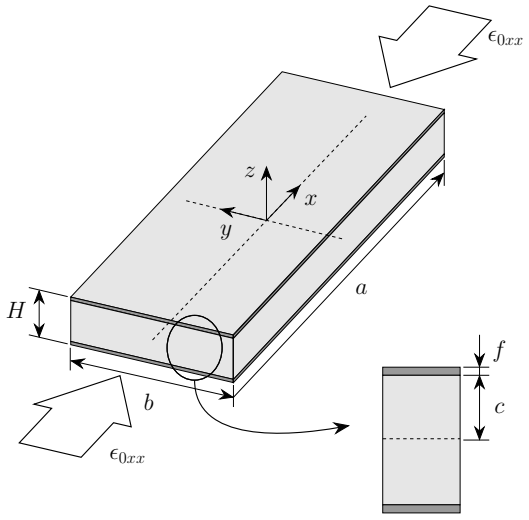

Figure 5.2: DO-TC: Sandwich beam-plate geometry.

Table 5.5: DO-TC: Geometric and material data.

$a = 5H;\ b = 1$ mm; $H = 50$ mm $f = R_f H;\ 2c = H - 2f$		
	Core (^{c})	Facesheet (^{f})
$\theta\,[^\circ]$	0	0
E_{11} [GPa]	χE^c_{33}	70
E_{22} [GPa]	χE^c_{33}	70
E_{33} [GPa]	kE^f_{11}	70
ν	0	0
G_{12} [GPa]	$0.5E^c_{11}$	35
G_{13} [GPa]	$0.5E^c_{33}$	35
G_{23} [GPa]	$0.5E^c_{33}$	35

The geometric and material properties are summarised in Table 5.5. The sandwich structure has a total thickness $H = 50$ mm. The length in the longitudinal direction is assumed to be $a = 5H$ in order to promote the short-wavelength wrinkling instability. Since the effects in the $y-$direction are disregarded, the width is set to $b = 1$ mm. The three parameters R_f, k and χ are introduced to define the following characteristic ratios:

- *face-to-core thickness ratio*: $R_f = \dfrac{f}{H}$
- *face-to-core stiffness ratio*: $k = \dfrac{E^f_x}{E^c_x}$
- *core orthotropy ratio*: $\chi = \dfrac{E^c_z}{E^c_x}$

Furthermore, in order to avoid spurious initial stresses in directions which are different from those in which the sandwich panel is strained (x-direction), all Poisson's ratios are set to zero. The structure is simply supported along the edges parallel to the $y-$direction. The plane strain condition is achieved by constraining the displacement u_y. The boundary conditions applied to the sandwich panel are thus:

$$u_z\left(x = \pm a/2, y, z\right) = u_y\left(x, y, z\right) = 0 \tag{5.32}$$

Convergence study. A preliminary analysis is carried out to establish the convergence behaviour of the present FE. Both linear four-node and quadratic eight-node

elements are investigated. The in-plane discretization involves $N = 32, 64, 128, 256$ QC4 or $N = 16, 32, 64, 128$ CL8 elements along the $x-$direction whereas only one element is used along the width direction of the panel.

Table 5.6 lists the critical buckling load N_{cr} for different combinations of the three parameters R_f, k and χ. The same formula of Eq. (5.31) is here employed to calculate the critical buckling load N_{cr}. In order to establish an "honest" correlation between QC4 and CL8 results, the number of nodes is appended, in subscript, to the number of elements. A displacement-based CUF model with an expansion order of four, namely LD4, is considered for this convergence analysis. It is worth noting, though, that no DOFs in $y-$direction are present, regardless of the model employed, since the plane strain condition is imposed.

Comparison is made with respect to the buckling load obtained with the Navier solution and the same LD4 model. The number of halfwaves along the $x-$direction and whether the buckled shape is antisymmetric (A) or symmetric (S) are written in superscript after the computed buckling load. The overall buckling load is characterized by only one halfwave and an antisymmetric shape. Local instabilities involve a higher number of halfwaves and a buckled shape which may be either symmetric or antisymmetric. For further insight about the definition of antisymmetric and symmetric buckled shapes readers may refer to [83]. For the sake of comparison, percent differences are also reported in parentheses.

The results show that overall buckling occurs for either thick faces ($R_f = 0.1$) or a stiff core ($k = 0.1$). In all other cases, the lowest critical load corresponds to a wrinkling-type instability, whose wave-length depends on the characteristic ratios of the sandwich section as well as on the core orthotropy ratio χ. This parameter is further shown to be important for defining wether the mode is antisymmetric or symmetric: it appears that the symmetric mode is triggered when the in-plane stiffness of the core is less than its transverse stiffness.

Table 5.6: DO-TC: Convergence of critical buckling load N_{cr} [N/mm] of LD4 model for both QC4 and CL8 elements. Number of halfwaves and modal shape (antisymmetric (A) or symmetric (S)) are appended in superscript. The values in parantheses indicate the percent differences with respect to Navier solution.

		R_f ($k = 0.002$, $\chi = 1.0$)		k ($R_f = 0.02$, $\chi = 1.0$)		χ ($R_f = 0.02$, $k = 0.02$)	
		0.01	0.1	0.001	0.1	0.001	0.1
	Navier	$839.00^{31,A}$	$3528.0^{1,A}$	$948.46^{12,A}$	$19791^{1,A}$	$2758.0^{24,S}$	$6689.1^{30,S}$
QC4	256_{514}	$842.12^{31,A}$ (0.37)	$3528.0^{1,A}$ (< 0.01)	$948.96^{12,A}$ (0.05)	$19792^{1,A}$ (< 0.01)	$2827.0^{23,S}$ (2.50)	$6725.7^{30,S}$ (0.55)
	128_{258}	$851.42^{30,A}$ (1.48)	$3528.1^{1,A}$ (< 0.01)	$950.51^{12,A}$ (0.22)	$19793^{1,A}$ (0.01)	$3025.6^{22,S}$ (9.70)	$6836.1^{29,S}$ (2.20)
	64_{130}	$886.64^{26,A}$ (5.68)	$3528.2^{1,A}$ (< 0.01)	$957.29^{12,A}$ (0.93)	$19798^{1,A}$ (0.03)	$3689.9^{20,S}$ (33.8)	$7250.9^{26,S}$ (8.40)
	32_{66}	$1012.3^{19,A}$ (20.6)	$3528.7^{1,A}$ (0.02)	$985.76^{11,A}$ (3.93)	$19819^{1,A}$ (0.14)	$5542.1^{16,S}$ (101)	$8587.2^{19,S}$ (28.4)
CL8	128_{642}	$839.08^{31,A}$ (0.01)	$3528.0^{1,A}$ (< 0.01)	$948.46^{12,A}$ (< 0.01)	$19791^{1,A}$ (< 0.01)	$2759.5^{24,S}$ (0.05)	$6690.0^{30,S}$ (0.01)
	64_{323}	$840.25^{31,A}$ (0.15)	$3528.0^{1,A}$ (< 0.01)	$948.50^{12,A}$ (< 0.01)	$19791^{1,A}$ (< 0.01)	$2773.6^{23,S}$ (0.57)	$6702.9^{30,S}$ (0.21)
	32_{163}	$848.73^{29,A}$ (1.16)	$3528.0^{1,A}$ (< 0.01)	$949.07^{12,A}$ (0.06)	$19791^{1,A}$ (< 0.01)	$2903.7^{22,S}$ (5.28)	$6841.2^{28,S}$ (2.27)
	16_{83}	$940.39^{11,A}$ (12.1)	$3528.0^{1,A}$ (< 0.01)	$956.42^{12,A}$ (0.84)	$19791^{1,A}$ (< 0.01)	3655.7^{-} (32.5)	$7812.0^{11,S}$ (16.8)

Subscript identifies the number of nodes in the mesh.

It is observed that the overall buckling load is easily grasped by the coarsest mesh, regardless of interpolation order (linear or quadratic). Nevertheless, a slight error in buckling load prediction is obtained for the linear element when compared to the quadratic one. Table 5.6 shows that local instabilities call for a refinement of the in-plane discretization. It is worth noting that this need for increased number of elements along the longitudinal direction strongly depends upon the number of halfwaves which characterize the buckled shape. Moreover, the error in buckling load value comes along with an erroneous prediction of the buckled shape: For all the configurations studied in this section, a percent difference of $< 0.5\%$ in the buckling load is found to provide the correct number of wrinkles of the buckling mode. It is worth noting that the convergence slows down for both linear and quadratic FEs as the axial rigidity of the core is weakened (i.e., for the case $\chi = 0.001$). As far as linear interpolation is concerned, four elements appear to be sufficient to properly resolve the half-wave of the wrinkling mode. Nevertheless, percent differences in the buckling load prediction may vary from $\approx 1.5\%$ for the thinnest face sheet configuration, up to $\approx 2\%$ and $\approx 10\%$ for orthotropic cores. On the other hand, the quadratic element looks more suited to grasp the wrinkling response characterized by short half-wavelength. Indeed, a mesh involving two elements per halfwave is proven to accurately predict both buckling load (percent differences $< 0.6\%$) and buckled shape.

Further insight about the convergence behaviour of the presented FE is given in Figure 5.3 (linear element) and Figure 5.4 (quadratic element). The percent differences reported in Table 5.6 are plotted, in log-log scale, against the number of nodes in the mesh. The buckled shape corresponding to the most refined mesh is also shown. All the conclusions previously drawn are demonstrated by referring to the convergence curves of Figure 5.3 and Figure 5.4. In addition, the convergence rate for the QC4 element is found to be quadratic, whereas the CL8 element exhibits a cubic convergence rate. It appears that the convergence rate of the buckling load is one order faster when compared to the static response (Section 2.4).

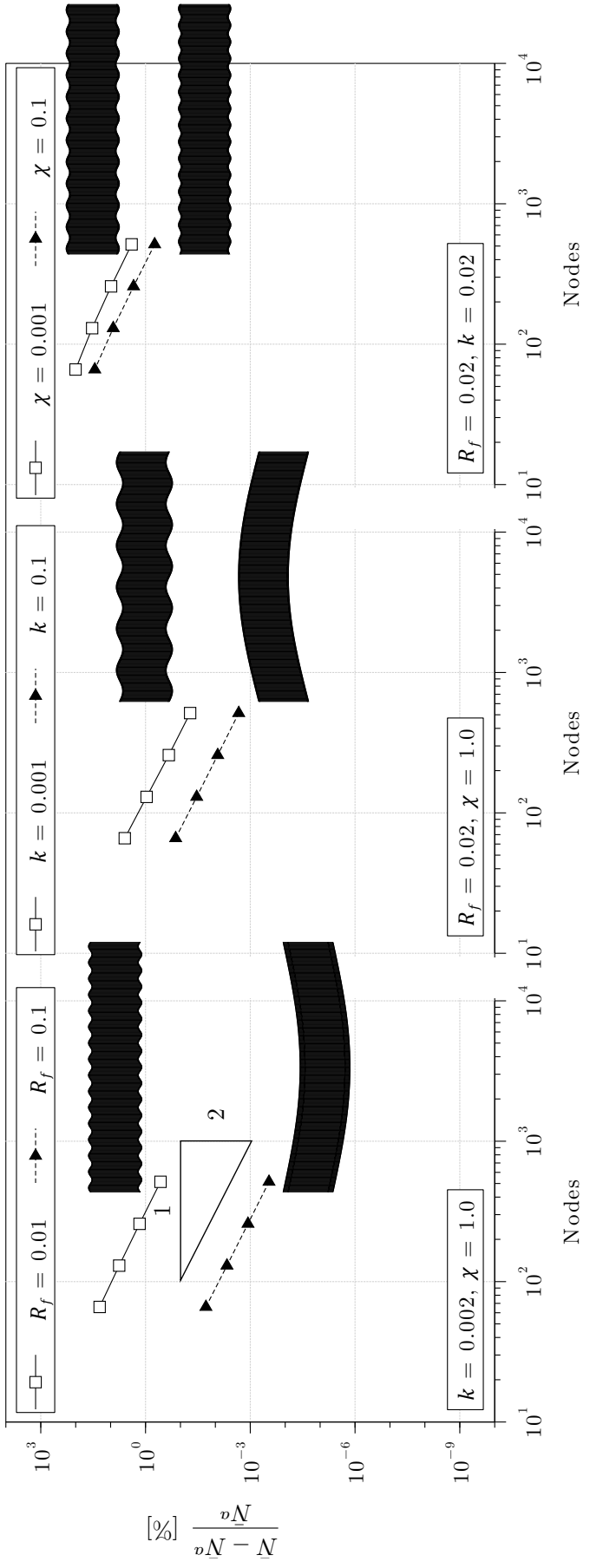

Figure 5.3: DO-TC: QC4 convergence rate of critical buckling load N_{cr} [N/mm] of LD4 model for different sandwich configurations.

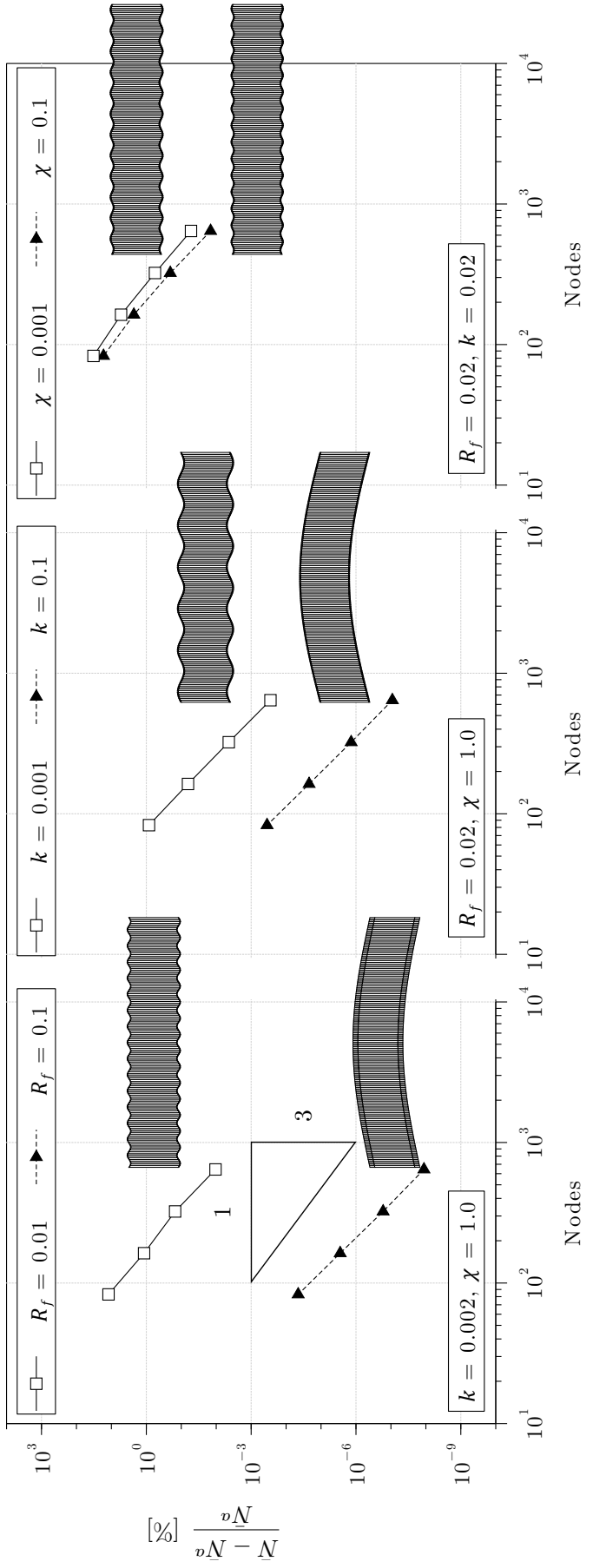

Figure 5.4: DO-TC: CL8 convergence rate of critical buckling load N_{cr} [N/mm] of LD4 model for different sandwich configurations.

Model assessement. A model assessment is next performed to investigate the influence of the plate theory used for the core ply on the critical buckling load. Based on the previous convergence study, a mesh of 64×1 CL8 elements will be used. Within the present FEM approach, the face sheets are modelled according to FSDT, whilst the core model is progressively refined by increasing the order of the theory, ranging from ED_{12} up to ED_{77} =ED7. Indeed, FSDT is found to be adequate to represent the buckling phenomenon in the thin face sheets [46]. On the other hand, according to the sandwich configuration, the through-thickness approximation in the core must be enhanced to grasp not only the correct buckling load, but also the correct number of halfwaves which characterize the buckled configuration [83]. The results are summarized in Table 5.7, where the buckling loads are reported for different sandwich configurations. Values in parentheses identify the number of nodal DOFs associated to the model. Entries in bold indicate converged solutions with respect to the core model, obtained with the lowest number of nodal DOFs. Two results presented by D'Ottavio in Ref.[83] are used for comparison:

Solid FEM: A converged FEM solution obtained with the commercial software Ansys. The problem is defined in the (xz)-plane by modelling the sandwich panel cross section. A linear four-node element under the plane strain assumption is employed. The FE mesh involves 256 elements along the longitudinal (x) direction, whereas 4 and 60 elements are used for the face sheets and the core, respectively.

Navier: A LM4 model whose through-the-thickness approximation is enhanced by subdividing the core ply into 3 computational layer. This model provides a converged solution in terms of both buckling load and buckled shape.

The Navier solution of the LD4 model of the previous convergence analysis is also reported as an additional comparison solution. As far as the overall buckling is concerned (for the sandwich configurations defined by $k = 0.002, R_f = 0.1, \chi = 1.0$ and $k = 0.1, R_f = 0.02, \chi = 1.0$), it is observed that the model ED_{32} ($N_{u_x} = 3, N_{u_z} = 2$) guarantees a converged solution, so long as at least a cubic expansion is assumed for the axial displacement. However, as the axial rigidity of the sandwich panel decreases, the short half-wavelength of the wrinkles calls for a refinement of the core theory. The SGUF model FSDT/ED_{76} has proven able to cope with the local response for all the sandwich panel configurations here presented, yielding quasi-3D solution while drastically reducing the number of DOFs with respect to the converged mixed model of Ref. [83].

Table 5.7: DO-TC: Uniaxial buckling loads N_{cr} [N/mm] of a sandwich panel loaded in compression with an imposed uniform strain: influence of core model for different sandwich configurations. Bold values identify the converged solution asking for the lowest number of nodal DOFs.

Model (nDOF)	R_f ($k=0.002$, $\chi=1.0$)		k ($R_f=0.02$, $\chi=1.0$)		χ ($R_f=0.02$, $k=0.02$)	
	0.01	0.1	0.001	0.1	0.001	0.1
Ansys [83]	$818.80^{31,A}$	$3528.0^{1,A}$	$945.93^{13,A}$	$19792^{1,A}$	$2767.6^{23,S}$	$6464.9^{33,A}$
Navier ${}^{3N_p^c}$LM4 [83] (126)	$813.47^{32,A/S}$	$3528.0^{1,A}$	$945.02^{13,A}$	$19791^{1,A}$	$2758.0^{24,S}$	$6426.9^{33,A/S}$
LD4 (39)	$840.25^{31,A}$	$3528.0^{1,A}$	$948.50^{12,A}$	$19791^{1,A}$	$2773.6^{23,S}$	$6702.9^{30,S}$
FSDT/ED7 (28)	$815.63^{31,A}$	$3528.2^{1,A}$	$945.40^{13,A}$	$19792^{1,A}$	$2776.7^{23,S}$	$6461.2^{33,A}$
FSDT/ED$_{76}$ (27)	$\mathbf{815.63^{31,A}}$	$3528.2^{1,A}$	$945.40^{13,A}$	$19792^{1,A}$	$2776.8^{23,S}$	$\mathbf{6461.2^{33,A}}$
FSDT/ED$_{75}$ (26)	$818.19^{31,S}$	$3528.2^{1,A}$	$945.40^{13,A}$	$19792^{1,A}$	$2776.8^{23,S}$	$6468.1^{33,S}$
FSDT/ED$_{74}$ (25)	$828.95^{30,A}$	$3528.2^{1,A}$	$\mathbf{945.40^{13,A}}$	$19792^{1,A}$	$2777.1^{23,S}$	$6476.2^{32,A}$
FSDT/ED$_{73}$ (24)	$875.97^{29,S}$	$3528.2^{1,A}$	$949.37^{13,S}$	$19792^{1,A}$	$2777.1^{23,S}$	$6695.7^{30,S}$
FSDT/ED$_{72}$ (23)	$1029.1^{26,A}$	$3528.2^{1,A}$	$960.12^{12,A}$	$19792^{1,A}$	$2807.2^{23,S}$	$7734.6^{25,A}$
FSDT/ED$_{67}$ (26)	$816.91^{31,S}$	$3528.2^{1,A}$	$945.51^{13,A}$	$19792^{1,A}$	$2776.7^{23,S}$	$6467.4^{33,S}$
FSDT/ED6 (25)	$818.19^{31,S}$	$3528.2^{1,A}$	$945.51^{13,A}$	$19792^{1,A}$	$2776.8^{23,S}$	$6468.1^{33,S}$
FSDT/ED$_{65}$ (24)	$818.19^{31,S}$	$3528.2^{1,A}$	$945.51^{13,A}$	$19792^{1,A}$	$2776.8^{23,S}$	$6468.1^{33,S}$
FSDT/ED$_{64}$ (23)	$830.84^{31,A}$	$3528.2^{1,A}$	$945.51^{13,A}$	$19792^{1,A}$	$2777.1^{23,S}$	$6486.6^{32,A}$
FSDT/ED$_{63}$ (22)	$875.97^{29,S}$	$3528.2^{1,A}$	$949.37^{13,S}$	$19792^{1,A}$	$2777.1^{23,S}$	$6695.7^{30,S}$
FSDT/ED$_{62}$ (21)	$1029.3^{26,A}$	$3528.2^{1,A}$	$960.15^{12,A}$	$19792^{1,A}$	$2807.2^{23,S}$	$7736.9^{25,A}$
FSDT/ED$_{57}$ (24)	$819.70^{31,A}$	$3528.2^{1,A}$	$945.51^{13,A}$	$19792^{1,A}$	$2776.7^{23,S}$	$6481.9^{32,A}$
FSDT/ED$_{56}$ (23)	$819.70^{31,A}$	$3528.2^{1,A}$	$945.51^{13,A}$	$19792^{1,A}$	$2776.8^{23,S}$	$6481.9^{32,A}$
FSDT/ED5 (22)	$825.58^{31,S}$	$3528.2^{1,A}$	$945.51^{13,A}$	$19792^{1,A}$	$2776.8^{23,S}$	$6486.6^{32,A}$
FSDT/ED$_{54}$ (21)	$830.84^{31,A}$	$3528.2^{1,A}$	$945.51^{13,A}$	$19792^{1,A}$	$2777.1^{23,S}$	$6486.6^{32,A}$
FSDT/ED$_{53}$ (20)	$877.92^{29,S}$	$3528.2^{1,A}$	$949.88^{13,S}$	$19792^{1,A}$	$2777.1^{23,S}$	$6719.9^{30,S}$
FSDT/ED$_{52}$ (19)	$1029.3^{26,A}$	$3528.2^{1,A}$	$960.15^{12,A}$	$19792^{1,A}$	$2807.2^{23,S}$	$7736.9^{25,A}$
FSDT/ED$_{47}$ (22)	$822.55^{32,S}$	$3528.2^{1,A}$	$948.67^{12,A}$	$19792^{1,A}$	$\mathbf{2776.7^{23,S}}$	$6586.5^{32,S}$
FSDT/ED$_{46}$ (21)	$825.11^{32,A}$	$3528.2^{1,A}$	$948.67^{12,A}$	$19792^{1,A}$	$2776.8^{23,S}$	$6595.8^{32,S}$
FSDT/ED$_{45}$ (20)	$825.58^{31,S}$	$3528.2^{1,A}$	$948.73^{12,A}$	$19792^{1,A}$	$2776.8^{23,S}$	$6595.8^{32,S}$
FSDT/ED4 (19)	$840.77^{31,A}$	$3528.2^{1,A}$	$948.73^{12,A}$	$19792^{1,A}$	$2777.1^{23,S}$	$6719.9^{30,S}$
FSDT/ED$_{43}$ (18)	$877.92^{29,S}$	$3528.2^{1,A}$	$949.88^{13,S}$	$19792^{1,A}$	$2777.1^{23,S}$	$6719.9^{30,S}$
FSDT/ED$_{42}$ (17)	$1030.5^{26,A}$	$3528.2^{1,A}$	$961.29^{12,A}$	$19792^{1,A}$	$2807.2^{23,S}$	$7780.7^{25,A}$
FSDT/ED$_{37}$ (20)	$824.17^{32,S}$	$3528.2^{1,A}$	$948.67^{12,A}$	$19792^{1,A}$	$2789.0^{23,S}$	$6880.0^{31,A}$
FSDT/ED$_{36}$ (19)	$825.11^{32,A}$	$3528.2^{1,A}$	$948.67^{12,A}$	$19792^{1,A}$	$2789.1^{23,S}$	$6880.0^{31,A}$
FSDT/ED$_{35}$ (18)	$827.64^{32,S}$	$3528.2^{1,A}$	$948.73^{12,A}$	$19792^{1,A}$	$2789.1^{23,S}$	$6967.5^{30,A}$
FSDT/ED$_{34}$ (17)	$840.77^{31,A}$	$3528.2^{1,A}$	$948.73^{12,A}$	$19792^{1,A}$	$2790.9^{23,S}$	$6967.5^{30,A}$
FSDT/ED3 (16)	$888.46^{30,S}$	$3528.2^{1,A}$	$960.60^{13,S}$	$19792^{1,A}$	$2790.9^{23,S}$	$7780.7^{25,A}$
FSDT/ED$_{32}$ (15)	$1030.5^{26,A}$	$\mathbf{3528.2^{1,A}}$	$961.29^{12,A}$	$\mathbf{19792^{1,A}}$	$2807.4^{23,S}$	$7780.7^{25,A}$
FSDT/ED$_{27}$ (18)	$824.17^{32,S}$	$3528.3^{1,A}$	$958.51^{13,S}$	$19877^{1,A}$	$2789.0^{23,S}$	$7182.2^{35,S}$
FSDT/ED$_{26}$ (17)	$826.32^{32,A}$	$3528.3^{1,A}$	$958.51^{13,S}$	$19877^{1,A}$	$2789.1^{23,S}$	$7188.4^{36,A}$
FSDT/ED$_{25}$ (16)	$827.64^{32,S}$	$3528.3^{1,A}$	$958.51^{13,S}$	$19877^{1,A}$	$2789.1^{23,S}$	$7222.9^{34,S}$
FSDT/ED$_{24}$ (15)	$841.24^{31,A}$	$3528.3^{1,A}$	$959.94^{13,A}$	$19877^{1,A}$	$2790.9^{23,S}$	$7381.4^{34,A}$
FSDT/ED$_{23}$ (14)	$888.46^{30,S}$	$3528.3^{1,A}$	$960.60^{13,S}$	$19877^{1,A}$	$2790.9^{23,S}$	$7810.7^{31,S}$
FSDT/ED2 (13)	$1037.4^{27,A}$	$3528.3^{1,A}$	$980.86^{12,A}$	$19877^{1,A}$	$2807.4^{23,S}$	$9245.2^{1,A}$
FSDT/ED$_{17}$ (16)	$826.32^{32,A}$	$3528.3^{1,A}$	$958.82^{13,S}$	$19877^{1,A}$	$6606.7^{36,S}$	$7186.8^{34,S}$
FSDT/ED$_{16}$ (15)	$826.32^{32,A}$	$3528.3^{1,A}$	$958.83^{13,S}$	$19877^{1,A}$	$6651.4^{35,S}$	$7188.4^{36,A}$
FSDT/ED$_{15}$ (14)	$841.24^{31,A}$	$3528.3^{1,A}$	$958.83^{13,S}$	$19877^{1,A}$	$6651.4^{35,S}$	$7224.6^{34,S}$
FSDT/ED$_{14}$ (13)	$841.24^{31,A}$	$3528.3^{1,A}$	$959.94^{13,A}$	$19877^{1,A}$	$6982.1^{35,A}$	$7381.4^{34,A}$
FSDT/ED$_{13}$ (12)	$909.37^{28,S}$	$3528.3^{1,A}$	$960.94^{13,S}$	$19877^{1,A}$	$7279.9^{33,S}$	$7830.1^{32,S}$
FSDT/ED$_{12}$ (11)	$1037.4^{27,A}$	$3528.3^{1,A}$	$980.86^{12,A}$	$19877^{1,A}$	$9032.1^{30,A}$	$9245.2^{1,A}$

5.3.2 Sandwich face sheets wrinkling under transverse load

The second example aims to demonstrate the capability of the present computational approach to compute wrinkling loads for sandwich panels that work in bending. Indeed, the compression stress state in one of the face sheets may result in local instability which propagates rapidly to the weak core. If the plate model is sufficiently rich, the present 2D FEM is capable of grasping this complex failure mechanism. The analysis refers to the three-point bending test studied by Yuan *et al.* [115], and therefore referred to as Yuan-TestCase (Y-TC). It considers a wide sandwich panel made up of two thin and stiff face sheets of Kevlar and a weak and thick foam core from Evonik industries, namely ROHACELL® 50. Both face sheet and core materials are assumed to be isotropic. The geometric and elastic properties are summarized in Table 5.8.

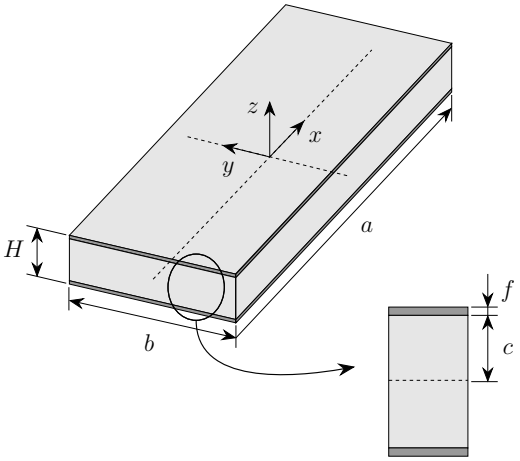

Figure 5.5: Y-TC: Sandwich beam-plate geometry.

Table 5.8: Y-TC: Geometric and material data.

$a = 300$ mm; $b = 60$ mm		
$f = 0.5$; $2c = 19.05$ mm		
$H = 20.05$ mm		
	ROHACELL® 50	Kevlar
E [MPa]	52.5	27400
ν	0.25	0.3
G [MPa]	21	10538.5

The sandwich panel is subjected to a concentrated force acting at the centre along the $z-$direction of the panel. The typically three-dimensional boundary conditions of the three-point bending test are reproduced in a very straightforward manner within the present SGUF modelling: the roller boundary condition can in fact be accurately reproduced by constraining the transverse displacement at the panel's bottom surface and at specific locations along the $x-$coordinate (see Figure 5.6). Since both loading and boundary conditions exhibit symmetry about the midspan, only the left half-panel is modelled. The problem is again studied under the plane strain assumption, which is obtained by constraining all displacements along y. With reference to the axes defined in Figure 5.5, the boundary conditions applied to the left half-panel are thus:

$$u_y(x, y, z) = u_x(0, y, z) = u_z(-a/2, y, -H/2) = 0 \tag{5.33}$$

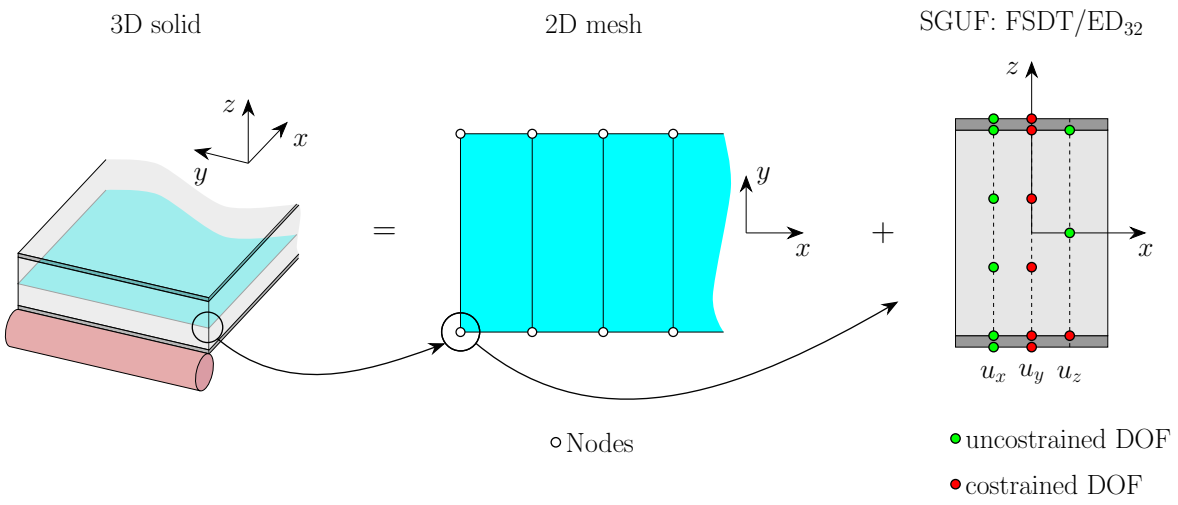

Figure 5.6: Y-TC: Roller boundary condition of the three-point bending test and plane strain assumption within the present bi-dimensional approach.

and the load is introduced as

$$\int_{-b/2}^{b/2} P_z\left(x=0, y, z=H/2\right)\ \mathrm{d}y = -P \tag{5.34}$$

Comparison is made with respect to the results of Ref.[115] along with a solid elasticity with 2D plane strain FEM solution obtained with the commercial software package Abaqus. In Ref.[115] authors employ the EHSAPT formulated by Phan [117] which corresponds to the SGUF model CLT/ED$_{32}$. For the sake of comparison with the results presented in Ref.[115], the present FE mesh involves 340 linear elements along the $x-$direction of the half-panel and only one element is used along the width direction. To properly describe the steep gradients in the proximity of the loaded area, the mesh is refined with a bias factor (bf) of 50 is set towards the symmetry axis, see Figure 5.7. Through the thickness direction, 4 elements are used for the face sheets and 15 for the core. The influence of the kinematic model of the core is investigated by considering

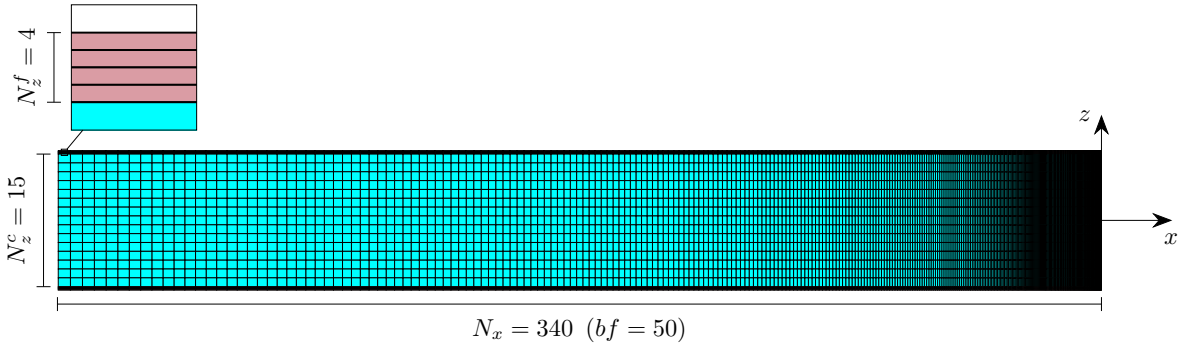

Figure 5.7: Y-TC: FE model in Abaqus.

four different SGUF models. The face sheets are always modelled according to FSDT,

whilst the core considers either theories retaining the full three-dimensional constitutive law or reduced stiffness coefficients.

Pre-buckling. The first analysis is about the static response of the sandwich panel in a three-point bending configuration. Since within the present FE approach large displacements and non-linear effects are neglected in the definition of the strains, only results concerning the geometrically linear EHSAPT will be addressed from Ref.[115]. In Figure 5.8 the applied load is plotted against the transverse displacement at the

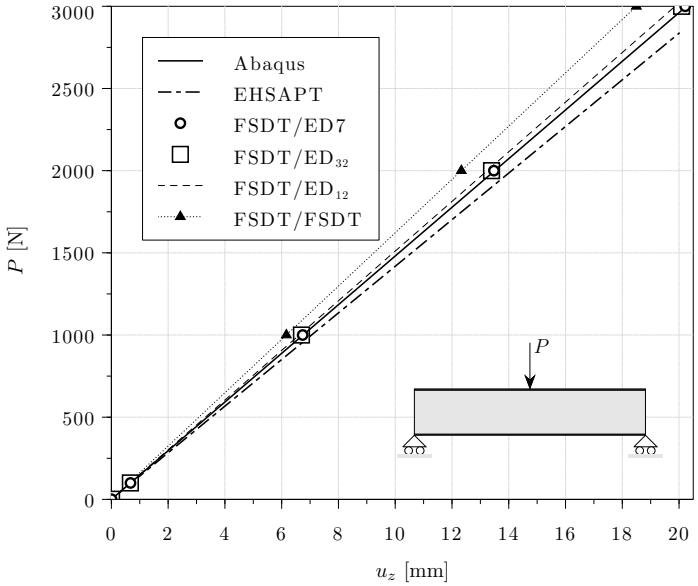

Figure 5.8: Y-TC: Transverse displacement u_z at sandwich panel midspan for different values of transversal load P.

middle point of the top surface. Results from Ref.[115] and the ones obtained with the commercial software Abaqus are included for comparison. Since all nonlinear terms are neglected, the displacement is proportional to the applied load. A good agreement is found between Abaqus and present FE results as long as the kinematics in the core takes into account the transverse compressibility. On the other hand, a small discrepancy is observed when referring to the EHSAPT solution.

Figure 5.9 shows the distributions of in-plane stress σ_{xx} and transverse normal stress σ_{zz} across the core ply at the symmetry plane ($x = 0$) and for a load $P = -1300$ N. Abaqus results are taken here as a reference solution. As expected, the model retaining a bi-dimensional constitutive law in the core fails to predict the pure three-dimensional stress state. The EHSAPT assumes for the core a cubic distribution of the in-plane displacement variables and a quadratic distribution for the transverse displacement. For this reason, the FSDT/ED$_{32}$ solution agrees very well with the

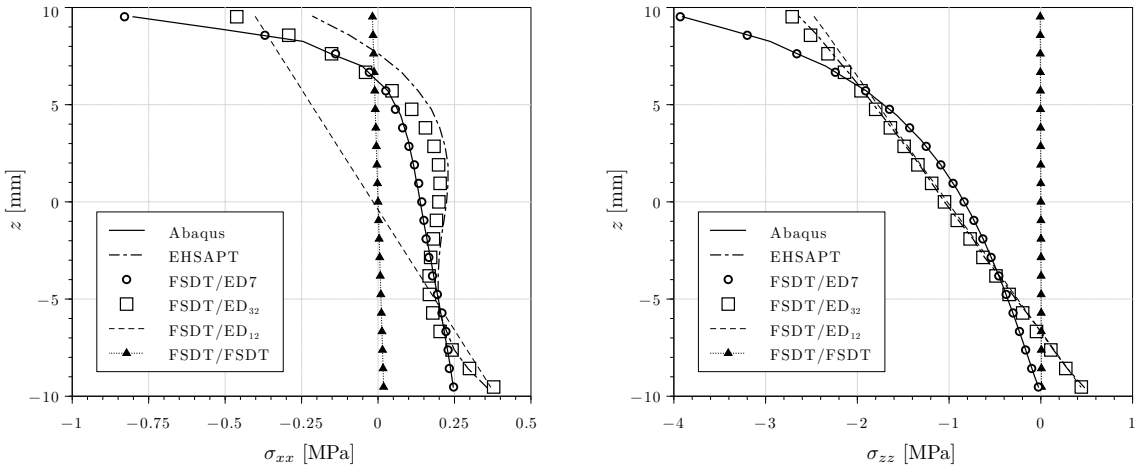

(a) Axial stress **(b)** Transverse normal stress

Figure 5.9: Y-TC: Stress distributions in the core at $x = 0$: a) axial stress, b) transverse normal stress.

geometrically linear EHSAPT solution reported in Ref.[115] obtained with the linear form of EHSAPT. Nevertheless, the FSDT/ED$_{32}$ provides a slightly better prediction of the stress magnitude at the upper face-core interface when compared to EHSAPT. This is attributed to the Kirchhoff hypothesis that EHSAPT retains for the behaviour of the face sheets. The quadratic approximation of the transverse displacement leads to a linear transverse strain ϵ_{zz} across the core. As a result, an erroneous linear distribution of the transverse normal stress is predicted. In particular, low-order theories and the linear EHSAPT underestimate the transverse normal stress at the upper face-core interface. On the other hand, FSDT/ED7 model yields a very accurate solution which is seen to perfectly match the Abaqus results.

The axial stress distribution across the face sheets is plotted in Figure 5.10 in order to comprehensively understand the onset of local instabilities. For the sake of clarity, the face sheets regions are shaded in gray. It is observed that, since the transverse load acts downwards, the lower face sheet is subjected to a tensile load ($\sigma_{xx} > 0$). However, the upper face sheet can experience both tension and compression across the thickness, depending on the theory used to model the core. This phenomenon can in fact be explained by the effect of the local indentation, which introduces a local bending of the top face sheet. So, the FSDT/FSDT model has a top skin that is entirely in compression since the core is not allowed to stretch. The slight discrepancy between Abaqus and present FE solutions suggests that a refinement of the theory in the upper face sheet may be required to cope with the steep gradients induced by the localized load.

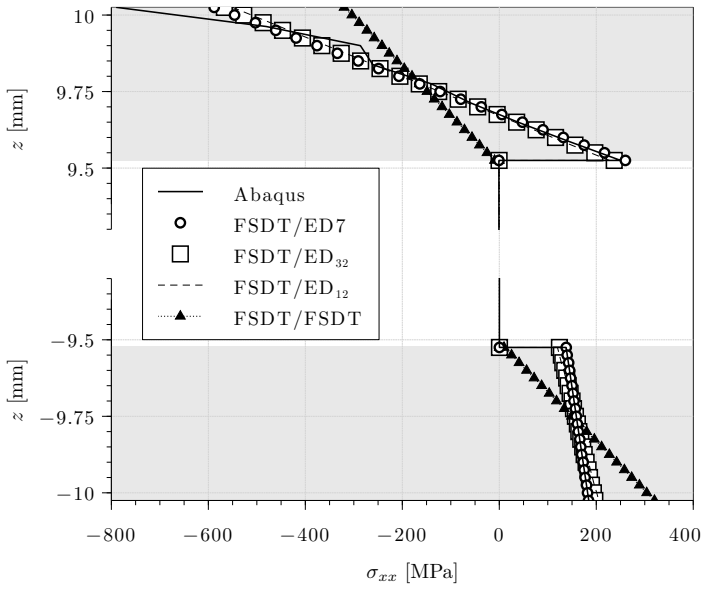

Figure 5.10: Y-TC: Axial stress distribution across the face sheets thickness at $x = 0$.

Buckling. The second analysis deals with the buckling response of the sandwich panel in the three-point bending configuration. By following the derivation presented in Section 5.1, the previous static analysis with $P = -1$ N is used to define the initial stress state.

Table 5.9: Y-TC: First three buckling loads of the sandwich strut in the three-point bending configuration.

Mode	Abaqus	FSDT/ED7 (28)	FSDT/ED$_{32}$ (15)	FSDT/ED$_{12}$ (11)	FSDT/FSDT (9)
1	-2264.2	-2248.2	-2359.2	-2431.1	-9.3e+12
2	2326.3	2283.3	2402.6	2519.7	-8.0e+14
3	-2464.3	-2453.0	-2582.5	-2692.5	-2.5e+15

The parentheses identify the number of nodal DOF associated to the model.

The bucking loads for the first 3 modes are listed in Table 5.9. The number of nodal DOFs is also included to provide a qualitative estimation of the computational effort associated with each hierarchical model. In order to provide a physical interpretation of the numerical values of Table 5.9, the buckled shapes of the first 2 modes are shown in Figure 5.11. At first, it is remarked that the first buckling mode is associated to a negative eigenvalue, irrespective of the model. Looking at Figure 5.11a, this mode is shown to correspond to a local instability (wrinkling) of the bottom face sheet — i.e., this wrinkling mode would occur if the sandwich was loaded with a force acting upwards. The reason for this is to be found in the local in-plane stress

distributions obtained from the pre-buckling analysis and reported in Figure 5.10. In fact, multiplying by -1 the acting load P, the bottom skin would buckle first because its initial stress would be entirely in compression, whilst the top face sheet is seen to experience a local bending with in-plane stresses that are partially in tension and partially in compression. The first positive eigenvalue is associated to the second mode, which corresponds to the local wrinkling of the top face sheet, as it would have been expected from the three-point bending configuration. It is worthwhile emphasising that the wrinkling modes cannot be grasped unless the kinematic model adopted for the core allows for its compressibility: results for the FSDT/FSDT model are obviously completely meaningless. Finally, it is noticed the very good agreement between the most refined FSDT/ED7 SGUF model and the quasi-3D solution provided by Abaqus in terms of both, the wrinkling load (a difference of less of 0.2% is obtained) and the modal shape.

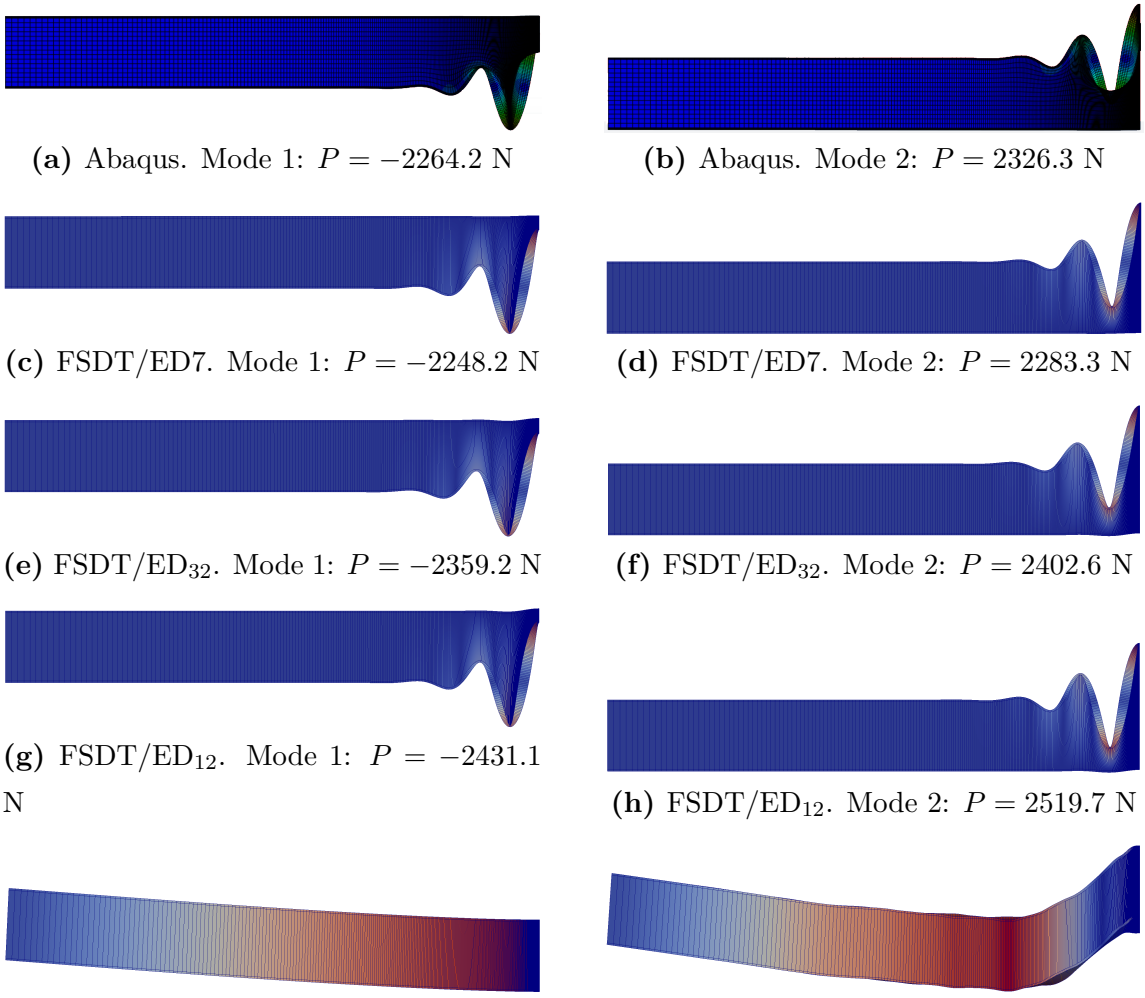

(a) Abaqus. Mode 1: $P = -2264.2$ N

(b) Abaqus. Mode 2: $P = 2326.3$ N

(c) FSDT/ED7. Mode 1: $P = -2248.2$ N

(d) FSDT/ED7. Mode 2: $P = 2283.3$ N

(e) FSDT/ED$_{32}$. Mode 1: $P = -2359.2$ N

(f) FSDT/ED$_{32}$. Mode 2: $P = 2402.6$ N

(g) FSDT/ED$_{12}$. Mode 1: $P = -2431.1$ N

(h) FSDT/ED$_{12}$. Mode 2: $P = 2519.7$ N

(i) FSDT/FSDT. Mode 1: $P = -9.3\text{e+}12$ N

(j) FSDT/FSDT. Mode 2: $P = -8.0\text{e+}14$ N

Figure 5.11: Y-TC: Buckled shapes of the sandwich strut in the three-point bending configuration for the first two buckling modes. Influence of the SGUF model on buckling pattern.

Chapter 6

Conclusions & Outlook

This PhD thesis has extended for the first time the variable kinematics plate modeling approach referred to as Sublaminate Generalized Unified Formulation (SGUF), to the general Finite Element framework. The idealisation of the composite stack into sublaminates allows to locally refine the theory to account for shear and transverse strain, whilst low-order theories can be still used in those regions where a three-dimensional stress state is not expected to occur. Bi-linear four-nodes and quadratic eight-nodes elements of general quadrilateral shape have been formulated for conventional displacement-based as well as RMVT-based mixed plate models. The adopted QC4/CL8 interpolations for the transverse shear strain makes the element locking-free and robust against distorted mesh. A new in-house code has been implemented from scratch to host the FE development. The proposed FE has been applied in the first place to investigate the static response of sandwich panels, ranging from global bending up to local indentation under a concentrated load. The results demonstrate the flexibility of the approach, that allows to adapt the number of DOF (i.e., the computational effort) depending on the desired accuracy and selecting independently the in-plane mesh density and the through-thickness model parameters. It has been shown that FE mesh refinement and dedicated high-order models for selected sublaminates allow to recover the complex three-dimensional response of the facesheets and the core with a number of DOF that is far below that required by currently available approaches in commercial FE packages. The possibility of exactly satisfying the transverse stress BC in RMVT-based models has been exploited thanks to the independent choice of expansion orders for displacement and stress fields, thus avoiding spurious oscillations induced by mismatches between the kinematic and static field approximations. Enhanced accuracy could be attained, as exemplarily demonstrated in the free-edge analysis of laminates: the bi-material interface singularity could be extremely well resolved with stress fields

accurately meeting the equilibrium conditions.

Subsequently, the dynamic behaviour of composite sandwich structures hosting one or more viscoelastic layers has been addressed. The frequency-dependent behaviour of the viscoelastic layer has been described within the Complex Modulus Approach by resorting to the Zener-type fractional derivative (FDZ) model and to a more conventional model relying on series expansions (ADF). Iterative procedures have also been implemented to deal with nonlinear generalized eigenvalue problem. Due to the possibility of optimizing the number of DOF, the SGUF approach proved to be a powerful tool whenever an iterative resolution algorithm is required for the problem to be solved. Natural frequencies and resonance peak amplitudes calculated with the proposed FE have been compared to those reported in the literature, pointing out the robustness and reliability of the present approach in predicting the dynamic response of a sandwich structure, irrespective of either the geometric or material properties of the viscoelastic layer.

The last part of the thesis set the focus on the stability of sandwich panels. Thanks to the refined models, long-wave (global) as well as short-wave buckling (wrinkling) have been addressed. The analysis is performed within the framework of classical linearised stability analysis. Different ways of defining the pre-buckling state have been implemented: the initial stress matrix can be computed starting from a direct definition of a strain or stress state (e.g. uniformly strained panels), or more generally from a preliminary static FE computation. It is worth noting that no post-processing of the preliminary static step is needed since the invariant *fundamental nuclei* defining the initial stress matrix have been directly derived in terms of displacement unknowns. First, a validation and assessment is given by considering an uniaxial compression obtained by uniformly straining the cross section of the panel. In this case, the initial stress is simply evaluated from the constitutive law. The buckling load sensitivity with respect to the face sheets thickness and material properties of the constituents has been investigated. The proposed FE has shown quasi-3D accuracy in recovering both periodic global and local buckling response of symmetric sandwich structures, irrespective of geometric or constitutive parameters used in the analysis. In particular, low-order core models retaining at least a quadratic distribution of the transverse displacement provide an accurate prediction of the overall buckling load. Nevertheless, they fail in describing the local buckling of the face sheets (wrinkling). Indeed, high-order core models are seen to be needed whenever local instabilities characterised by short half-wavelengths occur. Further studies have been conducted to establish the onset of local instabilities of a sandwich panel in the three-point bending configuration.

The proposed FE has been proven able to predict the expected non-periodic local instabilities arising in the proximity of the loaded area due to the compression stress state experienced by one of the face sheets.

Outlook. Future developments of the proposed FE code will be directed towards curved shell geometries as well as the solution of non-linear problems. The extension of the geometric non-linearity to the complete tangent operator and towards the full non-linear strains will allow to broaden substantially the field application of the developed computational tool. Material nonlinearities could be included in particular to analyse delamination. Industrially relevant problems such as skin-core debonding, ply drop-off and open- as well as filled-hole configurations could be analysed with the proposed FE tool. Furthermore, it is worthwhile exploring the possibility to couple the variable kinematics approach offered by the SGUF with the FEM so to adopt different models in different elements within a global-local modelling strategy. Relevant literature to this topic is already available [157, 158]. Finally, it is important to underline the practical relevance of the interfaces between theoretical modelling, numerical simulations and experimental evidence. In this sense, some activities directed towards a dialogue with experiments have been already started and shall be further developed. The identification of viscoelastic FDZ parameters from experimental FRF has been attempted within a collaboration with the IST of Lisbon in the framework of the French-Portuguese Pessoa program. SGUF models have been already challenged with respect to wrinkling problems of sandwich structures representative of the Elixir aircraft: this collaboration could be further extended to the FE program presented in this thesis, upon including e.g. imperfect geometries, material nonlinearities and more complex loading conditions.

Bibliography

[1] B. Castanie, C. Bouvet, and M. Ginot. Review of composite sandwich structure in aeronautic applications. *Compos. C*, 1:100004, 2020. doi:10.1016/j.jcomc.2020.100004. (cit. on p. xxi).

[2] G. Palomba, G. Epasto, and V. Crupi. Lightweight sandwich structures for marine applications: a review. *Mech. Adv. Mater. Struct.*, 0(0):1–26, 2021. doi:10.1080/15376494.2021.1941448. (cit. on p. xxi).

[3] J. M. Davies. *Lightweight sandwich construction*. Blackwell Science Ltd., Hoboken, NJ, 2008. (cit. on p. xxi).

[4] J. R. Vinson. *The Behavior of Sandwich Structures of Isotropic and Composite Materials*. Technomic Publishing Co., 2018. (cit. on pp. xxi and 5).

[5] P. R. Oliveira, M. May, T. H. Panzera, and S. Hiermaier. Bio-based/green sandwich structures: A review. *Thin-Wall. Struct.*, 177:109426, 2022. doi:10.1016/j.tws.2022.109426. (cit. on p. xxi).

[6] E. Reissner. On a certain mixed variational theorem and a proposed application. *Int. J. Numer. Meth. Eng*, 20(7):1366–1368, 1984. doi:10.1002/nme.1620200714. (cit. on pp. xxii, 2, and 10).

[7] E. Reissner. On a mixed variational theorem and on shear deformable plate theory. *Int. J. Numer. Meth. Eng*, 23(2):193–198, 1986. doi:10.1002/nme.1620230203. (cit. on pp. xxii, 2, and 10).

[8] E. Carrera and S. Brischetto. A comparison of various kinematic models for sandwich shell panels with soft core. *J. Compos. Mater.*, 43(20):2201–2221, 2009. doi:10.1177/0021998309343716. (cit. on pp. 1 and 32).

[9] I. M. Daniel, E. E. Gdoutos, K. Wang, and J. L. Abot. Failure Modes of Composite Sandwich Beams. *Int. J. Damage Mech.*, 11(4):309–334, 2002. doi:10.1106/105678902027247. (cit. on p. 1).

[10] L. A. Carlsson and G. A. Kardomateas. *Structural and Failure Mechanics of Sandwich Composites*. Springer, 2011. (cit. on pp. 1 and 5).

[11] V. Birman and G. A. Kardomateas. Review of current trends in research

and applications of sandwich structures. *Compos. B: Eng.*, 142:221–240, 2018. doi:10.1016/j.compositesb.2018.01.027. (cit. on p. 1).

[12] A. D. Hasanyan and A. M. Waas. Micropolar Constitutive Relations for Cellular Solids. *J. Appl. Mech.*, 83(4), 2016. doi:10.1115/1.4032115. (cit. on p. 1).

[13] A. T. Karttunen, J. N. Reddy, and J. Romanoff. Two-scale micropolar plate model for web-core sandwich panels. *Int. J. Appl. Mech.*, 170:82–94, 2019. doi:10.1016/j.ijsolstr.2019.04.026. (cit. on p. 1).

[14] F. Tornabene, M. Viscoti, R. Dimitri, and M. A. Aiello. Higher order formulations for doubly-curved shell structures with a honeycomb core. *Thin-Wall. Struct.*, 164:107789, 2021. doi:10.1016/j.tws.2021.107789. (cit. on p. 1).

[15] W. S. Burton and A. K. Noor. Assessment of computational models for sandwich panels and shells. *Comput. Meth. in Appl. Mech. Eng.*, 124(1):125–151, 1995. doi:10.1016/0045-7825(94)00750-H. (cit. on pp. 1 and 37).

[16] A. K. Noor, W. S. Burton, and C. W. Bert. Computational Models for Sandwich Panels and Shells. *Appl. Mech. Rev.*, 49(3):155–199, 1996. doi:10.1115/1.3101923. (cit. on p. 1).

[17] H. Hu, S. Belouettar, M. Potier-Ferry, and E. M. Daya. Review and assessment of various theories for modeling sandwich composites. *Compos. Struct.*, 84(3):282–292, 2008. doi:10.1016/j.compstruct.2007.08.007. (cit. on pp. 1 and 4).

[18] I. Kreja. A literature review on computational models for laminated composite and sandwich panels. *Cent. Eur. J. Engng.*, 1:59–80, 2011. doi:10.2478/s13531-011-0005-x. (cit. on p. 1).

[19] A. S. Sayyad and Y. M. Ghugal. On the free vibration analysis of laminated composite and sandwich plates: A review of recent literature with some numerical results. *Compos. Struct.*, 129:177–201, 2015. doi:10.1016/j.compstruct.2015.04.007. (cit. on p. 1).

[20] M. F. Caliri, A. J. M. Ferreira, and V. Tita. A review on plate and shell theories for laminated and sandwich structures highlighting the Finite Element Method. *Compos. Struct.*, 156:63–77, 2016. doi:10.1016/j.compstruct.2016.02.036. (cit. on p. 1).

[21] S. Irfan and F. Siddiqui. A review of recent advancements in finite element formulation for sandwich plates. *Chinese J. Aero.*, 32(4):785–798, 2019. doi:10.1016/j.cja.2018.11.011. (cit. on p. 1).

[22] F. Siddiqui and G. Kardomateas. Extended higher-order sandwich panel theory for plates with arbitrary aspect ratios. *J. Mech. Mater. Struct.*, 14(4):449–459, 2019. doi:10.2140/jomms.2019.14.449. (cit. on p. 1).

[23] F. Siddiqui and G. A. Kardomateas. Nonlinear static analysis of plates with arbitrary aspect ratios using Extended Higher Order Sandwich Panel Theory. *Int. J. Non-Lin. Mech.*, 132:103701, 2021. doi:10.1016/j.ijnonlinmec.2021.103701. (cit. on p. 1).

[24] V. L. Berdichevskii. Variational-asymptotic method of constructing a theory of shells. *J. Appl. Math. Mech.*, 43(4):711–736, 1979. doi:10.1016/0021-8928(79)90157-6. (cit. on p. 2).

[25] V. L. Berdichevskii. An asymptotic theory of sandwich plates. *Int. J. Eng. Sci*, 48(3):383–404, 2010. doi:10.1016/j.ijengsci.2009.09.001. (cit. on p. 2).

[26] S. Lee, C.-Y. Lee, and D. H. Hodges. On the mechanics of composite sandwich plates with three-dimensional stress recovery. *Int. J. Eng. Sci*, 157:103406, 2020. doi:10.1016/j.ijengsci.2020.103406. (cit. on p. 2).

[27] E. Carrera. Theories and Finite Elements for Multilayered Plates and Shells:A Unified compact formulation with numerical assessment and benchmarking. *Arch. Comput. Meth. Eng.*, 10(3):215–296, 2003. doi:10.1007/BF02736224. (cit. on p. 2).

[28] E. Carrera, M. Cinefra, M. Petrolo, and E. Zappino. *Finite element analysis of structures through unified formulation.* John Wiley & Sons, Ltd, 2014. (cit. on p. 2).

[29] E. Carrera, G. Giunta, and M. Petrolo. *Beam Structures: Classical and Advanced Theories.* John Wiley & Sons, 2011. (cit. on p. 2).

[30] L. Demasi. ∞^3 Hierarchy plate theories for thick and thin composite plates: The generalized unified formulation. *Compos. Struct.*, 84(3):256–270, 2008. doi:10.1016/j.compstruct.2007.08.004. (cit. on p. 2).

[31] L. Demasi. ∞^6 Mixed plate theories based on the Generalized Unified Formulation. Part I: Governing equations. *Compos. Struct.*, 87(1):1–11, 2009. doi:10.1016/j.compstruct.2008.07.013. (cit. on p. 2).

[32] L. Demasi. Partially Layer Wise advanced Zig Zag and HSDT models based on the Generalized Unified Formulation. *Eng. Struct.*, 53:63–91, 2013. doi:10.1016/j.engstruct.2013.01.021. (cit. on p. 2).

[33] E. Carrera. C_z^0 requirements—models for the two dimensional analysis of multilayered structures. *Compos. Struct.*, 37(3):373–383, 1997. doi:10.1016/S0263-8223(98)80005-6. (cit. on p. 2).

[34] L. Demasi. 2D, Quasi 3D and 3D Exact Solutions for Bending of Thick and Thin Sandwich Plates. *J. Sandwich Struct. Mater.*, 10(4):271–310, 2008. doi:10.1177/1099636208089311. (cit. on p. 2).

[35] E. Carrera, A. Garcia de Miguel, G. A. Fiordilino, and A. Pagani. Global/local analysis of free-edge stresses in composite laminates. In *AIAA Scitech 2019 Forum*, AIAA SciTech Forum. American Institute of Aeronautics and Astronautics, 2019. (cit. on p. 2).

[36] E. Carrera and M. Petrolo. Guidelines and Recommendations to Construct Theories for Metallic and Composite Plates. *AIAA J.*, 48(12):2852–2866, 2010. doi:10.2514/1.J050316. (cit. on p. 2).

[37] E. Carrera and M. Petrolo. On the Effectiveness of Higher-Order Terms in Refined Beam Theories. *J. App. Mech.*, 78(2), 2010. doi:10.1115/1.4002207. (cit. on p. 2).

[38] E. Carrera, F. Miglioretti, and M. Petrolo. Guidelines and Recommendations on the Use of Higher Order Finite Elements for Bending Analysis of Plates. *Int. J. Comput. Methods Eng.*, 12(6):303–324, 2011. doi:10.1080/15502287.2011.615792. (cit. on p. 2).

[39] L. Demasi and W. Yu. Assess the Accuracy of the Variational Asymptotic Plate and Shell Analysis Using the Generalized Unified Formulation. *Mech. Adv. Mater. Struct.*, 20(3):227–241, 2013. doi:10.1080/15376494.2011.584150. (cit. on p. 2).

[40] D. S. Mashat, E. Carrera, A. M. Zenkour, and S. A. Al Khateeb. Axiomatic/asymptotic evaluation of multilayered plate theories by using single and multi-points error criteria. *Compos. Struct.*, 106:393–406, 2013. doi:10.1016/j.compstruct.2013.05.047. (cit. on p. 2).

[41] M. Petrolo, M. Cinefra, A. Lamberti, and E. Carrera. Evaluation of mixed theories for laminated plates through the axiomatic/asymptotic method. *Compos. B: Eng.*, 76:260–272, 2015. doi:10.1016/j.compositesb.2015.02.027. (cit. on p. 2).

[42] M. Petrolo and A. Lamberti. Axiomatic/asymptotic analysis of refined layerwise theories for composite and sandwich plates. *Mech. Adv. Mater. Struct.*, 23(1):28–42, 2016. doi:10.1080/15376494.2014.924607. (cit. on p. 2).

[43] M. D'Ottavio. A Sublaminate Generalized Unified Formulation for the analysis of composite structures. *Compos. Struct.*, 142:187–199, 2016. doi:10.1016/j.compstruct.2016.01.087. (cit. on pp. 2, 8, 11, 12, and 13).

[44] M. Botshekanan Dehkordi, M. Cinefra, S. M. R. Khalili, and E. Carrera. Mixed LW/ESL models for the analysis of sandwich plates with composite faces. *Compos. Struct.*, 98:330–339, 2013. doi:10.1016/j.compstruct.2012.11.016. (cit. on p. 2).

[45] M. D'Ottavio, L. Dozio, R. Vescovini, and O. Polit. Bending analysis of composite laminated and sandwich structures using sublaminate variable-kinematic Ritz

models. *Compos. Struct.*, 155:45–62, 2016. doi:10.1016/j.compstruct.2016.07.036. (cit. on pp. 3 and 12).

[46] R. Vescovini, M. D'Ottavio, L. Dozio, and O. Polit. Buckling and wrinkling of anisotropic sandwich plates. *Int. J. Eng. Sci*, 130:136–156, 2018. doi:10.1016/j.ijengsci.2018.05.010. (cit. on pp. 3, 6, and 100).

[47] M. D'Ottavio, L. Dozio, R. Vescovini, and O. Polit. The Ritz – Sublaminate Generalized Unified Formulation approach for piezoelectric composite plates. *Int. J. Smart Nano Mater.*, 9(1):34–55, 2018. doi:10.1080/19475411.2017.1421275. (cit. on p. 3).

[48] A. Gorgeri, R. Vescovini, and L. Dozio. Analysis of multiple-core sandwich cylindrical shells using a sublaminate formulation. *Compos. Struct.*, 225:111067, 2019. doi:10.1016/j.compstruct.2019.111067. (cit. on pp. 3 and 65).

[49] M. D'Ottavio, A. Krasnobrizha, E. Valot, O. Polit, R. Vescovini, and L. Dozio. Dynamic response of viscoelastic multiple-core sandwich structures. *J. Sound Vibr.*, 491:115753, 2021. doi:10.1016/j.jsv.2020.115753. (cit. on pp. 3, 5, 54, 59, 60, 64, 65, 67, 68, 69, 70, and 72).

[50] M. D. Rao. Recent applications of viscoelastic damping for noise control in automobiles and commercial airplanes. *J. Sound Vib.*, 262(3):457–474, 2003. doi:10.1016/S0022-460X(03)00106-8. (cit. on p. 3).

[51] X. Q. Zhou, D. Y. Yu, X. Y. Shao, S. Q. Zhang, and S. Wang. Research and applications of viscoelastic vibration damping materials: A review. *Compos. Struct.*, 136:460–480, 2016. doi:10.1016/j.compstruct.2015.10.014. (cit. on p. 3).

[52] B. M. Shafer. An overview of constrained-layer damping theory and application. *Proc. Meet. Acoust.*, 19(1):065023, 2013. doi:10.1121/1.4800606. (cit. on p. 3).

[53] C. M. A. Vasques, R. Moreira, and J. Rodrigues. Viscoelastic Damping Technologies–Part I: Modeling and Finite Element Implementation. *J. Adv. Research Mech. Engng.*, 1, 2010. (cit. on p. 3).

[54] D. J. McTavish and P. C. Hughes. Modeling of Linear Viscoelastic Space Structures. *J. Vib. Acoust.*, 115(1):103–110, 1993. doi:10.1115/1.2930302. (cit. on p. 3).

[55] G. A. Lesieutre and E. Bianchini. Time Domain Modeling of Linear Viscoelasticity Using Anelastic Displacement Fields. *J. Vibr. Acoust.*, 117(4):424–430, 1995. doi:10.1115/1.2874474. (cit. on pp. 3, 56, and 69).

[56] R. L. Bagley and P. J. Torvik. A Theoretical Basis for the Application of Fractional Calculus to Viscoelasticity. *J. Rheol.*, 27(3):201–210, 1983. doi:10.1122/1.549724. (cit. on p. 3).

[57] R. C. Koeller. Applications of Fractional Calculus to the Theory of Viscoelasticity. *J. App. Mech.*, 51(2):299–307, 1984. doi:10.1115/1.3167616. (cit. on p. 3).

[58] R. L. Bagley and P. J. Torvik. On the Fractional Calculus Model of Viscoelastic Behavior. *J. Rheol.*, 30(1):133–155, 1986. doi:10.1122/1.549887. (cit. on p. 3).

[59] T. Pritz. Analysis of four-parameter fractional derivative model of real solid materials. *J. Sound Vib.*, 195(1):103–115, 1996. doi:10.1006/jsvi.1996.0406. (cit. on pp. 4 and 56).

[60] T. Pritz. Five-parameter fractional derivative model for polymeric damping materials. *J. Sound Vib.*, 265(5):935–952, 2003. doi:10.1016/S0022-460X(02)01530-4. (cit. on p. 4).

[61] Y. P. Lu, J. W. Killian, and G. C. Everstine. Vibrations of three layered damped sandwich plate composites. *J. Sound Vib.*, 64(1):63–71, 1979. doi:10.1016/0022-460X(79)90572-8. (cit. on p. 4).

[62] M. L. Soni and F. K. Bogner. Finite Element Vibration Analysis of Damped Structures. *AIAA J.*, 20(5):700–707, 1982. doi:10.2514/3.51127. (cit. on p. 4).

[63] C. D. Johnson and D. A. Kienholz. Finite Element Prediction of Damping in Structures with Constrained Viscoelastic Layers. *AIAA J.*, 20(9):1284–1290, 1982. doi:10.2514/3.51190. (cit. on pp. 4, 54, and 59).

[64] R. Moreira and J. Rodrigues. Constrained Damping Layer Treatments: Finite Element Modeling. *J. Vib. Control*, 10:575–595, 2004. doi:10.1177/1077546304039060. (cit. on p. 4).

[65] F. S. Barbosa and M. C. R. Farage. A finite element model for sandwich viscoelastic beams: Experimental and numerical assessment. *J. Sound Vib.*, 317(1):91–111, 2008. doi:10.1016/j.jsv.2008.03.013. (cit. on p. 4).

[66] A. J. M. Ferreira, A. L. Araújo, A. M. A. Neves, J. D. Rodrigues, E. Carrera, M. Cinefra, and C. M. Mota Soares. A finite element model using a unified formulation for the analysis of viscoelastic sandwich laminates. *Compos. B. Eng.*, 45(1):1258–1264, 2013. doi:10.1016/j.compositesb.2012.05.012. (cit. on pp. 4 and 5).

[67] R. A. S. Moreira and J. Dias Rodrigues. A layerwise model for thin soft core sandwich plates. *Comput. Struct.*, 84(19):1256–1263, 2006. doi:10.1016/j.compstruc.2006.01.020. (cit. on p. 4).

[68] E. M. Daya, L. Azrar, and M. Potier-Ferry. An amplitude equation for the non-linear vibration of viscoelastically damped sandwich beams. *J. Sound Vib.*, 271(3):789–813, 2004. doi:10.1016/S0022-460X(03)00754-5. (cit. on p. 4).

[69] A. L. Araújo, C. M. Mota Soares, and C. A. Mota Soares. A Viscoelastic Sandwich Finite Element Model for the Analysis of Passive, Active and Hybrid Structures. *Appl. Compos. Mater.*, 17(5):529–542, 2010. doi:10.1007/s10443-010-9141-3. (cit. on p. 4).

[70] A. L. Araújo, C. M. Mota Soares, C. A. Mota Soares, and J. Herskovits. Optimal design and parameter estimation of frequency dependent viscoelastic laminated sandwich composite plates. *Compos. Struct.*, 92(9):2321–2327, 2010. doi:10.1016/j.compstruct.2009.07.006. (cit. on p. 4).

[71] J. S. Moita, A. L. Araújo, P. Martins, C. M. Mota Soares, and C. A. Mota Soares. A finite element model for the analysis of viscoelastic sandwich structures. *Compos. Struct.*, 89(21):1874–1881, 2011. doi:10.1016/j.compstruc.2011.05.008. (cit. on p. 4).

[72] T. S. Plagianakos and D. A. Saravanos. High-order layerwise finite element for the damped free-vibration response of thick composite and sandwich composite plates. *Int. J. Numer. Methods Eng.*, 77(11):1593–1626, 2009. doi:10.1002/nme.2465. (cit. on p. 4).

[73] B. E. Douglas and J. C. S. Yang. Transverse compressional damping in the vibratory response of elastic-viscoelastic-elastic beams. *AIAA J.*, 16(9):925–930, 1978. doi:10.2514/3.7595. (cit. on p. 5).

[74] S. Ren, G. Zhao, and S. Zhang. A layerwise finite element formulation for vibration and damping analysis of sandwich plate with moderately thick viscoelastic core. *Mech. Adv. Mater. Struct.*, 27(14):1201–1212, 2020. doi:10.1080/15376494.2018.1504360. (cit. on p. 5).

[75] M. Filippi and E. Carrera. Various refined theories applied to damped viscoelastic beams and circular rings. *Acta Mech.*, 228(12):4235–4248, 2017. doi:10.1007/s00707-017-1948-7. (cit. on p. 5).

[76] R. P. Ley, W. Lin, and U. Mbanefo. Facesheet Wrinkling in Sandwich Structures. Technical Report NAS 1.26:208994, 1999. (cit. on p. 5).

[77] L. Fagerberg. The effect of local bending stiffness on the wrinkling of sandwich panels. *Proc. Inst. Mech. Eng*, 217(2):111–119, 2003. doi:10.1243/147509003321921355. (cit. on p. 5).

[78] L. Fagerberg. Wrinkling and Compression Failure Transition in Sandwich Panels. *J. Sandw. Struct. Mater.*, 6(2):129–144, 2004. doi:10.1177/1099636204030475. (cit. on p. 5).

[79] L. Fagerberg and D. Zenkert. Effects of Anisotropy and Multiaxial Loading on

the Wrinkling of Sandwich Panels. *J. Sandw. Struct. Mater.*, 7(3):177–194, 2005. doi:10.1177/109963205048525. (cit. on p. 5).

[80] L. Fagerberg and D. Zenkert. Imperfection-induced Wrinkling Material Failure in Sandwich Panels. *J. Sandw. Struct. Mater.*, 7(3):195–219, 2005. doi:10.1177/1099636205048526. (cit. on p. 5).

[81] A. J. Gutierrez and J. P. H. Webber. Flexural wrinkling of honeycomb sandwich beams with laminated faces. *Int. J. Solids Struct.*, 16(7):645–651, 1980. doi:10.1016/0020-7683(80)90023-2. (cit. on p. 5).

[82] B. Zalewski, W. Dial, and B. Bednarcyk. Methods for Assessing Honeycomb Sandwich Panel Wrinkling Failures. Technical Report NASA/TM—2012-217697, 2012. (cit. on p. 6).

[83] M. D'Ottavio and O. Polit. Linearized global and local buckling analysis of sandwich struts with a refined quasi-3D model. *Acta Mech.*, 226(1):81–101, 2015. doi:10.1007/s00707-014-1169-2. (cit. on pp. 6, 93, 95, 100, and 101).

[84] M. Ginot, M. D'Ottavio, O. Polit, C. Bouvet, and B. Castanié. Benchmark of wrinkling formulae and methods for pre-sizing of aircraft lightweight sandwich structures. *Compos. Struct.*, 273:114387, 2021. doi:10.1016/j.compstruct.2021.114387. (cit. on p. 6).

[85] W. Ji and A. M. Waas. Global and Local Buckling of a Sandwich Beam. *J. Eng. Mech.*, 133(2):230–237, 2007. doi:10.1061/(ASCE)0733-9399(2007)133:2(230). (cit. on p. 6).

[86] W. Ji and A. M. Waas. Wrinkling and Edge Buckling in Orthotropic Sandwich Beams. *J. Eng. Mech.*, 134(6):455–461, 2008. doi:10.1061/(ASCE)0733-9399(2008)134:6(455). (cit. on p. 6).

[87] W. Ji and A. M. Waas. 2D elastic analysis of the sandwich panel buckling problem: benchmark solutions and accurate finite element formulations. *Z. Angew. Math. Phys.*, 61(5):897–917, 2010. doi:10.1007/s00033-009-0041-z. (cit. on p. 6).

[88] B. K. Hadi and F. L. Matthews. Development of Benson–Mayers theory on the wrinkling of anisotropic sandwich panels. *Compos. Struct.*, 49(4):425–434, 2000. doi:10.1016/S0263-8223(00)00077-5. (cit. on p. 6).

[89] L. Léotoing, S. Drapier, and A. Vautrin. First applications of a novel unified model for global and local buckling of sandwich columns. *Eur. J. Mech. A Solids*, 21(4):683–701, 2002. doi:10.1016/S0997-7538(02)01229-9. (cit. on p. 6).

[90] L. Léotoing, S. Drapier, and A. Vautrin. Nonlinear interaction of geometrical and material properties in sandwich beam instabilities. *Int. J. Solids Struct.*, 39(13):3717–3739, 2002. doi:10.1016/S0020-7683(02)00181-6. (cit. on p. 6).

[91] M. A. Wadee, S. Yiatros, and M. Theofanous. Comparative studies of localized buckling in sandwich struts with different core bending models. *Int. J. Non Linear Mech.*, 45(2):111–120, 2010. doi:10.1016/j.ijnonlinmec.2009.10.001. (cit. on p. 6).

[92] A. Pagani and E. Carrera. Large-deflection and post-buckling analyses of laminated composite beams by Carrera Unified Formulation. *Compos. Struct.*, 170:40–52, 2017. doi:10.1016/j.compstruct.2017.03.008. (cit. on p. 6).

[93] A. Pagani and E. Carrera. Unified formulation of geometrically nonlinear refined beam theories. *Mech. Adv. Mater. Struct.*, 25(1):15–31, 2018. doi:10.1080/15376494.2016.1232458. (cit. on p. 6).

[94] A. Pagani, E. Daneshkhah, X. Xu, and E. Carrera. Evaluation of geometrically nonlinear terms in the large-deflection and post-buckling analysis of isotropic rectangular plates. *Int. J. Non Linear Mech.*, 121:103461, 2020. doi:10.1016/j.ijnonlinmec.2020.103461. (cit. on p. 6).

[95] M. D'Ottavio, O. Polit, W. Ji, and A. M. Waas. Benchmark solutions and assessment of variable kinematics models for global and local buckling of sandwich struts. *Compos. Struct.*, 156:125–134, 2016. doi:10.1016/j.compstruct.2016.01.019. (cit. on p. 6).

[96] J. N. Reddy. *Mechanics of Laminated Composite Plates and Shells: Theory and Analysis, Second Edition*. CRC Press, 2003. (cit. on p. 9).

[97] H. Murakami. Laminated Composite Plate Theory With Improved In-Plane Responses. *J. Appl. Mech.*, 53(3):661–666, 1986. doi:10.1115/1.3171828. (cit. on p. 11).

[98] E. Carrera. On the use of the Murakami's zig-zag function in the modeling of layered plates and shells. *Comput. Struct.*, 82(7):541–554, 2004. doi:10.1016/j.compstruc.2004.02.006. (cit. on p. 11).

[99] T. H. C. Le, M. D'Ottavio, P. Vidal, and O. Polit. A new robust quadrilateral four-node variable kinematics plate element for composite structures. *Finite Elements in Analysis and Design*, 133:10–24, 2017. doi:10.1016/j.finel.2017.05.002. (cit. on p. 14).

[100] T. H. C. Le, M. D'Ottavio, P. Vidal, and O. Polit. Robust Displacement and Mixed CUF-Based Four-Node and Eight-Node Quadrilateral Plate Elements. In H. Altenbach, E. Carrera, and G. Kulikov, editors, *Analysis and Modelling of Advanced Structures and Smart Systems*, Advanced Structured Materials, pages 89–118. Springer, Singapore, 2018. (cit. on p. 14).

[101] O. Polit. *Développement d'éléments finis de plaque semi-épaisse et de coque semi-épaisse à double courbure*. These de doctorat, Paris 6, 1992. (cit. on p. 14).

[102] E. N. Dvorkin and K. Bathe. A continuum mechanics based four-node shell element for general non-linear analysis. *Eng. Comput.*, 1(1):77–88, 1984. doi:10.1108/eb023562. (cit. on p. 14).

[103] M. Cinefra, M. D'Ottavio, O. Polit, and E. Carrera. Assessment of MITC plate elements based on CUF with respect to distorted meshes. *Compos. Struct.*, 238:111962, 2020. doi:10.1016/j.compstruct.2020.111962. (cit. on p. 14).

[104] N. Pagano. Exact Solutions for Rectangular Bidirectional Composites and Sandwich Plates. *J. Compos. Mater.*, 4(1):20–34, 1970. doi:10.1177/002199837000400102. (cit. on p. 16).

[105] G. A. Kardomateas. Three-Dimensional Elasticity Solution for Sandwich Plates With Orthotropic Phases: The Positive Discriminant Case. *J. Appl. Mech.*, 76(1), 2008. doi:10.1115/1.2966174. (cit. on p. 16).

[106] L. Demasi, E. Santarpia, and R. Cavallaro. Functional Reconstitution of Reissner Mixed Variational Theorem for Effective Finite Element Implementations. In *AIAA Scitech 2019 Forum*, AIAA SciTech Forum. American Institute of Aeronautics and Astronautics, 2019. (cit. on p. 21).

[107] T. H. H. Pian, D.-P. Chen, and D. Kang. A new formulation of hybrid/mixed finite element. *Comput. Struct.*, 16(1):81–87, 1983. doi:10.1016/0045-7949(83)90149-9. (cit. on p. 21).

[108] T. H. H. Pian and K. Sumihara. Rational approach for assumed stress finite elements. *Int. J. Numer. Methods Eng.*, 20(9):1685–1695, 1984. doi:10.1002/nme.1620200911. (cit. on p. 21).

[109] T. H. H. Pian and P. Tong. Relations between incompatible displacement model and hybrid stress model. *Int. J. Numer. Methods Eng.*, 22(1):173–181, 1986. doi:10.1002/nme.1620220112. (cit. on p. 21).

[110] S. W. Lee and J. J. Rhiu. A new efficient approach to the formulation of mixed finite element models for structural analysis. *Int. J. Numer. Methods Eng.*, 23(9):1629–1641, 1986. doi:10.1002/nme.1620230905. (cit. on p. 21).

[111] A. Wang and F. W. Crossman. Some New Results on Edge Effect in Symmetric Composite Laminates. *J. Compos. Mater.*, 11(1):92–106, 1977. doi:10.1177/002199837701100110. (cit. on pp. 25 and 28).

[112] M. Tahani and A. Nosier. Free edge stress analysis of general cross-ply composite laminates under extension and thermal loading. *Compos. Struct.*, 60(1):91–103, 2003. doi:10.1016/S0263-8223(02)00290-8. (cit. on pp. 25 and 28).

[113] R. L. Spilker. A traction-free-edge hybrid-stress element for the analysis of edge effects in cross-ply laminates. *Comput. Struct.*, 12(2):167–179, 1980. doi:10.1016/0045-7949(80)90002-4. (cit. on p. 25).

[114] G. A. Kardomateas and C. N. Phan. Three-dimensional elasticity solution for sandwich beams/wide plates with orthotropic phases: The negative discriminant case. *J. Sandwich Struct. Mater.*, 13(6):641–661, 2011. doi:10.1177/1099636211419127. (cit. on pp. 25, 32, 33, and 147).

[115] Z. Yuan, G. Kardomateas, and Y. Frostig. Geometric Nonlinearity Effects in the Response of Sandwich Wide Panels. *J. Appl. Mech.*, 83, 2016. doi:10.1115/1.4033651. (cit. on pp. 26, 102, 103, 104, and 105).

[116] P. Navarro, S. Abrate, J. Aubry, S. Marguet, and J. F. Ferrero. Analytical modeling of indentation of composite sandwich beam. *Composite Structures*, 100:79–88, 2013. doi:10.1016/j.compstruct.2012.12.017. (cit. on pp. 26, 43, and 49).

[117] C. N. Phan, Y. Frostig, and G. A. Kardomateas. Analysis of Sandwich Beams With a Compliant Core and With In-Plane Rigidity—Extended High-Order Sandwich Panel Theory Versus Elasticity. *J. Appl. Mech.*, 79(4), 2012. doi:10.1115/1.4005550. (cit. on pp. 26 and 103).

[118] V. S. Sokolinsky, H. Shen, L. Vaikhanski, and S. R. Nutt. Experimental and analytical study of nonlinear bending response of sandwich beams. *Compos. Struct.*, 60(2):219–229, 2003. doi:10.1016/S0263-8223(02)00293-3. (cit. on p. 26).

[119] D. Zhang, J. Ye, and H. Y. Sheng. Free-edge and ply cracking effect in cross-ply laminated composites under uniform extension and thermal loading. *Compos. Struct.*, 76(4):314–325, 2006. doi:10.1016/j.compstruct.2005.04.021. (cit. on p. 26).

[120] B. Pipes and N. Pagano. Interlaminar Stresses in Composite Laminates Under Uniform Axial Extension. *J. Compos. Mater.*, 4:538–548, 1970. doi:10.1177/002199837000400409. (cit. on p. 26).

[121] D. Boffi, F. Brezzi, and M. Fortin. *Mixed Finite Element Methods and Applications*, volume 44 of *Springer Series in Computational Mathematics*. Springer, Berlin, Heidelberg, 2013. (cit. on p. 27).

[122] L. Demasi. ∞^6 Mixed plate theories based on the Generalized Unified Formulation. Part V: Results. *Compos. Struct.*, 88(1):1–16, 2009. doi:10.1016/j.compstruct.2008.07.009. (cit. on pp. 27, 28, 29, and 40).

[123] M. D'Ottavio, G. Di Cara, T. H. C. Le, and O. Polit. Algebraic aspects of variable kinematics plate models based on RMVT. In *10th Design, Modelling*

and Experiments of Advanced Structures and Systems Conference, 2022. (cit. on pp. 28 and 29).

[124] R. L. Spilker and S. C. Chou. Evaluation of a Hybrid-Stress Formulation for Thick Multilayer Laminates. In E. M. Lenoe, D. W. Oplinger, and J. J. Burke, editors, *Fibrous Composites in Structural Design*, pages 399–410. Springer US, Boston, MA, 1980. (cit. on p. 29).

[125] Y. B. Cho and R. C. Averill. First-order zig-zag sublaminate plate theory and finite element model for laminated composite and sandwich panels. *Compos. Struct.*, 50(1):1–15, 2000. doi:10.1016/S0263-8223(99)00063-X. (cit. on p. 36).

[126] H. R. Meyer-Piening. Application of the Elasticity Solution to Linear Sandwich Beam, Plate and Shell Analyses. *J. Sandwich Struct. Mater.*, 6(4):295–312, 2004. doi:10.1177/1099636204035395. (cit. on p. 43).

[127] U. N. Leontev and V. Z. Vlasov. *Beams, plates and shells on elastic foundations.* 1966. (cit. on p. 49).

[128] I.-B. Teodoru. EBBEF2p-A Computer Code for Analyzing Beams on Elastic Foundations. *Intersections*, 6:28–44, 2009. (cit. on p. 49).

[129] F. Bogner and M. Soni. Finite element vibration analysis of damped structures. In *22nd Structures, Structural Dynamics and Materials Conference*. American Institute of Aeronautics and Astronautics, 1981. (cit. on pp. 54 and 60).

[130] M. Bilasse, L. Azrar, and E. M. Daya. Complex modes based numerical analysis of viscoelastic sandwich plates vibrations. *Comput. Struct.*, 89(7):539–555, 2011. doi:10.1016/j.compstruc.2011.01.020. (cit. on pp. 54, 60, 61, 62, and 68).

[131] F. Simon, T. Haase, O. Unruh, G. Ghiringhelli, A. Parrinello, and R. Vescovini. Benchmark for modelization of acoustic transmission loss applied to helicopter trim panels. In *42nd European Rotorcraft Forum (ERF 2016)*, LILLE, France, 2016. (cit. on pp. 54 and 64).

[132] R. M. Christensen. *Theory of viscoelasticity.* Dover Publications, Mineola, N.Y, 2nd ed edition, 2003. (cit. on p. 54).

[133] L. Rouleau, J. F. Deü, A. Legay, and F. Le Lay. Application of Kramers–Kronig relations to time–temperature superposition for viscoelastic materials. *Mech. Mater.*, 65:66–75, 2013. doi:10.1016/j.mechmat.2013.06.001. (cit. on pp. 54 and 55).

[134] F. Mastroddi, F. Martarelli, M. Eugeni, and C. Riso. Time- and frequency-domain linear viscoelastic modeling of highly damped aerospace structures. *Mech. Syst. Signal Process.*, 122:42–55, 2019. doi:10.1016/j.ymssp.2018.12.023. (cit. on p. 55).

[135] H. K. Milne. The impulse response function of a single degree of freedom system with hysteretic damping. *J. Sound Vib.*, 100:590–593, 1985. doi:10.1016/S0022-460X(85)80010-9. (cit. on p. 55).

[136] S. H. Crandall. Dynamic Response of Systems with Structural Damping. 1961. (cit. on p. 55).

[137] C. Friedrich, H. Schiessel, and A. Blumen. Constitutive behavior modeling and fractional derivatives. In D. A. Siginer, D. De Kee, and R. P. Chhabra, editors, *Rheology Series*, volume 8 of *Advances in the Flow and Rheology of Non-Newtonian Fluids*, pages 429–466. Elsevier, 1999. (cit. on p. 56).

[138] A. A. Markou and G. D. Manolis. A fractional derivative Zener model for the numerical simulation of base isolated structures. *Bull. Earthquake Eng.*, 14(1):283–295, 2016. doi:10.1007/s10518-015-9801-7. (cit. on p. 56).

[139] L. Wei, W. Li, Z.-Q. Feng, and J. Liu. Applying the fractional derivative Zener model to fitting the time-dependent material viscoelasticity tested by nanoindentation. *Biosurface Biotribology*, 4, 2018. doi:10.1049/bsbt.2018.0011. (cit. on p. 56).

[140] L.-J. Shen. Fractional derivative models for viscoelastic materials at finite deformations. *Int. J. Solids Struct.*, 190:226–237, 2020. doi:10.1016/j.ijsolstr.2019.10.025. (cit. on p. 56).

[141] M. Caputo and F. Mainardi. Linear models of dissipation in anelastic solids. *La Rivista del Nuovo Cimento*, 1(2):161–198, 1971. doi:10.1007/BF02820620. (cit. on p. 56).

[142] M. Caputo and F. Mainardi. A new dissipation model based on memory mechanism. *PAGEOPH*, 91(1):134–147, 1971. doi:10.1007/BF00879562. (cit. on p. 56).

[143] I. R. Henriques, L. Rouleau, D. A. Castello, L. A. Borges, and J. F. Deü. Viscoelastic behavior of polymeric foams: Experiments and modeling. *Mech. Mater.*, 148:103506, 2020. doi:10.1016/j.mechmat.2020.103506. (cit. on p. 57).

[144] W. E. Arnoldi. The principle of minimized iterations in the solution of the matrix eigenvalue problem. *Q. Appl. Math.*, 9(1):17 – 29, 1951. doi:10.1090/qam/42792. (cit. on p. 58).

[145] C. M. d. A. Vasques. *Vibration control of adaptive structures : modeling, simulation and implementation of viscoelastic and piezoelectric damping technologies*. PhD Thesis, 2008. (cit. on pp. 58 and 72).

[146] D. Mead. The Effect of a Damping Compound on Jet-Efflux Excited Vibrations: An Article in Two Parts Presenting Theory and Results of Experimental Investi-

gation. *Aircr. Eng. Aerosp. Technol.*, 32(4):106–113, 1960. doi:10.1108/eb033235. (cit. on p. 59).

[147] E. E. Ungar and E. M. Kerwin. Loss Factors of Viscoelastic Systems in Terms of Energy Concepts. *J. Acoust. Soc. Am.*, 34(7):954–957, 1962. doi:10.1121/1.1918227. (cit. on p. 59).

[148] E. M. Daya and M. Potier-Ferry. A numerical method for nonlinear eigenvalue problems application to vibrations of viscoelastic structures. *Comput. Struct.*, 79(5):533–541, 2001. doi:10.1016/S0045-7949(00)00151-6. (cit. on p. 60).

[149] D. K. Rao. Frequency and Loss Factors of Sandwich Beams under Various Boundary Conditions. *J. Mech. Eng. Sci.*, 20(5):271–282, 1978. doi:10.1243/JMES_JOUR_1978_020_047_02. (cit. on pp. 61 and 62).

[150] M. Bilasse, I. Charpentier, E. M. Daya, and Y. Koutsawa. A generic approach for the solution of nonlinear residual equations. Part II: Homotopy and complex nonlinear eigenvalue method. *Comput. Methods Appl. Mech. Eng.*, 198(49):3999–4004, 2009. doi:10.1016/j.cma.2009.09.015. (cit. on pp. 61 and 62).

[151] M. A. Trindade. *Contrôle hybride actif-passif des vibrations de structures par des matériaux piézoélectriques et viscoélastiques : poutres sandwich/multicouches intelligentes*. phdthesis, Conservatoire national des arts et metiers - CNAM, 2000. (cit. on p. 68).

[152] M. Bilasse and D. C. D. Oguamanam. Forced harmonic response of sandwich plates with viscoelastic core using reduced-order model. *Comput. Struct.*, 105:311–318, 2013. doi:10.1016/j.compstruct.2013.05.042. (cit. on pp. 72 and 73).

[153] F. Cortés and I. Sarría. Dynamic Analysis of Three-Layer Sandwich Beams with Thick Viscoelastic Damping Core for Finite Element Applications. *Shock Vib.*, 2015:e736256, 2015. doi:10.1155/2015/736256. (cit. on pp. 74 and 76).

[154] F. Cortés and M. J. Elejabarrieta. Viscoelastic materials characterisation using the seismic response. *Mater. Des.*, 28(7):2054–2062, 2007. doi:10.1016/j.matdes.2006.05.032. (cit. on p. 74).

[155] A. K. Noor. Stability of multilayered composite plates. *J. Fiber Sci. Technol.*, 8(2):81–89, 1975. doi:10.1016/0015-0568(75)90005-6. (cit. on pp. 79, 87, 88, 89, 90, and 91).

[156] K. Washizu. *Variational Methods in Elasticity and Plasticity*. Elsevier Science & Technology, 1974. (cit. on p. 80).

[157] C. Wenzel, P. Vidal, M. D'Ottavio, and O. Polit. Coupling of heterogeneous kinematics and Finite Element approximations applied to composite beam structures.

Compos. Struct., 116:177–192, 2014. doi:10.1016/j.compstruct.2014.04.022. (cit. on p. 111).

[158] E. Zappino, G. Li, A. Pagani, and E. Carrera. Global-local analysis of laminated plates by node-dependent kinematic finite elements with variable ESL/LW capabilities. *Compos. Struct.*, 172:1–14, 2017. doi:10.1016/j.compstruct.2017.03.057. (cit. on p. 111).

[159] B. Fraeijs de Veubeke. *Displacement and equilibrium models in the finite element method*. John Wiley and Sons, Hoboken, NJ, 1965. (cit. on p. 147).

Appendix A

Constitutive arrays of a lamina

A.1 Classic form of Hooke's law

Referring to the contracted (Voigt-Kelvin) notation, the generalised Hook's law for an anisotropic material in the orthogonal Cartesian coordinate system (x_1, x_2, x_3) reads:

$$\sigma_i = \bar{C}_{ij}\epsilon_j \tag{A.1}$$

where σ_i and ϵ_j are the stress and strain components respectively and $\bar{C}_{ij}$ the stiffness coefficients. For a general *hyperelastic material*, i.e., a material for which there is a strain energy density function $U_0(\epsilon_i)$ such that $\sigma_i = \partial U_0/\partial\epsilon_i = \bar{C}_{ij}\epsilon_j$, the stiffness matrix $\bar{\mathbf{C}}$ has 21 independent elastic coefficients since $\bar{C}_{ij} = \bar{C}_{ji}$, hence Eq. (A.1) can be written as:

$$\begin{Bmatrix} \sigma_1 \\ \sigma_2 \\ \sigma_3 \\ \sigma_4 \\ \sigma_5 \\ \sigma_6 \end{Bmatrix} = \begin{bmatrix} \bar{C}_{11} & \bar{C}_{12} & \bar{C}_{13} & \bar{C}_{14} & \bar{C}_{15} & \bar{C}_{16} \\ & \bar{C}_{22} & \bar{C}_{23} & \bar{C}_{24} & \bar{C}_{25} & \bar{C}_{26} \\ & & \bar{C}_{33} & \bar{C}_{34} & \bar{C}_{35} & \bar{C}_{36} \\ & & & \bar{C}_{44} & \bar{C}_{45} & \bar{C}_{46} \\ & \text{sym} & & & \bar{C}_{55} & \bar{C}_{56} \\ & & & & & \bar{C}_{66} \end{bmatrix} \begin{Bmatrix} \epsilon_1 \\ \epsilon_2 \\ \epsilon_3 \\ \epsilon_4 \\ \epsilon_5 \\ \epsilon_6 \end{Bmatrix} \tag{A.2}$$

If the material has three mutually orthogonal planes of symmetry (*orthotropic material*) the number of material parameters is reduced to 9 :

$$\begin{Bmatrix} \sigma_1 \\ \sigma_2 \\ \sigma_3 \\ \sigma_4 \\ \sigma_5 \\ \sigma_6 \end{Bmatrix} = \begin{bmatrix} \bar{C}_{11} & \bar{C}_{12} & \bar{C}_{13} & & & \\ & \bar{C}_{22} & \bar{C}_{23} & & & \\ & & \bar{C}_{33} & & & \\ & & & \bar{C}_{44} & & \\ & \text{sym} & & & \bar{C}_{55} & \\ & & & & & \bar{C}_{66} \end{bmatrix} \begin{Bmatrix} \epsilon_1 \\ \epsilon_2 \\ \epsilon_3 \\ \epsilon_4 \\ \epsilon_5 \\ \epsilon_6 \end{Bmatrix} \tag{A.3}$$

The stiffness coefficients $\bar{C}_{ij}$ are evaluated from the engineering parameters as follows:

$$\begin{aligned}
\bar{C}_{11} &= \frac{1-\nu_{23}\nu_{23}}{E_2E_3\Delta}, \quad \bar{C}_{12} = \frac{\nu_{21}+\nu_{31}\nu_{23}}{E_2E_3\Delta} = \frac{\nu_{12}+\nu_{32}\nu_{13}}{E_1E_3\Delta} \\
\bar{C}_{13} &= \frac{\nu_{31}+\nu_{21}\nu_{32}}{E_2E_3\Delta} = \frac{\nu_{13}-\nu_{12}\nu_{23}}{E_1E_2\Delta} \\
\bar{C}_{22} &= \frac{1-\nu_{13}\nu_{31}}{E_1E_3\Delta}, \quad \bar{C}_{23} = \frac{\nu_{32}+\nu_{12}\nu_{31}}{E_1E_3\Delta} = \frac{\nu_{23}+\nu_{21}\nu_{13}}{E_1E_3\Delta} \\
\bar{C}_{33} &= \frac{1-\nu_{12}\nu_{21}}{E_1E_2\Delta}, \quad \bar{C}_{44} = G_{23}, \quad \bar{C}_{55} = G_{31}, \quad \bar{C}_{66} = G_{12} \\
\Delta &= \frac{1-\nu_{12}\nu_{21}-\nu_{23}\nu_{32}-\nu_{31}\nu_{13}-2\nu_{21}\nu_{32}\nu_{13}}{E_1E_2E_3}
\end{aligned} \tag{A.4}$$

where E_i is the Young's modulus in the i direction, G_{ij} is the shear modulus in the $i-j$ plane, and ν_{ij} is the Poisson's ratio of the strain in the j direction to the strain in the i direction due to an applied stress in the i direction.

A unidirectional fiber-reinforced lamina can be treated as an orthotropic material by assuming the material symmetry planes to be parallel and transverse to the fiber direction. However, in the most common case, the layer-specific orientation of the lamina doesn't coincide with the laminate coordinate system the lamina belongs to, except for the transverse normal direction to the lamina ($z \equiv x_3$). Thus, it is necessary to introduce the transformation relations to map the stresses and strains from the material (m) to the laminate (l) frame. By referring to Figure A.1, where θ^p indicates the fiber orientation of layer p w.r.t. the material coordinate, the transformation matrices for a rotation about a transverse normal to the lamina read:

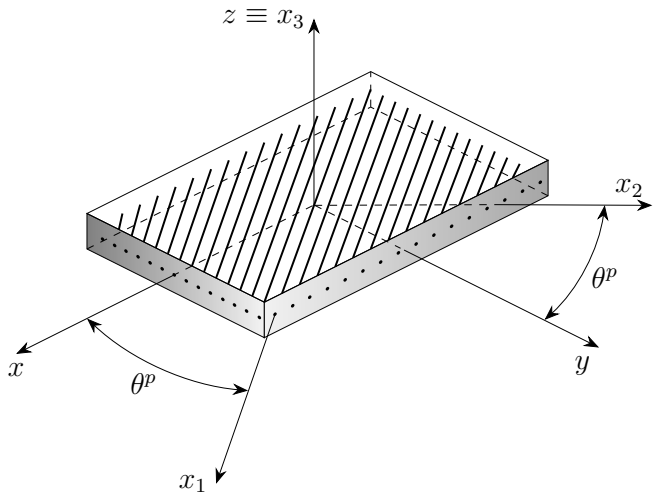

Figure A.1: Material (x_1, x_2, x_3) and laminate (x, y, z) coordinate system of a lamina

$$\mathbf{T}^p_{\boldsymbol{\sigma}_m \to \boldsymbol{\sigma}_l} = \mathbf{T}^p = \begin{bmatrix} \cos^2\theta^p & \sin^2\theta^p & 0 & 0 & 0 & -\sin 2\theta^p \\ \sin^2\theta^p & \cos^2\theta^p & 0 & 0 & 0 & \sin 2\theta^p \\ 0 & 0 & 1 & 0 & 0 & 0 \\ 0 & 0 & 0 & \cos\theta^p & \sin\theta^p & 0 \\ 0 & 0 & 0 & -\sin\theta^p & \cos\theta^p & 0 \\ \sin\theta^p\cos\theta^p & -\sin\theta^p\cos\theta^p & 0 & 0 & 0 & \cos^2\theta^p - \sin^2\theta^p \end{bmatrix} \tag{A.5}$$

$$\mathbf{T}^p_{\boldsymbol{\epsilon}_m \to \boldsymbol{\epsilon}_l} = \mathbf{T}^{pT} = \begin{bmatrix} \cos^2\theta^p & \sin^2\theta^p & 0 & 0 & 0 & \sin\theta^p\cos\theta^p \\ \sin^2\theta^p & \cos^2\theta^p & 0 & 0 & 0 & -\sin\theta^p\cos\theta^p \\ 0 & 0 & 1 & 0 & 0 & 0 \\ 0 & 0 & 0 & \cos\theta^p & -\sin\theta^p & 0 \\ 0 & 0 & 0 & \sin\theta^p & \cos\theta^p & 0 \\ -\sin 2\theta^p & \sin 2\theta^p & 0 & 0 & 0 & \cos^2\theta^p - \sin^2\theta^p \end{bmatrix} \tag{A.6}$$

where T is the transposition operator. The material stiffness matrix in the laminate frame, for an orthotropic lamina, is given by:

$$\tilde{\mathbf{C}}^p = \mathbf{T}^p \bar{\mathbf{C}}^p \mathbf{T}^{pT} = \begin{bmatrix} \tilde{C}_{11} & \tilde{C}_{12} & \tilde{C}_{13} & 0 & 0 & \tilde{C}_{16} \\ & \tilde{C}_{22} & \tilde{C}_{23} & 0 & 0 & \tilde{C}_{26} \\ & & \tilde{C}_{33} & 0 & 0 & \tilde{C}_{36} \\ & & & \tilde{C}_{44} & \tilde{C}_{45} & 0 \\ & \text{sym} & & & \tilde{C}_{55} & 0 \\ & & & & & \tilde{C}_{66} \end{bmatrix}^p \tag{A.7}$$

The strain and stress fields are split into their in-plane (subscript Ω), transverse normal (subscript n) and transverse shear (subscript s) components as

$$\begin{aligned} \boldsymbol{\epsilon}_\Omega &= \begin{bmatrix} \epsilon_{xx} & \epsilon_{yy} & 2\epsilon_{xy} \end{bmatrix}^T; \quad \epsilon_n = \epsilon_{zz}; \quad \boldsymbol{\epsilon}_s = \begin{bmatrix} 2\epsilon_{yz} & 2\epsilon_{xz} \end{bmatrix}^T \\ \boldsymbol{\sigma}_\Omega &= \begin{bmatrix} \sigma_{xx} & \sigma_{yy} & \sigma_{xy} \end{bmatrix}^T; \quad \sigma_n = \sigma_{zz}; \quad \boldsymbol{\sigma}_s = \begin{bmatrix} \sigma_{xz} & \sigma_{yz} \end{bmatrix}^T \end{aligned} \tag{A.8}$$

Finally, the constitutive link for each physical ply p is expressed in matrix form in the laminate frame (x, y, z) as

$$\begin{bmatrix} \boldsymbol{\sigma}_\Omega \\ \sigma_n \\ \boldsymbol{\sigma}_s \end{bmatrix}^p = \begin{bmatrix} \tilde{\mathbf{C}}_{\Omega\Omega} & \tilde{\mathbf{C}}_{\Omega n} & 0 \\ \tilde{\mathbf{C}}_{n\Omega} & \tilde{C}_{nn} & 0 \\ 0 & 0 & \tilde{\mathbf{C}}_{ss} \end{bmatrix}^p \begin{bmatrix} \boldsymbol{\epsilon}_\Omega \\ \epsilon_n \\ \boldsymbol{\epsilon}_s \end{bmatrix}^p \tag{A.9}$$

where

$$\tilde{\mathbf{C}}^p_{\Omega\Omega} = \begin{bmatrix} \tilde{C}_{11} & \tilde{C}_{12} & \tilde{C}_{16} \\ \tilde{C}_{12} & \tilde{C}_{22} & \tilde{C}_{26} \\ \tilde{C}_{16} & \tilde{C}_{26} & \tilde{C}_{66} \end{bmatrix}^p ; \quad \tilde{\mathbf{C}}^p_{\Omega n} = \begin{bmatrix} \tilde{C}_{13} \\ \tilde{C}_{23} \\ \tilde{C}_{63} \end{bmatrix}^p ; \quad \tilde{C}^p_{nn} = \tilde{C}^p_{33}; \tag{A.10}$$

$$\tilde{\mathbf{C}}_{n\Omega} = \begin{bmatrix} \tilde{C}_{13} & \tilde{C}_{23} & \tilde{C}^p_{63} \end{bmatrix}^p ; \quad \tilde{\mathbf{C}}^p_{ss} = \begin{bmatrix} \tilde{C}_{44} & \tilde{C}_{45} \\ \tilde{C}_{45} & \tilde{C}_{55} \end{bmatrix}^p$$

Appendix B

FE Approximations and arrays

B.1 QC4/CL8 interpolation schemes

The modified field-compatible shape functions $\mathcal{N}_i^{r\mathcal{U}}$ (with $\mathcal{U} \in \{u_x, u_y, u_z\}$ and $r \in \{x, y\}$) used to interpolate the $z-$ constant part of the transverse shear strains γ_{xz}^0 and γ_{yz}^0 in Eq. (2.19) are:

$$\begin{bmatrix} \mathcal{N}_i^x \\ \mathcal{N}_i^y \end{bmatrix}^{\mathcal{U}} = \mathbf{J}_{(GP)}^{-1} \begin{bmatrix} \mathcal{N}_i^\xi \\ \mathcal{N}_i^\eta \end{bmatrix}^{\mathcal{U}} = \begin{bmatrix} j_{11} & j_{12} \\ j_{21} & j_{22} \end{bmatrix}^{(GP)} \begin{bmatrix} \mathcal{N}_i^\xi \\ \mathcal{N}_i^\eta \end{bmatrix}^{\mathcal{U}} \tag{B.1}$$

where $j_{\alpha\beta}^{(GP)}$ (with $\alpha, \beta \in \{1, 2\}$) are the inverse terms of Jacobian matrix at Gauss point.

$$\begin{aligned} \mathcal{N}_i^{\xi\mathcal{U}} &= \sum_{I=1}^{2} C_{\xi_I}(\xi, \eta)\, \gamma_i^{\xi\mathcal{U}}(\xi_I, \eta_I) \\ \mathcal{N}_i^{\eta\mathcal{U}} &= \sum_{J=1}^{2} C_{\eta_J}(\xi, \eta)\, \gamma_i^{\eta\mathcal{U}}(\xi_J, \eta_J) \end{aligned} \tag{B.2}$$

where $\gamma_i^{\xi\mathcal{U}}$ and $\gamma_i^{\eta\mathcal{U}}$ are the $z-$constant reduced transverse shear strains evaluated at tying points (see Figure B.1 and Figure B.2). The explicit expressions of the interpolation functions are

- QC4 interpolation functions

$$\begin{aligned} C_{\xi_1}(\xi, \eta) &= \frac{1-\eta}{2}; \quad C_{\xi_2}(\xi, \eta) = \frac{1+\eta}{2} \\ C_{\eta_1}(\xi, \eta) &= \frac{1-\xi}{2}; \quad C_{\eta_2}(\xi, \eta) = \frac{1+\xi}{2} \end{aligned} \tag{B.3}$$

- CL8 interpolation functions

$$
\begin{aligned}
C_{\xi_1}(\xi,\eta) &= -\frac{1}{4}\left(\eta + \sqrt{3}\xi\right)(1-\eta)\,; & C_{\eta_1}(\xi,\eta) &= -\frac{1}{4}\left(\xi + \sqrt{3}\eta\right)(1-\xi)\\
C_{\xi_2}(\xi,\eta) &= -\frac{1}{4}\left(\eta - \sqrt{3}\xi\right)(1-\eta)\,; & C_{\eta_2}(\xi,\eta) &= -\frac{1}{4}\left(\xi - \sqrt{3}\eta\right)(1-\xi)\\
C_{\xi_3}(\xi,\eta) &= \frac{1}{4}\left(\eta + \sqrt{3}\xi\right)(1+\eta)\,; & C_{\eta_3}(\xi,\eta) &= \frac{1}{4}\left(\xi + \sqrt{3}\eta\right)(1+\xi)\\
C_{\xi_4}(\xi,\eta) &= \frac{1}{4}\left(\eta - \sqrt{3}\xi\right)(1+\eta)\,; & C_{\eta_4}(\xi,\eta) &= \frac{1}{4}\left(\xi - \sqrt{3}\eta\right)(1+\xi)\\
C_{\xi_5}(\xi,\eta) &= (1-\eta^2)\,; & C_{\eta_5}(\xi,\eta) &= (1-\xi^2)
\end{aligned}
\tag{B.4}
$$

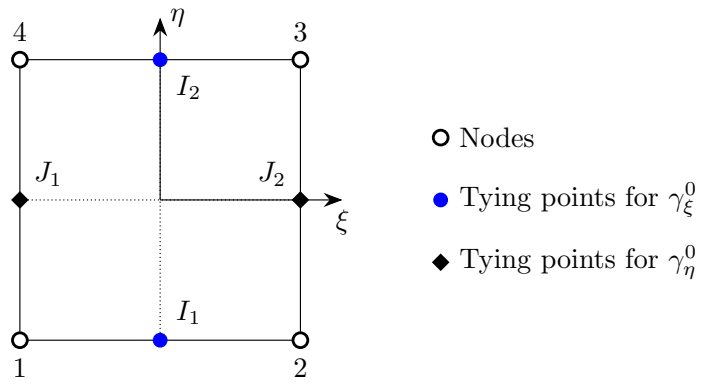

Figure B.1: Tying points for the QC4 iterpolation functions.

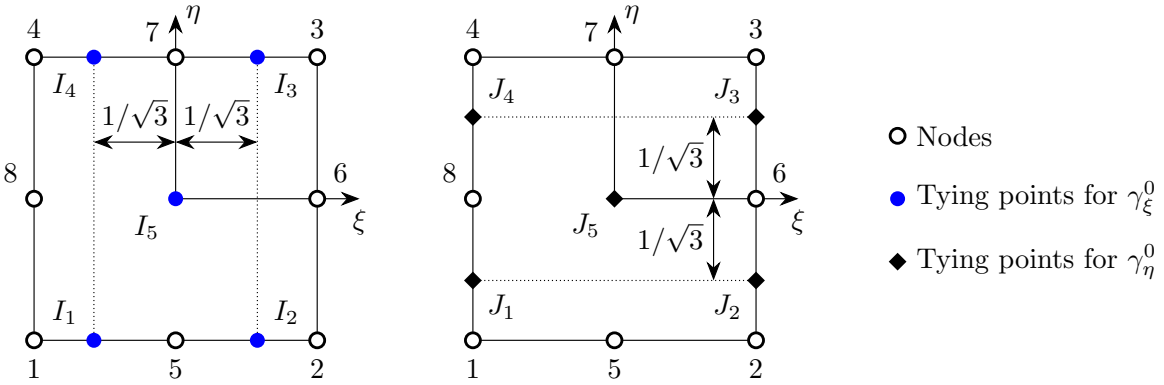

Figure B.2: Tying points for the CL8 iterpolation functions.

Using Einstein notation, the transverse shear strains components in Eq. (B.2) are

written as

$$\begin{aligned}
\gamma_i^{\xi u_x}(\xi_I,\eta_I) &= N_i(\xi_I,\eta_I)\, J_{11}^{(I)}(\xi_I,\eta_I) + N_{i,\xi}^{RT}(\xi_I,\eta_I)\\
\gamma_i^{\xi u_y}(\xi_I,\eta_I) &= N_i(\xi_I,\eta_I)\, J_{12}^{(I)}(\xi_I,\eta_I) + N_{i,\xi}^{ST}(\xi_I,\eta_I)\\
\gamma_i^{\xi u_z}(\xi_I,\eta_I) &= N_{i,\xi}(\xi_I,\eta_I)\\
\gamma_i^{\eta u_x}(\xi_J,\eta_J) &= N_i(\xi_J,\eta_J)\, J_{21}^{(J)}(\xi_J,\eta_J) + N_{i,\eta}^{RT}(\xi_J,\eta_J)\\
\gamma_i^{\eta u_y}(\xi_J,\eta_J) &= N_i(\xi_J,\eta_J)\, J_{22}^{(J)}(\xi_J,\eta_J) + N_{i,\eta}^{ST}(\xi_J,\eta_J)\\
\gamma_i^{\eta u_z}(\xi_J,\eta_J) &= N_{i,\eta}(\xi_J,\eta_J)
\end{aligned} \tag{B.5}$$

where $J_{\alpha\beta}^{(t)}$ (with $t \in \{1,2\}$) are the terms of Jacobian matrix evaluated at tying point t. The functions N_i^{RT} and N_i^{ST} for the four-node element are given as:

- four-node finite element

$$\begin{aligned}
N_{i|\,i=1,2}^{RT}(\xi,\eta) &= \frac{1}{8}\left[(-1)^i J_{11}^{(i)}\xi\left(1-\xi^2\right)(1+\eta_i\eta) - J_{21}^{(i)}(1+\xi_i\xi)\,\eta\left(1-\eta^2\right)\right]\\
N_{i|\,i=3,4}^{RT}(\xi,\eta) &= \frac{1}{8}\left[(-1)^{i+1} J_{11}^{(i)}\xi\left(1-\xi^2\right)(1+\eta_i\eta) + J_{21}^{(i)}(1+\xi_i\xi)\,\eta\left(1-\eta^2\right)\right]\\
N_{i|\,i=1,2}^{ST}(\xi,\eta) &= \frac{1}{8}\left[(-1)^i J_{12}^{(i)}\xi\left(1-\xi^2\right)(1+\eta_i\eta) - J_{22}^{(i)}(1+\xi_i\xi)\,\eta\left(1-\eta^2\right)\right]\\
N_{i|\,i=3,4}^{ST}(\xi,\eta) &= \frac{1}{8}\left[(-1)^{i+1} J_{12}^{(i)}\xi\left(1-\xi^2\right)(1+\eta_i\eta) + J_{22}^{(i)}(1+\xi_i\xi)\,\eta\left(1-\eta^2\right)\right]
\end{aligned} \tag{B.6}$$

- eight-node finite element

$$\begin{aligned}
N_{i|\,i=1,2,3,4}^{RT}(\xi,\eta) &= \frac{1}{12}\left[-J_{11}^{(i)}\xi\left(\xi^2-1\right)(1+\eta_i\eta) - J_{21}^{(i)}(1+\xi_i\xi)\,\eta\left(\eta^2-1\right)\right]\\
N_{i|\,i=5,7}^{RT}(\xi,\eta) &= \frac{1}{6}\left[J_{11}^{(i)}\xi\left(\xi^2-1\right)(1+\eta_i\eta)\right]\\
N_{i|\,i=6,8}^{RT}(\xi,\eta) &= \frac{1}{6}\left[J_{21}^{(i)}(1+\xi_i\xi)\,\eta\left(\eta^2-1\right)\right]\\
N_{i|\,i=1,2,3,4}^{ST}(\xi,\eta) &= \frac{1}{12}\left[-J_{12}^{(i)}\xi\left(\xi^2-1\right)(1+\eta_i\eta) - J_{22}^{(i)}(1+\xi_i\xi)\,\eta\left(\eta^2-1\right)\right]\\
N_{i|\,i=5,7}^{ST}(\xi,\eta) &= \frac{1}{6}\left[J_{12}^{(i)}\xi\left(\xi^2-1\right)(1+\eta_i\eta)\right]\\
N_{i|\,i=6,8}^{ST}(\xi,\eta) &= \frac{1}{6}\left[J_{22}^{(i)}(1+\xi_i\xi)\,\eta\left(\eta^2-1\right)\right]
\end{aligned} \tag{B.7}$$

where $J_{\alpha\beta}^{(i)}$ are the terms of Jacobian matrix at node i.

B.2 Arrays containing the thickness and in-plane interpolation functions

The arrays containing the through-thickness approximations and the shape functions (and their derivatives) introduced in the definition of the strain field in Eq. (2.19) are:

$$\mathbf{F}_{b\mu_{\mathcal{U}}}(z_p) = \begin{bmatrix} F_{\mu_{u_x}}(z_p) & 0 & 0 & 0 \\ 0 & F_{\mu_{u_y}}(z_p) & 0 & 0 \\ 0 & 0 & F_{\mu_{u_x}}(z_p) & F_{\mu_{u_y}}(z_p) \end{bmatrix} \tag{B.8}$$

$$\mathbf{F}_{n\mu_{\mathcal{U}}}(z_p) = \begin{bmatrix} 0 & 0 & F_{\mu_{u_{z,z}}}(z_p) \end{bmatrix} \tag{B.9}$$

$$\mathbf{F}^0_{s\mu_{\mathcal{U}}} = \begin{bmatrix} F^0_{\mu_{u_{x,z}}} & F^0_{\mu_{u_{y,z}}} & F^0_{\mu_{u_z}} & 0 & 0 & 0 \\ 0 & 0 & 0 & F^0_{\mu_{u_{x,z}}} & F^0_{\mu_{u_{y,z}}} & F^0_{\mu_{u_z}} \end{bmatrix} \tag{B.10}$$

$$\mathbf{F}^h_{s\mu_{\mathcal{U}}}(z_p) = \begin{bmatrix} F^h_{\mu_{u_{x,z}}}(z_p) & 0 & F^h_{\mu_{u_z}}(z_p) & 0 \\ 0 & F^h_{\mu_{u_{y,z}}}(z_p) & 0 & F^h_{\mu_{u_z}}(z_p) \end{bmatrix} \tag{B.11}$$

$$\mathbf{B}_{bi}(x,y) = \begin{bmatrix} N_{i,x}(x,y) & 0 & N_{i,y}(x,y) & 0 \\ 0 & N_{i,y}(x,y) & 0 & N_{i,x}(x,y) \\ 0 & 0 & 0 & 0 \end{bmatrix}^T \tag{B.12}$$

$$\mathbf{B}_{ni}(x,y) = \begin{bmatrix} 0 & 0 & 0 & 0 \\ 0 & 0 & 0 & 0 \\ 0 & 0 & 0 & N_i(x,y) \end{bmatrix}^T \tag{B.13}$$

$$\bar{\mathbf{B}}_{si}(x,y) = \begin{bmatrix} \mathcal{N}_i^{xu_x}(x,y) & 0 & 0 \\ 0 & \mathcal{N}_i^{xu_y}(x,y) & 0 \\ 0 & 0 & \mathcal{N}_i^{xu_z}(x,y) \\ \mathcal{N}_i^{yu_x}(x,y) & 0 & 0 \\ 0 & \mathcal{N}_i^{yu_y}(x,y) & 0 \\ 0 & 0 & \mathcal{N}_i^{yu_z}(x,y) \end{bmatrix} \tag{B.14}$$

$$\mathbf{B}_{si}(x,y) = \begin{bmatrix} N_i(x,y) & 0 & 0 & 0 \\ 0 & N_i(x,y) & 0 & 0 \\ 0 & 0 & N_{i,x}(x,y) & N_{i,y}(x,y) \end{bmatrix}^T \tag{B.15}$$

Appendix C

Fundamental nuclei of the Sublaminate-Generalized Unified Formulation

C.1 Displacement-based formulation

The fundamental nuclei of the displacement-based formulation derived from Eq. (2.7) are

$$
\begin{aligned}
K_{u_x u_x}^{p\mu_{u_x}\tau_{u_x} ij} = {} & Z_{u_x u_x 11}^{p\mu_{u_x}\tau_{u_x}} \lhd N_{i,x} N_{j,x} \rhd_\Omega + Z_{u_x u_x 16}^{p\mu_{u_x}\tau_{u_x}} \lhd N_{i,y} N_{j,x} \rhd_\Omega + \\
& + Z_{u_x u_x 16}^{p\mu_{u_x}\tau_{u_x}} \lhd N_{i,x} N_{j,y} \rhd_\Omega + Z_{u_x u_x 66}^{p\mu_{u_x}\tau_{u_x}} \lhd N_{i,y} N_{j,y} \rhd_\Omega + \\
& + Z_{u_x u_x 44}^{p\mu_{u_x,z}\tau_{u_x,z}00} \lhd \mathcal{N}_i^{yu_x} \mathcal{N}_j^{yu_x} \rhd_\Omega + Z_{u_x u_x 45}^{p\mu_{u_x,z}\tau_{u_x,z}00} \lhd \mathcal{N}_i^{xu_x} \mathcal{N}_j^{yu_x} \rhd_\Omega + \\
& + Z_{u_x u_x 45}^{p\mu_{u_x,z}\tau_{u_x,z}00} \lhd \mathcal{N}_i^{yu_x} \mathcal{N}_j^{xu_x} \rhd_\Omega + Z_{u_x u_x 45}^{p\mu_{u_x,z}\tau_{u_x,z}h0} \lhd N_i \, \mathcal{N}_j^{yu_x} \rhd_\Omega + \\
& + Z_{u_x u_x 45}^{p\mu_{u_x,z}\tau_{u_x,z}0h} \lhd \mathcal{N}_i^{yu_x} N_j \rhd_\Omega + Z_{u_x u_x 55}^{p\mu_{u_x,z}\tau_{u_x,z}00} \lhd \mathcal{N}_i^{xu_x} \mathcal{N}_j^{xu_x} \rhd_\Omega + \\
& + Z_{u_x u_x 55}^{p\mu_{u_x,z}\tau_{u_x,z}0h} \lhd \mathcal{N}_i^{xu_x} N_j \rhd_\Omega + Z_{u_x u_x 55}^{p\mu_{u_x,z}\tau_{u_x,z}h0} \lhd N_i \, \mathcal{N}_j^{xu_x} \rhd_\Omega + \\
& + Z_{u_x u_x 55}^{p\mu_{u_x,z}\tau_{u_x,z}hh} \lhd N_i N_j \rhd_\Omega
\end{aligned}
\tag{C.1}
$$

$$
\begin{aligned}
K_{u_x u_y}^{p\mu_{u_x}\tau_{u_y} ij} &= Z_{u_x u_y 12}^{p\mu_{u_x}\tau_{u_y}} \lhd N_{i,x} N_{j,y} \rhd_\Omega + Z_{u_x u_y 26}^{p\mu_{u_x}\tau_{u_y}} \lhd N_{i,y} N_{j,y} \rhd_\Omega + \\
&+ Z_{u_x u_y 16}^{p\mu_{u_x}\tau_{u_y}} \lhd N_{i,x} N_{j,x} \rhd_\Omega + Z_{u_x u_y 66}^{p\mu_{u_x}\tau_{u_y}} \lhd N_{i,y} N_{j,x} \rhd_\Omega + \\
&+ Z_{u_x u_y 44}^{p\mu_{u_x,z}\tau_{u_y,z}\,00} \lhd \mathcal{N}_i^{yu_x} \mathcal{N}_j^{yu_y} \rhd_\Omega + Z_{u_x u_y 44}^{p\mu_{u_x,z}\tau_{u_y,z}\,0h} \lhd \mathcal{N}_i^{yu_x} N_j \rhd_\Omega + \\
&+ Z_{u_x u_y 45}^{p\mu_{u_x,z}\tau_{u_y,z}\,00} \lhd \mathcal{N}_i^{xu_x} \mathcal{N}_j^{yu_y} \rhd_\Omega + Z_{u_x u_y 45}^{p\mu_{u_x,z}\tau_{u_y,z}\,00} \lhd \mathcal{N}_i^{yu_x} \mathcal{N}_j^{xu_y} \rhd_\Omega + \\
&+ Z_{u_x u_y 45}^{p\mu_{u_x,z}\tau_{u_y,z}\,0h} \lhd \mathcal{N}_i^{xu_x} N_j \rhd_\Omega + Z_{u_x u_y 45}^{p\mu_{u_x,z}\tau_{u_y,z}\,h0} \lhd N_i\ \mathcal{N}_j^{yu_y} \rhd_\Omega + \\
&+ Z_{u_x u_y 45}^{p\mu_{u_x,z}\tau_{u_y,z}\,hh} \lhd N_i N_j \rhd_\Omega + Z_{u_x u_y 55}^{p\mu_{u_x,z}\tau_{u_y,z}\,00} \lhd \mathcal{N}_i^{xu_x} \mathcal{N}_j^{xu_y} \rhd_\Omega + \\
&+ Z_{u_x u_y 55}^{p\mu_{u_x,z}\tau_{u_y,z}\,h0} \lhd N_i\ \mathcal{N}_j^{xu_y} \rhd_\Omega \\
K_{u_x u_z}^{p\mu_{u_x}\tau_{u_z} ij} &= Z_{u_x u_z 13}^{p\mu_{u_x}\tau_{u_z,z}} \lhd N_{i,x} N_j \rhd_\Omega + Z_{u_x u_z 36}^{p\mu_{u_x}\tau_{u_z,z}} \lhd N_{i,y} N_j \rhd_\Omega + \\
&+ Z_{u_x u_z 44}^{p\mu_{u_x,z}\tau_{u_z}\,00} \lhd \mathcal{N}_i^{yu_x} \mathcal{N}_j^{yu_z} \rhd_\Omega + Z_{u_x u_z 44}^{p\mu_{u_x,z}\tau_{u_z}\,0h} \lhd \mathcal{N}_i^{yu_x} N_{j,y} \rhd_\Omega + \\
&+ Z_{u_x u_z 45}^{p\mu_{u_x,z}\tau_{u_z}\,00} \lhd \mathcal{N}_i^{xu_x} \mathcal{N}_j^{yu_z} \rhd_\Omega + Z_{u_x u_z 45}^{p\mu_{u_x,z}\tau_{u_z}\,00} \lhd \mathcal{N}_i^{yu_x} \mathcal{N}_j^{xu_z} \rhd_\Omega + \\
&+ Z_{u_x u_z 45}^{p\mu_{u_x,z}\tau_{u_z}\,0h} \lhd \mathcal{N}_i^{yu_x} N_{j,x} \rhd_\Omega + Z_{u_x u_z 45}^{p\mu_{u_x,z}\tau_{u_z}\,0h} \lhd \mathcal{N}_i^{xu_x} N_{j,y} \rhd_\Omega + \\
&+ Z_{u_x u_z 45}^{p\mu_{u_x,z}\tau_{u_z}\,h0} \lhd N_i\ \mathcal{N}_j^{yu_z} \rhd_\Omega + Z_{u_x u_z 45}^{p\mu_{u_x,z}\tau_{u_z}\,hh} \lhd N_i N_{j,y} \rhd_\Omega + \\
&+ Z_{u_x u_z 55}^{p\mu_{u_x,z}\tau_{u_z}\,00} \lhd \mathcal{N}_i^{xu_x} \mathcal{N}_j^{xu_z} \rhd_\Omega + Z_{u_x u_z 55}^{p\mu_{u_x,z}\tau_{u_z}\,0h} \lhd \mathcal{N}_i^{xu_x} N_{j,x} \rhd_\Omega + \\
&+ Z_{u_x u_z 55}^{p\mu_{u_x,z}\tau_{u_z}\,h0} \lhd N_i\ \mathcal{N}_j^{xu_z} \rhd_\Omega + Z_{u_x u_z 55}^{p\mu_{u_x,z}\tau_{u_z}\,hh} \lhd N_i N_{j,x} \rhd_\Omega \\
K_{u_y u_y}^{p\mu_{u_y}\tau_{u_y} ij} &= Z_{u_y u_y 22}^{p\mu_{u_y}\tau_{u_y}} \lhd N_{i,y} N_{j,y} \rhd_\Omega + Z_{u_y u_y 26}^{p\mu_{u_y}\tau_{u_y}} \lhd N_{i,x} N_{j,y} \rhd_\Omega + \\
&+ Z_{u_y u_y 26}^{p\mu_{u_y}\tau_{u_y}} \lhd N_{i,y} N_{j,x} \rhd_\Omega + Z_{u_y u_y 66}^{p\mu_{u_y}\tau_{u_y}} \lhd N_{i,x} N_{j,x} \rhd_\Omega + \\
&+ Z_{u_y u_y 44}^{p\mu_{u_y,z}\tau_{u_y,z}\,00} \lhd \mathcal{N}_i^{yu_y} \mathcal{N}_j^{yu_y} \rhd_\Omega + Z_{u_y u_y 44}^{p\mu_{u_y,z}\tau_{u_y,z}\,h0} \lhd N_i\ \mathcal{N}_j^{yu_y} \rhd_\Omega + \\
&+ Z_{u_y u_y 44}^{p\mu_{u_y,z}\tau_{u_y,z}\,0h} \lhd \mathcal{N}_i^{yu_y} N_j \rhd_\Omega + Z_{u_y u_y 44}^{p\mu_{u_y,z}\tau_{u_y,z}\,hh} \lhd N_i N_j \rhd_\Omega + \\
&+ Z_{u_y u_y 45}^{p\mu_{u_y,z}\tau_{u_y,z}\,00} \lhd \mathcal{N}_i^{xu_y} \mathcal{N}_j^{yu_y} \rhd_\Omega + Z_{u_y u_y 45}^{p\mu_{u_y,z}\tau_{u_y,z}\,00} \lhd \mathcal{N}_i^{yu_y} \mathcal{N}_j^{xu_y} \rhd_\Omega + \\
&+ Z_{u_y u_y 45}^{p\mu_{u_y,z}\tau_{u_y,z}\,0h} \lhd \mathcal{N}_i^{xu_y} N_j \rhd_\Omega + Z_{u_y u_y 45}^{p\mu_{u_y,z}\tau_{u_y,z}\,h0} \lhd N_i\ \mathcal{N}_j^{xu_y} \rhd_\Omega + \\
&+ Z_{u_y u_y 55}^{p\mu_{u_y,z}\tau_{u_y,z}\,00} \lhd \mathcal{N}_i^{xu_y} \mathcal{N}_j^{xu_y} \rhd_\Omega
\end{aligned}
$$

$$
\begin{aligned}
K_{u_y u_z}^{p\mu_{u_y}\tau_{u_z} ij} = {} & Z_{u_y u_z 23}^{p\mu_{u_y}\tau_{u_z,z}} \lhd N_{i,y} N_j \rhd_\Omega + Z_{u_y u_z 36}^{p\mu_{u_y}\tau_{u_z,z}} \lhd N_{i,x} N_j \rhd_\Omega + \\
& + Z_{u_y u_z 44}^{p\mu_{u_y,z}\tau_{u_z} 00} \lhd \mathcal{N}_i^{yu_y} \mathcal{N}_j^{yu_z} \rhd_\Omega + Z_{u_y u_z 44}^{p\mu_{u_y,z}\tau_{u_z} 0h} \lhd \mathcal{N}_i^{yu_y} N_{j,y} \rhd_\Omega + \\
& + Z_{u_y u_z 44}^{p\mu_{u_y,z}\tau_{u_z} h0} \lhd N_i \, \mathcal{N}_j^{yu_z} \rhd_\Omega + Z_{u_y u_z 44}^{p\mu_{u_y,z}\tau_{u_z} hh} \lhd N_i N_{j,y} \rhd_\Omega + \\
& + Z_{u_y u_z 45}^{p\mu_{u_y,z}\tau_{u_z} 00} \lhd \mathcal{N}_i^{xu_y} \mathcal{N}_j^{yu_z} \rhd_\Omega + Z_{u_y u_z 45}^{p\mu_{u_y,z}\tau_{u_z} 00} \lhd \mathcal{N}_i^{yu_y} \mathcal{N}_j^{xu_z} \rhd_\Omega + \\
& + Z_{u_y u_z 45}^{p\mu_{u_y,z}\tau_{u_z} 0h} \lhd \mathcal{N}_i^{yu_y} N_{j,x} \rhd_\Omega + Z_{u_y u_z 45}^{p\mu_{u_y,z}\tau_{u_z} 0h} \lhd \mathcal{N}_i^{xu_y} N_{j,y} \rhd_\Omega + \\
& + Z_{u_y u_z 45}^{p\mu_{u_y,z}\tau_{u_z} h0} \lhd N_i \, \mathcal{N}_j^{xu_z} \rhd_\Omega + Z_{u_y u_z 45}^{p\mu_{u_y,z}\tau_{u_z} hh} \lhd N_i N_{j,x} \rhd_\Omega + \\
& + Z_{u_y u_z 55}^{p\mu_{u_y,z}\tau_{u_z} 00} \lhd \mathcal{N}_i^{xu_y} \mathcal{N}_j^{xu_z} \rhd_\Omega + Z_{u_y u_z 55}^{p\mu_{u_y,z}\tau_{u_z} 0h} \lhd \mathcal{N}_i^{xu_y} N_{j,x} \rhd_\Omega + \\
K_{u_z u_z}^{p\mu_{u_z}\tau_{u_z} ij} = {} & Z_{u_z u_z 33}^{p\mu_{u_y,z}\tau_{u_z,z}} \lhd N_i N_j \rhd_\Omega + Z_{u_z u_z 44}^{p\mu_{u_z}\tau_{u_z} 00} \lhd \mathcal{N}_i^{yu_z} \mathcal{N}_j^{yu_z} \rhd_\Omega + \\
& + Z_{u_z u_z 44}^{p\mu_{u_z}\tau_{u_z} 0h} \lhd \mathcal{N}_i^{yu_z} N_{j,y} \rhd_\Omega + Z_{u_z u_z 44}^{p\mu_{u_z}\tau_{u_z} h0} \lhd N_{i,y} \, \mathcal{N}_j^{yu_z} \rhd_\Omega + \\
& + Z_{u_z u_z 44}^{p\mu_{u_z}\tau_{u_z} hh} \lhd N_{i,y} N_{j,y} \rhd_\Omega + Z_{u_z u_z 45}^{p\mu_{u_z}\tau_{u_z} 00} \lhd \mathcal{N}_i^{xu_z} \mathcal{N}_j^{yu_z} \rhd_\Omega + \\
& + Z_{u_z u_z 45}^{p\mu_{u_z}\tau_{u_z} 00} \lhd \mathcal{N}_i^{yu_z} \mathcal{N}_j^{xu_z} \rhd_\Omega + Z_{u_z u_z 45}^{p\mu_{u_z}\tau_{u_z} 0h} \lhd \mathcal{N}_i^{yu_z} N_{j,x} \rhd_\Omega + \\
& + Z_{u_z u_z 45}^{p\mu_{u_z}\tau_{u_z} 0h} \lhd \mathcal{N}_i^{xu_z} N_{j,y} \rhd_\Omega + Z_{u_z u_z 45}^{p\mu_{u_z}\tau_{u_z} h0} \lhd N_{i,y} \, \mathcal{N}_j^{xu_z} \rhd_\Omega + \\
& + Z_{u_z u_z 45}^{p\mu_{u_z}\tau_{u_z} h0} \lhd N_{i,x} \, \mathcal{N}_j^{yu_z} \rhd_\Omega + Z_{u_z u_z 45}^{p\mu_{u_z}\tau_{u_z} hh} \lhd N_{i,y} N_{j,x} \rhd_\Omega + \\
& + Z_{u_z u_z 45}^{p\mu_{u_z}\tau_{u_z} hh} \lhd N_{i,x} N_{j,y} \rhd_\Omega + Z_{u_z u_z 55}^{p\mu_{u_z}\tau_{u_z} 00} \lhd \mathcal{N}_i^{xu_z} \mathcal{N}_j^{xu_z} \rhd_\Omega + \\
& + Z_{u_z u_z 55}^{p\mu_{u_z}\tau_{u_z} 0h} \lhd \mathcal{N}_i^{xu_z} N_{j,x} \rhd_\Omega + Z_{u_z u_z 55}^{p\mu_{u_z}\tau_{u_z} h0} \lhd N_{i,x} \, \mathcal{N}_j^{xu_z} \rhd_\Omega + \\
& + Z_{u_z u_z 55}^{p\mu_{u_z}\tau_{u_z} hh} \lhd N_{i,x} N_{j,x} \rhd_\Omega
\end{aligned}
$$

where $\lhd \quad \rhd_\Omega$ denotes the integral over the in-plane domain Ω.

C.2 RMVT-based formulation

The fundamental nuclei of the RMVT-based formulation derived from Eq. (2.8) are

$$
\begin{aligned}
K^{p\mu_{u_x}\tau_{u_x}ij}_{u_xu_x} &= Z^{p\mu_{u_x}\tau_{u_x}}_{u_xu_x11} \lhd N_{i,x}N_{j,x} \rhd_\Omega + Z^{p\mu_{u_x}\tau_{u_x}}_{u_xu_x16} \lhd N_{i,y}N_{j,x} \rhd_\Omega + \\
&\quad + Z^{p\mu_{u_x}\tau_{u_x}}_{u_xu_x16} \lhd N_{i,x}N_{j,y} \rhd_\Omega + Z^{p\mu_{u_x}\tau_{u_x}}_{66u_xu_x} \lhd N_{i,y}N_{j,y} \rhd_\Omega \\
K^{p\mu_{u_x}\tau_{u_y}ij}_{u_xu_y} &= Z^{p\mu_{u_x}\tau_{u_y}}_{u_xu_y12} \lhd N_{i,x}N_{j,y} \rhd_\Omega + Z^{p\mu_{u_x}\tau_{u_y}}_{u_xu_y26} \lhd N_{i,y}N_{j,y} \rhd_\Omega + \\
&\quad + Z^{p\mu_{u_x}\tau_{u_y}}_{u_xu_y16} \lhd N_{i,x}N_{j,x} \rhd_\Omega + Z^{p\mu_{u_x}\tau_{u_y}}_{u_xu_y66} \lhd N_{i,y}N_{j,x} \rhd_\Omega \\
K^{p\mu_{u_x}\tau_{s_x}ij}_{u_xs_x} &= Z^{p\mu_{u_x,z}\tau_{s_x}0a}_{u_xs_x} \lhd \mathcal{N}^{xu_x}_i N_j \rhd_\Omega + Z^{p\mu_{u_x,z}\tau_{s_x}ha}_{u_xs_x} \lhd N_iN_j \rhd_\Omega \\
K^{p\mu_{u_x}\tau_{s_y}ij}_{u_xs_y} &= Z^{p\mu_{u_x,z}\tau_{s_y}0a}_{u_xs_y} \lhd \mathcal{N}^{yu_x}_i N_j \rhd_\Omega \\
K^{p\mu_{u_x}\tau_{s_z}ij}_{u_xs_z} &= Z^{p\mu_{u_x}\tau_{s_z}}_{u_xs_z13} \lhd N_{i,x}N_j \rhd_\Omega + Z^{p\mu_{u_x}\tau_{s_z}}_{u_xs_z63} \lhd N_{i,y}N_j \rhd_\Omega \\
K^{p\mu_{u_y}\tau_{u_y}ij}_{u_yu_y} &= Z^{p\mu_{u_y}\tau_{u_y}}_{u_yu_y22} \lhd N_{i,y}N_{j,y} \rhd_\Omega + Z^{p\mu_{u_y}\tau_{u_y}}_{u_yu_y26} \lhd N_{i,x}N_{j,y} \rhd_\Omega + \\
&\quad + Z^{p\mu_{u_y}\tau_{u_y}}_{u_yu_y26} \lhd N_{i,y}N_{j,x} \rhd_\Omega + Z^{p\mu_{u_y}\tau_{u_y}}_{u_yu_y66} \lhd N_{i,x}N_{j,x} \rhd_\Omega \\
K^{p\mu_{u_y}\tau_{s_x}ij}_{u_ys_x} &= Z^{p\mu_{u_y,z}\tau_{s_x}0a}_{u_ys_x} \lhd \mathcal{N}^{xu_y}_i N_j \rhd_\Omega \\
K^{p\mu_{u_y}\tau_{s_y}ij}_{u_ys_y} &= Z^{p\mu_{u_y,z}\tau_{s_y}0a}_{u_ys_y} \lhd \mathcal{N}^{yu_y}_i N_j \rhd_\Omega + Z^{p\mu_{u_y,z}\tau_{s_y}ha}_{u_ys_y} \lhd N_iN_j \rhd_\Omega \\
K^{p\mu_{u_y}\tau_{s_z}ij}_{u_ys_z} &= Z^{p\mu_{u_y}\tau_{s_z}}_{u_ys_z23} \lhd N_{i,y}N_j \rhd_\Omega + Z^{p\mu_{u_y}\tau_{s_z}}_{u_ys_z63} \lhd N_{i,x}N_j \rhd_\Omega \\
K^{p\mu_{u_z}\tau_{s_x}ij}_{u_zs_x} &= Z^{p\mu_{u_z}\tau_{s_x}0a}_{u_zs_x} \lhd \mathcal{N}^{xu_z}_i N_j \rhd_\Omega + Z^{p\mu_{u_z}\tau_{s_x}ha}_{u_zs_x} \lhd N_{i,x}N_j \rhd_\Omega \\
K^{p\mu_{u_z}\tau_{s_y}ij}_{u_zs_y} &= Z^{p\mu_{u_z}\tau_{s_y}0a}_{u_zs_y} \lhd \mathcal{N}^{yu_z}_i N_j \rhd_\Omega + Z^{p\mu_{u_z}\tau_{s_y}ha}_{u_zs_y} \lhd N_{i,y}N_j \rhd_\Omega \\
K^{p\mu_{u_z}\tau_{s_z}ij}_{u_zs_z} &= Z^{p\mu_{u_z,z}\tau_{s_z}}_{u_zs_z} \lhd N_iN_j \rhd_\Omega \\
K^{p\mu_{s_x}\tau_{s_x}ij}_{s_xs_x} &= -Z^{p\mu_{s_x}\tau_{s_x}}_{s_xs_x55} \lhd N_iN_j \rhd_\Omega \\
K^{p\mu_{s_x}\tau_{s_y}ij}_{s_xs_y} &= -Z^{p\mu_{s_x}\tau_{s_y}}_{s_xs_y45} \lhd N_iN_j \rhd_\Omega \\
K^{p\mu_{s_y}\tau_{s_y}ij}_{s_ys_y} &= -Z^{p\mu_{s_y}\tau_{s_y}}_{s_ys_y44} \lhd N_iN_j \rhd_\Omega \\
K^{p\mu_{s_z}\tau_{s_z}ij}_{s_zs_z} &= -Z^{p\mu_{s_z}\tau_{s_z}}_{s_zs_z33} \lhd N_iN_j \rhd_\Omega
\end{aligned}
\tag{C.2}
$$

Appendix D

Comparison between conventional 3D and refined 2D FEM

This Appendix aims at establishing a honest comparison between the conventional 3D FEM and the refined 2D modelling techniques developed throughout the thesis, with particular emphasis on the analysis of sandwich structures. The main drawback of 3D FEs in modelling the thin facesheets of sandwich panels lies in the fact that to obtain an accurate description of the transverse stress field, several solid elements across the thickness may be required. As a result, the element slenderness (ratio between the main dimension and the thickness) increases, entailing a risk of accuracy degradation. Simultaneously refining the in-plane domain discretization is the acknowledged manner to avoid the numerical issues which may arise due to excessive slenderness of 3D FEs. The resulting model may hence come along with a heavy computational effort.

Contrary to most works available in open literature, the analysis presented in this Appendix intends to carry out the 3D vs 2D comparison by allowing the 3D FE to have a non-unit slenderness ratio. The sandwich panel investigated in Section 2.4 and Section 3.2.1 is addressed. The 3D FEM solution is obtained with the commercial software package Abaqus. The 20 nodes brick element with reduced integration of the standard element library, namely the C3D20R element, is used for the analysis. The influence of the element slenderness is studied by keeping fixed the in-plane discretization and by progressively increasing the number of elements used through-the-thickness. In particular, 16 C3D20R elements are used along both x and y directions; the number of elements across the facesheets ranges from 1 to 7 ($N_{\text{elt}}^{\text{skin}} \in \{1, 7\}$), while the discretization in the core layer involves 1 to 5 elements ($N_{\text{elt}}^{\text{core}} \in \{1, 5\}$). Table D.1 lists the aspect ratio of the most slender element in the mesh, referred to as ${}^{w}S_{\text{elt}}$, where the superscript w stands for *worst*, as the number of 3D elements used in the facesheets varies.

Tables from D.2 to D.5 report the maximum value of the out-of-plane displacement u_z, the bending stress σ_{xx}, the transverse shear stress σ_{xz} and the transverse normal stress σ_{zz}, respectively, for different discretization parameter pairs $N_{\text{elt}}^{\text{skin}} - N_{\text{elt}}^{\text{core}}$. Bold values identify the converged solution which is defined as the value obtained with the most refined discretization, i.e. $N_{\text{elt}}^{\text{skin}} = 7$ and $N_{\text{elt}}^{\text{core}} = 5$.

Table D.1: Aspect ratio of the most slender 3D element.

	$N_{\text{elt}}^{\text{skin}}$						
	1	2	3	4	5	6	7
${}^{w}S_{\text{elt}}$	3.125	6.25	9.375	12.5	15.625	18.75	21.875

Table D.2: Maximum value of the transverse displacement u_z [mm] of a simply-supported sandwich panel with increasing the FE discretization across the thickness.

		$N_{\text{elt}}^{\text{skin}}$						
$u_z^{\max}$		1	2	3	4	5	6	7
$N_{\text{elt}}^{\text{core}}$	1	2.55631	2.55635	2.55635	2.55635	2.55635	2.55635	2.55635
	2	2.55631	2.55635	2.55635	**2.55636**	**2.55636**	**2.55636**	**2.55636**
	3	2.55631	2.55635	2.55635	**2.55636**	**2.55636**	**2.55636**	**2.55636**
	4	2.55631	2.55635	2.55635	**2.55636**	**2.55636**	**2.55636**	**2.55636**
	5	2.55631	2.55635	2.55635	**2.55636**	**2.55636**	**2.55636**	**2.55636**

Bold values identify the converged solution

Table D.3: Maximum value of the in-plane stress σ_{xx} [MPa] of a simply-supported sandwich panel with increasing the FE discretization across the thickness.

		$N_{\text{elt}}^{\text{skin}}$						
$\sigma_{xx}^{\max}$		1	2	3	4	5	6	7
$N_{\text{elt}}^{\text{core}}$	1	164.213	164.276	164.305	164.318	164.324	164.328	**164.330**
	2	164.213	164.276	164.305	164.318	164.324	164.328	**164.330**
	3	164.213	164.276	164.305	164.318	164.324	164.328	**164.330**
	4	164.213	164.276	164.305	164.318	164.324	164.328	**164.330**
	5	164.213	164.276	164.305	164.318	164.324	164.328	**164.330**

Bold values identify the converged solution

It is worth noticing that the element slenderness ranges from ${}^{w}S_{\text{elt}} \approx 3$ up to ${}^{w}S_{\text{elt}} \approx 22$, thus deviating even significantly from the widely suggested unitary value. Nevertheless, no accuracy degradation is observed, demonstrating the reliability and robustness of the C3D20R element even for high values of the slenderness ratio.

Table D.4: Maximum value of the transverse shear stress σ_{xz} [MPa] of a simply-supported sandwich panel with increasing the FE discretization across the thickness.

$\sigma_{xz}^{\max}$		$N_{\text{elt}}^{\text{skin}}$						
		1	2	3	4	5	6	7
$N_{\text{elt}}^{\text{core}}$	1	2.71967	2.23114	2.32143	2.32544	2.30610	2.28414	2.28921
	2	2.71966	2.23124	2.32143	2.32541	2.30608	2.28411	**2.28922**
	3	2.71967	2.23125	2.32140	2.32541	2.30607	2.28411	**2.28922**
	4	2.71967	2.23125	2.32140	2.32541	2.30607	2.28411	**2.28922**
	5	2.71967	2.23125	2.32140	2.32541	2.30607	2.28411	**2.28922**

Bold values identify the converged solution

Table D.5: Maximum value of the transverse normal stress σ_{zz} [MPa] of a simply-supported sandwich panel with increasing the FE discretization across the thickness.

$\sigma_{zz}^{\max}$		$N_{\text{elt}}^{\text{skin}}$						
		1	2	3	4	5	6	7
$N_{\text{elt}}^{\text{core}}$	1	1.00958	1.00439	1.00249	1.00164	1.00115	1.00081	**1.00054**
	2	1.00958	1.00439	1.00249	1.00164	1.00115	1.00081	**1.00054**
	3	1.00958	1.00439	1.00249	1.00164	1.00115	1.00081	**1.00054**
	4	1.00958	1.00439	1.00249	1.00164	1.00115	1.00081	**1.00054**
	5	1.00958	1.00439	1.00249	1.00164	1.00115	1.00081	**1.00054**

Bold values identify the converged solution

Since the physics of the problem does not involve important gradients in the core layer, only one element is sufficient to provide a converged solution, irrespective of the variable of interest. Furthermore, no significant improvement in terms of local maximum values is observed by increasing the number of elements across the facesheets beyond 2. However, a mesh refinement is still required if a thorough description of the transverse stress field across the facesheets is sought. The through-thickness distributions of the transverse shear stress σ_{xz} and transverse normal stress σ_{zz} are plotted in Figure D.1 and Figure D.2, respectively. One element for the core layer is considered whereas the discretization parameter $N_{\text{elt}}^{\text{skin}}$ is varied from the coarsest value ($N_{\text{elt}}^{\text{skin}} = 1$) up to the most refined one ($N_{\text{elt}}^{\text{skin}} = 7$). It is observed that the quadratic and cubic distribution of the σ_{xz} and σ_{zz}, respectively, is only achieved by increasing the number of elements used across the facesheet. The refinement allows also to reduce the discontinuity at facesheet-core interfaces and to fulfill the traction conditions at the top surface. Moreover, at least 5 elements are needed for meeting the condition $\sigma_{zz,z} = 0$ at the top surface. It is worth noticing that the most refined discretization provides the most accurate 3D solution, even if the slenderness ratio of the facesheets elements

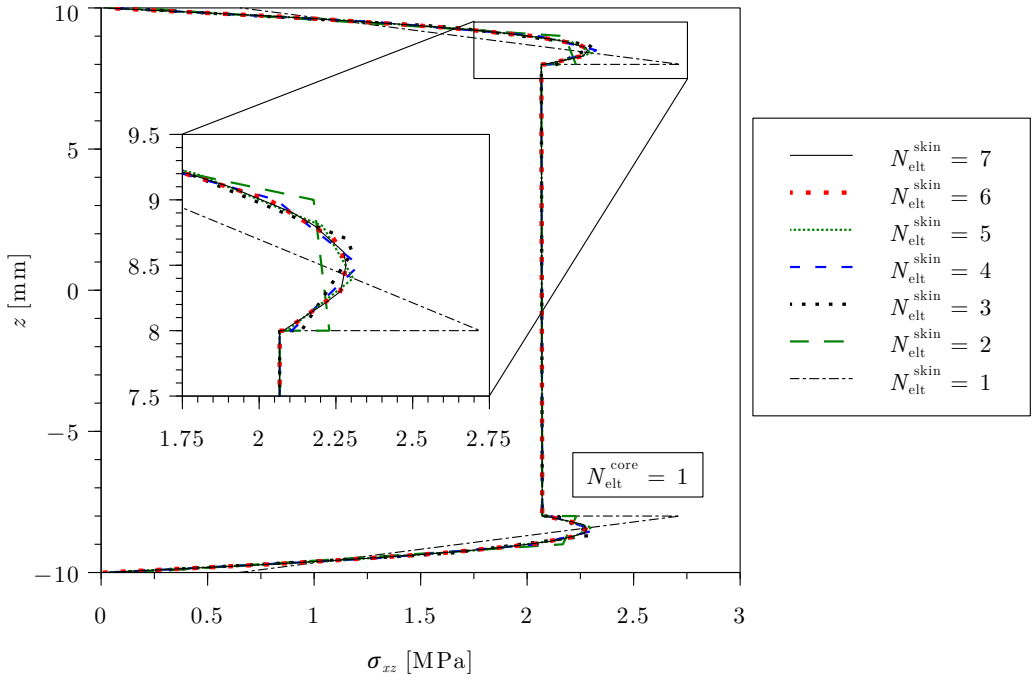

Figure D.1: Through-thickness distribution of the transverse shear stress σ_{xz} at $(x = -a/2, y = 0)$. Comparison between 3D solutions by varying the number of FEs across the skins.

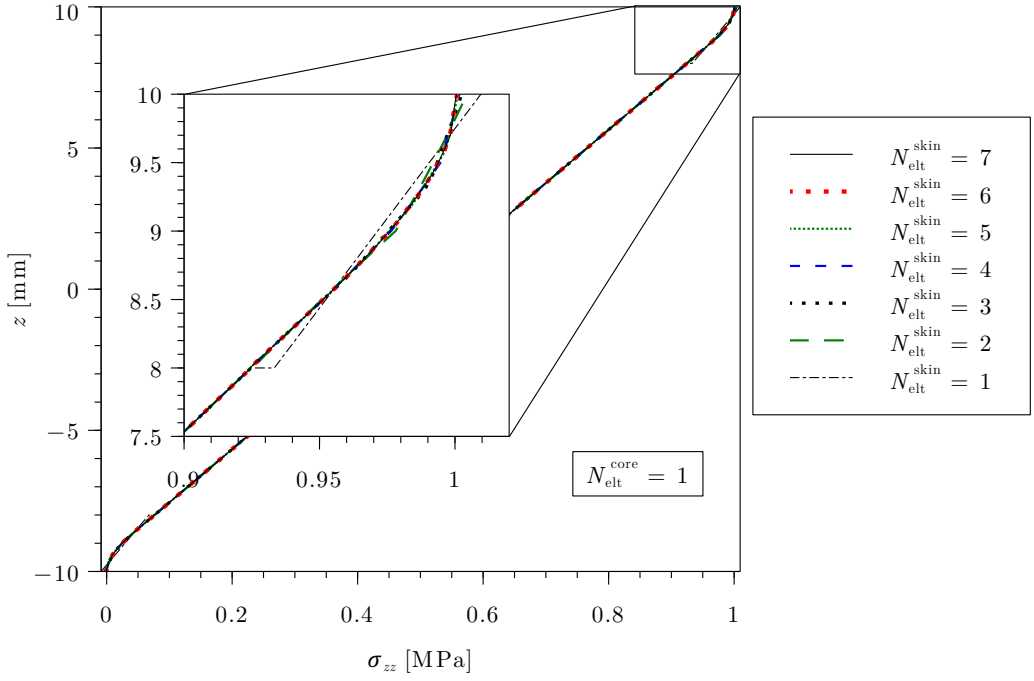

Figure D.2: Through-thickness distribution of the transverse normal stress σ_{zz} at $(x = 0, y = 0)$. Comparison between 3D solutions by varying the number of FEs across the skins.

is ≈ 22. To sum up, the following conclusions can be drawn:

- FE elements implemented in commercial software packages are based on displace-

ment formulations and therefore require the use of a large number of 3D elements along the thickness direction to provide a thorough description of the transverse stresses distributions across the sandwich panel's thickness.

- Due to the robustness of the C3D20R element, a slenderness ratio greater than 1 is not found to lead to any accuracy degradation.
- The global size of the problem may significantly increase whenever steep gradients across the thickness are to be grasped.

The last point paves the way for a comparison between the 3D and 2D modelling approaches. Based on the previous convergence analysis, two conventional 3D models are selected: the computationally efficient and accurate model with $N_{\text{elt}}^{\text{skin}} = 5$ and the most refined one ($N_{\text{elt}}^{\text{skin}} = 7$). Both models consider one element across the core layer. As far as the 2D modelling approach is concerned, the same in-plane discretization f the 3D models is adopted: a 16×16 CL8 mesh is therefore used. Four different models along the thickness direction are investigated:

LD3. A layerwise displacement-based CUF model with a cubic expansion order along the thickness direction for the displacement variables.

LM3. A layerwise mixed CUF model with a cubic expansion order along the thickness direction for both displacement and transverse stress variables.

$\mathbf{LM_{33}^{3\natural 3}}$. LM3 model, but with homogeneous boundary conditions on transverse shear stresses exactly verified at plate's top/bottom surfaces.

$\mathbf{EM_{33}^{3\natural 3}/EM_{12}^{01}}$. A mixed SGUF model with one sublaminates for each ply. The facesheets are modelled according to $\text{LM}_{33}^{3\natural 3}$, while a low-order mixed model retaining a quadratic distribution of the transverse displacement is employed for the core layer, namely the EM_{12}^{01} model.

Figure D.3 and Figure D.4 show the through-thickness distributions of the transverse stress variables σ_{xz} and σ_{zz}. It is observed that the LD3 model overestimates the maximum value of the transverse shear stress σ_{xz} of nearly 9%. Moreover, the interlaminar continuity as well as the homogeneous condition of the transverse shear stress at plate's top/bottom surfaces and of the transverse normal stress at plate's bottom surface are violated. No significant improvement is introduced when referring to the

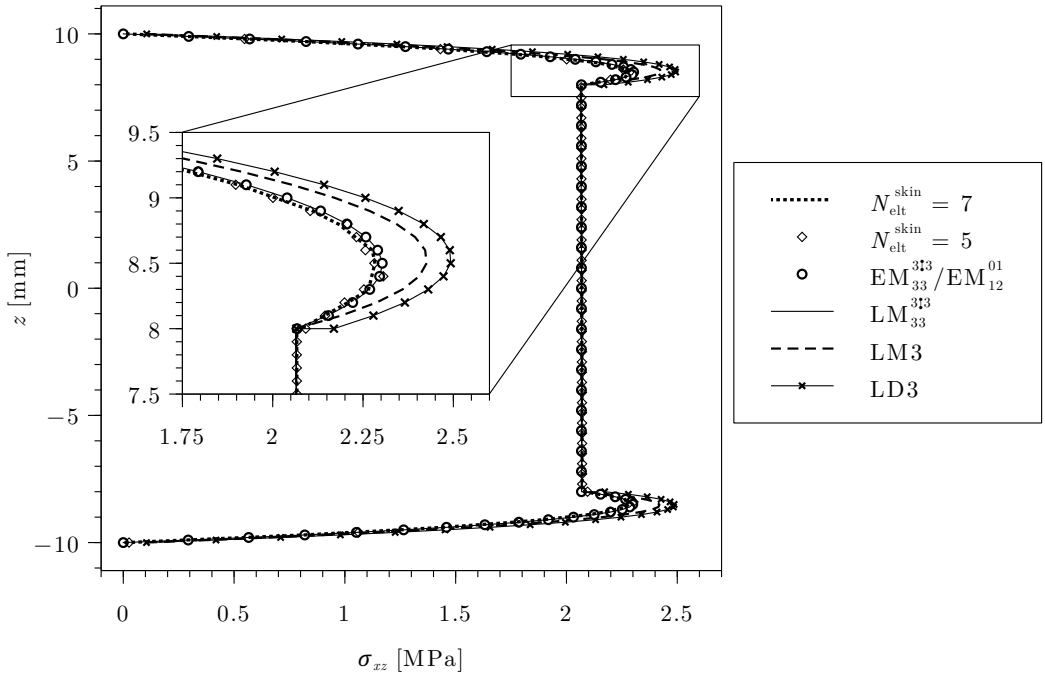

Figure D.3: Through-thickness distribution of the transverse shear stress σ_{xz} at $(x = -a/2, y = 0)$. Comparison between 3D and present 2D solutions. 3D models involve only one element in the core $(N_{\text{elt}}^{\text{core}} = 1)$.

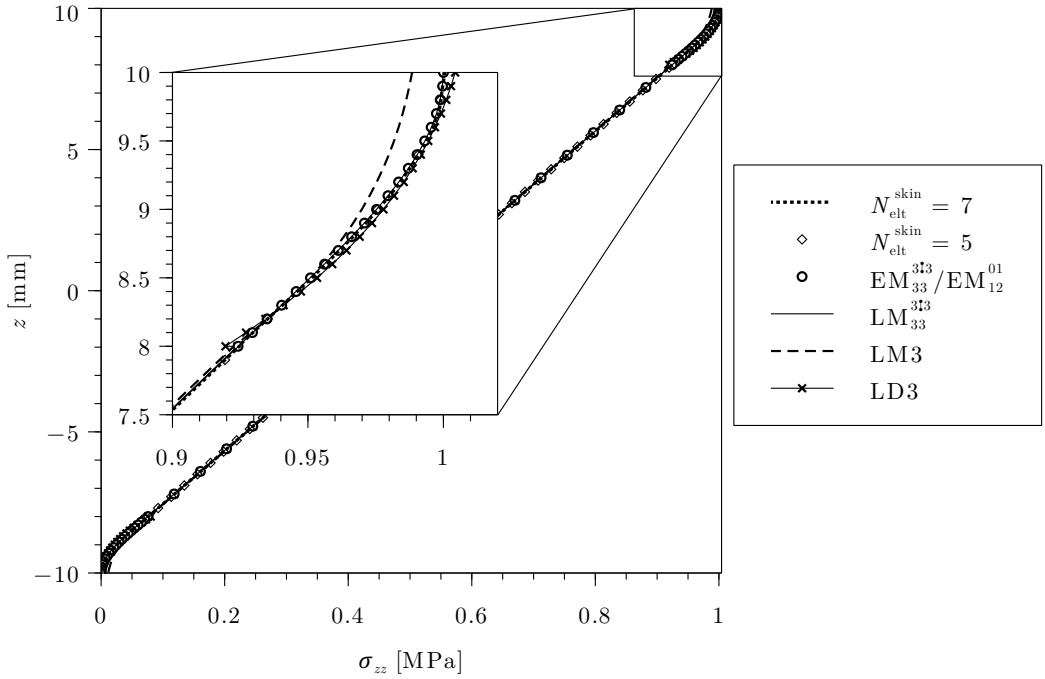

Figure D.4: Through-thickness distribution of the transverse normal stress σ_{zz} at $(x = 0, y = 0)$. Comparison between 3D and present 2D solutions. 3D models involve only one element in the core $(N_{\text{elt}}^{\text{core}} = 1)$.

Table D.6: Local response and DOFs comparison between analytical solution [114], conventional 3D FEM and 2D models.

Model	z [mm]	σ_{xz} [MPa]	$\Delta_{\sigma_{xz}}$ [%]	σ_{zz} [MPa]	$\Delta_{\sigma_{zz}}$ [%]	DOFs
Ref [114]	10	0.00000		1.00000		-
	8^+	2.06377	0.00	0.92377	0.00	
	8^-	2.06377		0.92377		
$N_{\text{elt}}^{\text{skin}} = 7, N_{\text{elt}}^{\text{core}} = 1$	10	0.01418		1.00054		52989
	8^+	2.07851	1.18	0.92430	0.04	
	8^-	2.06669		0.92469		
$N_{\text{elt}}^{\text{skin}} = 5, N_{\text{elt}}^{\text{core}} = 1$	10	0.02688		1.00115		39525
	8^+	2.09134	2.46	0.92437	0.03	
	8^-	2.06669		0.92469		
LD3	10	0.10570		1.00433		24990
	8^+	2.16930	10.4	0.91958	0.44	
	8^-	2.06541		0.92397		
LM3	10	0.10129		0.98845		49980
	8^+	2.06482	0.00	0.92267	0.00	
	8^-	2.06482		0.92267		
$\text{LM}_{33}^{3\overset{\bullet}{1}3}$	10	0.00000		0.99984		49980
	8^+	2.06418	0.00	0.92437	0.00	
	8^-	2.06418		0.92437		
$\text{EM}_{33}^{3\overset{\bullet}{1}3}/\text{EM}_{12}^{01}$	10	0.00000		1.00002		39151
	8^+	2.06751	0.00	0.92421	0.00	
	8^-	2.06751		0.92421		

LM3 model except for the interlaminar continuity of the transverse stress field, which is a priori fulfilled thanks to RMVT. Indeed, in order to improve the corresponding displacement-based solution, the assumed stress field in the mixed approach should be somehow constrained, as stated by Fraejis de Veubeke [159]. A very accurate prediction is hence obtained when the LM3 model is constrained by imposing the homogeneous static conditions on the transverse shear field ($\text{LM}_{33}^{3\overset{\bullet}{1}3}$ model). The SGUF model allows to recover the $\text{LM}_{33}^{3\overset{\bullet}{1}3}$ model solution while drastically reducing the DOFs in the core layer.

Finally, Table D.6 provides a measure of both accuracy and computational burden associated to each model. Conventional 3D FEM and refined 2D solutions are compared to the analytical solution given by Kardomateas in [114]. In particular, the static condition at top surface is studied along with the facesheet-core discontinuity by

extracting the values of both transverse shear stress σ_{xz} and transverse normal stress σ_{zz} at coordinate $z \in \{8^-, 8^+, 10\}$. The measure of the interlaminar discontinuity is given by referring to the jump Δ defined as follows:

$$\Delta_{\mathcal{S}} = \left| \mathcal{S}\left(z = 8^+\right) - \mathcal{S}\left(z = 8^-\right) \right| \times 100 \tag{D.1}$$

with $\mathcal{S} \in \{\sigma_{xz}, \sigma_{zz}\}$. It is worth noticing that the conventional 3D FEM fails to meet the interlaminar continuity condition, suggesting a further refinement of the discretization in both facesheet and core layers with a consequent increase in the number of DOFs. The displacement-based LD3 model requires the lowest computational overhead but it is found to be inadequate when it comes to accurately predict the transverse shear stresses. On the other hand, the LM3 model and its improvement towards exact fulfilment of the homogeneous top/bottom conditions ($\mathrm{LM}_{33}^{3\updownarrow3}$), both involve a number of DOFs comparable to those required by the conventional 3D FEM. The global/local modelling technique offered by the SGUF model allows to find an excellent compromise between the accuracy of the solution and the computational effort required by the analysis.